UNIVERSITY OF READING

Department of Meteorology

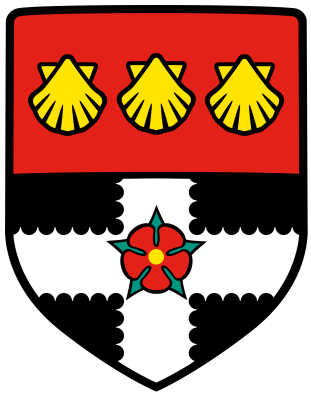

Baroclinic and Barotropic Aspects of Extratropical Wave-Mean Flow Interaction

Lina Boljka

A thesis submitted for the degree of Doctor of Philosophy

June 2018

Declaration

I confirm that this is my own work and the use of all material from other sources has been properly and fully acknowledged.

Lina Boljka

Abstract

Baroclinic and barotropic processes are the key components of midlatitude tropospheric dynamics. Baroclinic processes are involved in the growth of extratropical storms, whereas barotropic processes are involved in their decay, suggesting the two processes are closely linked. Their links are conventionally studied through wave-mean flow interaction theory and through modes of variability, and both planetary and synoptic scale waves play an important role in interacting with the baroclinic and barotropic mean flow.

These processes are studied using multiscale asymptotic methods, which provide a framework for studying wave-mean flow interactions on different spatial and temporal scales. This framework is used to derive the full set of equations for small amplitude planetary and synoptic scale waves and for the zonal mean flow and its interactions with planetary and synoptic waves. In a zonally inhomogeneous framework (planetary-wave amplitudes comparable to synoptic-wave amplitudes) this theory predicts a coupling of baroclinic and barotropic processes through the planetary scale waves, and the interactions between the planetary and synoptic waves only occurring via the zonal mean flow or diabatic and frictional processes. However, in a zonally homogeneous framework (negligible planetary waves) baroclinic and barotropic processes are decoupled, with eddy momentum fluxes only affecting the barotropic flow and eddy heat fluxes only affecting the baroclinic flow, consistent with some recent observational studies.

The latter somewhat counterintuitive result is studied in a zonally homogeneous idealized model and in Southern Hemisphere observations, using the baroclinic and barotropic annular modes of variability at different timescales. This shows that the decoupling of the two processes can indeed occur, but is frequency-dependent. The important role of planetary scale waves is explored in a zonally inhomogeneous idealized model and in Northern Hemisphere observations through the variability

in the barotropic and baroclinic mean flows in storm track regions, and links with teleconnection patterns are established.

Acknowledgements

I am extremely grateful to my supervisors, Ted Shepherd, Mike Blackburn and Brian Hoskins, for giving me this opportunity and for their continuous support and advice throughout this project. I am also thankful to my monitoring committee members, Clare Watt, Tom Frame and Mike Lockwood, as well as my examiners, Tom Frame and Peter Haynes, for providing their feedback.

I am also grateful for the funding provided by the European Research Council (Advanced Grant ACRCC, "Understanding the atmospheric circulation response to climate change" Project 339390). This work also used the ARCHER U.K. national supercomputing service and the U.K. research data facility (http://www.archer.ac.uk) for data analysis and model integrations.

I would like to thank ECMWF for the ERA-Interim data, NOAA for the teleconnection data, and the Met Office for providing their Unified Model. I am also thankful to NCAS-CMS, Chris Smith, Ian Boutle, Annelize van Niekerk, and Terry Davies for help with the model, as well as to Stamen Dolaptchiev, Rupert Klein, Alan Plumb, Aditi Sheshadri, Nick Byrne, Inna Polichtchouk, Talia Tamarin-Brodsky, Lenka Novak, Tapio Schneider, John Methven, Shannon Mason and Simon Peatman for helpful discussions.

Finally, I would like to thank the other PhD students and all the members of Ted's group for their help and companionship throughout the years, and to my family and friends who always supported and helped me.

Contents

List of Figures

1

Introduction

1.1 Barotropic Aspects of the Atmospheric Mean Flow

One of the most prominent features of the extratropical (midlatitude) dynamics (general circulation) is the jet stream: a belt of strong upper-tropospheric westerly winds. In the Earth's atmosphere there are, conceptually, two jet streams in each hemisphere, one subtropical and one eddy-driven (sometimes referred to as the subpolar jet) (Vallis, 2006). The former is associated with the strong temperature gradients at the edge of the Hadley cell and exhibits a strong vertical wind shear (weak or easterly winds at the surface, strong westerlies aloft). The latter is driven by the midlatitude eddies (e.g. extratropical cyclones), as the name suggests, and exhibits a quasi-barotropic vertical structure (i.e. weak vertical wind shear, westerly winds throughout the troposphere). The two jets are often merged, especially in the zonal mean perspective. Fig. 1.1 shows the annual mean zonal mean zonal wind, which clearly shows the eddy-driven and subtropical jets in the Southern Hemisphere (SH), centred around 50°S and 30°S, respectively, whereas in the Northern Hemisphere (NH) they appear as one merged jet centred around 40°N. The jet stream exhibits large seasonal and geographical variations. In this thesis, only the eddy-driven jet is studied and will henceforth be referred to as the midlatitude jet.

As the midlatitude jet has little vertical wind shear, its dynamics (driving mechanisms and its maintenance) can be largely explained by looking at the barotropic dynamics, i.e. representing the midlatitude baroclinic eddies as stirring (in a momentum conserving way) and examining

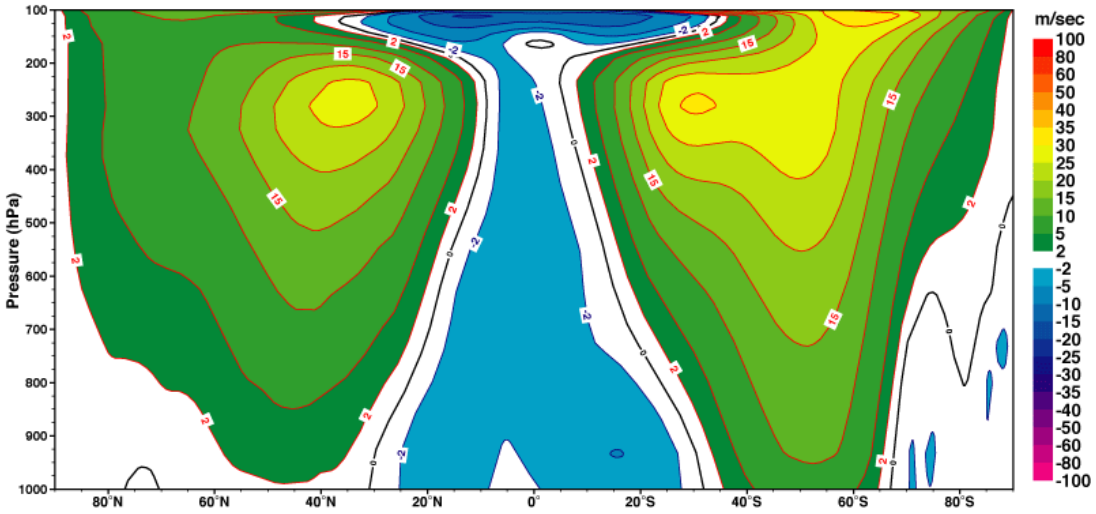

Figure 1.1: Tropospheric annual mean zonal mean zonal wind. - Units are m s^{-1}. Source: ERA-40 Atlas.

the vertically integrated zonal momentum budget (e.g. Lorenz and Hartmann 2001)

$$\frac{\partial\langle[u]\rangle}{\partial t} = -\frac{\partial\langle[u^*v^*]\rangle}{\partial y} - \frac{\langle[u]\rangle}{\tau} \tag{1.1}$$

where u is zonal velocity, v is meridional velocity, $[.]$ represents zonal mean, asterisk $(^*)$ represents deviations therefrom, $\langle.\rangle$ represents vertical mean, y is latitude, t is time, and $\langle[u]\rangle/\tau$ denotes damping of $\langle[u]\rangle$ with τ a constant. The latter is heuristic and includes frictional effects.

As the midlatitudes are stirred, Rossby waves — large scale waves that owe their existence to Earth's rotation (via Coriolis parameter and absolute vorticity gradient) — are generated and propagate away from the source region. If the stirring region is uniform across, for example, midlatitudes (as in Fig. 1.2), the waves propagate out of this region meridionally, generating meridional momentum fluxes ($[u^*v^*]$) in the opposite sense to the wave propagation (e.g. Held and Hoskins 1985) [see also section 1.3.1]. This leads to converging momentum fluxes ($\partial\langle[u^*v^*]\rangle/\partial y < 0$) and acceleration of the zonal mean flow [via (1.1)] in the source region as shown in Fig. 1.2. This picture is supported by the climatological momentum fluxes (Fig. 1.3), which exhibit a dipolar structure with the largest gradients (i.e. momentum flux convergence) in the midlatitudes where the eddy-driven jet is located.

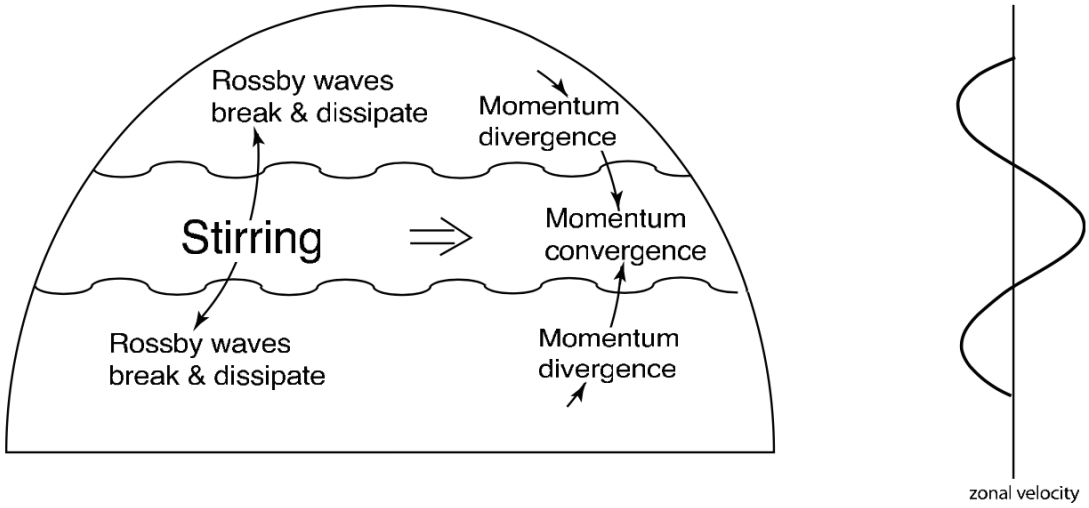

Figure 1.2: Generation of (barotropic) zonal mean flow on a rotating sphere. - Stirring in mid-latitudes generates Rossby waves that propagate away from the source region (disturbance). Momentum thus converges in the region of stirring, producing westerlies there and weaker easterlies on its flanks (see text for details). Source: Vallis (2006), Fig. 12.3.

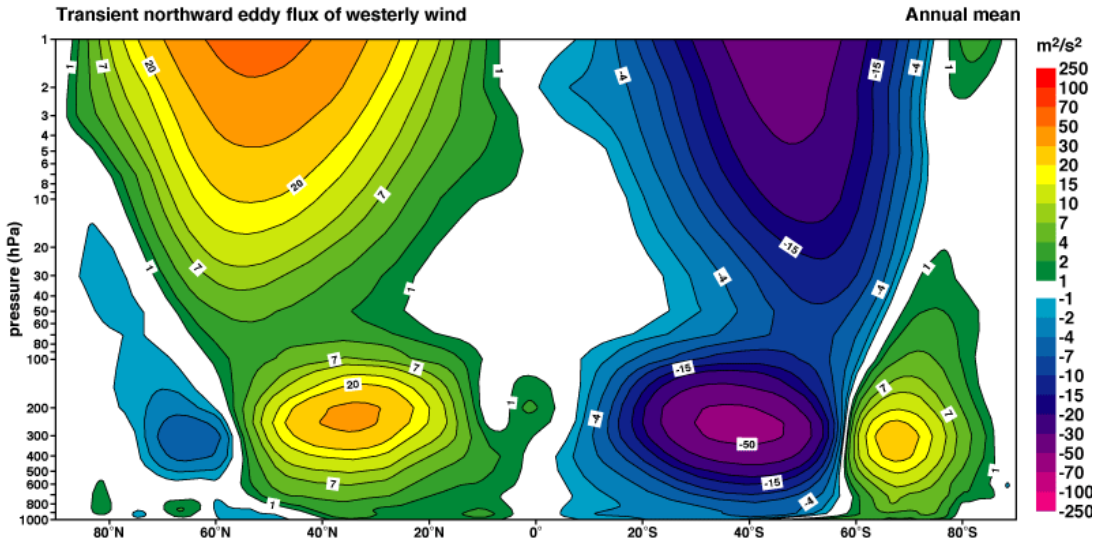

Figure 1.3: Annual mean zonal mean meridional momentum fluxes. - Units are $m^2\ s^{-2}$. Source: ERA-40 Atlas.

1.1.1 Barotropic Annular Modes

One of the commonly used indicators of midlatitude jet variability is the annular modes of variability (known as Southern (SAM) and Northern (NAM) Annular Modes, sometimes referred to as Antarctic and Arctic Oscillations, respectively) (e.g. Thompson and Wallace 2000). They

are the most important modes of variability in the extratropical atmosphere and occur in extratropical latitudinal bands (hence annular), representing north-south shifts of the midlatitude jet within a zonal mean framework. The decorrelation timescales associated with them are typically about 10 days (e.g. Hartmann and Lo 1998), but can be longer (up to about 30 days) in the seasons when there is coupling with the stratospheric polar vortex, leading to more persistent tropospheric behaviour (e.g. Simpson et al. 2011), and are also typically longer in idealised model configurations (e.g. Gerber et al. 2008), such as that of Held and Suarez (1994).

Note that in the NH midlatitudes there are also regional patterns of variability, e.g. the North Atlantic Oscillation, hence the NAM may include some power from its regional components (e.g. Ambaum et al. 2001). These patterns are further discussed in Chapter 4. Nonetheless, the annular modes still have a meaning via (1.1).

The annular modes are usually calculated using empirical orthogonal function (EOF) analysis (a method that identifies the pattern that explains the most variance of climate variability) on horizontal geopotential height, surface pressure or zonal mean zonal wind (e.g. Thompson and Wallace 2000). The ordering of modes is determined by the amount of variance explained by each EOF (e.g. here the first/leading EOF explains the most variance in the field and is usually referred to as annular mode). The successively higher modes tend to have successively more complex spatial structure and represent (significantly) less variability in the field.

Annular modes are linked to the momentum fluxes, as expected from the barotropic dynamics (1.1). This is clearly shown in Fig. 1.4, which shows the leading EOF of the zonal mean zonal wind (SAM) in contours, showing a dipolar structure, centred at the maximum of the climatological zonal mean zonal wind, which represents north-south shifts of the jet. The colours in Fig. 1.4 show momentum flux regression onto the timeseries associated with SAM and clearly show a maximum at the centre of the dipolar SAM structure, which gives momentum flux convergence on the poleward flank of the jet, and momentum flux divergence on the equatorward flank (note that this is the Southern Hemisphere, hence the maximum momentum flux is negative), consistent with acceleration (westerly forcing) and deceleration (easterly forcing) of the westerly zonal mean flow, respectively. This acceleration on one flank of the jet and deceleration on the other flank leads to a jet shift (Fig. 1.4 shows a poleward shift). For the climatological midlatitude jet structure, refer to Fig. 1.1.

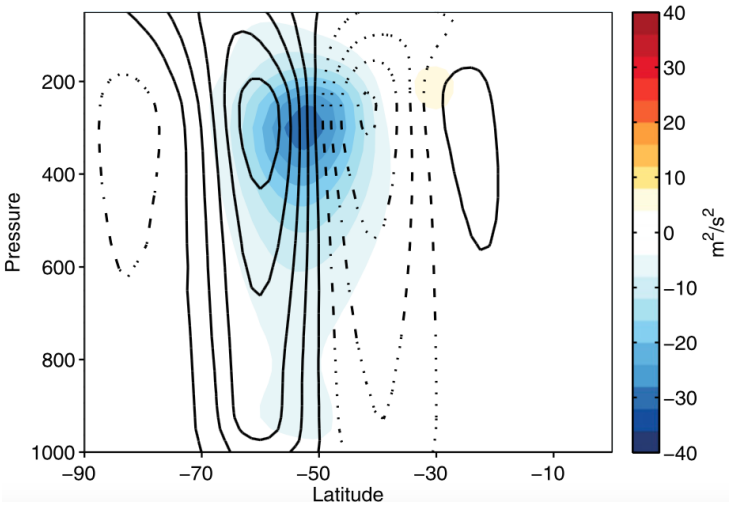

Figure 1.4: Vertical structure of the SAM and the momentum fluxes associated with it. - Contours show the leading mode of variability in zonal mean zonal wind ($[u]$; contour interval is -0.5, 0.5, 1.5, ... m s^{-1}), and shading shows momentum flux ($[u^*v^*]$; m^2 s^{-2}) regression onto this leading mode. Here the regressions of momentum fluxes lead the SAM index by 1 day. Data is from SH ERA-Interim reanalyses. Source: Thompson and Woodworth (2014), Fig. 2a.

1.2 Linking Barotropic and Baroclinic Aspects of the Atmospheric Mean Flow

While the midlatitude jet stream dynamics can be well explained, at least in an approximate sense, through the barotropic mechanisms described above, they are not the only mechanisms affecting it. The horizontal temperature gradients directly affect the winds via the vertical wind shear. The horizontal temperature gradients are also important for the formation of baroclinic eddies (cyclones) through baroclinic instability, which stir the atmosphere and give rise to the momentum fluxes and the strong midlatitude jet stream (as described above).

Baroclinic instability occurs in fluids with strong vertical wind shear of the mean flow (baroclinic region), which is related to the equatorward horizontal temperature gradient (baroclinicity) through thermal wind balance. The baroclinic instability is then 'triggered' when there is a localised (heating) anomaly or advection across the baroclinic region in the atmosphere, which leads to the generation of baroclinic eddies. These eddies then grow through baroclinic instability by converting the available potential energy (P_M) (related to horizontal temperature gradients and diabatic heating) into eddy kinetic energy (K_E) [related to eddy velocity squared: $0.5(u^{*2} + v^{*2})$] (e.g. Holton 2004). The eddy kinetic energy is shown in Fig. 1.5, which shows

its peak in the upper troposphere in a similar region as the midlatitude jet stream in Fig. 1.1.

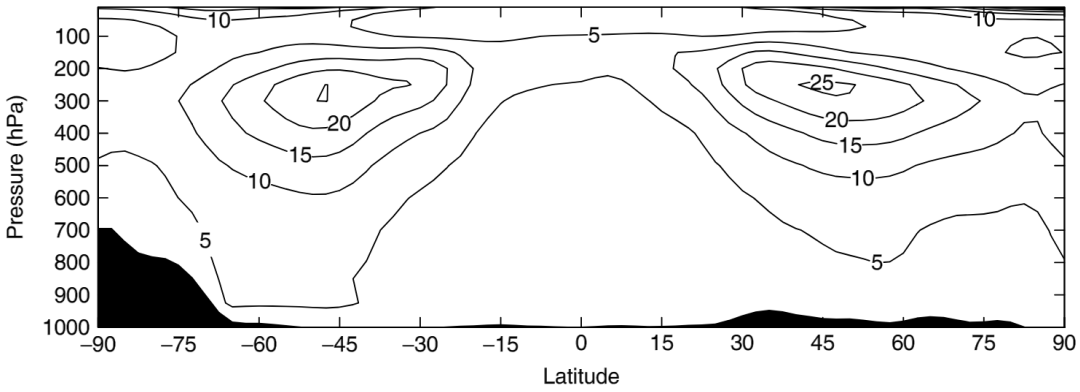

Figure 1.5: Tropospheric annual mean zonal mean eddy kinetic energy per volume. - Units are J m^{-2} Pa^{-1} (to obtain units m^2 s^{-2}, multiply the values by the graviatational acceleration, $g = 9.81$ m s^{-2}). Volume in pressure coordinates is longitude × latitude × pressure. Data is from ERA-40. Source: Marques et al. (2009), Fig. 5.

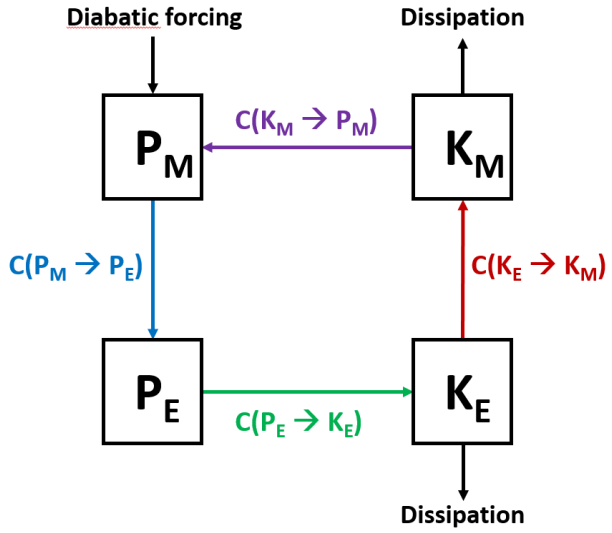

Figure 1.6: A schematic of the Lorenz energy cycle. - P_M represents available potential energy of the zonal mean, P_E represents eddy potential energy, K_E represents eddy kinetic energy and K_M represents the mean flow kinetic energy. The coloured arrows represent the conversion terms between these energies: $C(P_M \rightarrow P_E)$ is conversion from P_M to P_E (blue), $C(P_E \rightarrow K_E)$ is conversion from P_E to K_E (green), $C(K_E \rightarrow K_M)$ is conversion from K_E to K_M (red), and $C(K_M \rightarrow P_M)$ is conversion from K_M to P_M (purple). Note that diabatic forcing is mainly related to the Equator-to-pole temperature gradients (arising from the gradient in solar radiation). See text for further details. Figure is adapted from Lorenz (1955), Plumb (1983), Fig. 1, and Thompson and Woodworth (2014), Fig. 1.

The energy conversion occurs through the poleward and upward transport of heat by the

eddies [i.e. meridional ($v^*\theta^*$) and vertical ($w^*\theta^*$) heat fluxes, with θ potential temperature and w vertical velocity], which is shown in Fig. 1.6 through the conversion terms $C(P_M \rightarrow P_E)$ and $C(P_E \rightarrow K_E)$. The conversions occur simultaneously and are dominated by the conversion via the meridional heat fluxes [$C(P_M \rightarrow P_E)$]. The meridional heat fluxes are shown in Fig. 1.7 and peak in the lower troposphere in a similar latitudinal region as K_E in Fig. 1.5. Further energy conversions in Fig. 1.6 occur between K_E and K_M (kinetic energy of the mean flow) [$C(K_E \rightarrow K_M)$] and between K_M and P_M [$C(K_M \rightarrow P_M)$], and are dominanted by the former which occur via the eddy momentum fluxes, whereas the latter are weaker and related to the mean meridional circulation. The conversion between K_E and K_M represents the barotropic dynamics presented above (i.e. eddies propagate out of the baroclinic region, leading to mean flow acceleration via eddy momentum fluxes), which eventually restore the available potential energy (P_M). This cycle is refered to as the 'Lorenz energy cycle'.

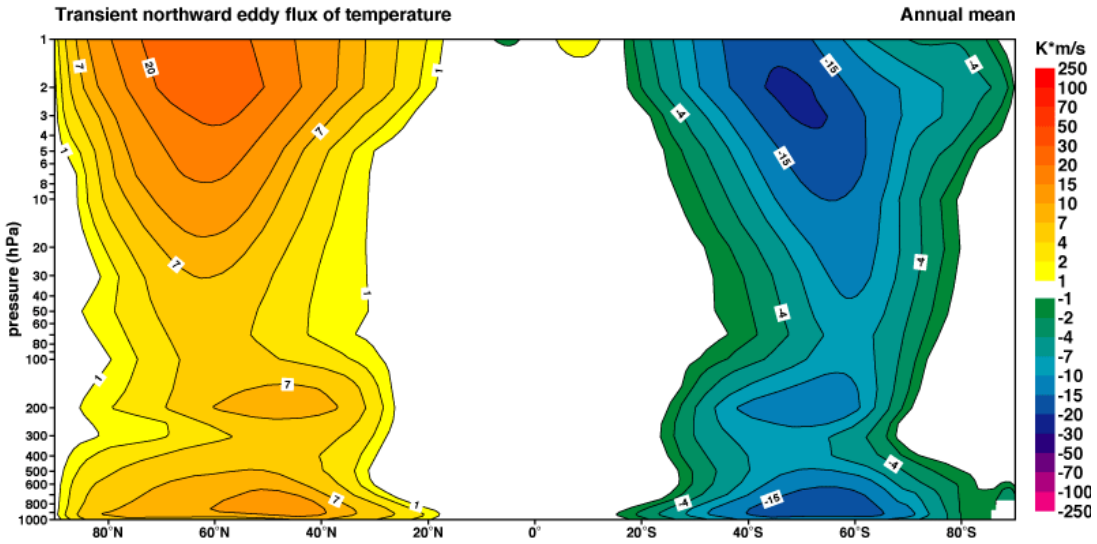

Figure 1.7: Annual mean zonal mean meridional heat flux. - Units are K m s^{-1}. Source: ERA-40 Atlas.

This conversion of energy can also be used to understand baroclinic life cycles (Simmons and Hoskins, 1978), which are depicted in Fig. 1.8. The figure shows the eddy kinetic energy (top panel) evolution throughout a life cycle of a midlatitude cyclone and the energy conversions (bottom panel) that were already described above for the Lorenz energy cycle. The figure demonstrates that eddy heat fluxes [$C(P_M \rightarrow P_E)$, $C(P_E \rightarrow K_E)$] lead to the eddy kinetic energy growth (growth of a cyclone) as their values increase simultaneously in Fig. 1.8, whereas eddy momentum fluxes [$C(K_E \rightarrow K_M)$] lead to a dissipation of K_E (decay of a cyclone) as they

peak during the decay of K_E in Fig. 1.8. At the same time this cycle leads to acceleration of the zonal mean flow (Haynes and Shepherd 1989) as mentioned above. Through this baroclinic life cycle experiment, Simmons and Hoskins (1978) linked the baroclinic (growth of K_E) and barotropic (decay of K_E and mean flow acceleration) processes.

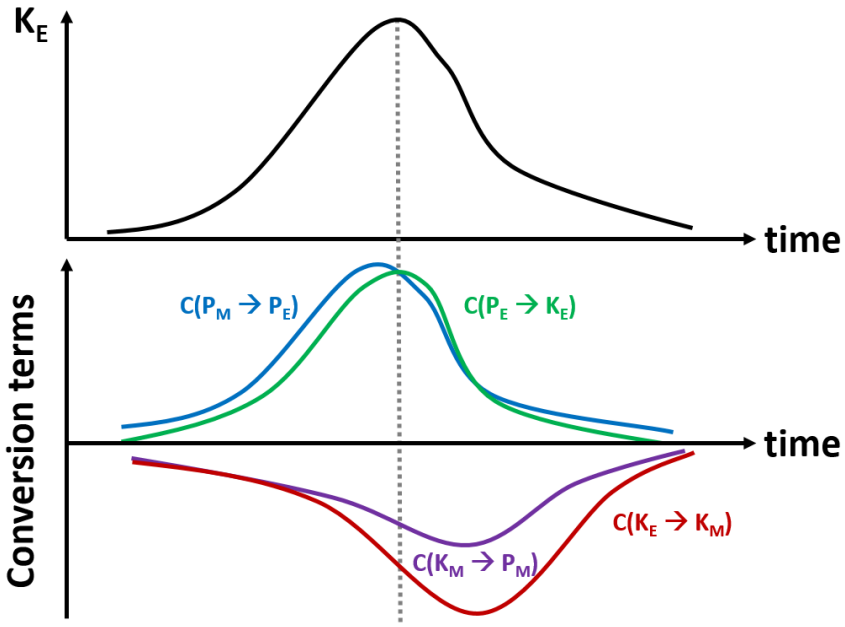

Figure 1.8: A schematic of eddy kinetic energy conversion during a baroclinic life cycle. - Top panel shows K_E during a baroclinic life cycle, and the bottom panel shows the conversion terms (colours and labels as in Fig. 1.6). The timescale in the graph is about 15 days. See text for further details. Figure is adapted from Simmons and Hoskins (1978), Figs. 4 and 5.

As the baroclinic life cycles with a baroclinic source in midlatitudes lead to acceleration of the zonal mean flow in the same region (via barotropic processes), a long term average over the baroclinic zone shows that the midlatitude jet moves together with the regions of high baroclinic eddy activity, which is referred to as the positive baroclinic feedback mechanism (Robinson, 2000) [see also section 1.3.1].

1.2.1 Baroclinic Annular Modes

Given that the eddy kinetic energy (hereafter EKE) is linked to the heat and momentum fluxes, which are then further linked to the zonal mean zonal wind (mean flow kinetic energy), one can test these links using the annular mode analysis on EKE and zonal mean zonal wind. This was done by Thompson and Woodworth (2014), who looked at the leading modes of variability in EKE (baroclinic annular mode or BAM, based on the first EOF of EKE, representing EKE pulsation - contours in Fig. 1.9) and zonal mean zonal wind (SAM), and regressed the momentum and heat fluxes onto these two modes (Figs. 1.4, 1.9). Surprisingly, they found that heat fluxes were linked to the BAM only, momentum fluxes were linked to the SAM only, and essentially no correlation was found between the BAM and SAM (and their regressions onto each other were weak as well), which led to the conclusion that barotropic and baroclinic processes may be decoupled. This is counterintuitive compared to baroclinic life cycle experiments (Simmons and Hoskins, 1978) where the momentum and heat fluxes are linked through eddy growth and decay. It is further confusing due to the quasi-steady (long-term average) positive baroclinic feedback mechanism (Robinson, 2000), which states that the storm tracks move together with the jet shifts, or rather that heat fluxes together with momentum fluxes reinforce the jet stream, i.e. neither storm tracks nor heat fluxes are independent of the barotropic flow (or barotropic annular modes).

Based on the decoupling of the baroclinic flow from barotropic processes, Thompson and Barnes (2014) developed a baroclinic oscillator model between baroclinicity and heat fluxes — namely a zonal mean baroclinicity equation that links heat fluxes to baroclinicity:

$$\frac{\partial [b]}{\partial t} = \alpha_b [v^* \theta^*] - \frac{[b]}{\tau_b} \tag{1.2}$$

where $b = \partial\theta/\partial y$ is baroclinicity, α_b is a constant scaling factor, and $[b]/\tau_b$ represents damping of baroclinicity. Note that in contrast to (1.1), (1.2) does not follow from the equations directly and is merely a heuristic. Thompson and Barnes (2014) found oscillations between baroclinicity and heat flux with about a 25 day period, which was also found in EKE variability (BAM). This suggested an intermediate frequency variability that could be independent of the barotropic dynamics, as suggested by Thompson and Woodworth (2014). Such behaviour is not dynamically implausable, since it arises in weakly nonlinear models of baroclinic instability (Pedlosky, 1970).

Understanding these baroclinic (BAM) and barotropic (SAM, NAM) modes of variability and their (de)coupling is thus important for further understanding of the atmospheric dynamics

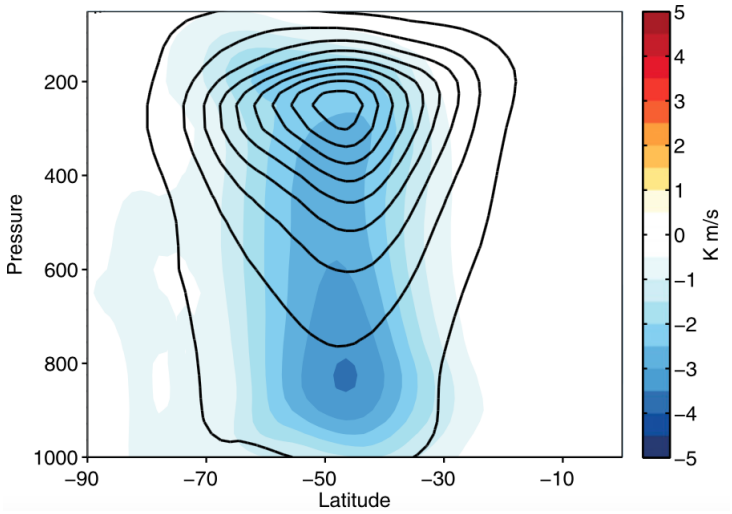

Figure 1.9: Vertical structure of BAM and heat fluxes associated with it. - Contours show the leading mode of variability in EKE (contour interval is -3, 3, 9, ... m^2 s^{-2}), and shading shows heat flux (in K m s^{-1}) regression onto this leading mode. Here the regressions of heat fluxes lead the BAM index by 1 day. Data is from SH ERA-Interim reanalyses. Source: Thompson and Woodworth (2014), Fig. 2f.

on different timescales, and is therefore further addressed in Chapter 3.

1.3 Wave Activity Theory

The sections above focused on mechanistic description of the baroclinic and barotropic aspects of the atmospheric flow and their links. While it was not directly stated in the previous section, the links between the eddies and the mean flow are usually referred to as **wave-mean flow interaction**. The energetics perspective taken above is a useful basis for describing these interactions and provides a simple physical interpretation, however perturbation (eddy/wave) energy is not conserved during the wave-mean flow interaction due to the possibility of exchange of energy between the waves and mean flow (this is how the waves grow in instabilities, e.g. baroclinic instability). Hence a different mathematical description is needed, namely Eliassen-Palm wave activity (after Eliassen and Palm 1961, who first formalised it), which is a "quantity that is quadratic in the amplitude of the perturbation and that is conserved in the absence of forcing and dissipation" (e.g. Vallis 2006), and serves as a generalisation of eddy energy (such as EKE), as it incorporates eddy and mean flow dynamics into one quantity. The aim of this section is thus to provide a mathematical perspective on the above mechanistic approach.

1.3.1 The Zonal Mean Perspective

To derive wave activity (WA) theory, one generally starts from a potential vorticity (PV) equation. Potential vorticity is a quantity that is "conserved following the motion in adiabatic and frictionless flow" (Holton, 2004), and generally represents the ratio between the absolute vorticity (sum of relative and planetary vorticity, i.e. the curl of absolute velocity) and the depth of the vortex (e.g. when the flow/vortex encounters a warm surface anomaly, the column above it stretches, i.e. the depth of the vortex increases, hence also vorticity must increase to conserve PV, leading to a positive/cyclonic relative vorticity anomaly and potentially to baroclinic instability). For simplicity, the derivation of the wave activity theory is described using a small amplitude approximation and quasi-geostrophic (QG) theory. The QG theory provides the minimal model for the atmosphere that permits baroclinic instability, which is essential for the growth of midlatitude eddies (as mentioned above) and provides a simple set of equations that is simpler to interpret than e.g. the full primitive equations. The small amplitude approximation allows a simple treatment of the eddies as perturbations from the zonal mean (e.g. using Reynolds averaging), and provides some qualitative insight into the finite amplitude problem (where eddies are 'permitted' to grow to large amplitudes).

Theory

The QG theory requires some assumptions based on scale analysis (e.g. Vallis 2006, Holton 2004), namely the beta plane approximation to the Coriolis parameter (i.e. small variation of Coriolis parameter, $f = f_o + \beta y$ where f_o is a constant and $\beta = \partial f/\partial y$), the flow is in hydrostatic balance, the horizontal velocity is a sum of geostrophic and ageostrophic winds ($\mathbf{u} = \mathbf{u}_g + \mathbf{u}_a$) with ageostrophic winds (representing the difference between total horizontal velocity and geostrophic wind) much smaller than geostrophic winds (in pressure coordinates: $\mathbf{u}_g = f_o^{-1}\mathbf{e}_r \times \nabla\Phi$ with $\mathbf{e}_r$ vertical unit vector, ∇ horizontal gradient, and Φ is geopotential height), and thermal wind balance holds (using geostrophic velocities and hydrostatic balance: $\partial\mathbf{u}_g/\partial \ln p = -f^{-1}R\mathbf{e}_r \times \nabla T$, where $R = 287$ J K^{-1} kg^{-1} is gas constant, T is temperature and p is pressure). Note that the divergence of the geostrophic wind is zero ($\nabla \cdot \mathbf{u}_g = 0$), and that the vertical motion hence arises from the ageostrophic winds and can be neglected to leading order (i.e. advection occurs in the horizontal plane by geostrophic winds only).

Using these assumptions and supposing there is a zonal mean flow (denoted by [.]) and a perturbation to that flow (denoted by *), one can derive the linearised PV equation [a similar

PV equation is derived in detail in Chapter 2], which yields (e.g. Vallis 2006)

$$\frac{\partial q^*}{\partial t} + [u_g]\frac{\partial q^*}{\partial x} + v_g^*\frac{\partial [q]}{\partial y} = S_q^* \tag{1.3}$$

where S_q are the source-sink terms of PV; q is QG PV defined as

$$q = f + f_o^{-1}\nabla^2\Phi + \frac{\partial}{\partial p}\left(\frac{f_o}{\sigma}\frac{\partial \Phi}{\partial p}\right) \tag{1.4}$$

with $\sigma = -p^{-1}RT_o\partial \ln\theta/\partial p$ as a static stability parameter (linked to Brunt-Väisälä frequency N as $\sigma = (N/\rho_o g)^2$, $T_o(p)$ as background temperature, $\rho_o(p)$ as background density, and g gravitational acceleration); $\partial[q]/\partial y$ is background PV gradient, defined as

$$\frac{\partial [q]}{\partial y} = \beta + \frac{\partial [\zeta_g]}{\partial y} + \frac{\partial}{\partial p}\left(\frac{f_o}{\sigma}\frac{\partial}{\partial p}\frac{\partial [\Phi]}{\partial y}\right) \tag{1.5}$$

with $\partial[\Phi]/\partial y = -f_o[u_g]$ through geostrophic balance, and $\partial[\zeta_g]/\partial y = -\partial^2[u_g]/\partial y^2$ (QG vorticity is the curl of geostrophic velocity).

If we assume further that $[q]$ is steady in time (or evolving slower than eddy q^*) for simplicity, then a wave activity (density) equation can be derived by multiplying (1.3) by q^*, dividing the resulting enstrophy equation (enstrophy is q^{*2}) by the background PV gradient, and taking a zonal mean of the final equation. This gives

$$\frac{\partial \mathcal{A}}{\partial t} + \nabla_x \cdot \mathbf{F} = \mathcal{D} \tag{1.6}$$

where $\mathcal{A} = [q^{*2}]/(2\partial[q]/\partial y)$ is wave activity density, $\mathcal{D} = [S_q^* q^*]/(\partial[q]/\partial y)$ is the wave activity source-sink term, and $\nabla_x \cdot \mathbf{F} = [v^* q^*]$ is Eliassen-Palm (EP) flux divergence (or meridional PV flux), $\nabla_x = (\partial/\partial y, \partial/\partial p)$, and $\mathbf{F}$ is EP flux, defined as

$$\mathbf{F} = \left(-[u^*v^*], \frac{f_o[v^*T^*]}{T_o\partial \ln\theta/\partial p}\right) \tag{1.7}$$

with $\partial\Phi/\partial p$ replaced by $-RT/p$ (via hydrostatic balance), and σ replaced by $-p^{-1}RT_o\partial \ln\theta/\partial p$.

The wave activity equation (1.6) is an equation for the eddies, and the wave activity density's volume integral is conserved in the absence of forcing and dissipation ($\mathcal{D} = 0$), as wave activity density incorporates eddy dynamics through enstrophy and mean flow dynamics through

background PV gradient (conserved for interactions).

In order to find the eddy influence on the mean flow (and vice versa), Andrews and McIntyre (1976) derived the so-called transformed Eulerian mean (TEM) system of equations, which linked the EP flux divergence to the zonal momentum equation, e.g.

$$\mathcal{L}_1\left(\frac{\partial[u]}{\partial t}\right) = \mathcal{L}_2\left(\nabla_x \cdot \mathbf{F}, S_u\right) \tag{1.8}$$

where $\mathcal{L}_1$ is an invertible operator, $\mathcal{L}_2$ is another operator, and S_u are source-sink terms. This is now the basis for the wave-mean flow interaction theory, as the EP flux divergence links the equation for the zonal mean flow (1.8) and the equation for the eddies (1.6), i.e. providing the interaction between the two components of the flow. Note that $\mathcal{L}_1$ (e.g. $\mathcal{L}_1 \propto \partial^2/\partial y^2 + \partial^2/\partial p^2$) and $\mathcal{L}_2$ (e.g. $\mathcal{L}_2 \propto \partial^2/\partial y^2$) [e.g. Andrews et al. 1987] depend on the regime considered. To simplify (1.8), we can vertically average (1.8) [integrating out the vertical derivative in $\mathcal{L}_1$ leading to $\mathcal{L}_1 = \mathcal{L}_2$ in the above example], and substitute EP flux divergence with wave activity using vertically averaged (1.6), yielding

$$\frac{\partial\langle[u]\rangle}{\partial t} = -\frac{\partial\langle\mathcal{A}\rangle}{\partial t} + \langle S_u\rangle + \langle\mathcal{D}\rangle. \tag{1.9}$$

In the abscence of forcing and dissipation (1.9) then reduces to

$$\frac{\partial\langle[u]\rangle}{\partial t} + \frac{\partial\langle\mathcal{A}\rangle}{\partial t} = 0, \tag{1.10}$$

which means that if wave activity increases in some part of the domain, the zonal mean wind must decrease there, and vice versa. If further the waves are steady and conservative ($\mathcal{A}$ = const.) then also $[u]$ = const., which is also referred to as the non-acceleration theorem.

This perspective also links the baroclinic and barotropic aspects of the atmospheric flow, i.e. recall the baroclinicity equation (1.2) which includes heat fluxes and the barotropic zonal momentum equation (1.1) which includes momentum fluxes, which are now linked through EP flux and wave activity theory (1.8, 1.9). Consequently, this also provides a clearer picture for the baroclinic life cycles and positive baroclinic feedback (see below).

Visualising Wave-Mean Flow Interaction

Assume now that the source-sink term of wave activity ($\mathcal{D}$) can be decomposed into forcing and dissipation contributions (where the forcing dominates in a meridionally confined stirring region, and dissipation dominates outside that region, e.g. Fig. 1.10), and use simple damping on zonal mean wind as in (1.1) for S_u, then (1.9) becomes (Vallis, 2006)

$$\frac{\partial\langle[u]\rangle}{\partial t} + \frac{\partial\langle\mathcal{A}\rangle}{\partial t} = -\frac{\langle[u]\rangle}{\tau} + \frac{\langle\mathcal{A}_F\rangle}{\tau_A} - \frac{\langle\mathcal{A}_D\rangle}{\tau_A}. \tag{1.11}$$

where subscripts F and D represent forcing and dissipation, respectively, and τ_A is a constant. In a quasi-steady state the left-hand-side of (1.11) vanishes and a steady solution for zonal mean wind can be obtained via wave activity forcing ($\mathcal{A}_F/\tau_A$) and dissipation ($\mathcal{A}_D/\tau_A$). In a region where the stirring dominates (e.g. the baroclinic eddy stirring region of midlatitudes) $[u]$ will be proportional to forcing $\mathcal{A}_F$, i.e. $[u] > 0$ or westerly in this region (Fig. 1.10). On the other hand, in the region where damping dominates (regions outside the midlatitudes) $[u]$ will be proportional to damping $-\mathcal{A}_D$, i.e. $[u] < 0$ or easterly in this region (Fig. 1.10). This

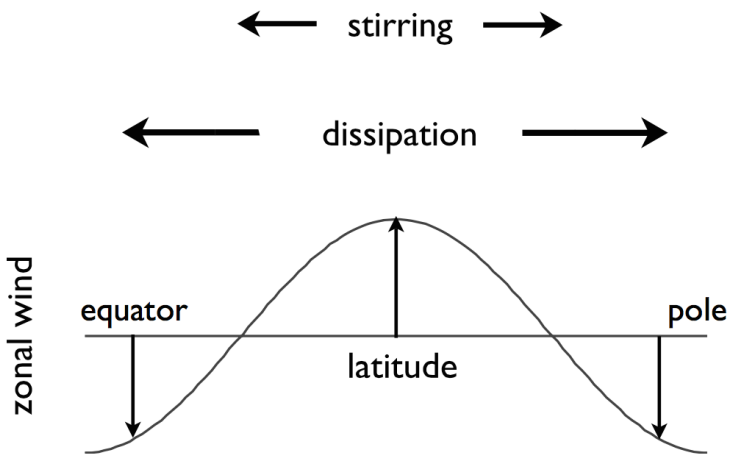

Figure 1.10: Zonal mean flow generation by a meridionally confined stirring. - As Rossby waves propagate away from the source region, the distribution of the dissipation region becomes broader than that of the forcing region, and the sum of the two leads to the zonal wind distribution shown (westerlies in stirring region). Source: Vallis (2006), Fig. 12.5.

is consistent with the barotropic picture discussed at the beginning of this chapter, where the upgradient momentum fluxes caused a westerly acceleration in midlatitudes (stirring region) and an easterly acceleration elsewhere. Note that the wave forcing region here is mainly associated with the baroclinic growth, where the meridional heat fluxes play a large role, and since the zonal

mean zonal wind ($[u]/\tau$) is proportional to wave activity ($\mathcal{A}_F/\tau_A$) with positive proportionality constant (i.e. westerly forcing), this can be related to the positive baroclinic feedback mechanism (Robinson, 2000), where baroclinic regions move with the jet streams (i.e. the wave activity generation region is where the winds are westerly); this is only possible if the waves break outside this region (meridional propagation of the waves), which leads to a net westerly wind generation (through momentum fluxes).

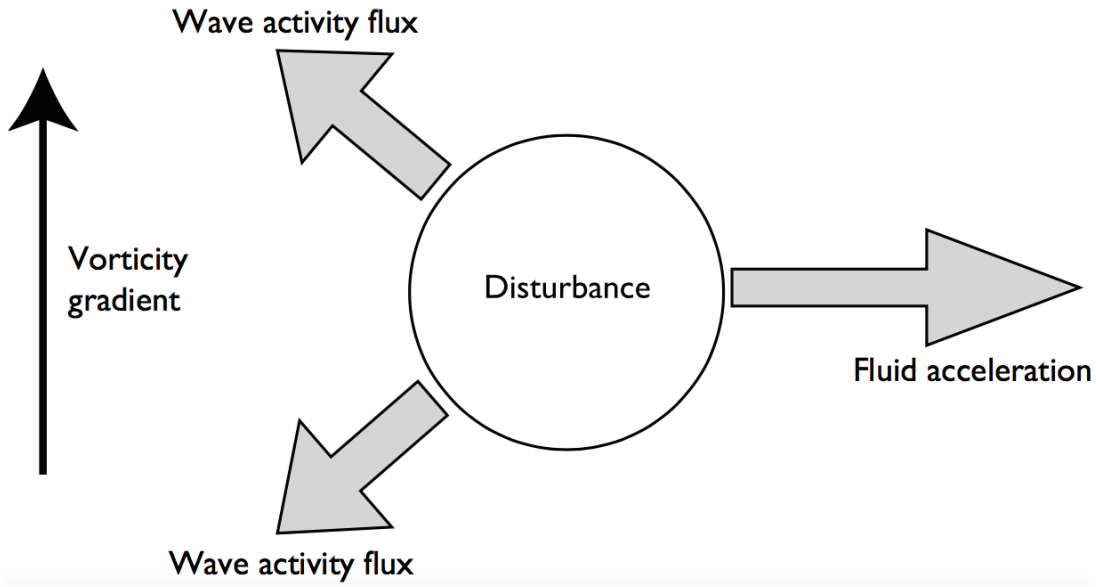

Figure 1.11: A schematic of wave activity flux propagation and its mean flow acceleration. - If a region of fluid is stirred this leads to Rossby wave (wave activity density flux) propagation out of that region, leading to divergence of wave activity in the stirring region and acceleration of the mean flow via (1.10). Source: Vallis (2006), Fig. 12.6.

It can further be shown that EP flux is related to wave activity and the group velocity of Rossby waves as (e.g. Vallis 2006)

$$\langle \mathbf{F} \rangle = \langle F^y \rangle \mathbf{e}_\phi = \langle c_g^y \mathcal{A} \rangle \mathbf{e}_\phi \tag{1.12}$$

where $F^y = -[u^* v^*]$, c_g^y is meridional group velocity, and $\mathbf{e}_\phi$ is meridional unit vector. This helps interpreting the wave (and wave activity) propagation by using EP flux. In this vertically integrated case, when the EP flux is positive there is poleward propagation of the waves (in NH), and the opposite is true for negative meridional EP flux (e.g. wave activity flux arrows in Fig. 1.11). This relation also clearly shows that the momentum fluxes act in the opposite sense to the wave propagation as $c_g^y \mathcal{A} = -[u^* v^*]$, which leads to momentum flux convergence into the

source region and zonal flow acceleration there (e.g. fluid acceleration arrow in Fig. 1.11), as mentioned at the beginning of the Chapter. This is further confirmed by the non-acceleration theorem (1.10), which shows that if the wave activity is propagating away from the source region (the stirring region creates wave activity which then propagates away), $\partial\mathcal{A}/\partial t < 0$ and hence the zonal mean zonal wind acceleration is westerly there; in the region the wave activity propagates into (outside the stirring region) $\partial\mathcal{A}/\partial t > 0$, hence providing easterly zonal mean zonal wind acceleration (Fig. 1.11). This is consistent with the baroclinic life cycles (Simmons and Hoskins, 1978; Edmon et al., 1980) and their overall acceleration of the mean flow in the baroclinic region (Haynes and Shepherd, 1989).

This again shows that the wave activity (and TEM) picture clearly links the heat and momentum fluxes to both wave activity and zonal mean zonal wind, however the baroclinic annular mode (section 1.2.1), which is based on EKE (in some sense a proxy for wave activity) is decoupled from the zonal mean zonal wind (barotropic annular mode). To describe that, a different theory for wave activity is necessary — one that would decouple the two parts of the flow. This is addressed in Chapter 2.

1.3.2 The Zonally Inhomogeneous Perspective

The above section took a zonally homogeneous perspective on wave-mean flow interaction, which can be relevant for atmospheres without strong zonal asymmetries (such as land-sea contrasts, localised heating and orography). This can be applied to some extent to Earth's SH, however the NH is highly non-homogeneous and the zonal mean perspective can often lead to a misleading picture (e.g. Ambaum et al. 2001 for an example of annular modes). In the zonally homogeneous case the wave activity addresses interactions between eddies (perturbations to zonal mean flow) and zonal mean flow, but does not address interactions between different types of eddies, such as planetary (waves of length scale of order of Earth's radius) and synoptic (eddies of order 1000 km, or baroclinic cyclones) waves. The planetary waves become important on local scales as they are excited by local asymmetries in the atmosphere, and can influence the paths of synoptic eddies as well as the zonal mean flow. This is clear, for example, from the NH storm tracks (average paths of the baroclinic eddies, usually seen through time mean EKE maps and cyclone tracks, e.g. Fig. 1.12), which are tilted south-west to north-east, which is also the general jet stream propagation due to deflection of the flow around the orography (e.g. the Rockies in North America, the Himalayas in Asia) and continents, which typically has a planetary scale wave

signature (e.g. Valdes and Hoskins 1989, 1991). Due to large land-sea temperature contrasts and strong western boundary currents, the storm tracks generally begin in the western ocean basins (where baroclinicity is the strongest) (e.g. Hoskins and Valdes 1990). The storms then propagate away from the baroclinic source region, generally in the direction of the jet stream (i.e. tilted) where they dissipate through barotropic mechanisms. This requires a 3D (x, y, z) theory and cannot be fully explained by the zonal mean picture.

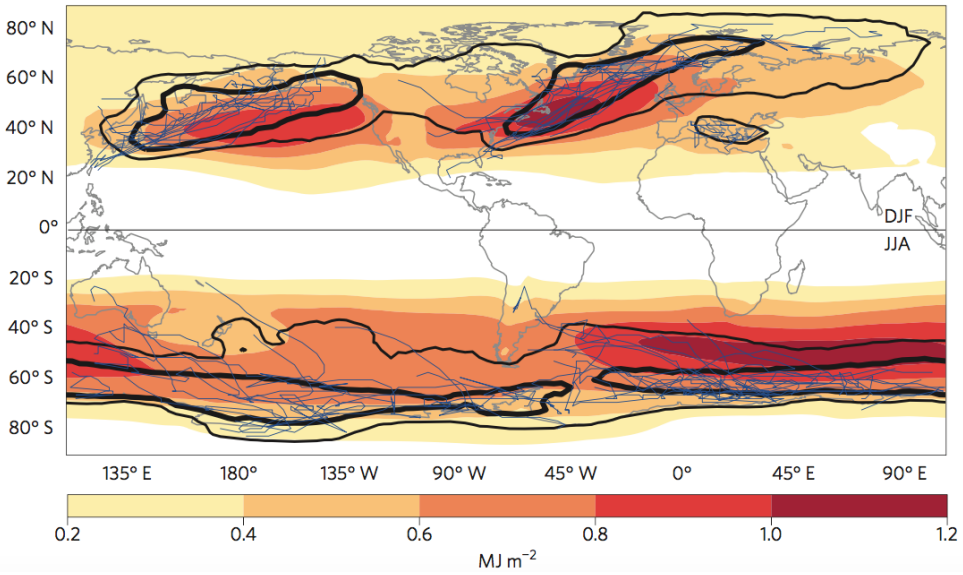

Figure 1.12: Vertically integrated, ten-day high-pass filtered EKE. - EKE is in shading (in MJ m^{-2}), blue lines show individual cyclone tracks for the most intense cyclones (of each region). Black contours show cyclone track density (thin contour represents 10 tracks per season; thick contour represents 20 tracks per season). The data is from ERA-Interim reanalyses; NH data is from boreal winter (DJF) and SH data is from austral winter (JJA). Source: Shaw et al. (2016), Fig. 1a.

Hoskins et al. (1983) and Plumb (1985, 1986) have thus attempted 3D wave, mean-flow interaction theories. Plumb (1985, 1986) derived a 3D wave activity equation for stationary and transient eddies, respectively, whereas Hoskins et al. (1983) derived an equation for the 3D mean flow with an influence of the eddies onto it through the divergence of the E-vector, a 'quasi-vector' resembling EP flux ('extended EP flux'). The E-vector, $\mathbf{E} = (\overline{v'^2} - \overline{u'^2}, -\overline{u'v'}, f_o\overline{v'\theta'}/(\partial\Theta/\partial p))$ (with overline denoting time mean, prime denoting perturbation therefrom, and $\partial\Theta/\partial p$ related to stability parameter σ) therefore provides an insight into the eddy feedback onto the mean flow and its links to the storm tracks. This work has provided insight into 3D flow propagation and eddy interaction with the mean flow, however none of these theories linked the (zonal) momentum and the wave activity equations, which still remains an open question.

1.4 Multiscale Asymptotic Methods and Model Simulations

Atmospheric processes occur on different temporal and spatial scales, and to better understand these processes, a scale analysis of the flow is usually performed (as was done to derive the QG system of equations above), which reduces the full system of equations to leading contributions to the atmospheric flow of interest (in QG scaling, the synoptic eddies are of interest). This also helps in reducing numerical models to reduce computational cost. By doing this one can build a hierarchy of theoretical and numerical models, in order to better understand the dynamics and also, for example, the model response to different forcings. This approach was already used above, namely first a barotropic system was introduced, explaining the mechanism of eddy-driven jets via upgradient momentum fluxes, then baroclinicity was added into the system (e.g. QG model), and explanation of phenomena was attempted through energetics and the more complex wave activity perspective for the zonal mean, and finally also for zonally inhomogeneous atmospheric flow. Below we describe a self-consistent approach to deriving the theoretical models (asymptotic methods), and how the numerical models can help us achieve better understanding of atmospheric dynamics (hierarchies of models).

1.4.1 Multiscale Asymptotic Methods

Klein (2000, 2004) proposed a self-consistent mathematical framework for deriving equations for atmospheric flow on different spatial and temporal scales, the multi-scale asymptotic theory. The asymptotic theory alone can provide leading order equations for atmospheric flow by assuming the properties of the system (similar to scale analysis for e.g. QG system), however it does not account for the different scales that can interact and come into play at the same order of the equations. The multi-scale approach fills that gap and provides a systematic way of treating different atmospheric phenomena simultaneously.

The asymptotic methods generally require a definition of a small parameter (e.g. $\varepsilon \ll 1$), which is then used to separate the different spatial and temporal scales, as well as to expand the variables in the system (e.g. in compressible primitive equations) in asymptotic series

$$\mathcal{U} = \sum_i \varepsilon^i \mathcal{U}^{(i)} \left(..., \frac{t}{\varepsilon}, t, \varepsilon t, ..., \frac{\mathbf{x}}{\varepsilon}, \mathbf{x}, \varepsilon \mathbf{x}, ..., \frac{z}{\varepsilon}, z, \varepsilon z, ... \right) \tag{1.13}$$

where $\mathbf{x} = (x, y)$, $\mathcal{U}$ is one of the variables of the system of interest (e.g. in atmospheric dynamics $\mathcal{U}$ can be a velocity (u, v, w), temperature (T or θ), pressure (p), or density (ρ)). $\mathcal{U}$ depends on

different spatial and temporal scales that are separated by a factor of ε (in the above definition).

Dolaptchiev and Klein (2009, 2013) used this approach to derive planetary geostrophic equations for planetary scale waves, and to derive equations involving planetary-synoptic scale interactions using different temporal and spatial scales for different types of waves (planetary waves have a temporal scale of about a week, synoptic scale eddies have a temporal scales of the order of a few days, and their spatial scales are as defined above). By doing so, they were able to derive potential vorticity equations for the planetary and synoptic scales, which showed direct interaction terms between synoptic and planetary waves at leading orders. Thus, even though the resulting synoptic PV resembled the QG PV, the PV equations now included interaction of waves acting on different time and spatial scales. While they provided the PV equations, they did not derive the wave activity equation, which is essential for studying wave-mean flow interactions (see Chapter 2). The multiscale asymptotic methods thus provide an opportunity for studying the extratropical wave-mean flow interaction on different scales, bridging the gap between zonally homogeneous and inhomogeneous flow theories.

1.4.2 Model Simulations

As with using the theoretical framework to build simple models to better understand the atmospheric processes, we can also use the modelling framework, the so-called model hierarchies (e.g. Held 2005). For large scale dynamics involving storm tracks, the model hierarchy is shown in Fig. 1.13 (Shaw et al., 2016). This typically involves dry dynamical core models ranging from one-layer barotropic, two-layer quasi-geostrophic (baroclinic) to multi-layer Held and Suarez (1994) type models; moist dynamical core models with prescribed sea surface temperatures (SST) ranging from idealised moist core, to aquaplanet and Earth atmospheric general circulation models (GCMs); and finally to coupled atmosphere-ocean models, ranging from idealised slab ocean aquaplanet GCMs to fully coupled Earth GCMs, which are usually used for climate change studies (such as the Intergovernmental Panel for Climate Change (IPCC) reports).

The focus of this thesis spans the dry and moist dynamical cores, i.e. the Held-Suarez and prescribed SST aquaplanet experiments. Both configurations are generally zonally homogeneous, i.e. no flow asymmetries are introduced through, for example, localised heating or orography. This provides a framework for studying zonal mean wave-mean flow interactions, with different atmospheric variabilities, for example by warming or cooling the stratosphere and consequently moving the tropospheric jet equatorwards or polewards (see Chapter 3). It also

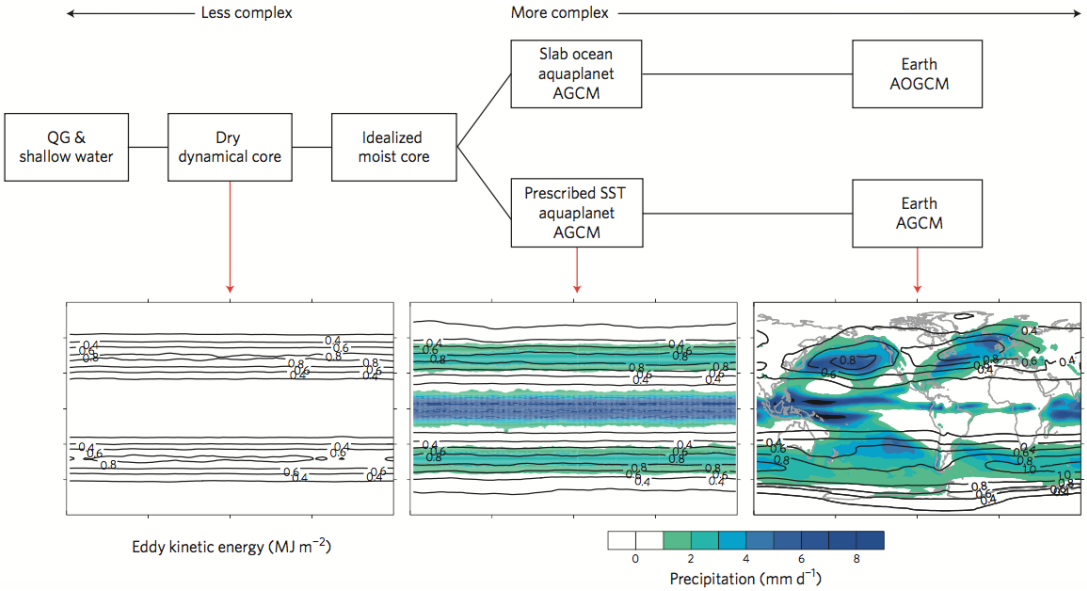

Figure 1.13: Schematic of idealised model hierarchy. - The bottom panels show typical precipitation (colours) and EKE structure (contours) for different types of models. Source: Shaw et al. (2016), Fig. B2.

provides a framework for analysing the differences in atmospheric flow response to local asymmetries compared to a zonally homogeneous configuration, i.e. the strength of planetary scale waves and their influence on synoptic waves and the zonal mean flow, and studying local wave-mean flow interaction (see Chapter 4). These zonally homogeneous and inhomogeneous model configurations are therefore used to test the multiscale asymptotic theory mentioned above (see Chapter 2).

1.5 Aims of the Thesis and Outline

The overall aim of this thesis is to elucidate the interplay between baroclinic and barotropic processes in both zonally homogeneous and inhomogeneous frameworks on different temporal and spatial scales in order to clarify some of the unresolved aspects of the theoretical (synoptic and planetary wave interaction with the zonal mean flow) and empirical results (e.g. baroclinic and barotropic annular modes and their coupling).

Chapter 2 thus first extends the multiscale asymptotic work of Dolaptchiev and Klein (2009, 2013), by deriving the wave activity theory as well as the equations for the mean flow, providing a wave-mean flow interaction theory for small amplitude planetary and synoptic waves and

their interactions with the zonal mean flow. This Chapter also explicitly addresses the zonally homogeneous framework (i.e. without forced planetary waves), which reveals a decoupling of the baroclinic and barotropic components of the flow. This work is based on Boljka and Shepherd (2018).

The coupling (or not) of the baroclinic and barotropic flows in a zonally homogeneous framework is then further addressed in Chapter 3, using the baroclinic and barotropic annular modes. Their coupling is studied at different timescales, and for the first two barotropic annular modes as well as the first three baroclinic annular modes, extending the work of Thompson and Woodworth (2014). By analysing the baroclinic and barotropic variability, this Chapter also tests the extent to which the multiscale asymptotic theory of Chapter 2 works in a zonally homogeneous framework, as well as the robustness of the results to different model climatologies. This work is based on Boljka et al. (2018).

As Chapter 3 addresses the zonally homogeneous framework only, Chapter 4 addresses zonally inhomogeneous baroclinic and barotropic mean flows, which rounds off the analysis of the theory presented in Chapter 2. This analysis examines the relative importance of planetary and synoptic waves for forcing the mean flow in a zonal mean perspective as well as for the localised storm track regions, again looking at the variability on different timescales as well as in the time mean.

Chapter 5 concludes the thesis by summarising the results and providing suggestions for future work that could extend the results from this thesis.

Note that the methodology is described within each Chapter where necessary. Appendices A-L provide additional information for Chapters 2-4 and are referenced therein.

2

Multiscale Asymptotic Theory

2.1 Introduction

The interaction between jet variability and eddies is a long-studied topic, but the interaction is not yet understood well enough to identify causal mechanisms for variability or sources of systematic errors in models [see also Chapter 1]. There are well-developed theoretical frameworks for the zonally homogeneous case (e.g. annular-mode variability discussed in section 1.1.1), however zonally asymmetric analyses including planetary scale interactions are more complicated and only partial theories for this case exist (Hoskins et al., 1983; Plumb, 1985, 1986) [see section 1.3.2]. Yet longitudinal variations and synoptic-planetary scale interactions are important for the location and strength of the storm tracks and blocking episodes (Hoskins et al., 1983; Luo, 2005; Simpson et al., 2014). These phenomena strongly affect the regional climate and its climate change. As the dynamical aspects of climate are not yet well understood, there is low confidence in circulation patterns simulated by global and regional models and their response to climate change (Shepherd, 2014).

An important aspect of wave-mean flow interaction concerns barotropic and baroclinic processes and their links through eddy momentum and heat fluxes [e.g. sections 1.2 and 1.3]. It has recently been shown from observations for the Southern and Northern Annular Modes in Thompson and Woodworth (2014) and Thompson and Li (2015) that the zonal mean flow is affected only by momentum fluxes and not by heat fluxes, while the opposite is true for a so-called baroclinic annular mode (BAM) that is based on eddy kinetic energy (EKE) [see sections 1.1.1 and 1.2.1]. This decoupling goes against the usual Transformed Eulerian Mean (TEM) perspec-

tive, first introduced by Andrews and McIntyre (1976), within which both heat and momentum fluxes affect the zonal mean flow tendency through the Eliassen-Palm (EP) flux divergence [see section 1.3.1]. The decoupling was further investigated in Thompson and Barnes (2014), who found an oscillating relationship between EKE and heat flux with time periods of 20-30 days [see section 1.2.1]. A similar relationship was found between wave activity and heat flux in Wang and Nakamura (2015, 2016).

To derive a theoretical framework for understanding planetary-synoptic scale interactions and the apparent decoupling of the baroclinic and barotropic parts of the flow, we use multi-scale asymptotic methods as introduced in Dolaptchiev and Klein (2009, 2013) (hereafter DK09 and DK13, respectively). This approach is taken as such methods provide a self-consistent (albeit idealised) framework for studying interactions between processes on different length and time scales, starting from a minimal set of assumptions [see section 1.4]. While the derived theory using these methods may not be quantitatively accurate for the atmosphere, it can still provide qualitative value, especially when trying to determine the causal relationships that are so elusive in standard budget calculations. This is analogous to the use of the quasi-geostrophic approximation, which provides a clear qualitative picture of the large scale flow and both planetary and synoptic scale eddies, however for accurate representation of the flow (e.g. in weather prediction), the primitive equations are used. Therefore, the aim of this work is to find a theoretical framework by which to better understand the emergent properties of observations and model behavior, rather than developing a predictive theory.

DK13 used a separation of length scales in the meridional and zonal directions, with an isotropic scaling for the synoptic scales, as well as a temporal scale separation between the synoptic and planetary waves. Isotropic scaling for the synoptic scales is standard in quasi-geostrophic (QG) theory (Pedlosky, 1987), and a meridional scale separation has been argued to be a useful and physically realizable idealization of baroclinic instability (Haidvogel and Held, 1980). These assumptions allowed DK13 to study planetary and synoptic scale interactions. However, they did not derive a wave activity equation or develop explicit equations for the interaction with a zonal mean flow. These aspects are the focus of this Chapter. For simplicity, we derive the asymptotic equations for the case of small-amplitude eddies evolving in the presence of a zonal mean flow, which is an important special case of the DK13 framework. As well as giving a theoretical description for the interaction of a zonal mean flow with planetary and synoptic scale waves, this setting also allows a study of the link between baroclinic and barotropic processes, and the relative importance of planetary and synoptic scale waves for these processes.

The outline of the Chapter is as follows. Section 2.2 gives the equations and assumptions used to derive the potential vorticity (section 2.3), wave activity and mean flow equations (section 2.4), and the angular momentum budget for the zonal mean flow (section 2.5). The momentum, continuity, thermodynamic and vorticity equations at different asymptotic orders, which are needed for the derivations, are given in Appendix A. Further details on the derivations of the mean flow and angular momentum equations, and the non-acceleration theorem, are given in Appendices B, C and D. The zonally homogeneous case with weak planetary scale waves is discussed in section 2.6, conclusions of this Chapter are given in section 2.7, and a section on dimensionalising the asymptotic theory is given in Appendix E.

2.2 The multiscale asymptotic model

2.2.1 Nondimensional compressible flow equations

The asymptotic system of equations is derived starting from the nondimensionalised compressible flow equations in spherical coordinates with a small parameter ε[1] (DK09). To obtain the nondimensional equations the DK09 and DK13 scaling parameters[2] are used, based on the assumption that the waves are not propagating faster than the speed of sound. In this process, the following nondimensional numbers appear (DK09): Rossby[3] ($Ro_{QG} = u_{ref}/2\Omega L_{QG}$ with $L_{QG} = \varepsilon^{-2} h_{sc}$), Mach ($Ma = u_{ref}/\sqrt{p_{ref}/\rho_{ref}}$), Froude ($Fr = u_{ref}/\sqrt{g h_{sc}}$) and the ratio of density and potential temperature scale heights $\sqrt{h_{sc}/H_\theta}$. These are related to the small parameter ε according to $\sqrt{Ma} \approx \sqrt{Fr} \approx Ro_{QG} \approx \sqrt{h_{sc}/H_\theta} \approx \varepsilon$ (DK09). This procedure yields

[1] ε is defined as $\left(a^* \Omega^2 g^{-1}\right)^{1/3}$ (global atmospheric aspect ratio), where Ω is Earth's rotation rate, a^* is Earth's radius and g the Earth's gravitational acceleration. ε is a constant within the range 1/8 to 1/6.

[2] Pressure $p_{ref} = 10^5$ Pa, air density $\rho_{ref} = 1.25$ kg m^{-3}, characteristic flow velocity $u_{ref} = 10$ m s^{-1}, scale height $h_{sc} = p_{ref}/g\rho_{ref} \approx 10$ km, gravitational acceleration $g \approx 10$ m s^{-2}, and time scale $t_{ref} = h_{sc}/u_{ref} \approx 20$ min.

[3] Note that the Rossby number (Ro) used in DK09 and DK13 is $\varepsilon^{-2} Ro_{QG}$ as they used the vertical instead of the horizontal length scale to define it.

the system (the full derivation is given in DK09):

$$\frac{Du}{Dt} - \varepsilon^3\left(\frac{uv\tan\phi}{R} - \frac{uw}{R}\right) + \varepsilon(w\cos\phi - v\sin\phi) = -\frac{\varepsilon^{-1}}{R\rho\cos\phi}\frac{\partial p}{\partial\lambda} + S_u \tag{2.1a}$$

$$\frac{Dv}{Dt} + \varepsilon^3\left(\frac{u^2\tan\phi}{R} + \frac{vw}{R}\right) + \varepsilon u\sin\phi = -\frac{\varepsilon^{-1}}{R\rho}\frac{\partial p}{\partial\phi} + S_v \tag{2.1b}$$

$$\frac{Dw}{Dt} - \varepsilon^3\left(\frac{u^2}{R} + \frac{v^2}{R}\right) - \varepsilon u\cos\phi = -\frac{\varepsilon^{-4}}{\rho}\frac{\partial p}{\partial z} - \varepsilon^{-4} + S_w \tag{2.1c}$$

$$\frac{D\theta}{Dt} = S_\theta \tag{2.1d}$$

$$\frac{D\rho}{Dt} + \frac{\varepsilon^3\rho}{R\cos\phi}\left(\frac{\partial u}{\partial\lambda} + \frac{\partial(v\cos\phi)}{\partial\phi}\right) + \rho\frac{\partial w}{\partial z} + \frac{\varepsilon^3 2w\rho}{R} = 0 \tag{2.1e}$$

$$\rho\theta = p^{1/\gamma} \tag{2.1f}$$

where S denotes source-sink terms ($S_{u,v,w}$ are the frictional terms, while S_θ represents diabatic effects), $\sin\phi = f$ is the nondimensional Coriolis parameter, p is nondimensional pressure, θ is nondimensional potential temperature, ρ is nondimensional density, (u, v, w) represent the nondimensional 3-D velocity field, $R = \varepsilon^3 r$, [1] $r = \varepsilon^{-3}a + z$ where z is altitude from the ground, $a = a^*\varepsilon^3/h_{sc}$ is nondimensional Earth's radius, ϕ is latitude, λ is longitude, t is time, all parameters are nondimensional, and

$$\frac{D}{Dt} = \frac{\partial}{\partial t} + \frac{\varepsilon^3 u}{R\cos\phi}\frac{\partial}{\partial\lambda} + \frac{\varepsilon^3 v}{R}\frac{\partial}{\partial\phi} + w\frac{\partial}{\partial z}. \tag{2.2}$$

Note that the shallow-atmosphere limit $R \to a$ is used here unless otherwise stated (this approximation is used as it holds well to leading order). Expanding R, the material derivative (2.2) involves horizontal advection terms $-a^{-1}\varepsilon^6 z(u\{a\cos\phi_p\}^{-1}\partial/\partial\lambda + va^{-1}\partial/\partial\phi)$ that become relevant at 5^{th} and higher orders.

[1] r is the distance of air parcle from the Earth's core, generally $r^* = a^* + z^*$ (e.g. Holton 2004). z^* is nondimensionalised by h_{sc}, hence $z = z^*/h_{sc}$, whereas a^* is also nondimensionalised by h_{sc} but is three orders of magnitude ($\mathcal{O}(\varepsilon^{-3})$) larger than h_{sc}, hence $\varepsilon^{-3}a = a^*/h_{sc}$, which could be considered an additional scaling argument. If r^* is also nondimensionalised by h_{sc} then the expression for r is $r = \varepsilon^{-3}a + z$. To get variations nondimensionalised by the Earth's radius a^* we need to multiply r by ε^3, which is included in R that is used in equations (2.1a)-(2.2).

2.2.2 Assumptions for multiscale asymptotic methods

In order to derive the multiscale asymptotic version of the equations, some assumptions must be made. In particular, we assume small-amplitude eddies in the presence of a zonal mean flow. This approximation is made in order to gain qualitative insight into the behavior of the system, and to allow connection with previous theories of wave, mean-flow interaction. This can be considered a special case of DK13, with the eddies (but not the zonal mean flow) scaled down by one order of ε. The assumptions for the scale separation between the synoptic, planetary and mean flow in time, height, latitude and longitude are given in Table 2.1 (following DK13), where the subscripts m, p and s represent mean, planetary and synoptic scales, respectively. Note that $\phi_s \gg \phi_p$ (similarly for other coordinates) since the same meridional distance is a much larger number when measured on synoptic scales compared to planetary or zonal mean scales. Here λ_m is not considered as the zonal mean flow is uniform in longitude, λ_p and ϕ_p represent variations of the flow on planetary scales (those of order a^*), λ_s and ϕ_s represent variations on synoptic scales (of order 1000 km), and the time scales are well separated between the mean flow, planetary and synoptic scale eddies, where t_s is of order a day, t_p is of order a week and t_m is a seasonal timescale. The time scales emerge naturally from the equations; t_m is ε^2 slower than t_p because the eddy fluxes driving the zonal mean flow changes are quadratic in eddy amplitude. (In the finite-amplitude theory of DK13, there is no distinction between the two timescales.) As this is the small-amplitude limit of the system, we expect that in practice the zonal mean flow time scale would be shorter. Note that from the above assumptions we see that there is a separation of scales in the meridional direction, which has implications for the final results (see further discussion in sections 2.3, 2.4 and 2.6).

Table 2.1: The assumptions for the scale separations between planetary (p), synoptic (s) and zonal mean flow (m).

	longitude	latitude	height	time
planetary	$\lambda_p = \lambda$	$\phi_p = \phi$	$z_p = z$	$t_p = \varepsilon^3 t$
synoptic	$\lambda_s = \varepsilon^{-1}\lambda_p$	$\phi_s = \varepsilon^{-1}\phi_p$	$z_s = z_p = z$	$t_s = \varepsilon^2 t = \varepsilon^{-1} t_p$
mean		$\phi_m = \phi_p$	$z_m = z_p = z$	$t_m = \varepsilon^5 t = \varepsilon^2 t_p$

Using these scales, we can write asymptotic series for all variables; examples for potential

temperature (which provides stratification) and zonal wind are (following DK09, DK13):

$$\theta(\lambda,\phi,z,t) = 1 + \varepsilon^2\theta^{(2)}(\phi_p,t_m,z) + \varepsilon^3\theta^{(3)}(\mathbf{X}_p,z) + \varepsilon^4\theta^{(4)}(\mathbf{X}_p,\mathbf{X}_s,z) + ... \tag{2.3}$$

$$u(\lambda,\phi,z,t) = u^{(0)}(\phi_p,t_m,z) + \varepsilon u_p^{(1)}(\mathbf{X}_p,z) + \varepsilon u_s^{(1)}(\mathbf{X}_p,\mathbf{X}_s,z) + ... \tag{2.4}$$

where the number in parentheses in superscript represents the order of the variable, $\mathbf{X}_p = (\lambda_p,\phi_p,t_p)$, $\mathbf{X}_s = (\lambda_s,\phi_s,t_s)$, and $u^{(0)}$, $u_p^{(1)}$ and $u_s^{(1)}$ are explicitly defined in Appendix A [in (A.4) and under (A.5)]. Here the first order term has been omitted as $h_{sc}/H_\theta \propto \Delta\theta/\theta_0 \approx \varepsilon^2$; to make this $\mathcal{O}(\varepsilon)$ would lead to stronger wind variations (of order 70 m s^{-1}) (DK09), which would require a different treatment. Therefore, (2.3) is an assumption, whereas (2.4) follows from the derivation of equations (Appendix A). Note that here the leading order variation in potential temperature $\theta^{(2)}$ depends on ϕ_p and z, not only on z as is the case for the static stability parameter in QG theory. Note also that in DK13 a form of (2.3) was considered, such that $\theta^{(2)}$ represented planetary variations (as for $\theta^{(3)}$ here) and $\theta^{(3)}$ represented additional synoptic variations (as for $\theta^{(4)}$ here), whereas separate zonal mean flow variations (as for $\theta^{(2)}$ here) were not present in DK13. This means that the system considered here is a special small amplitude variation of DK13 as stated above.

In order to have a well defined asymptotic expansion (2.3) the sublinear growth condition (DK13) is required. This means that variables at any order grow slower than linearly in any of the synoptic coordinates, which effectively means that any averaging over the synoptic scales ($\mathbf{X}_s$) sets the derivatives over synoptic scales to zero (for more details see DK13).

The full set of equations at different asymptotic orders using the assumptions from this section is given in Appendix A. This includes the momentum, thermodynamic and continuity equations, thermal wind, hydrostatic balance and the vorticity equation. These equations are used in the following sections to derive potential vorticity, wave activity and mean flow equations.

2.3 Potential vorticity equation

To derive the potential vorticity (PV) equation, a vorticity equation has to be derived first. To do so (see Appendix A for the full derivation), take $\mathbf{e}_r \cdot \nabla_s \times \mathcal{O}(\varepsilon^3)$ momentum equation (A.6) and use the $\mathcal{O}(\varepsilon^4)$ continuity equation (A.15), which yields

$$\frac{\partial}{\partial t_s}\zeta^{(1)} + \mathbf{u}^{(0)} \cdot \nabla_s \zeta^{(1)} - \frac{f}{\rho^{(0)}}\frac{\partial}{\partial z}\left(\rho^{(0)} w^{(4)}\right) + \beta v^{(1)} = S_\zeta \tag{2.5}$$

where $\nabla_s = \big((a\cos\phi_p)^{-1}\partial/\partial\lambda_s, a^{-1}\partial/\partial\phi_s\big)$, $\mathbf{u}^{(0)} = u^{(0)}\mathbf{e}_\lambda$ is horizontal velocity of the mean flow, $\beta = a^{-1}\partial f/\partial\phi_p$, $\zeta^{(1)} = \mathbf{e}_r \cdot \nabla_s \times \mathbf{u}^{(1)}$ is relative vorticity, $\mathbf{u}^{(1)} = (u^{(1)}, v^{(1)})$ is horizontal velocity at first order, $S_\zeta = \mathbf{e}_r \cdot \nabla_s \times \mathbf{S}_u^{(3)}$, and $w^{(4)}$ is known from the $\mathcal{O}(\varepsilon^6)$ thermodynamic equation (A.11)

$$w^{(4)} = -\frac{1}{\partial\theta^{(2)}/\partial z}\left[\frac{\partial\theta^{(3)}}{\partial t_p} + \frac{\partial\theta^{(4)}}{\partial t_s} + \mathbf{u}^{(0)}\cdot\nabla_p\theta^{(3)} + \mathbf{u}^{(0)}\cdot\nabla_s\theta^{(4)} + \mathbf{u}^{(1)}\cdot\nabla_p\theta^{(2)} - S_\theta^{(6)}\right] \tag{2.6}$$

where $\nabla_p = \big((a\cos\phi_p)^{-1}\partial/\partial\lambda_p, a^{-1}\partial/\partial\phi_p\big)$. Substituting (2.6) into (2.5) gives

$$\frac{f}{\rho^{(0)}}\frac{\partial}{\partial z}\left(\frac{\rho^{(0)}}{\partial\theta^{(2)}/\partial z}\left[\frac{\partial\theta^{(3)}}{\partial t_p} + \frac{\partial\theta^{(4)}}{\partial t_s} + \mathbf{u}^{(0)}\cdot\nabla_p\theta^{(3)} + \mathbf{u}^{(0)}\cdot\nabla_s\theta^{(4)} + \mathbf{u}^{(1)}\cdot\nabla_p\theta^{(2)} - S_\theta^{(6)}\right]\right) + \frac{\partial}{\partial t_s}\zeta^{(1)} + \mathbf{u}^{(0)}\cdot\nabla_s\zeta^{(1)} + \beta v^{(1)} = S_\zeta. \tag{2.7}$$

The first term in brackets on the left-hand-side of (2.7) can be simplified. Firstly notice that $\rho^{(0)}$, $\theta^{(2)}$ and f do not depend on t_s, thus $\partial/\partial t_s$ can be brought outside the brackets. The other terms in the first term can be simplified using thermal wind balance (A.9a, A.9b). This leads to cancellation of terms with $\partial u^{(0)}/\partial z$, $\partial\mathbf{u}_s^{(1)}/\partial z$, or $\partial\mathbf{u}_p^{(1)}/\partial z$ (with $\mathbf{u}_p^{(1)}$ and $\mathbf{u}_s^{(1)}$ as the horizontal velocities for planetary and synoptic scales, respectively), which means that velocities can be taken out of the $\partial/\partial z$ derivative. This yields the potential vorticity equation

$$\left(\frac{\partial}{\partial t_s} + u_m^{(0)}\frac{1}{a\cos\phi_p}\frac{\partial}{\partial\lambda_s}\right)q_s^{(4)} + \left(\frac{\partial}{\partial t_p} + u_m^{(0)}\frac{1}{a\cos\phi_p}\frac{\partial}{\partial\lambda_p}\right)q_p^{(3)} + (v_s^{(1)} + v_p^{(1)})\hat{\beta} = S^{PV} \tag{2.8}$$

where

$$q_s^{(4)}(\mathbf{X}_p, \mathbf{X}_s, z) = \frac{1}{f}\nabla_s^2 \pi^{(4)} + \frac{f}{\rho^{(0)}}\frac{\partial}{\partial z}\left(\frac{\rho^{(0)}\theta^{(4)}}{\partial\theta^{(2)}/\partial z}\right), \tag{2.9a}$$

$$q_p^{(3)}(\mathbf{X}_p, z) = \frac{f}{\rho^{(0)}}\frac{\partial}{\partial z}\left(\frac{\rho^{(0)}\theta^{(3)}}{\partial\theta^{(2)}/\partial z}\right), \tag{2.9b}$$

$$\hat{\beta}(\phi_p, t_m, z) = \beta + \frac{f}{\rho^{(0)}}\frac{\partial}{\partial z}\left(\frac{\frac{\partial}{a\partial\phi_p}\left(\rho^{(0)}\theta^{(2)}\right)}{\partial\theta^{(2)}/\partial z}\right), \tag{2.9c}$$

$$S_p^{PV} = \frac{f}{\rho^{(0)}}\frac{\partial}{\partial z}\left(\frac{\rho^{(0)}\overline{S_\theta^{(6)}}^{x_s,t_s,y_s}}{\partial\theta^{(2)}/\partial z}\right), \tag{2.9d}$$

$$S_s^{PV} = \mathbf{e}_r \cdot \nabla_s \times \mathbf{S}_u^{(3)} + \frac{f}{\rho^{(0)}}\frac{\partial}{\partial z}\left(\frac{\rho^{(0)}\left(S_\theta^{(6)} - \overline{S_\theta^{(6)}}^{x_s,t_s,y_s}\right)}{\partial\theta^{(2)}/\partial z}\right), \tag{2.9e}$$

$S^{PV} = S_s^{PV} + S_p^{PV}$, $u_m^{(0)} = u^{(0)}$ is the zonal velocity of the zonal mean flow, here $\theta^{(3)}$ and $\theta^{(4)}$ correspond to planetary and synoptic scale potential temperature, respectively, $\theta^{(2)}$ is the leading order potential temperature of the mean flow, $\pi^{(i)} = p^{(i)}/\rho^{(0)}$, $\theta^{(i=2,3,4)} = \partial\pi^{(i=2,3,4)}/\partial z$, $q_p^{(3)}$ is planetary scale PV, $q_s^{(4)}$ is synoptic scale PV, $\hat{\beta}$ is the effective background PV gradient, $\zeta^{(1)} = f^{-1}\nabla_s^2\pi^{(4)}$ is relative vorticity on the synoptic scale, and S^{PV}, S_s^{PV} and S_p^{PV} represent the source-sink terms for the full PV, synoptic scale PV and planetary scale PV, respectively. A similar equation to (2.8) can be obtained by linearising (A5) in DK13, though without the planetary scale PV as it is then absorbed in the background PV gradient as the zonal mean flow. Similarly, (2.10) below can be linked to (44) in DK13.

Equation (2.8) can then be split into planetary and synoptic PV equations, by averaging over synoptic scales: only the planetary scale terms remain, and the residual represents the synoptic scale equation (DK13). This yields

$$\left(\frac{\partial}{\partial t_s} + u_m^{(0)}\frac{1}{a\cos\phi_p}\frac{\partial}{\partial\lambda_s}\right) q_s^{(4)} + v_s^{(1)}\hat{\beta} = S_s^{PV} \tag{2.10}$$

for synoptic scales, and

$$\left(\frac{\partial}{\partial t_p} + u_m^{(0)}\frac{1}{a\cos\phi_p}\frac{\partial}{\partial\lambda_p}\right) q_p^{(3)} + v_p^{(1)}\hat{\beta} = S_p^{PV} \tag{2.11}$$

for planetary scales. The synoptic scale PV equation (2.10) closely resembles the QG PV equation (1.3), with the main differences arising in the background PV gradient.

The background PV gradient $\hat{\beta}$ resembles the background PV gradient used in Charney's baroclinic instability model (e.g. Hoskins and James 2014). However, in Charney's model (and also in the QG model) there is no dependence of the static stability N^2 (linked to background potential temperature) on latitude (ϕ_p), as there is here since $\theta^{(2)} = \theta^{(2)}(\phi_p, t_m, z)$. The QG background PV gradient (1.5), on the other hand, includes the mean flow relative vorticity gradient ($-\partial^2 u_m^{(0)}/\partial\phi_p^2$), which is not present here due to the planetary scaling. This means that $\hat{\beta}$ represents planetary geostrophy (e.g. Phillips 1963, DK09), but it is more realistic than in QG due to the dependence of background PV gradient on latitude.

The planetary scale PV equation (2.11) also resembles the QG PV equation, however the planetary scale PV (2.9b) only includes the stretching term (again due to the chosen planetary scaling). Note that the planetary and synoptic scale PV equations are independent of each other in this small amplitude limit, which implies no direct interaction between planetary and synoptic scales — their interaction only occurs via source-sink terms, the mean flow, or at higher order. This independence is not present in DK13's finite amplitude theory where the synoptic and planetary scale waves interact at leading order.

This analysis suggests that the QG approximation can be used locally for both planetary and synoptic scale PV. Note, however, that this is only true in this small amplitude case (in the finite amplitude theory of DK13 this approach is not applicable for the planetary scales).

The potential vorticity equation can be written in a different form (the one used in DK13 for the planetary scale), with a vertical advection term in the PV equation, starting from (2.7). Following the derivations in DK09 and DK13, we get

$$\frac{\rho^{(0)}}{\partial\theta^{(2)}/\partial z}\left[\left(\mathbf{u}^{(1)}\cdot\nabla_m + w^{(4)}\frac{\partial}{\partial z}\right)q_m^{(2)} + \left(\frac{\partial}{\partial t_s} + \mathbf{u}_m^{(0)}\cdot\nabla_s\right)q_{s,2}^{(4)} + \left(\frac{\partial}{\partial t_p} + \mathbf{u}_m^{(0)}\cdot\nabla_p\right)q_{p,2}^{(3)}\right] = S^{PV2} \tag{2.12}$$

where

$$q_{s,2}^{(4)} = \frac{\zeta^{(1)}}{\rho^{(0)}}\frac{\partial\theta^{(2)}}{\partial z} + \frac{f}{\rho^{(0)}}\frac{\partial\theta^{(4)}}{\partial z},$$

$$q_{p,2}^{(3)} = \frac{f}{\rho^{(0)}}\frac{\partial\theta^{(3)}}{\partial z},$$

$$q_m^{(2)} = \frac{f}{\rho^{(0)}}\frac{\partial\theta^{(2)}}{\partial z}, \text{ and}$$

$$S^{PV2} = S_\zeta + \frac{f}{\partial\theta^{(2)}/\partial z}\frac{\partial S_\theta^{(6)}}{\partial z}.$$

Here $q_{s,2}^{(4)}$, $q_{p,2}^{(3)}$, $q_m^{(2)}$, and S^{PV2} are the DK synoptic, planetary and mean flow PVs, and the corresponding PV source term, respectively.

The PV equation (2.12) is closely related to the Ertel PV equation. However, it includes vertical advection, which is problematic with respect to obtaining a QG wave activity equation. As shown in (2.8) we can eliminate the vertical advection term by including it in the stretching term of the synoptic or planetary scale PV. This is similar to the classical QG approximation of Charney and Stern (1962), in which they point out that the QG PV equation is the QG approximation to the PV equation, however the QG PV is not the QG approximation to the Ertel PV (because the QG PV equation only includes horizontal advection). Notice that in (2.12) there is also the mean flow PV, whereas equation (2.8) only has the background PV gradient that came from this mean flow PV (but not via the direct meridional derivative of $q_m^{(2)}$, i.e. $\hat{\beta} \neq \partial q_m^{(2)}/\partial y_p$). This means that the QG approximation of PV would not work for the zonal mean flow, which is consistent with the arguments above on the relation between the QG PV and the Ertel PV.

2.4 Wave activity equation and the equations for the mean flow

2.4.1 Wave activity equation

Wave activity is a quantity that is quadratic in amplitude and is conserved in the absence of forcing and dissipation (e.g. Vallis 2006) [see also section 1.3]. To derive an equation for wave activity, known as the Eliassen-Palm (EP) relation, we multiply the PV equations (2.10) and (2.11) by $q_s^{(4)}$ and $q_p^{(3)}$, respectively, and divide them by $\hat{\beta}$ (as done in e.g. Plumb 1985). This yields

$$\frac{\partial \mathcal{A}_s}{\partial t_s} + \nabla_s^{3D} \cdot \mathbf{F}_s = S_s^{wa} \tag{2.13}$$

$$\frac{\partial \mathcal{A}_p}{\partial t_p} + \nabla_p^{3D} \cdot \mathbf{F}_p = S_p^{wa} \tag{2.14}$$

where

$$\mathcal{A}_s = \frac{\rho^{(0)} {q_s^{(4)}}^2}{2\hat{\beta}},$$

$$\mathcal{A}_p = \frac{\rho^{(0)} {q_p^{(3)}}^2}{2\hat{\beta}}$$

are synoptic and planetary scale wave activities, respectively, $S_s^{wa} = S_s^{PV}\rho^{(0)}q_s^{(4)}/\hat{\beta}$ and $S_p^{wa} = S_p^{PV}\rho^{(0)}q_p^{(3)}/\hat{\beta}$ are wave activity source-sink terms,

$$\mathbf{F}_s = \left(u_m^{(0)}\mathcal{A}_s + \frac{\rho^{(0)}}{2}\left({v_s^{(1)}}^2 - {u_s^{(1)}}^2 - \frac{{\theta^{(4)}}^2}{\partial\theta^{(2)}/\partial z}\right), -\rho^{(0)}v_s^{(1)}u_s^{(1)}, \rho^{(0)}f\frac{v_s^{(1)}\theta^{(4)}}{\partial\theta^{(2)}/\partial z}\right),$$

$$\mathbf{F}_p = \left(u_m^{(0)}\mathcal{A}_p - \frac{\rho^{(0)}}{2}\frac{{\theta^{(3)}}^2}{\partial\theta^{(2)}/\partial z}, 0, \rho^{(0)}f\frac{v_p^{(1)}\theta^{(3)}}{\partial\theta^{(2)}/\partial z}\right)$$

are synoptic and planetary Eliassen-Palm (EP) fluxes, respectively, and ∇^{3D} means that the divergence includes the vertical derivative.

Note how the planetary scale EP flux does not have a meridional component (no momentum flux), and that the synoptic scale EP flux closely resembles Plumb (1985)'s total flux $\mathbf{B}^{(T)}$, with the main difference, again, arising in $\hat{\beta}$. Also, $u_s^{(1)}$ is actually composed of $u_s^{(1)} = [u]_s^{(1)} + u_s^{*(1)}$ (with [.] as zonal mean and * as perturbation from zonal mean), which is another difference to Plumb's $\mathbf{B}^{(T)}$ flux.

We can also relate these expressions to Hoskins et al. (1983)'s E-vector, where the difference is in the zonal component of the E-vector, which lacks the wave activity advection ($[u]\mathcal{A}$) and potential temperature ($\propto -\theta^{*2}$) terms.

Nonetheless, the synoptic scale EP flux is similar to the QG form of EP flux (1.7) [see also Edmon et al. 1980], especially if zonally averaged. The planetary scale wave activity implies that the momentum fluxes and hence barotropic processes at those scales are less important than heat fluxes and baroclinic processes. Also, this emphasises the fact that planetary and synoptic scales do not interact directly, but rather through other processes (source-sink terms or the mean flow) as the two wave activity equations are at different orders and have no "cross" terms. The wave activity equations are at different orders as the planetary (2.11) and synoptic (2.10) PV equations are multiplied by $q_p^{(3)}$ and $q_s^{(4)}$, respectively, which are of different orders. This is because they have different horizontal derivatives associated with them (q_s has synoptic and q_p has planetary).

Averaging over synoptic scales (λ_s, ϕ_s, t_s; denoted by overline and s) in (2.13) and over

planetary scales (λ_p, t_p; denoted by overline and p) in (2.14) gives

$$\frac{\partial}{\partial z}\left(\rho^{(0)} f \overline{\frac{v_s^{(1)}\theta^{(4)}}{\partial\theta^{(2)}/\partial z}}^{s}\right) = \overline{S_s^{wa}}^{s} \approx -r_s \overline{\mathcal{A}_s}^{s} \tag{2.15}$$

$$\frac{\partial}{\partial z}\left(\rho^{(0)} f \overline{\frac{v_p^{(1)}\theta^{(3)}}{\partial\theta^{(2)}/\partial z}}^{p}\right) = \overline{S_p^{wa}}^{p} \approx -r_p \overline{\mathcal{A}_p}^{p} \tag{2.16}$$

where $r_{s,p}$ are effective damping coefficients. Note that the approximation $\overline{S_{s,p}^{wa}}^{s,p} \approx -r_{s,p}\overline{\mathcal{A}_{s,p}}^{s,p}$ does not follow from the equations themselves, but is a heuristic relation used as a device to help us better understand the physical interpretation of the equations. These equations imply that under these averages both synoptic and planetary scale wave activities change via heat flux terms on timescales longer than t_s or t_p (as we averaged over those) - e.g. timescale $\varepsilon^4 t$ (between t_p and t_m) or t_m. Averaging only over the zonal and time dimensions, the synoptic scale wave activity would still be influenced by the synoptic scale momentum fluxes.

2.4.2 Barotropic equation

As the wave activity equation represents the equation for the eddies, we need additional equations for the mean flow to get the influence from the eddies on the mean flow. The barotropic pressure equation is derived (following DK13) from the $\mathcal{O}(\varepsilon^5)$ momentum equation (A.8) using the relevant thermodynamic, hydrostatic, thermal wind, momentum and continuity equations averaged not only over t_s, λ_s, ϕ_s and t_p, λ_p, but also over z (denoted by overline and z). This yields momentum equation (B.6) (see Appendix B for more details), which can be used to derive the barotropic pressure equation, taking $\partial/\partial\tilde{y}_p$ of (B.6), eliminating the term $\partial\left(\overline{v^{(4)}\rho^{(0)}}^{s,p,z}\right)/\partial\tilde{y}_p$ via (B.5), multiplying it by f and recalling (A.4):

$$\frac{\partial}{\partial t_m}\left(\frac{\partial}{\partial\tilde{y}_p}\frac{1}{f}\frac{\partial}{\partial y_p}\overline{p^{(2)}}^{s,p,z} - \frac{\beta}{f^2}\frac{\partial}{\partial y_p}\overline{p^{(2)}}^{s,p,z} - f\overline{p^{(2)}}^{s,p,z}\right) - \frac{\partial}{\partial\tilde{y}_p}N_1 + \frac{\beta}{f}N_1 - fN_2 = -S_{barotropic} \tag{2.17}$$

with

$$N_1 = \frac{\partial}{\partial\tilde{y}_p}\overline{\left(\rho^{(0)}\underline{\underline{v_p^{(1)}u_p^{(1)}}} + \rho^{(0)}\underline{\underline{v_s^{(1)}u_s^{(1)}}}\right)}^{s,p,z} - \frac{\tan\phi_p}{a}\overline{\left(\rho^{(0)}\underline{\underline{v_p^{(1)}u_p^{(1)}}} + \rho^{(0)}\underline{\underline{v_s^{(1)}u_s^{(1)}}}\right)}^{s,p,z},$$

$$N_2 = \frac{\partial}{\partial \tilde{y}_p}\left(\underline{\underline{\overline{\rho^{(0)} v_p^{(1)} \theta^{(3)}}^{s,p,z}}}\right),$$

$$S_{barotropic} = \overline{f\rho^{(0)} S_\theta^{(7)}}^{s,p,z} + f\frac{\partial}{\partial \tilde{y}_p}\left(\overline{\left(\rho^{(2)} + \rho^{(0)}\theta^{(2)}\right)\frac{S_u^{(3)}}{f}}^{s,p,z}\right)$$
$$+\left(\frac{\partial}{\partial \tilde{y}_p} - \frac{\beta}{f}\right)\left[\overline{\rho^{(0)} S_u^{(5)}}^{s,p,z} + \left\{\frac{\partial}{\partial \tilde{y}_p} - \frac{\tan\phi_p}{a}\right\}\left(\overline{\frac{S_u^{(3)}}{f} u^{(0)}\rho^{(0)}}^{s,p,z}\right) - \frac{\rho^{(0)}\overline{S_\theta^{(6)}}^{s,p,z}\cos\phi_p}{f\partial\theta^{(2)}/\partial z}\right]$$

where the underlined terms represent eddy forcing of the mean flow, $\partial/\partial\tilde{y}_p \equiv (a\cos\phi_p)^{-1}\partial\cos\phi_p/\partial\phi_p$, and $\partial/\partial y_p \equiv a^{-1}\partial/\partial\phi_p$. This evolution equation (2.17) for $p^{(2)}$ on the t_m scale is similar to DK13's $p^{(2)}$ evolution on the t_p scale when no source terms are considered. Using geostrophic balance for $u^{(0)}$, (2.17) can be rewritten as

$$\left(\frac{\partial}{\partial \tilde{y}_p} - \frac{\beta}{f}\right)\frac{\partial\overline{\rho^{(0)}u^{(0)}}^{s,p,z}}{\partial t_m} + f\frac{\partial\overline{p^{(2)}}^{s,p,z}}{\partial t_m} + \left(\frac{\partial}{\partial \tilde{y}_p} - \frac{\beta}{f}\right)N_1 + fN_2 = S_{barotropic}. \tag{2.18}$$

This equation implies that although both the synoptic and planetary scale momentum fluxes affect the barotropic part of the mean flow, only the planetary scale heat fluxes N_2 are relevant.

The zonal mean flow equations at different orders can be further written in TEM form (Andrews and McIntyre, 1976; Edmon et al., 1980), from which a non-acceleration theorem can be derived using the wave activity equations. This is addressed in Appendix D. Note that an evolution equation for $p^{(3)}$ can also be derived, however under the $\lambda_p, \lambda_s, t_s, \phi_s, z$ average it only evolves through diabatic and frictional processes (D.9).

2.4.3 Baroclinic equation

The barotropic equation (2.18) shows how barotropic processes affect the zonal mean flow, however we are also interested in the baroclinic processes. Therefore, a baroclinic equation for the zonal mean flow (i.e. equation for baroclinicity $\propto \partial u^{(0)}/\partial z$) is derived from the $\mathcal{O}(\varepsilon^7)$ thermodynamic equation (A.12), using the relevant continuity and momentum equations averaged over t_s, λ_s, t_p, λ_p (denoted with overline), and taking $\partial/\partial y_p$ of the resulting equation (B.7b). The relevant equations (and their derivations) are given in Appendix B, hence using (B.10-B.14)

yields:

$$-\frac{\partial}{\partial t_m}\left(\overline{f\rho^{(0)}\frac{\partial u^{(0)}}{\partial z}}^{\lambda_s,t_s,p}\right)+\frac{\partial}{\partial y_p}\left[\frac{\partial}{\partial \tilde{y}_p}\left(\overline{v_p^{(1)}\rho^{(0)}\theta^{(3)}}^{\lambda_s,t_s,p}\right)+\frac{\partial}{\partial \tilde{y}_s}\left(\overline{v_s^{(1)}\rho^{(0)}\theta^{(4)}}^{\lambda_s,t_s,p}\right)\right]$$
$$-\frac{\partial}{\partial y_p}\left[\frac{\partial}{\partial z}\left(\overline{v_p^{(1)}\rho^{(0)}\theta^{(3)}}^{\lambda_s,t_s,p}\frac{\partial\theta^{(2)}/\partial y_p}{\partial\theta^{(2)}/\partial z}\right)-\overline{\rho^{(0)}u_s^{(1)}\frac{\partial\theta^{(3)}}{\partial x_p}}^{\lambda_s,t_s,p}\right]$$
$$-\frac{\partial}{\partial y_p}\left[\frac{\partial\theta^{(2)}}{\partial z}\int_0^{z_{max}}\rho^{(0)}\frac{\partial}{\partial\tilde{y}_s}\left(\frac{\partial}{\partial\tilde{y}_s}\left(\frac{\overline{v_s^{(1)}u_s^{(1)}}^{\lambda_s,t_s,p}}{f}\right)\right)\mathrm{d}z\right]=S_{baroclinic} \quad (2.19)$$

with

$$S_{baroclinic}=\frac{\partial}{\partial y_p}\left[\frac{\partial}{\partial\tilde{y}_s}\left(\overline{\frac{S_u^{(3)}}{f}\rho^{(0)}\theta^{(3)}}^{\lambda_s,t_s,p}\right)-\frac{\rho^{(0)}\overline{\theta^{(3)}S_\theta^{(6)}}^{\lambda_s,t_s,p}}{\partial\theta^{(2)}/\partial z}+\rho^{(0)}\frac{\overline{S_u^{(3)}}^{\lambda_s,t_s,p}}{f}\frac{\partial\theta^{(2)}}{\partial y_p}\right]$$
$$+\frac{\partial}{\partial y_p}\left[\overline{S_\theta^{(7)}\rho^{(0)}}^{\lambda_s,t_s,p}-S_{w5}\frac{\partial\theta^{(2)}}{\partial z}-\frac{\partial}{\partial\tilde{y}_s}\left(\frac{z}{a}\frac{\overline{S_u^{(3)}}^{\lambda_s,t_s,p}}{f}\right)+\frac{\partial}{\partial z}\left(\frac{z}{a}\frac{\overline{S_\theta^{(6)}}^{\lambda_s,t_s,p}}{\partial\theta^{(2)}/\partial z}\right)\right],$$

$$S_{w5}=-\int_0^{z_{max}}\left[\frac{\partial}{\partial\tilde{y}_s}\left(\rho^{(0)}\left\{\frac{\overline{S_\theta^{(6)}}^{\lambda_s,t_s,p}}{f}\frac{\partial u^{(0)}/\partial z}{\partial\theta^{(2)}/\partial z}-\frac{\overline{S_u^{(4)}}^{\lambda_s,t_s,p}}{f}\right\}\right)-\frac{\partial}{\partial\tilde{y}_p}\left(\rho^{(0)}\frac{\overline{S_u^{(3)}}^{\lambda_s,t_s,p}}{f}\right)\right]\mathrm{d}z,$$

where the terms with z/a come from corrections to the shallow-atmosphere approximation of the thermodynamic and continuity equations. Averaging (2.19) over the synoptic meridional scale (ϕ_s) gives

$$-\frac{\partial}{\partial t_m}\left(\overline{f\rho^{(0)}\frac{\partial u^{(0)}}{\partial z}}^{s,p}\right)+\frac{\partial}{\partial y_p}\left[\frac{\partial}{\partial\tilde{y}_p}\left(\overline{v_p^{(1)}\rho^{(0)}\theta^{(3)}}^{s,p}\right)-\frac{\partial}{\partial z}\left(\overline{v_p^{(1)}\rho^{(0)}\theta^{(3)}}^{s,p}\frac{\partial\theta^{(2)}/\partial y_p}{\partial\theta^{(2)}/\partial z}\right)\right]$$
$$=\overline{S}^{\phi_s}_{baroclinic} \quad (2.20)$$

which implies that baroclinicity is not affected by the synoptic scale heat fluxes ($\rho^{(0)}v_s^{(1)}\theta^{(4)}$), only by baroclinic source terms ($S_{baroclinic}$) and planetary scale heat fluxes ($\rho^{(0)}v_p^{(1)}\theta^{(3)}$). The absence of a synoptic scale heat flux contribution to the baroclinicity tendency is discussed in section 2.6.

2.5 Angular momentum conservation

Apart from the mean flow equations (baroclinic and barotropic) and the eddy equations (wave activity), angular momentum conservation provides additional information about the transfer of angular momentum between the earth and the atmosphere, which has implications for the surface easterlies in the tropics and westerlies in the midlatitudes (e.g. Holton 2004). Hence, it is important to show that such a budget can be found also in the asymptotic model.

Generally, the angular momentum for the hydrostatic primitive equations takes the form (e.g. Holton 2004)

$$M = au\cos\phi + a^2\Omega\cos^2\phi \tag{2.21}$$

where a is the radius of the Earth, Ω is the Earth's rotation rate, ϕ is meridional coordinate, u is zonal velocity, and M is angular momentum per unit mass.

In the asymptotic regime, a nondimensional version of angular momentum must be used. To derive the nondimensional version of (2.21), define nondimensional terms (similarly as in section 2.2): $u = u^* u_{ref}$, $a = a^*\varepsilon^{-3}h_{sc}$, $\Omega = \frac{1}{2}\Omega^*(2\Omega_{ref})$ and $M = M^* u_{ref}h_{sc}\varepsilon^{-3}$, where u_{ref} and h_{sc} were defined in section 2.2, Ω_{ref} is the Earth's rotation rate (previously denoted Ω), $M \propto \varepsilon^{-3}$ as it needs to be of the same order as other terms, and the asterisk (*) denotes nondimensional parameters. Now divide (2.21) by $u_{ref}h_{sc}$ to get nondimensional angular momentum

$$\varepsilon^{-3}M^* = a^*\varepsilon^{-3}u^*\frac{u_{ref}h_{sc}}{u_{ref}h_{sc}}\cos\phi + (\varepsilon^{-3})^2(a^*)^2\frac{1}{2}\Omega^*\frac{h_{sc}}{h_{sc}}\frac{h_{sc}2\Omega_{ref}}{u_{ref}}\cos^2\phi. \tag{2.22}$$

Cancelling out a few terms, setting Ω^* to unity, recognising that[1] $h_{sc}2\Omega_{ref}/u_{ref} = Ro^{-1} \approx \varepsilon$, and omitting asterisks for simplicity, yields the nondimensional angular momentum

$$\varepsilon^{-3}M = \varepsilon^{-3}au\cos\phi + \varepsilon^{-3}\varepsilon^{-2}\frac{1}{2}a^2\cos^2\phi. \tag{2.23}$$

Taking the material derivative (2.2) of M in (2.23) gives the nondimensional angular momentum equation

$$\varepsilon^{-3}\frac{\mathrm{D}M}{\mathrm{D}t} = \varepsilon^{-3}a\cos\phi\frac{\mathrm{D}u}{\mathrm{D}t} - uv\sin\phi - \varepsilon^{-2}afv\cos\phi \tag{2.24}$$

using $\partial/\partial t = \varepsilon^5\partial/\partial t_m$, $w^{(0)} = w^{(1)} = w^{(2)} = w^{(3)} = 0$ (as derived in Appendix A), and all

[1]Here the Rossby number used is the same as the one defined in DK09, DK13: $Ro^{-1} \approx Ro_{QG} \approx \varepsilon$.

parameters are nondimensional. Notice that

$$\frac{\partial \cos^2 \phi}{\partial \phi} = -2 \cos \phi \sin \phi,$$

which means that the factor 2 from this equation cancels out the factor 1/2 in M (2.23). Here

$$v = \varepsilon^{-3} a \frac{D\phi}{Dt} = \varepsilon v^{(1)} + \varepsilon^2 v^{(2)} + ...,$$

$$u = u^{(0)} + \varepsilon u^{(1)} + \varepsilon^2 u^{(2)} + ...$$

The angular momentum equation and its conservation for the zonal mean flow ($u^{(0)}$) are derived in Appendix C. The second order angular momentum equation is

$$\rho \frac{\mathrm{D}M}{\mathrm{D}t_m} = a \cos \phi_p \rho^{(0)} \frac{\mathrm{D}u^{(0)}}{\mathrm{D}t_m} - (\rho^{(0)} u^{(1)} v^{(1)} + \rho^{(0)} u^{(0)} v^{(2)}) \sin \phi_p \\ -f(\rho^{(0)} v^{(4)} + \rho^{(2)} v^{(2)} + \rho^{(3)} v^{(1)}) a \cos \phi_p, \tag{2.25}$$

from which it is shown (Appendix C) that M is conserved (using the 5^{th} order momentum equation A.8) in the absence of source-sink terms and orography, yielding

$$\iiint_{Vp} \frac{\partial \overline{(\rho M)^{(2)}}^{s,t_p}}{\partial t_m} \mathrm{d}V_p = 0 \tag{2.26}$$

where V_p is volume on planetary scales (λ_p, ϕ_p, z).

The barotropic pressure equation (2.18) can now be rewritten using the angular momentum equation (Appendix C) as

$$\left(\frac{\partial}{\partial \tilde{y}_p} - \frac{\beta}{f} \right) \left\{ \overline{\frac{\rho}{a \cos \phi_p} \frac{DM}{Dt_m}}^{s,p,z} \right\} - f \frac{\partial \overline{\rho^{(2)}}^{s,p,z}}{\partial t_m} = -f \frac{\partial \overline{p^{(2)}}^{s,p,z}}{\partial t_m} - f \frac{\partial}{\partial \tilde{y}_p} \left(\overline{\rho^{(0)} v_p^{(1)} \theta^{(3)}}^{s,p,z} \right) \tag{2.27}$$

where the overbar denotes average over $t_s, t_p, \lambda_s, \lambda_p, \phi_s, z$. This shows that the angular momentum (2.25) and barotropic (2.18) budgets are directly linked, since the barotropic budget can be written by using angular momentum M instead of zonal wind $u_m^{(0)}$ (2.27).

Note that the surface pressure tendency $\partial \overline{p^{(2)}}^{s,p,z} / \partial t_m$ in (2.18) and (2.27) reflects the response of planetary angular momentum to an imposed torque, via mass redistribution, and is

an essential component of the angular momentum equation at planetary scales (Haynes and Shepherd, 1989). The present analysis has shown further that the planetary-scale meridional heat flux contributes to this meridional mass redistribution. That the synoptic scale heat flux does not so contribute can be anticipated from the scaling arguments of Haynes and Shepherd (1989).

2.6 The zonally homogeneous case

If there are no forced planetary scale waves in the system, then there is no justification for separate λ_p and t_p scales. If the zonal and synoptic scale (including ϕ_s) average is taken in such a case, then the wave activity, barotropic and baroclinic equations become:

$$\frac{\partial}{\partial z}\left(\rho^{(0)} f \frac{\overline{v_s^{(1)}\theta^{(4)}}^{s}}{\partial\theta^{(2)}/\partial z}\right) \approx -r_s \overline{\mathcal{A}_s}^{s}, \tag{2.28a}$$

$$\left(\frac{\partial}{\partial\tilde{y}_p} - \frac{\beta}{f}\right)\frac{\partial\overline{\rho^{(0)}u^{(0)}}^{s,p,z}}{\partial t_m} - f\frac{\partial\overline{p^{(2)}}^{s,p,z}}{\partial t_m} + \left(\frac{\partial}{\partial\tilde{y}_p} - \frac{\beta}{f}\right)\overline{N_1}^{s,p,z} = \overline{S_{barotropic}}^{s,p,z}, \tag{2.28b}$$

$$-\frac{\partial}{\partial t_m}\left(\overline{f\rho^{(0)}\frac{\partial u^{(0)}}{\partial z}}^{s,p}\right) = \overline{S_{baroclinic}}^{s,p}. \tag{2.28c}$$

These equations imply that under synoptic scale averaging, and to leading order, the wave activity is only affected by the heat fluxes through a quasi-steady balance, the barotropic part of the zonal mean flow tendency is only affected by the momentum fluxes (in N_1), and the baroclinicity tendency is only affected by source-sink terms. The latter can, however, be related to the source-sink terms in the wave activity and barotropic pressure equations. The most surprising of these relations are (2.28a) and (2.28c), which depend crucially on the averaging over ϕ_s. When the equations are not averaged over ϕ_s, then momentum fluxes appear in the wave activity equation and heat fluxes appear in the baroclinicity tendency equation.

These findings may help explain the empirical results of Thompson and Woodworth (2014), who found that the barotropic and baroclinic parts of the Southern Hemisphere (SH) flow variability were decoupled, with the barotropic part of the flow (characterised by the Southern Annular Mode (SAM), based on zonal mean zonal wind) being only affected by the momentum fluxes, and the baroclinic part of the flow (characterised by the baroclinic annular mode (BAM),

based on EKE) being only affected by the heat fluxes [see also section 1.2.1]. We assume here that the wave activity is closely linked to EKE. Indeed, Wang and Nakamura (2015, 2016) found that wave activity during the SH summer is only affected by the heat fluxes under an average over a few latitudinal bands (approximately 10^{o}), giving an equation similar to (2.28a). Here we put this view into a self-consistent mathematical perspective.

In a separate study, Thompson and Barnes (2014) found an oscillating relationship between the baroclinicity and the heat fluxes with a timescale of 20-30 days. In their model, baroclinicity is affected by synoptic scale heat fluxes [see (1.2)], through the assumption that

$$\frac{\partial^2[v^*T^*]}{\partial y^2} = -l^2[v^*T^*],$$

where l is meridional wave number, T is temperature, [.] represents zonal mean and asterisk (*) represents perturbations therefrom. This relation is not present here due to the chosen scaling and the averaging over synoptic scales. Equation (2.19) does in fact have the heat fluxes, acting on synoptic scales, which due to the sublinear growth condition (DK13) disappear in (2.28c), as mentioned above.

Pfeffer (1987, 1992) argued that heat fluxes (vertical EP fluxes) grow in the part of the domain with low stratification parameter S. Pfeffer's S can be related to ε as $S = (L_R/a^*)^2 \approx \varepsilon^2$, where $L_R \approx \varepsilon a^*$ is Rossby deformation radius (a typical synoptic scale) and a^* is Earth's radius (a typical planetary scale). Since here we consider the case with $\varepsilon \ll 1$, we are then in a regime where $S \ll 1$ and hence the heat fluxes act to drive the residual meridional circulation rather than the zonal mean flow, and the vertical derivative of the zonal mean flow (i.e. baroclinicity) is not related to EP flux divergence to leading order (see equations (6)-(9) in Pfeffer 1992). This suggests a barotropic response of the zonal mean flow to eddy fluxes after averaging over synoptic scales, which is consistent with (2.28b) and (2.28c).

Zurita-Gotor (2017) showed further that there is a low frequency suppression of heat fluxes (at periods longer than 20-30 days) and concluded that at longer timescales (considered here) the meridional circulation and diabatic processes are more important for the baroclinicity than the synoptic scale heat fluxes (consistent with (2.28c)).

2.7 Conclusions

In this Chapter we have provided a theoretical framework for planetary-synoptic-zonal mean flow interactions in the small amplitude limit with a scale separation in the meridional direction, as well as in the zonal direction, between planetary and synoptic scales. Thus the synoptic scale eddies are assumed to be isotropic (which is the case also in QG theory). These assumptions allow us to derive strong results, e.g. a lack of direct interaction between the planetary and synoptic waves, and a lack of a direct link between the baroclinic and barotropic components of the flow when only synoptic scale fluxes are considered.

We derived planetary and synoptic scale PV equations [(2.11), (2.10)], and equations for the eddies [wave activity equations (2.15-2.16)], the barotropic part of the zonal mean flow (2.18) and the baroclinic part of the zonal mean flow (2.20). A crucial step in deriving these equations was finding a form of the PV equation that eliminated the effect of vertical advection. The synoptic scale PV then resembled QG PV and the planetary PV resembled that of planetary geostrophy, i.e. with only stretching vorticity representing PV on planetary scales (e.g. Phillips 1963). These equations provide an alternative view to the conventional Transformed Eulerian Mean (TEM) framework (first introduced in Andrews and McIntyre 1976), which combines all components into two equations that are linked through the Eliassen-Palm flux. This means that instead of one mean flow equation there are two (one for baroclinic and one for barotropic flow), which is consistent with Pfeffer (1987, 1992)'s scaling arguments [e.g. only momentum fluxes drive the zonal mean zonal wind (barotropic flow) and the heat fluxes drive the residual circulation].

The background PV gradient (2.9c) that emerged from the equations lacks the relative vorticity term as in planetary geostrophy (Phillips, 1963), implying the dominance of baroclinic processes for eddy generation. Thus this PV gradient resembles that of Charney's baroclinic instability model (e.g. Hoskins and James 2014), but is more general as it includes variations in static stability in both the vertical and meridional directions. The latter should be stressed as this is the main difference to QG dynamics in this model.

In terms of the baroclinic life cycle (Simmons and Hoskins, 1978), the barotropic pressure equation (2.18) would be relevant in the breaking region of the storm track and the baroclinic equation (2.20) would be more relevant in the source region. We also showed that only the planetary scale heat fluxes affect the baroclinicity (2.20), that both planetary and synoptic scale momentum fluxes, as well as planetary scale heat fluxes, affect the barotropic zonal mean flow

(2.18), and that the planetary waves and synoptic scale eddies only interact via the zonal mean flow, the source-sink terms or at higher order approximations. Since both the barotropic (2.18) and baroclinic (2.20) parts of the zonal mean flow are affected by the planetary scale heat fluxes, the latter could provide a link between upstream and downstream development of storm tracks. The barotropic equation (2.18) was also directly linked to the angular momentum equation (2.27), which has not been noted in previous work. This linkage revealed the importance of planetary scale heat fluxes (via meridional mass transport) for the angular momentum budget (Haynes and Shepherd, 1989).

The importance of planetary scale waves was also noted in Kaspi and Schneider (2011, 2013), who found that the termination of storm tracks downstream is related to stationary waves and the baroclinicity associated with them. Stationary waves are especially important locally in contributing to heat fluxes, which enhance temperature gradients upstream, and reduce them downstream.

When considering only the synoptic scale eddies (when planetary scale eddies are weak, as e.g. in aquaplanet simulations or in the Southern Hemisphere), we find that under synoptic scale averaging the barotropic zonal mean flow (2.28b) is only affected by the momentum fluxes, the baroclinicity (2.28c) is only affected by the source-sink terms, and wave activity (2.28a) is only related to heat fluxes (as in Thompson and Woodworth 2014). This suggests that the baroclinicity is primarily diabatically driven. Understanding the decoupling of the baroclinic and barotropic parts of the flow (in the case of weak planetary scale waves) is addressed in Chapter 3, where it is shown that at timescales longer than synoptic the EKE is only affected by the heat fluxes and not momentum fluxes, confirming relation (2.28a).

As well as helping to understand a variety of previous results in the literature, one potential use of the theory presented here could be to help understand the barotropic response to climate change, which is fundamentally thermally driven. In general, we need a better understanding of the interaction between the baroclinic and barotropic parts of the flow, where planetary scale heat fluxes and diabatic processes may play an important role.

This theoretical framework could be extended by allowing finite amplitude eddies (as in DK13) and by relaxing the assumption of a separation of scales in latitude (e.g. Dolaptchiev 2008). These points are further addressed in Appendix L.

3

Baroclinic and Barotropic Modes of Variability

3.1 Introduction

The midlatitude dynamics of the Southern Hemisphere (SH) exhibit two distinct so-called annular modes of variability [see also sections 1.1.1 and 1.2.1]: the Southern Annular Mode (SAM) (e.g. Kidson 1988; Hartmann and Lo 1998) and the Baroclinic Annular Mode (BAM) (Thompson and Woodworth, 2014). The former is based on empirical orthogonal function (EOF) analysis of zonal mean zonal wind and represents north-south shifts of the jet stream, which are mainly driven by corresponding shifts in eddy momentum fluxes (e.g. Hartmann and Lo 1998; Lorenz and Hartmann 2001). The latter is based on EOF analysis of eddy kinetic energy (EKE) and represents amplitude variations of this field, which are mainly driven by corresponding variations in eddy heat fluxes (Thompson and Woodworth, 2014). The SAM has an equivalent barotropic vertical structure and is often referred to as a barotropic mode of variability, whereas the BAM has a stronger vertical structure, as well as being directly linked to heat fluxes, and is therefore related to variability in baroclinic processes.

Thompson and Woodworth (2014) found that the SAM was essentially uncorrelated with eddy heat fluxes, the BAM was essentially uncorrelated with eddy momentum fluxes, and there was only a small (negligible) correlation between the SAM and BAM [section 1.2.1]. These findings led to the conclusion that the eddy momentum and heat fluxes are somewhat independent, hence there is a decoupling between baroclinic and barotropic modes of variability. This

was a somewhat counterintuitive result as the momentum and heat fluxes (and also baroclinic and barotropic processes) are usually viewed as linked through eddy growth and decay in the Eliassen-Palm (EP) wave activity perspective (e.g. Simmons and Hoskins 1978; Edmon et al. 1980) [see also sections 1.2 and 1.3], and both Robinson (2000) and Lorenz and Hartmann (2001) identified a baroclinic feedback associated with annular mode anomalies.

However, it is perfectly conceivable to have barotropic variability with fixed baroclinic wave sources (e.g. Vallis et al. 2004) [section 1.1]. In particular, different momentum fluxes can arise from the same heat fluxes, depending on the upper-tropospheric conditions, as in LC1 (equatorward wave breaking) and LC2 (poleward wave breaking) life-cycle experiments (Thorncroft et al., 1993). Moreover, Pfeffer (1987, 1992) argued that typical aspect ratios implied that heat fluxes mainly act to drive the residual circulation, whereas momentum fluxes mainly drive the zonal mean flow tendency, implying irrelevance of heat fluxes for the zonal mean flow. This argument has been formalised in Chapter 2, which, using multiscale asymptotic methods, showed that under such conditions and under synoptic temporal and spatial scale averaging, wave activity (generalised eddy kinetic energy) and the vertical component of EP flux (related to heat flux) are indeed related on timescales longer than synoptic, and that momentum fluxes do not directly affect this coupling on such timescales.

Thompson and Barnes (2014) further found an oscillator model between EKE and heat flux with a timescale of 20-30 days, which was reflected in the BAM mode [section 1.2.1]. This model has no influence from the momentum fluxes and is purely baroclinic by nature with a relationship with baroclinicity (vertical wind shear). A similar oscillator model was also found for the Northern Hemisphere in Ambaum and Novak (2014). Such an oscillating relationship is consistent with weakly nonlinear models of baroclinic instability, such as in Pedlosky (1970).

Wang and Nakamura (2015, 2016) also pointed out a relationship between wave activity and heat flux with a similar timescale as in Thompson and Barnes (2014), but only for the Southern Hemisphere (SH) summer. This suggests that not all seasons exhibit the oscillating behavior (between EKE and heat flux). Wang and Nakamura (2015) further pointed out that momentum and heat fluxes primarily act at different timescales: heat fluxes act primarily at about 20 to 30 day periods, whereas momentum fluxes act at shorter periods. Wang and Nakamura (2016) investigated the relationship between wave activity and heat fluxes and found that the meridionally confined baroclinic zone in SH summer provides a wave guide that lets different modes interfere and produce larger amplitude heat fluxes with a 20-30 day periodicity.

Here we look into the behavior discussed above using different configurations of a simplified model and the ERA-Interim reanalysis (described in section 3.2.1 and in Appendix F). The different model configurations are not intended to realistically mimic the real atmosphere but rather to examine the baroclinic-barotropic coupling across a wide range of dynamical regimes. They also facilitate comparison to previous work done on the baroclinic and barotropic modes of variability using simplified models (e.g. Sparrow et al. 2009; Sheshadri and Plumb 2017). The methods are given in section 3.2, and the theoretical background in section 3.3. We first examine in detail one particular (equinox) configuration of the model, in section 3.4, in order to understand the nature of baroclinic-barotropic interactions on various timescales. In section 3.5 we assess the generality of our results by comparing them with the winter and summer hemispheres of a solstice configuration of the model, and use these findings to interpret the SH behavior seen in ERA-Interim. Conclusions of this Chapter are given in section 3.6. Appendices F-H provide more details about model configuration (in Appendix F) and EOF analysis (in Appendix G), as well as the analysis of the asymptotic momentum, thermodynamic and continuity budgets from Appendix A (in Appendix H, where also the so-called density weighted velocities are introduced).

3.2 Methods

3.2.1 Data

The numerical model used for this study is the dry dynamical core version of the UK Met Office Unified Model (UM) version 8.6 with ENDGame semi-Lagrangian dynamical core (Walters et al., 2014). The model configuration follows Held and Suarez (1994) with some modifications, being forced through Newtonian relaxation of the temperature field to a prescribed equilibrium profile, with linear frictional and thermal damping. The model resolution used is N96L63 with a model top at 32 km (1.875^o in longitude, 1.25^o in latitude and varying vertical resolution - from approximately 200 m in the lower troposphere to approximately 1000 m in the stratosphere) and is run for 10800 days, of which the first 1440 days are taken as a spin-up period. The output is analysed at daily resolution and in height coordinates.

Two different model configurations were used for this study: *(i)* the usual Held-Suarez configuration with perpetual equinox conditions as specified in Held and Suarez (1994), and *(ii)* a stratospheric perpetual solstice configuration, following Polvani and Kushner (2002)'s strong

polar vortex forcing ($\gamma = 4$) with a troposphere to stratosphere transition at 200 hPa (as used in Sheshadri et al. 2015). Note that the tropospheric equilibrium temperature profile was not modified, only the stratospheric profile. In this configuration the winter hemisphere (with a strong polar vortex) is in the Southern Hemisphere (SH) and the summer hemisphere (with a warmer stratosphere) is in the Northern Hemisphere (NH). There is no orography or other longitudinal asymmetries (such as land-sea contrast) that would give rise to forced stationary planetary waves, and the lack of a seasonal cycle or other sources of external variability means that the model simulations are statistically stationary. For further details on model configurations see Appendix F.

The different model configurations exhibit climatological jets at different latitudes and with different strengths, and thereby give rise to different variability. We have three different model climatologies to compare: equinox, winter and summer. The equinox configuration gives a strong jet centred at 40^o (Fig. 3.1a), whereas the winter and summer hemispheres of the solstice configuration have weaker jets around 45^o and 35^o latitude (Fig. 3.1b,c), respectively.

In order to test the relationships found in the simplified model in a more realistic setting, the model data are compared to the ERA-Interim observational reanalysis dataset from the European Centre for Medium-Range Weather Forecasts (Dee et al., 2011). The data are analysed as daily mean (from four times daily resolution – the eddy fluxes are first computed at 6-hourly resolution and then averaged over 24 h) for the time period between 1 January 1981 and 31 December 2010 (10957 days) on a grid with a resolution of 0.7^o in latitude and longitude, and 27 pressure levels between 1000 hPa and 100 hPa. The temporal anomalies were formed by removing the seasonal cycle (subtracting the climatology of each calendar day), hence no specific season is analysed. Only Southern Hemisphere observed data were analysed in this study, where the climatological jet is centred around 50^o latitude (Fig. 3.1d).

3.2.2 EOF and regression analysis

Empirical orthogonal function (EOF) analysis is adopted to obtain the leading modes of variability of various fields. The EOF of zonal mean zonal wind ($[u]$) is called SAM (after Southern Annular Mode), where the dipolar mode (representing shifting of the jet) is called SAM1 (usually the leading mode of variability) and the tripolar mode (representing sharpening and strengthening of the jet) is called SAM2 (usually the second mode of variability). The EOF of eddy kinetic energy (EKE $= 0.5\left[u^{*2} + v^{*2}\right]$) is called BAM (after Baroclinic Annular Mode found in

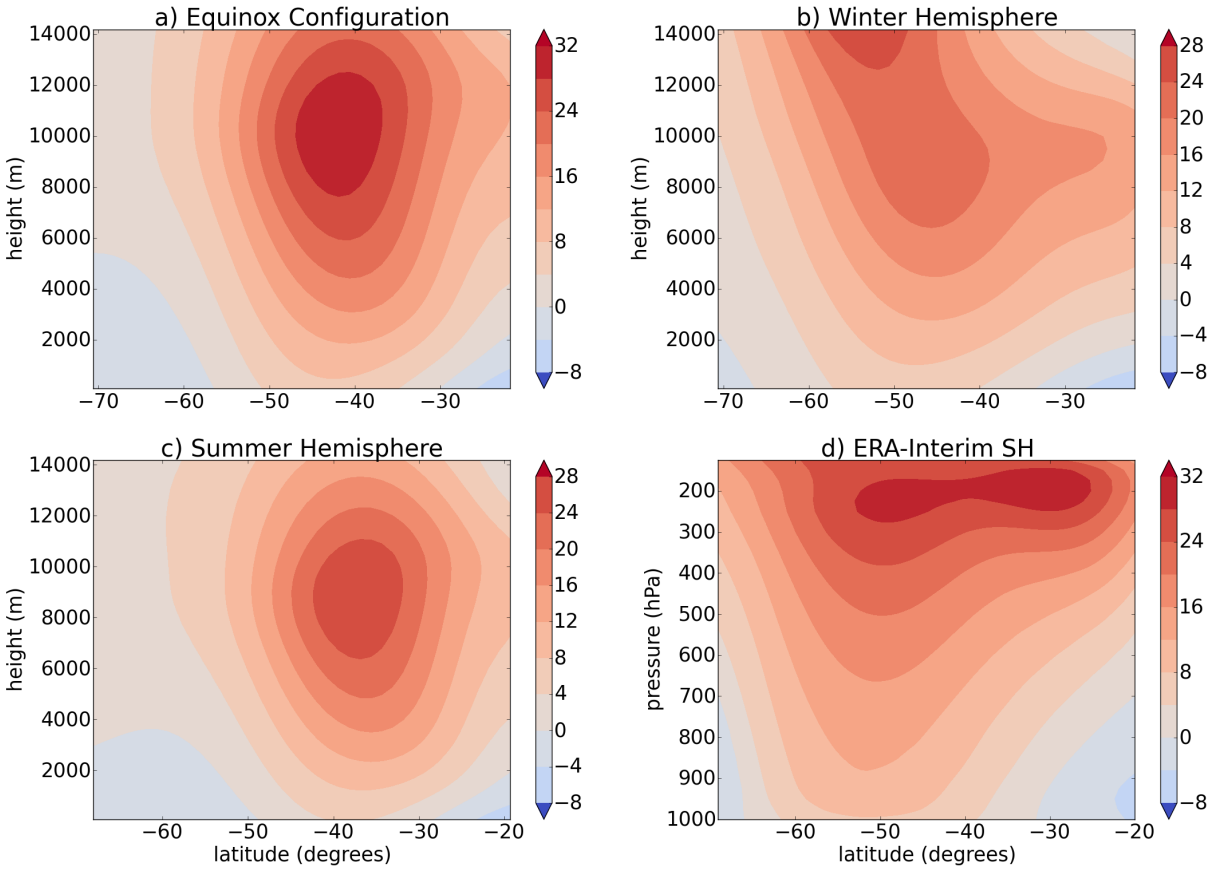

Figure 3.1: Meridional-vertical cross sections of zonal mean zonal wind. - For (a) equinox, (b) winter, (c) summer model configurations, and (d) ERA-Interim. Note that the summer hemisphere data were plotted as Southern Hemisphere (SH) for easier comparison with other configurations.

Thompson and Woodworth 2014), where BAM1 represents the monopolar mode (representing amplitude variations in the EKE field), BAM2 the dipolar mode (representing latitudinal shifts of the field) and BAM3 the tripolar mode (representing sharpening and strengthening of the field). Here the square brackets ([.]) represent the zonal mean, the asterisk (*) represents perturbations from the zonal mean, u is zonal velocity and v is meridional velocity. We recognize that the different EOFs are statistical rather than physically distinct entities, so are used only as a basis for our analysis which focuses on the coupling between barotropic and baroclinic components of the variability.

Additional modes of variability are defined based on eddy momentum ($[v^*u^*]$) and heat ($[v^*\theta^*]$) fluxes, called EMF and EHF, respectively, where θ is potential temperature. Here

Table 3.1: Variance explained (in %) for the first two SAM modes and the first three BAM modes for different model configurations and for ERA-Interim under a Lanczos 50-day low pass filter. Note that the modes are numbered according to spatial structure and not variance explained.

configuration	SAM1	SAM2	BAM1	BAM2	BAM3
equinox	84	11	19	70	6
summer	86	9	24	65	6
winter	59	31	32	42	13
ERA-Interim	59	25	38	23	14

EMF1 and EHF1 are monopolar modes (representing amplitude variations), EMF2 and EHF2 are dipolar modes (representing latitudinal shifts) and EHF3 is a tripolar mode (representing sharpening and strengthening of the field). Note that the modes are numbered according to their spatial structure and not by the variance explained, hence in some cases the leading modes can be SAM2, BAM2 etc. (as shown in Table 3.1).

Before calculating the EOFs of the fields, a mass weighted vertical average is applied to the zonal mean model fields in height coordinates:

$$\langle \mathcal{B} \rangle = \frac{\sum_{k=0}^{N} [\rho \mathcal{B}]_k (z_{k+1/2} - z_{k-1/2})}{\sum_{k=0}^{N} [\rho]_k (z_{k+1/2} - z_{k-1/2})} \tag{3.1}$$

where $\mathcal{B}$ is the zonally averaged field of interest, ρ is density, $\langle . \rangle$ is vertical average, k represents the vertical levels of the given quantity, $k \pm 1/2$ represents the half levels (vertical levels between k levels), N is the top vertical level of interest and z is the vertical coordinate. For ERA-Interim a pressure weighted vertical average is applied: $\langle \mathcal{B} \rangle = p_o^{-1} \sum_{k=0}^{N} [\mathcal{B}]_k (p_{k-1/2} - p_{k+1/2})$ where p is pressure and $p_o = \sum_{k=0}^{N} (p_{k-1/2} - p_{k+1/2})$. The vertical average is taken from the surface up to 11.5km (200 hPa for ERA-Interim), except for heat flux where 5 km (500 hPa for ERA-Interim) was used since θ increases rapidly with height. Thus only tropospheric variability is represented in these diagnostics. These vertically averaged fields, weighted by $\sqrt{\cos \phi}$, are then used to calculate EOFs of zonal mean zonal wind, EKE, eddy heat and eddy momentum flux. For further details on EOF (and regression) analysis see Appendix G.

After calculating the EOFs, various fields are regressed onto the principal components (PC) of these modes of variability. The regressed fields include zonal mean zonal wind, EKE, eddy heat and eddy momentum flux. These show the relationship between the different dynamical fields involved in each mode of variability as well as identify the leading modes of variability in

Table 3.2: Correlation between SAM1 and BAM2 at lag 0 for different model configurations and for ERA-Interim for unfiltered, low and high pass filtered data. Only statistically significant correlations (exceeding 95% threshold) are given.

configuration	unfiltered	low pass	high pass
equinox	0.45	0.87	-0.55
summer	0.62	0.92	-0.55
winter	0.29	0.66	-0.31
ERA-Interim	-0.05	0.63	-0.28

Table 3.3: As in Table 3.2, but for SAM2 and BAM1.

configuration	unfiltered	low pass	high pass
equinox	-0.28		-0.53
summer	-0.34	0.07	-0.57
winter	-0.32	-0.65	-0.27
ERA-Interim	-0.31	-0.42	-0.29

terms of their spatial structure. The correlations between different PC timeseries of SAM and BAM modes of variability are given in Tables 3.2-3.4, and are discussed later, in context.

For reference, the contours in Fig. 3.2 show regressions of zonal mean zonal wind on SAM1,2, of EKE on BAM1,2,3, of momentum flux on EMF1,2 and of heat flux on EHF1,2,3, for the model equinox configuration using unfiltered data and without any time lags. The colours in the figures show the climatologies of the regressed fields. The horizontal pairing of panels reflects the dominant relationships between modes (e.g. SAM1 has a clear relationship with EMF1 through the zonal momentum equation). The figure illustrates the typical spatial structures that these modes have, as described above.

3.2.3 Power spectrum, temporal filtering and cross-spectrum analysis

To calculate the power spectra of the PC timeseries of the EOF fields (e.g. SAM, BAM, EHF, EMF), we follow the methodology used in Byrne et al. (2016). The data are first windowed using a Hanning window, then a periodogram is calculated and finally the fields are smoothed using Daniell filters following Bloomfield (2000).

These power spectra (based on unfiltered data) were used to determine the frequency bands

Table 3.4: As in Table 3.2, but for SAM2 and BAM3.

configuration	unfiltered	low pass	high pass
equinox	0.30	0.81	0.03
summer	0.32	0.75	
winter	0.27	0.50	0.04
ERA-Interim	0.05	0.27	0.09

at which different dynamical processes take place (section 3.4). The original data (not PC timeseries) were then filtered according to the frequency bands using the Lanczos filter (Duchon, 1979) and EOFs were re-calculated from the filtered data. Note that the EKE, heat flux and momentum flux time series are filtered, not each component of them separately (e.g. u, v, θ) as we are interested in the wave-mean flow interaction on different timescales, rather than in which waves (low or high frequency) contribute to the behavior.

The cross-spectrum analysis was computed following Lorenz and Hartmann (2001). We first obtained the relevant unfiltered timeseries (section 3.3), then we divided them into 256 or 512-day sections (for comparison) overlapped by 128 or 256 days, respectively, and windowed each section by a Hanning window. These gave at least 72 or 36 degrees of freedom, respectively. The cross-spectra of each section were then averaged and smoothed using Daniell filters (as for the power spectra).

3.3 Theoretical background

Wave-mean flow interactions are usually studied using the zonal momentum budget and Eliassen-Palm (EP) wave activity theory, and the Transformed Eulerian Mean (TEM) perspective (Andrews and McIntyre, 1976) yields a direct link between the two quantities [section 1.3]. However, the BAM modes are based on EKE [section 1.2]. Whilst EKE may be considered a proxy for EP wave activity, there is also an EKE equation derivable within the TEM framework, which in log-pressure coordinates is (Plumb, 1983)

$$\frac{\partial[K_E]}{\partial t} = C(P_E \rightarrow K_E) - C(K_E \rightarrow K_M) - \frac{1}{p_{ln}} \nabla \cdot \mathbf{B}(K_E) + S(K_E) \tag{3.2}$$

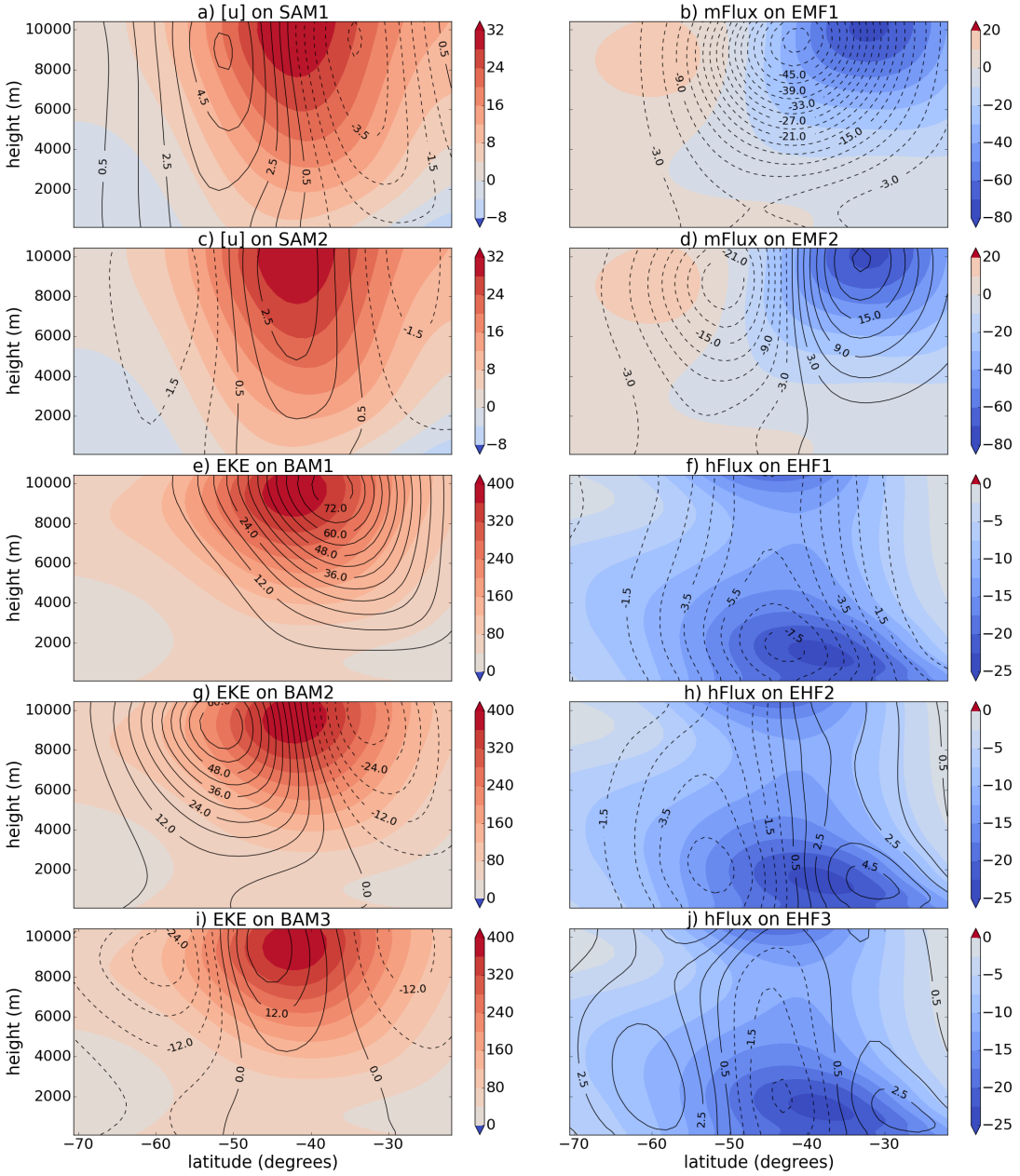

Figure 3.2: Regressions on different modes of variability. - Contours show regressions of zonal mean zonal wind ($[u]$) on a) SAM1 and c) SAM2 (contour interval is 1 m s^{-1}), of EKE on e) BAM1, g) BAM2 and i) BAM3 (contour interval is 6 m^2 s^{-2}), of momentum flux (v^*u^*) on b) EMF1 and d) EMF2 (contour interval is 3 m^2 s^{-2}), and of heat flux ($v^*\theta^*$) on f) EHF1, h) EHF2 and j) EHF3 (contour interval is 1 m K s^{-1}). Colours show the climatologies of the regressed fields. Data are from the equinox model configuration and were not filtered.

where

$$C(P_E \rightarrow K_E) = \frac{Rp_{ln}^{\kappa}}{H} \frac{[\mathbf{u}^*\theta^*] \cdot \nabla[\theta]}{\partial[\theta]/\partial z_{ln}} \tag{3.3}$$

represents the conversion from eddy potential energy (P_E) to EKE (K_E), $C(K_E \rightarrow K_M) = p_{ln}^{-1}[u]\nabla \cdot \mathbf{F}$ represents the conversion from EKE (K_E) to zonal mean kinetic energy (K_M), $\mathbf{B}(K_E) = p_{ln}[\mathbf{u}^*\phi^*] + [u]\mathbf{F}$ is the EKE flux term and $S(K_E) = [\mathbf{u}^* \cdot \mathbf{L}^*]$ is the source-sink term of EKE. Here

$$\mathbf{F} = p_{ln}\left(-[u^*v^*], \frac{f[v^*\theta^*]}{\partial[\theta]/\partial z_{ln}}\right)$$

is the QG EP flux (its divergence represents the eddy torque on the mean flow), $\nabla = (\partial/\partial y, \partial/\partial z_{ln})$, p_{ln} = pressure/1000 hPa, $z_{ln} = -H \ln p_{ln}$ is log-pressure vertical coordinate, $\kappa = R/c_p$, R is gas constant, c_p is specific heat at constant pressure, y represents latitude, $\mathbf{L}$ is frictional force, ϕ is geopotential, $\mathbf{u} = (u, v, w)$ is velocity vector, H is a constant scale height (approximately 10 km), and f is the Coriolis parameter.

Here note that TEM version [(3.2) and (3.3)] of Lorenz's energy cycle [from section 1.2] combines the conversion terms $C(P_M \rightarrow P_E)$ and $C(P_E \rightarrow K_E)$ from Fig. 1.6 into $C(P_E \rightarrow K_E)$ in (3.3). However, in both cases the conversion from available potential energy to EKE is dominated by the meridional heat fluxes (as also mentioned below).

3.3.1 Simplified TEM equations

Lorenz and Hartmann (2001) used cross-spectrum analysis to show that the vertically averaged zonal mean zonal wind ($z_u = \langle[u]\rangle$) and eddy momentum flux convergence ($m = -\partial_y(\langle\rho_o[u^*v^*]\rangle)$ with $\partial_y = \partial/\partial y$ and ρ_o vertical density profile) were linearly related according to [see also (1.1)]

$$\frac{\partial z_u}{\partial t} = m - \frac{z_u}{\tau}, \tag{3.4}$$

with τ a constant. This relationship follows from the zonal momentum equation under QG scaling provided the source-sink term can be represented as a linear damping $-z_u/\tau$ (dominated by boundary layer friction). As discussed in Chapter 2, the relationship between m and $\partial z_u/\partial t$ is only approximate, since planetary scale heat fluxes also contribute to angular momentum via meridional mass redistribution [see (2.18)], but the latter are negligible in QG scaling (Haynes and Shepherd, 1989). Applying a spectral analysis (Fourier Transform) yields a cross-spectrum

relationship (Lorenz and Hartmann, 2001)

$$\frac{Z^c M}{Z^c Z} = i\omega + \frac{1}{\tau} \tag{3.5}$$

where Z and M represent the Fourier transforms of z_u and m, respectively, the superscript c denotes the complex conjugate, and ω is the angular frequency. τ is determined by finding an empirical linear regression to the cross spectrum (as described in Appendix A of Lorenz and Hartmann 2001)

$$\frac{Z^c M}{Z^c Z} = \chi + i\vartheta\omega,$$

from which $\tau = \vartheta/\chi$.

The relationship (3.5) suggests that the real part of the cross spectrum $Z^c M/Z^c Z$ is constant (τ^{-1}), while the imaginary part of the cross spectrum changes linearly with ω. This is illustrated in section 3.4.

Thompson and Woodworth (2014) and Thompson and Barnes (2014) suggested there existed a relationship between EKE and heat flux, independent of momentum flux convergence or zonal mean zonal wind. Thompson et al. (2017) hence suggested a relationship between EKE and heat flux that is similar to (3.4), namely

$$\frac{\partial[K_E]}{\partial t} = \alpha_{EKE}[v^*\theta^*] - \frac{[K_E]}{\tau_{EKE}} \tag{3.6}$$

where $|\alpha_{EKE}| \approx 3\times10^{-5}$ m K^{-1} s^{-2} and $\tau_{EKE} \approx 3$ days are constants, EKE is taken at 300 hPa, heat flux is taken at 850 hPa and both quantities were averaged meridionally between 40^o and 60^o latitude where EKE peaks (in ERA-Interim data). Thompson et al. (2017) found that such a simple model reproduced the oscillator model of Thompson and Barnes (2014), thus we test this relationship using cross-spectrum analysis to see how well it holds at different timescales. The cross-spectrum relationship corresponding to (3.6) is

$$\alpha_{EKE}\frac{E^c H}{E^c E} = i\omega + \frac{1}{\tau_{EKE}}, \tag{3.7}$$

where E and H now represent Fourier Transforms of EKE and heat flux, respectively. In contrast to (3.5), there is now an empirical factor, α_{EKE} (since (3.6) is not exact), which is determined by finding a linear regression to $E^c H/E^c E$ at frequencies lower than 0.1 cycles per day so that the imaginary part of $\alpha_{EKE}E^c H/E^c E$ is proportional to ω.

Equation (3.6) is simplified compared to the TEM EKE equation (3.2), only representing $C(P_E \rightarrow K_E)$ (3.3) explicitly (assuming $[w^*\theta^*] \propto [v^*\theta^*]$, which is valid under QG scaling), with the other terms subsumed in the linear damping term. Although latitudinal averaging will eliminate the EKE flux component of (3.2), it will not eliminate the $C(K_E \rightarrow K_M)$ term unless $[u]$ is slowly varying compared to $\nabla \cdot \mathbf{F}$, which is not the case. In this respect, the wave activity equation is much cleaner (Wang and Nakamura, 2015, 2016). Our approach here is not to justify the approximation (3.6) but rather to examine how well it holds across timescales, as a way of understanding the observed BAM-SAM decoupling. Based on the analysis of Chapter 2 we expect that (in addition to latitudinal averaging) the relationship (3.6) would only hold at timescales longer than synoptic (and not necessarily at quasi-steady states), which is also tested below.

3.4 Equinox results

3.4.1 Cross-spectra

Lorenz and Hartmann (2001) have shown in observations that cross spectrum analysis (3.5) supports the relationship between vertically averaged zonal mean zonal flow and eddy momentum flux convergence described by (3.4). Indeed, Fig. 3.3a shows that these two quantities are related in the equinox model configuration at all frequencies as the real part of the cross spectrum is constant and proportional to τ^{-1} with $\tau \approx 10.6$ days, and the imaginary part of the cross spectrum nicely follows the ω slope. Fig. 3.3b shows that the phase difference between m and z_u at low frequencies is small (they are in phase), whereas at the highest frequencies, corresponding to synoptic timescales of 5-10 days, they are nearly 90^o out of phase. These two figures thus clearly illustrate that at very low frequencies $z_u/\tau \approx m$ whereas at the highest frequencies $\partial z_u/\partial t \approx m$, as expected from (3.4).

In section 3.3 we presented a simplified theory for the EKE budget (3.6,3.7), which is analogous to Lorenz and Hartmann (2001)'s approximation for the zonal momentum equation (3.4,3.5). Here we test this theory using cross spectrum analysis (3.7) after averaging over different latitudinal bands.

First, we test the relationship for a 20-degree latitudinal band (EKE taken at 9000 m, heat flux at 1500 m, and both averaged between 30^o and 50^o latitude where both quantities peak, Fig. 3.2e-j in colours) for the equinox model configuration, using different lengths of segments:

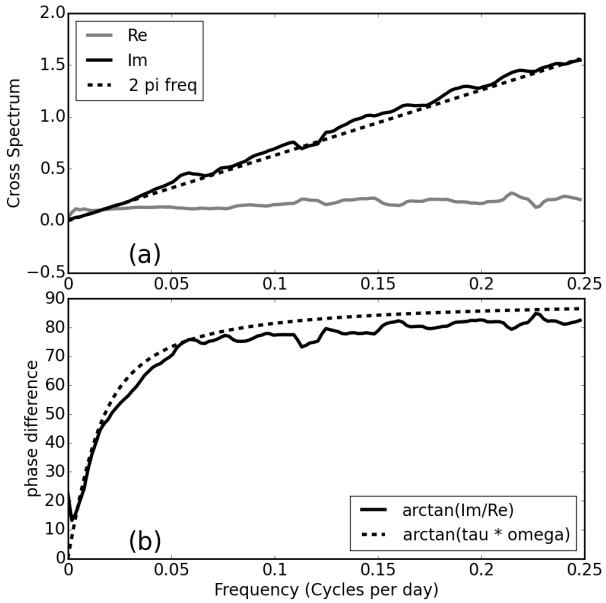

Figure 3.3: Imaginary and Real parts of cross-spectrum (a) and phase difference (b) between zonal mean zonal wind and eddy momentum flux convergence. - Data were split into 512-day long segments overlapped by 256 days. Vertically averaged (full depth) zonal mean zonal wind (Z) and momentum flux convergence (M) were regressed onto EOF1 of $[u]$ to obtain timeseries. Data are from the equinox model configuration and were not filtered. Note that a similar figure can be obtained for EOF2 of $[u]$.

256 and 512 (Fig. 3.4). In general, for both lengths of segments the relationship holds well at frequencies lower than 0.1 cycles per day, above which the imaginary part of the cross spectrum becomes constant with frequency or even decreases, while the real part of the cross spectrum remains reasonably constant. Different segment lengths show that the peaks apparent at synoptic timescales are reasonably random and that noise increases as longer segments are taken due to fewer degrees of freedom and finer frequency resolution. $|\alpha_{EKE}|$ varies between 7 and 8.5 $\times 10^{-5}$ m K^{-1} s^{-2}, and τ_{EKE} varies between 2.5 to 4.2 days. The poor approximation at synoptic timescales suggests that at these timescales the other terms in (3.2) (such as momentum fluxes and EKE fluxes) indeed matter. Nonetheless, Fig. 3.4 shows that such a simple relationship holds reasonably well at periods longer than 10 days. This is consistent with the prediction of the multiscale asymptotic theory [Chapter 2], after averaging over synoptic time and spatial scales. Similar results can be obtained also with a 10^o and 90^o latitudinal band (not shown), which means that the relationship is robust for latitudinal averages of 10 degrees and wider. This is consistent with Wang and Nakamura (2015, 2016).

Note that the real and imaginary parts of the cross-spectra cross at a higher frequency than

for the momentum flux convergence and zonal mean zonal wind, due to the damping timescale τ_{EKE} being significantly smaller than τ, implying stronger baroclinic damping processes compared to the barotropic ones. Consequently, the phase difference (Fig. 3.4a,b ii) increases more gradually than for the barotropic processes (Fig. 3.3b) and by frequency 0.25 cycles per day reaches just below 80°. This suggests that the quasi-steady relationship $[K_E]/\tau \approx \alpha_{EKE}[v^*\theta^*]$ holds down to periods of about 20 days for EKE and heat flux, whereas for momentum flux convergence and zonal mean zonal wind it only holds at periods longer than about 50 days. We thus consider the low-frequency range with periods longer than 50 days to be in a quasi-steady balance.

3.4.2 Power spectra

Power spectra for the model equinox configuration are calculated for the PC timeseries of EOF fields (SAM, BAM, EHF and EMF) for the first two or three modes of variability in Fig. 3.5. The frequency spectra for the tendency of SAM and BAM are also shown as these two modes show mainly low frequency behavior, whereas their tendencies reflect the higher frequency behavior as well. This is clearly shown in Fig. 3.5 where SAM1,2 and BAM2,3 show predominantly low frequency behavior with the highest peaks well beyond 50 days, whereas their tendencies show higher frequency behavior on synoptic timescales with continuous spectra peaked around 10 days. These spectra suggest that at lower frequencies, zonal mean zonal wind and EKE are related to the eddy fluxes (the lower frequency part of the EMF1,2 and EHF2,3 spectra), whereas at higher frequencies it is rather their tendencies that are related to the eddy fluxes (the higher frequency part of the EMF1,2 and EHF2,3 spectra), distinguishing the different behavior anticipated from (3.4) and (3.6).

The power spectrum for BAM1 instead has a high frequency peak around a 40 day period and has another peak at lower frequencies, while its tendency shows a continuous spectrum peaked around a 20 day period. This suggests that the lower and higher frequency behaviors (reflected in EKE and in the tendency of EKE) for BAM1 are not well separated and overlap in the frequency domain, in contrast to the other modes. EHF1 and the tendency of BAM1 both show a distinct peak at about the 20-30 day period, which is consistent with the results of Thompson and Barnes (2014) and Wang and Nakamura (2015) who found an oscillatory behavior between EKE (or wave activity) and heat flux with similar periods. The spectra suggest that

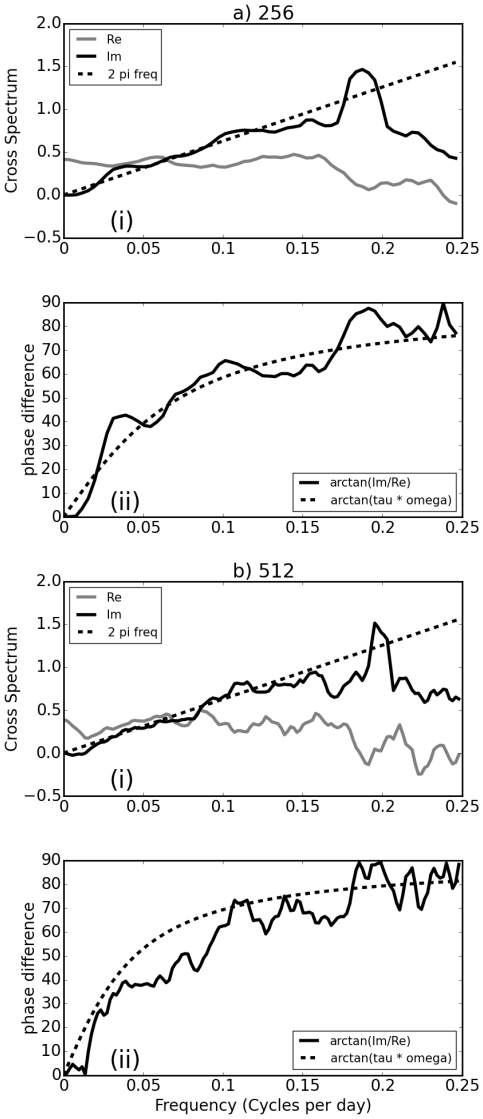

Figure 3.4: Imaginary and Real parts of cross-spectrum (i) and phase difference (ii) between EKE and eddy heat flux. - Data were split into (a) 256, and (b) 512-day long segments overlapped by a half-length. EKE (E) was taken at 9000 m and heat flux (H) was taken at 1500 m. Both were averaged between $30^{o}S$ and $50^{o}S$. Data are from the equinox model configuration and were not filtered.

this oscillatory behavior at these periods is distinct (i.e. the timescale of the BAM1 and EHF1 is different to those of the other modes).

From the power spectra a frequency cut-off can be determined for the high-pass and low-pass filtering. The thick solid grey line in Fig. 3.5 shows the chosen cut-off period of 50 days, which

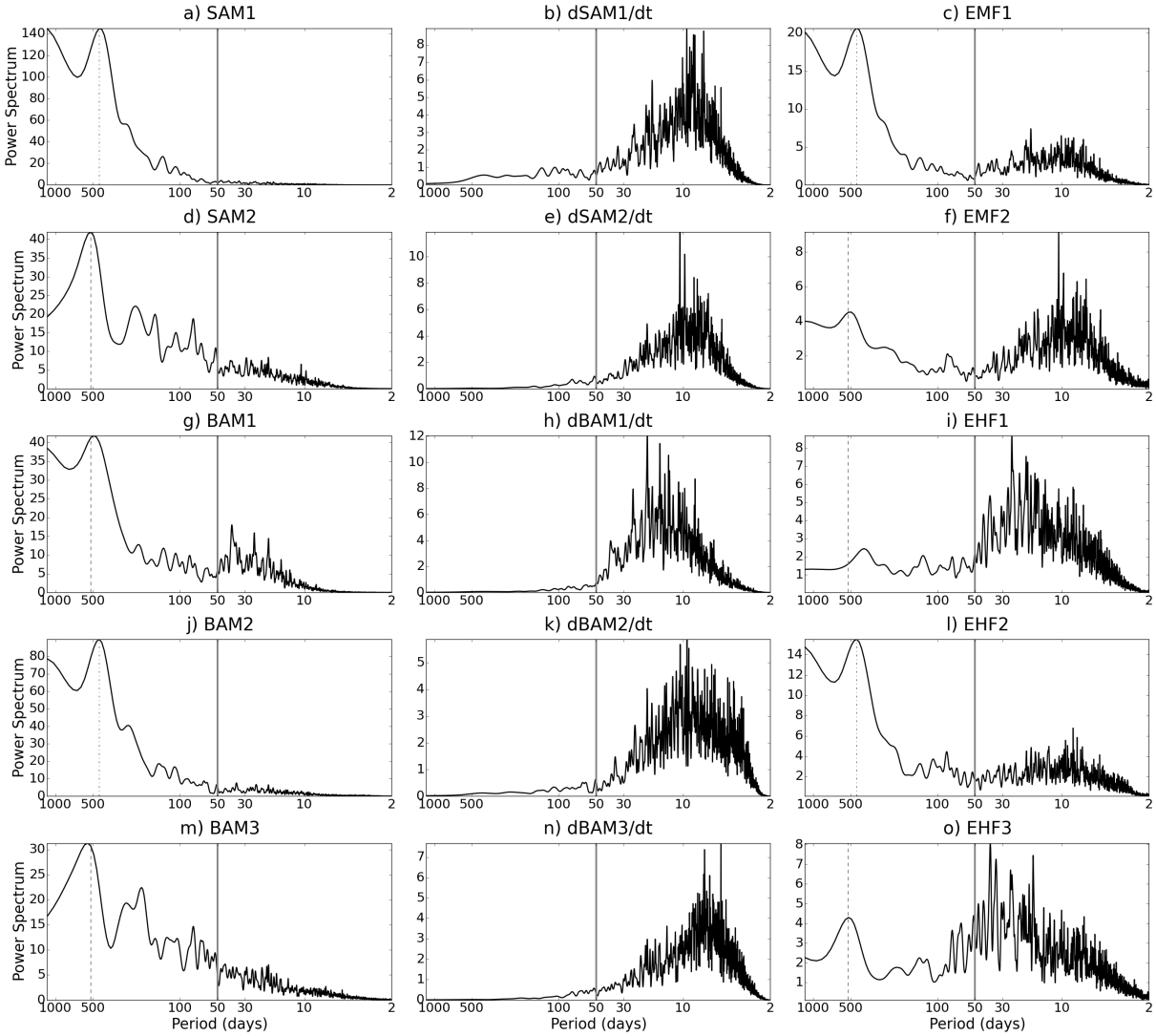

Figure 3.5: Power spectra (1/day) of unfiltered PC timeseries of different fields as labelled. - See text for description of modes, also Fig. 3.2. Vertical grey dash-dotted and dashed lines indicate the main peaks in SAM1 and SAM2 power spectra, respectively, and the grey solid line indicates the frequency cut-off used later for filtering. Data are from the equinox model configuration.

distinguishes between the distinct behavior in the two frequency bands (i.e. low pass includes periods longer than 50 days and high pass includes periods shorter than 50 days). Note that the cut-off period of 30 days that was used in previous studies (e.g. Sparrow et al. 2009) would not be a good choice here. While the low pass data represent modes of variability in quasi-steady balance, the high pass data include both synoptic timescale variability as well as intermediate timescales (timescales longer than synoptic and shorter than quasi-steady balance) where both

the time tendency and linear damping terms in (3.4, 3.6) are non-negligible.

It is clear from the power spectra that higher frequencies overlap and it is hard to separate the high-frequency behavior of EHF1 and BAM1 from that of EHF2,3, EMF1,2, BAM2,3 or SAM1,2 from the power spectra alone. However, at low frequencies there are distinct spectral peaks indicated in Fig. 3.5 (and also in Figs. 3.6, 3.9-3.11 below) by vertical dash-dotted and dashed lines. Because the model set-up is statistically stationary, these spectral peaks presumably arise from a limited sampling of red-noise variability. We can use this feature to our advantage, because it provides a clear fingerprint of covariability when the peaks match between different quantities. While the peaks themselves are not robust to subsampling (e.g. Fig. 3.6), all of the conclusions below are robust to subsampling and indeed that robustness provides more confidence in the presented results.

The dash-dotted and dashed lines in Fig. 3.5 show the peaks in the SAM1 and SAM2 power spectra, respectively, for periods between 50 and 1000 days. In order to be identified, the peaks had to be separated by at least 10 data points (with frequency resolution of 1/9360 days^{-1}) and had to be higher than 5/6 of the maximum value in the low-frequency part of the spectrum. The SAM1 peaks were then projected on the BAM2, EHF2 and EMF1 panels, whereas the SAM2 peaks were projected on the BAM1, BAM3, EHF1, EHF3 and EMF2 panels to locate matching peaks. If the main peaks approximately match, then this provides prima facie evidence for a relation between the modes. For the model equinox configuration this shows a clear low-frequency relation between SAM1, EMF1, BAM2 and EHF2. The relations between SAM1 and EMF1, and between BAM2 and EHF2, reflect the quasi-steady limit of (3.4) and (3.6) (i.e. $z_u/\tau \approx m$ and $[K_E]/\tau_{EKE} \approx \alpha_{EKE}[v^*\theta^*]$), but the cross-relation between SAM1 and BAM2 is non-trivial. The strong positive correlation for low-pass data is shown in the top row of Table 3.2. Similarly, there is a different low-frequency relation between SAM2, EMF2, BAM3 and EHF3, pointing to a non-trivial relation between SAM2 and BAM3. The strong positive correlation for low-pass data is shown in the top row of Table 3.4. The link between any of these modes and BAM1 or EHF1 is weaker (see also top row of Table 3.3). Therefore, we find no evidence of a quasi-steady cross-mode relationship between SAM1 and BAM1, which was the correlation examined (using unfiltered data) by Thompson and Woodworth (2014). Note that the correlations shown in Tables 3.2-3.4 are robust to subsampling, i.e. high correlations are robustly high and small or non-robust correlations are consistently small or non-robust.

These power spectra and correlations thus reveal three main mechanisms:

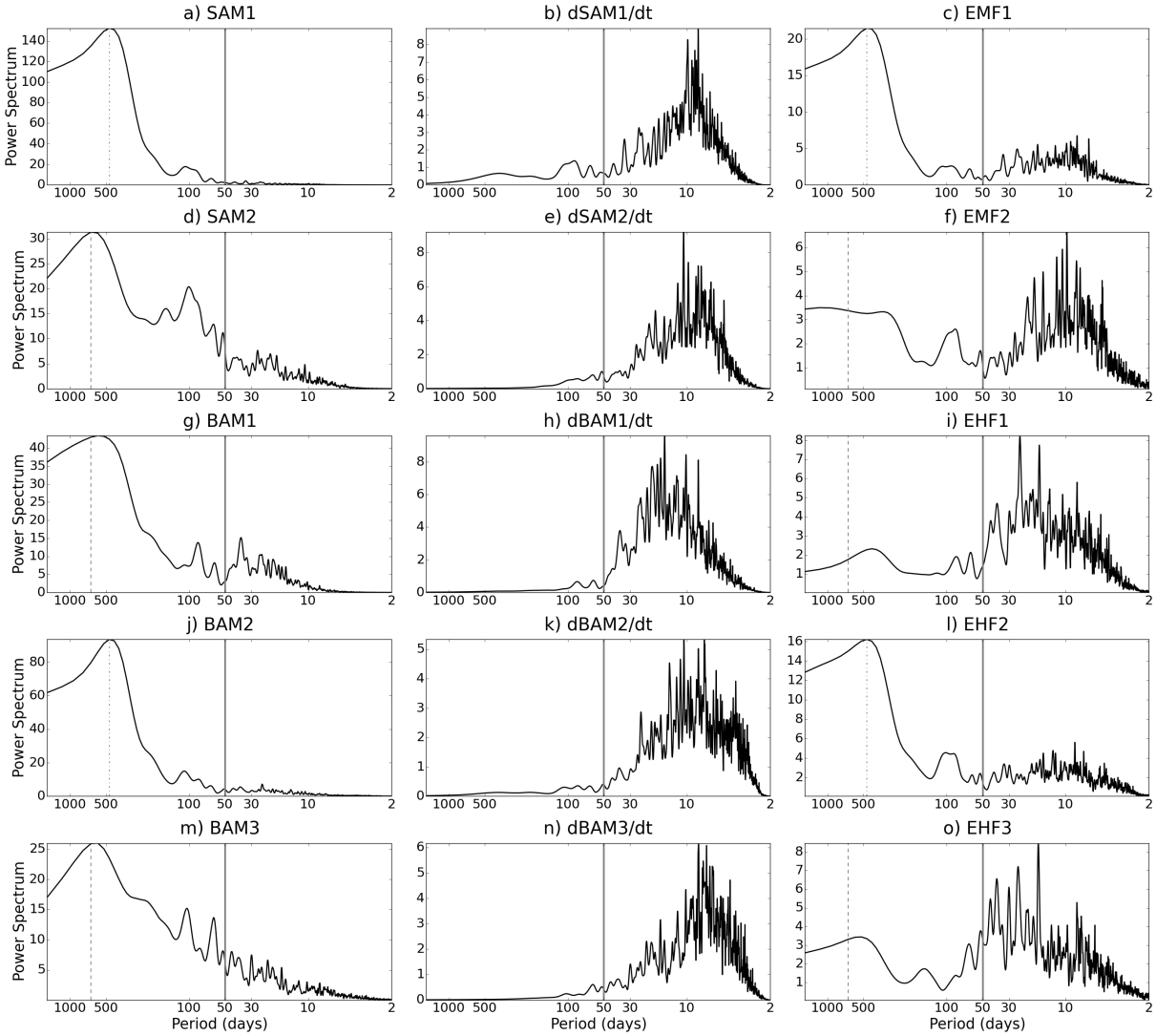

Figure 3.6: As in Fig. 3.5 but for only one half of the timeseries (subsample).

- The Thompson and Woodworth (2014) and Thompson and Barnes (2014) picture of a relationship between BAM1 and EHF1 through the oscillator model, with periods of 20-30 days (intermediate timescale);

- The classical (quasi-steady) positive baroclinic feedback picture (e.g. Robinson 2000) where the storm tracks move with the jet shifts (this feedback is possible if the eddies are absorbed at a different latitude than their source region). This is reflected in the positive correlations at low frequencies between SAM1 and BAM2/EHF2, and between SAM2 and

BAM3/EHF3, and in the regressions of EKE on low frequency SAM1,2 (see next section); and

- The higher frequency (synoptic timescale) picture of transient wave-mean flow interaction (e.g. Edmon et al. 1980), in which SAM1,2, EMF1,2, BAM2,3 and EHF2,3, all show power peaking around 10 days, and there are negative correlations (at zero lag) in high-pass data between SAM1 and BAM2 (see further discussion in section 3.5).

3.5 Comparison to other model configurations and to SH observations

The results from the equinox model configuration are now compared to the summer and winter hemispheres of the solstice model configuration, as well as to the SH in ERA-Interim. This is important as the different model configurations can exhibit different variability, because of different climatologies. Fig. 3.7 shows the low pass zonal mean zonal wind timeseries at 10 km for the different model configurations. It is clear that the summer and equinox configurations exhibit more persistence in their jet variability compared with the winter configuration. In particular, the shifting modes (SAM1, BAM2) in these two configurations show a clear dominance over the rest of the modes (Table 3.1).

Fig. 3.8 shows the EKE and eddy heat flux cross spectrum analysis for the winter (a) and summer (b) model configurations, and for ERA-Interim (c). These, together with Fig. 3.4a, show the robustness of the relationship (3.6) between EKE and eddy heat flux for periods longer than 10 days and for an average over a few latitudinal bands. (A 10 degree average is sufficient, but the signal is stronger for a 20 degree average, hence the former was omitted for brevity.) This is consistent with the decoupling of baroclinic and barotropic modes of variability under synoptic scale averaging (as predicted by asymptotic theory in Chapter 2) and is robust for all model configurations and for ERA-Interim (i.e. independent of setting), in the sense that the momentum fluxes are not needed to account for EKE variability at intermediate timescales. The EKE damping timescale τ_{EKE} varies between 1.5 and 4.2 days, while the parameter $|\alpha_{EKE}|$ varies between 5.6 and 11.4 $\times 10^{-5}$ m K^{-1} s^{-2}. While τ_{EKE} is consistent with the value found in Thompson et al. (2017), $|\alpha_{EKE}|$ is larger. This is because Thompson et al. (2017) regressed the tendency of EKE onto the heat flux to calculate $|\alpha_{EKE}|$, and the former is dominated by higher frequencies (as shown through power spectra, e.g. Fig. 3.5), whereas here we calculate

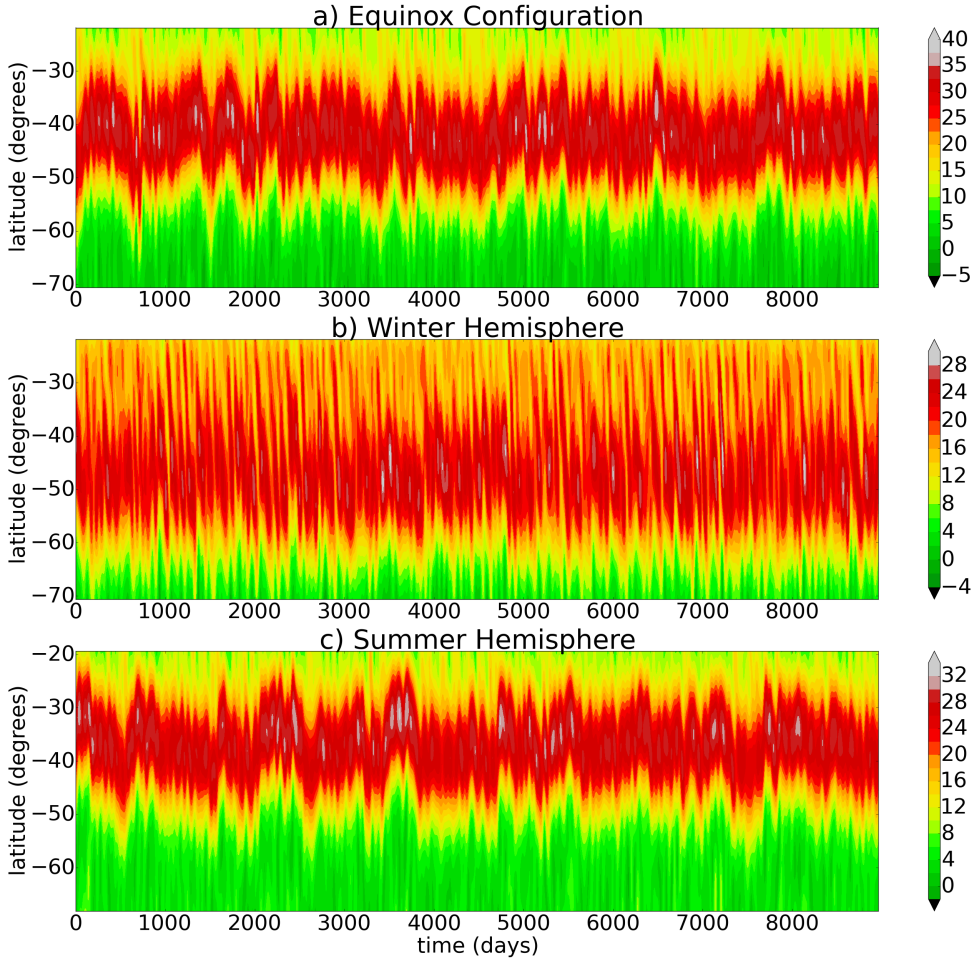

Figure 3.7: Low-pass zonal mean zonal wind timeseries at 10 km for different model setups. - (a) equinox, (b) winter hemisphere, and (c) summer hemisphere model configurations. Note that the summer hemisphere data were plotted as SH for easier comparison with other configurations.

it for periods longer than 10 days where the relationship (3.6) is robust, and the EKE, not its tendency, is used for calculations.

Figs. 3.9-3.11 show the power spectra for the winter and summer model configurations, and for ERA-Interim (with the same panels as in Fig. 3.5). These power spectra imply robust relationships between SAM and EMF modes, and between BAM and EHF modes, at all frequency ranges, according to (3.4) and (3.6), respectively. BAM1 and EHF1 exhibit power in the intermediate frequency range, for which the cross spectra showed a decoupling from the barotropic dynamics, whereas the rest of the modes exhibit the synoptic timescale (around 10 day periods) and quasi-steady (periods much longer than 50 days) behavior. While the links between SAM

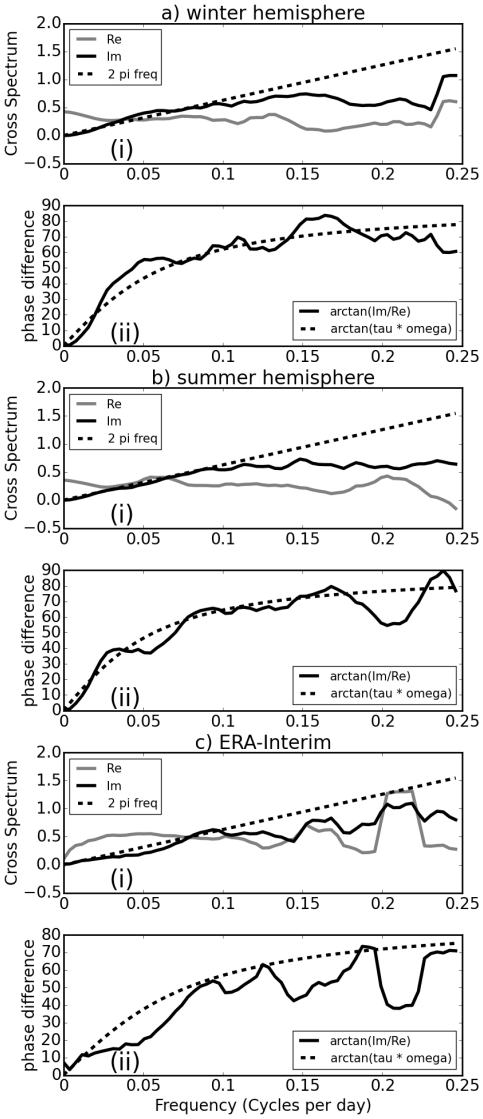

Figure 3.8: Imaginary and Real parts of cross-spectrum (i) and phase difference (ii) between unfiltered EKE and eddy heat flux for (a) winter hemisphere, (b) summer hemisphere, (c) ERA-Interim. - Data were split into 256-day long segments overlapped by 128 days. EKE (E) was taken at 9000 m (300 hPa for ERA-Interim) and heat flux (H) was taken at 1500 m (850 hPa for ERA-Interim). Both were averaged between: (a) 35° and 55°, (b) 25° and 45° and (c) 40° and 60° latitude.

and EMF modes and between BAM and EHF modes follow from the theory presented in section 3.3, the links between the SAM and BAM modes are non-trivial. To elucidate these links, the correlations between different SAM and BAM modes are given in Tables 3.2-3.4, to complement the power spectra in Figs. 3.5, 3.9-3.11.

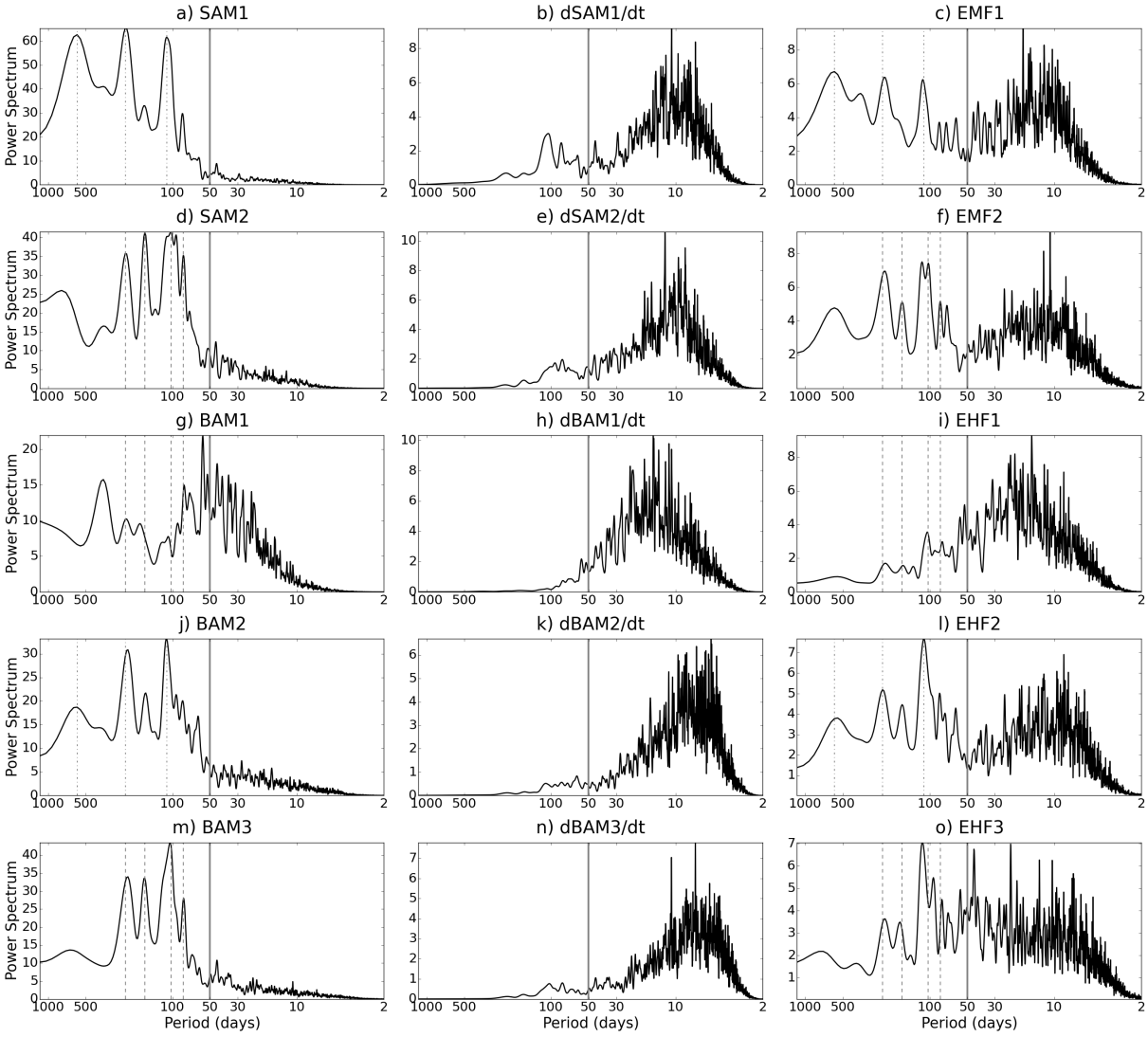

Figure 3.9: As in Fig. 3.5 but for the winter hemisphere model configuration.

The high pass data in Tables 3.2 and 3.3 show robust negative correlations between the SAM1,2 and BAM2,1 modes, respectively. This seems broadly consistent with TEM theory. Since $\partial[u]/\partial t$ is proportional to $\nabla \cdot \mathbf{F}$ (e.g. (2.3a) in Edmon et al. 1980) and $\partial[K_E]/\partial t$ is proportional to $-\nabla \cdot \mathbf{F}$ (3.2) (note that $[u]$ is generally westerly in the midlatitudes and hence does not affect the sign of the correlations), a negative correlation between corresponding SAM and BAM modes is expected on synoptic timescales as the tendencies reflect the high frequency behavior (as seen from the power spectra). SAM1 is a dipolar mode and thus matches BAM2. Although SAM2 is a tripolar mode and therefore might be expected to match BAM3, the

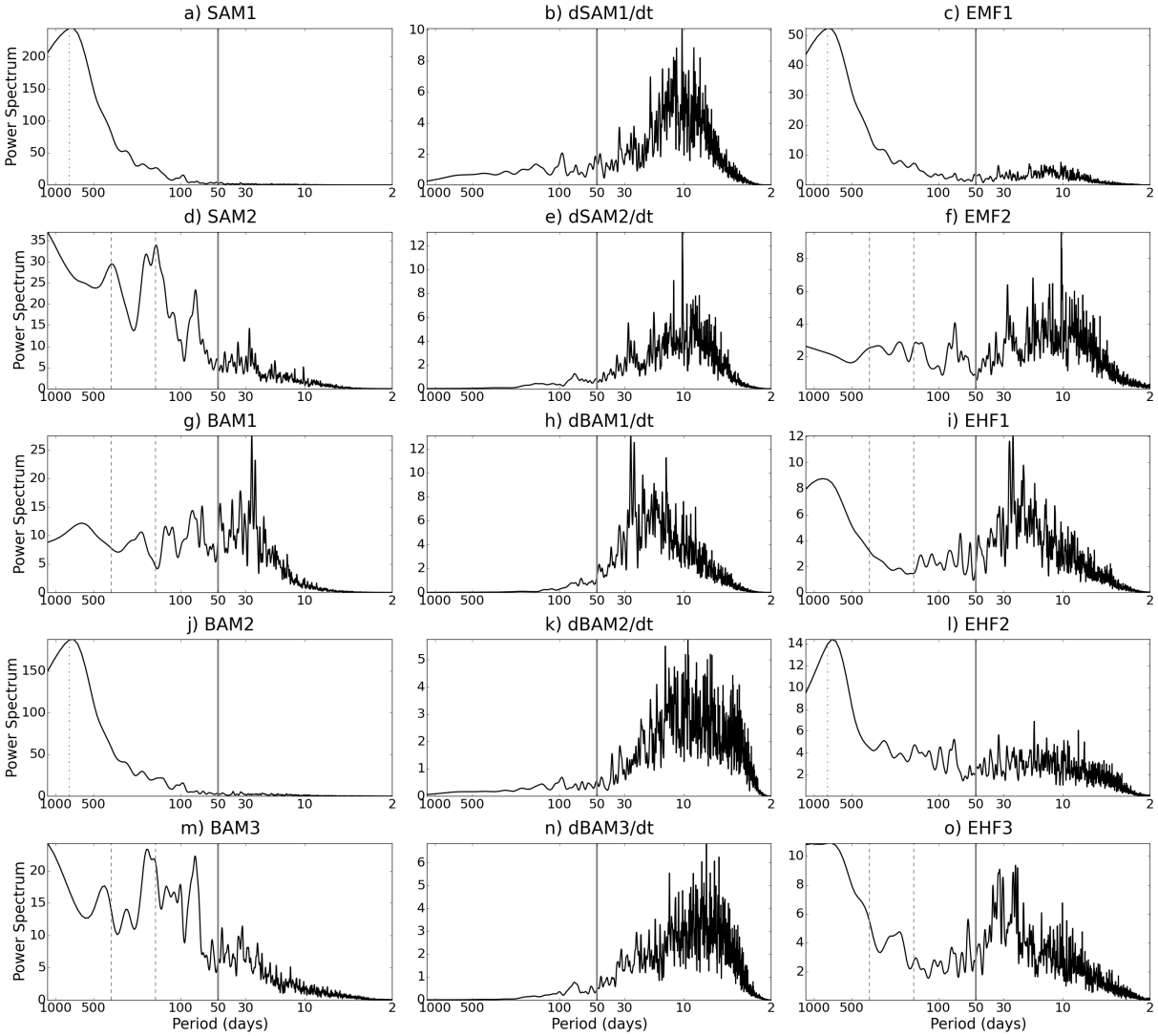

Figure 3.10: As in Fig. 3.5 but for the summer hemisphere model configuration.

correlation between SAM2 and BAM3 at high frequencies (Table 3.4) is non-robust or even negligible. Instead, SAM2 is seen to be negatively correlated with BAM1, which projects onto the center of SAM2. These negative correlations between SAM1 and BAM2 and between SAM2 and BAM1 are further confirmed in Figs. 3.12 and 3.13, where the regressions of high-pass EKE (shading) on high-pass SAM modes tend to exhibit the opposite sign to high-pass $[u]$ (contours) regressions on the same modes.

The low pass data in Tables 3.2 and 3.4 show robust positive correlations between the SAM1,2 and BAM2,3 modes, respectively, consistent with the quasi-steady positive baroclinic feedback

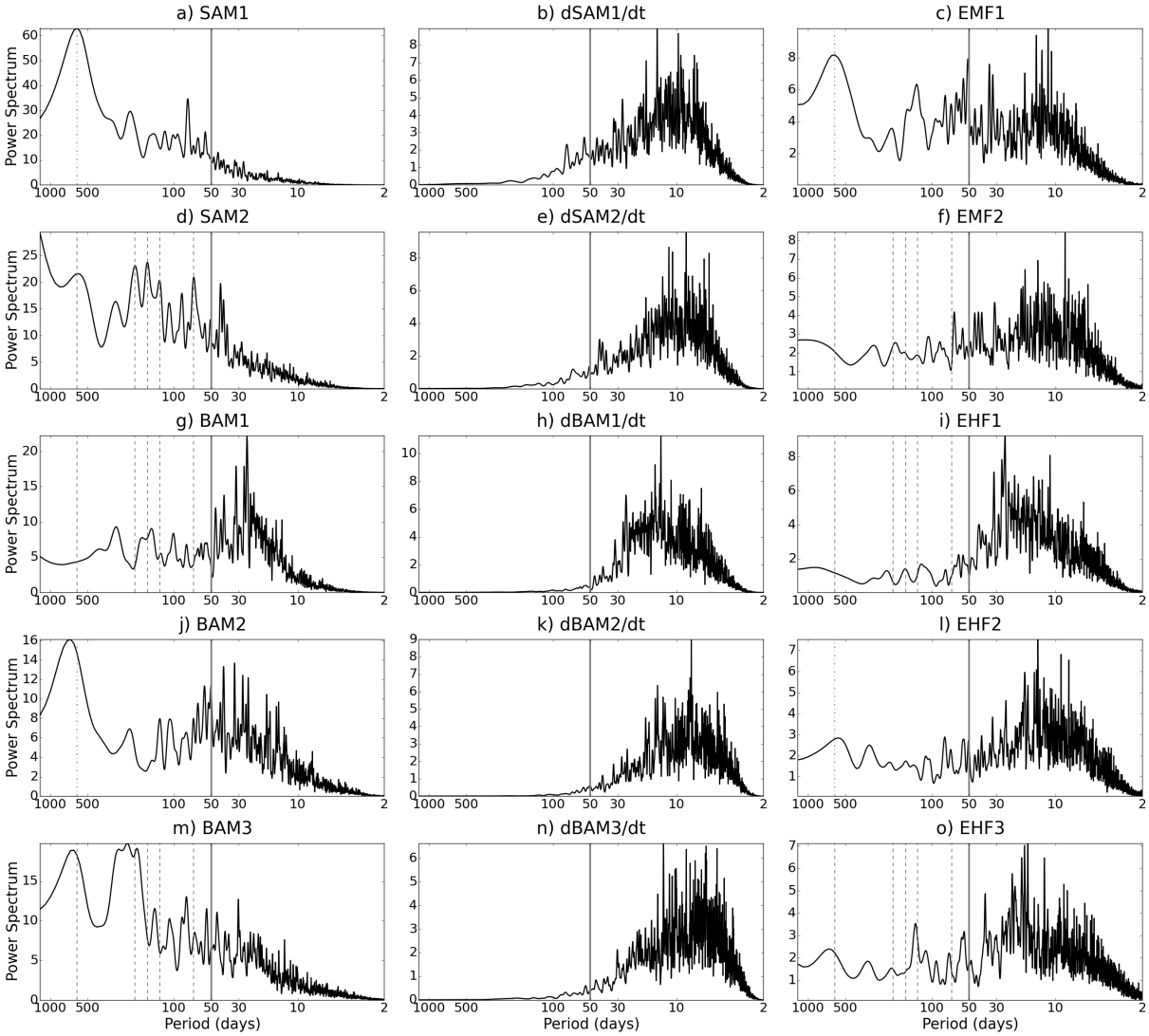

Figure 3.11: As in Fig. 3.5 but for ERA-Interim.

(Robinson, 2000) described in section 3.4.2. Moreover, there is a clear correspondence between the SAM1,2 and BAM2,3 low-frequency spectral peaks in all cases (Figs. 3.5, 3.9-3.11). Figs. 3.14 and 3.15 further show that the regression of low-pass EKE on low-pass SAM1 and SAM2 reflects BAM2- and BAM3-like behavior, respectively, and that positive SAM modes are related to positive BAM modes (i.e. positive wind anomaly is associated with positive EKE anomaly indicating a storm track shift with the jet stream, a positive baroclinic feedback mechanism), consistent with the correlations. Figs. 3.16 and 3.17 also show that the spatial structures of the SAM1,2 and BAM2,3 modes for all model configurations and for ERA-Interim are in phase, i.e.

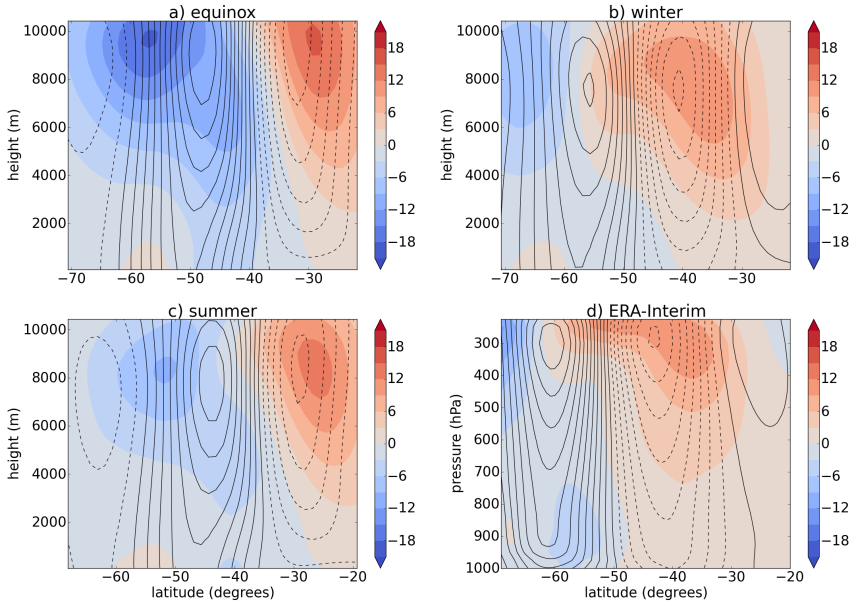

Figure 3.12: Regressions of high pass EKE (in shading) and high pass zonal mean zonal wind (in contours) on high-pass SAM1. - For (a) equinox, (b) winter, (c) summer model configurations, and (d) ERA-Interim. The units for EKE are $m^2\ s^{-2}$, and for the zonal mean zonal wind are $m\ s^{-1}$. The contour interval is $0.3\ m\ s^{-1}$ (..., -0.3, 0, 0.3, 0.6, ...). The dashed lines represent negative values and solid lines represent positive values.

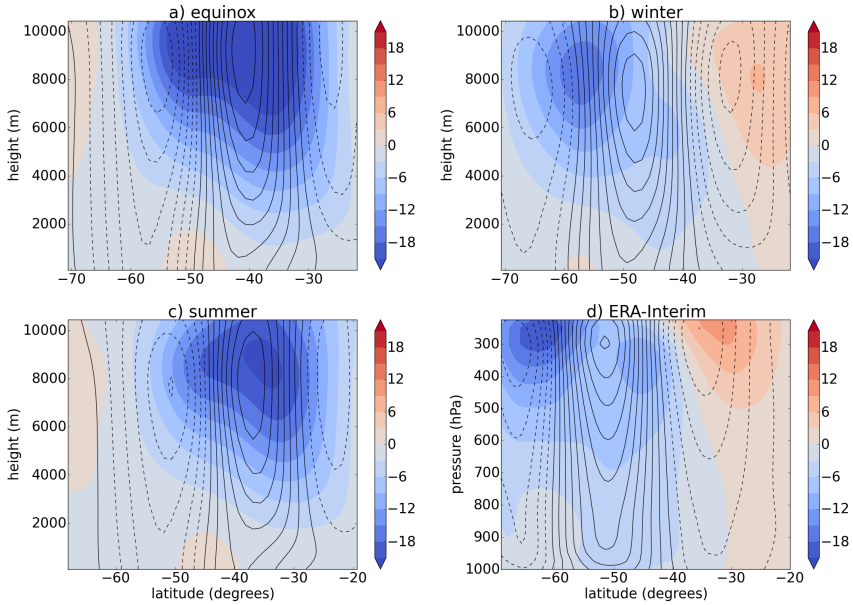

Figure 3.13: As in Fig. 3.12 but for the regressions on high pass SAM2.

the major peaks in the SAM and BAM modes closely follow each other.

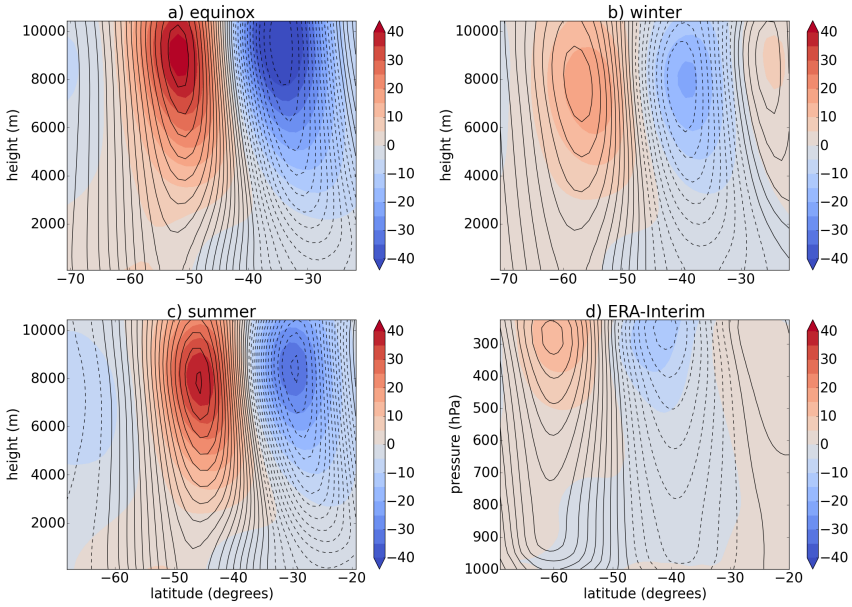

Figure 3.14: Regressions of low-pass EKE (in shading) and low pass zonal mean zonal wind (in contours) on low-pass SAM1. - For (a) equinox, (b) winter, (c) summer model configurations, and (d) ERA-Interim. The units for EKE are $m^2\ s^{-2}$, and for the zonal mean zonal wind are $m\ s^{-1}$. The contour interval is 0.3 $m\ s^{-1}$ (..., -0.3, 0, 0.3, 0.6, ...). The dashed lines represent negative values and solid lines represent positive values.

On the other hand, the low pass correlations between SAM2 and BAM1 are non-robust (Table 3.3), and there is no clear correspondence between their low-frequency spectral peaks (Figs. 3.5, 3.9-3.11). This implies that any link between the SAM2 and BAM1 modes is state-dependent. This is further demonstrated in Fig. 3.17, which shows the spatial structures of the SAM2 and BAM1 modes. While it is clear from this figure that the main peaks in SAM2 and BAM1 for ERA-Interim are in phase and could explain the high correlation between the two modes, it is less clear for the model configurations. The winter configuration shows a high correlation between SAM2 and BAM1, however the spatial structures are out of phase, suggesting that the high correlation could be a consequence of the chosen cut-off period (50 days) as in this case the BAM1 power spectrum peaks around 50 days (Fig. 3.9).

The correlations for the unfiltered data reflect the combination of high and low frequency behavior. This is especially true for SAM1 and BAM2 (Table 3.2) where the unfiltered correlations are dominated by the low frequencies, however the weaker correlations in the unfiltered case suggest the influence of the negative high frequency correlations (consistent with Sparrow

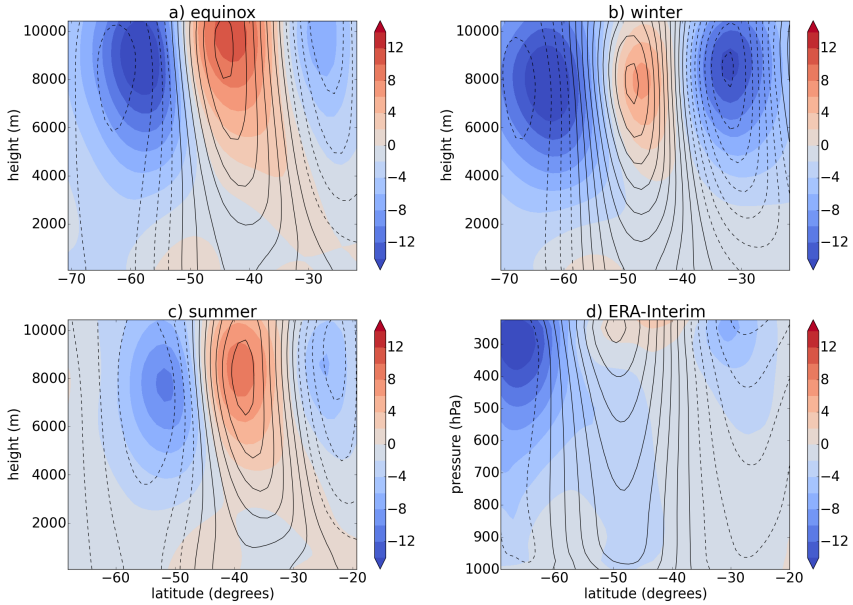

Figure 3.15: As in Fig. 3.14 but for the regressions on low-pass SAM2. - Note that the colourscale was adjusted to the values of EKE regression on this mode.

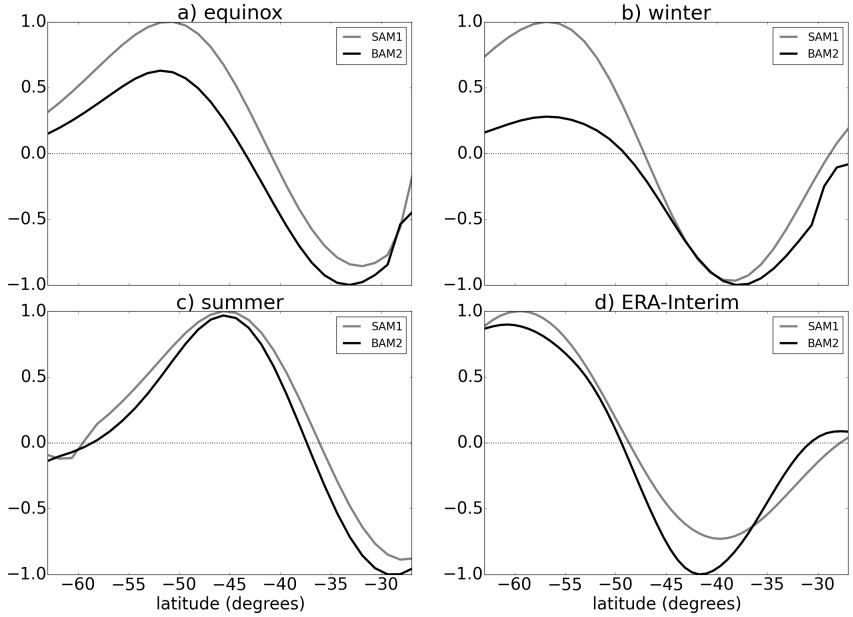

Figure 3.16: EOF structure of SAM1 and BAM2 modes. EOFs were normalised by the maximum value in their domain. - (a) for equinox, (b) for winter, (c) for summer model configurations, and (d) for ERA-Interim. All data were low-pass filtered. Note that the summer hemisphere data were plotted as SH for easier comparison with other configurations.

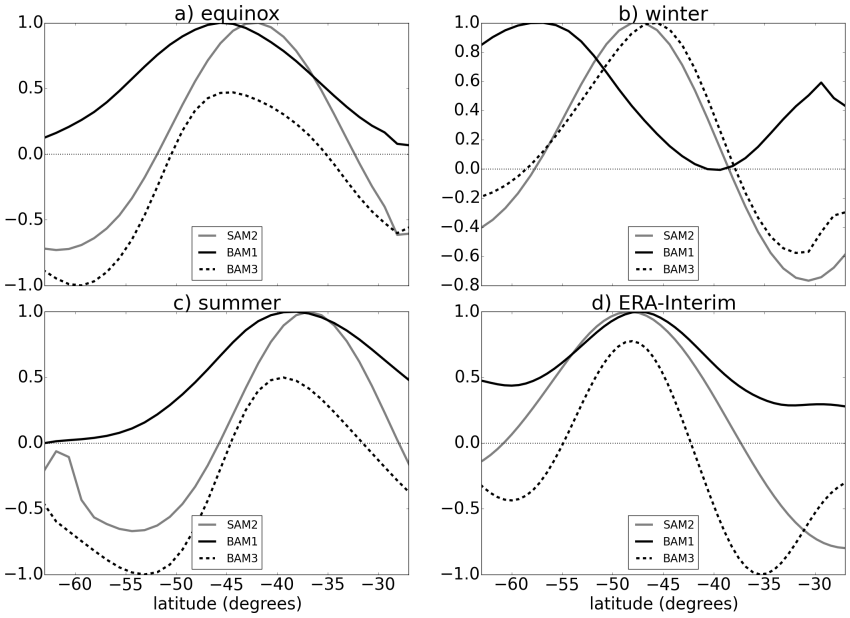

Figure 3.17: As in Fig. 3.16 but for the SAM2, BAM1 and BAM3 modes.

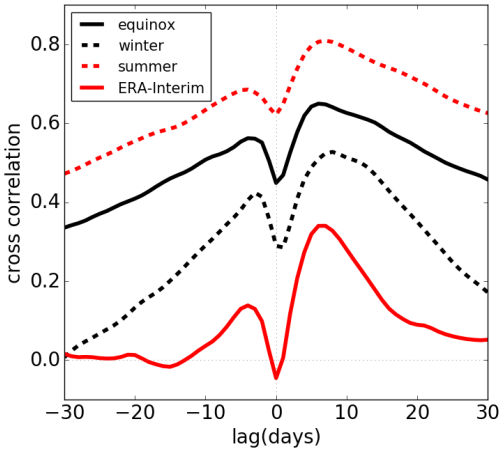

Figure 3.18: Lagged correlations between SAM1 and BAM2 (unfiltered). - For equinox (black solid line), winter (black dashed line) and summer (red dashed line) model configurations, and ERA-Interim (red solid line).

et al. 2009). Fig. 3.18 further demonstrates this through a much lower correlation at zero lags which increases at positive and negative lags (approximately ±5 days). Thus, the negative high-frequency correlations depress the correlations at short time lags. This behavior also explains the negative correlation between SAM1 and BAM2 for ERA-Interim at zero lag. Table

3.4 shows that the unfiltered correlations between SAM2 and BAM3 are dominated by low frequency behavior. In contrast, Table 3.3 shows that the unfiltered correlations between SAM2 and BAM1 for the equinox and summer model configurations are dominated by the high frequency behavior, whereas for the winter model configuration and ERA-Interim a combination of low and high frequency behaviour is reflected in the unfiltered correlations. Note also that SAM1 and SAM2 can exhibit significant correlations at non-zero lags, especially for the winter configuration where the separation of modes is smaller (Sheshadri and Plumb 2017; note that they used the same winter and summer model configurations as used here). Hence, the SAM1 and SAM2 modes could together represent propagating modes of variability and should not necessarily be considered separately (Sparrow et al., 2009; Sheshadri and Plumb, 2017). Examining the low-frequency spectral peaks is a way to determine whether there is co-variability of SAM1 and SAM2.

3.6 Conclusions

This Chapter has investigated the coupling between the baroclinic (BAM) and barotropic (SAM) modes of variability using power- and cross-spectrum analyses, regressions, and correlations in different Held-Suarez model configurations and in ERA-Interim SH reanalysis.

We have shown through the cross-spectrum analysis that there is a robust relationship across timescales between EKE and eddy heat fluxes (3.6), analogous to that between zonal mean zonal wind and eddy momentum flux convergence (3.4) (Lorenz and Hartmann, 2001). However, the former relationship is weaker as it fails for periods shorter than about 10 days, and the quasi-steady balance between EKE and heat flux is non-negligible at intermediate timescales (at least for periods longer than 20 days, consistent with the oscillator model of Thompson and Barnes 2014). This is a consequence of a robustly shorter damping timescale on EKE ($\tau_{EKE} \approx 3$ days) compared to the zonal mean zonal wind damping timescale ($\tau \approx 10$ days), and is reflected in the reduced curvature of the phase difference plot in Fig. 3.4a(ii) compared with Fig. 3.3b. The weaker relationship between EKE and heat flux is understandable due to the presence of additional terms in the EKE equation (3.2), moreover asymptotic theory [Chapter 2] shows that one needs to average over the synoptic temporal and spatial scales to obtain this relationship. A stronger relationship might be possible using wave activity instead of EKE; this is left for future work.

These cross-spectra relationships suggest a proximate link between zonal mean zonal wind and eddy momentum flux only (3.4), and between EKE and eddy heat flux only (3.6), recognising that the eddies are themselves baroclinic. The latter link is consistent with a decoupling of the baroclinic (BAM) from the barotropic (SAM) modes of variability (as in Thompson and Woodworth 2014), at least at periods longer than 10 days, as predicted by the asymptotic model for intermediate timescales (i.e. not for quasi-steady-state).

The frequency power spectra of eddy momentum and heat fluxes reveal that they generally exhibit a broad peak at higher frequencies ($<$ 30 day periods), as well as distinct peaks at lower frequencies ($>$ 50 day periods). The higher frequency eddy fluxes are related to the tendencies of EKE and of zonal mean zonal wind (i.e. $\partial z_u/\partial t \approx m$, $\partial[K_E]/\partial t \approx \alpha_{EKE}[v^*\theta^*]$), whereas the lower frequency peaks relate to the quantities themselves (EKE or zonal mean zonal wind; i.e. $z_u/\tau \approx m$, $[K_E]/\tau_{EKE} \approx \alpha_{EKE}[v^*\theta^*]$). This was indeed confirmed by the cross spectrum analysis as mentioned above.

There is a direct quasi-steady relationship between EMF and SAM, and between EHF and BAM, which applies mode by mode, as can be seen through direct matching of low-frequency peaks in the power spectra and is seen in all model configurations and in ERA-Interim. There are also cross-mode relationships at quasi-steady-state. There is a robust positive relation between SAM1 and BAM2 (shifted jet and storm track) and between SAM2 and BAM3 (strengthened jet and storm track), reflecting a positive baroclinic feedback (Robinson, 2000). The relationships between the SAM2 and BAM1 modes are less robust and depend on model climatology and variability. These relationships could be the subject of future investigations, but can be expected to be state-dependent. We find no evidence of a cross-mode relationship between SAM1 and BAM1, which was the correlation examined by Thompson and Woodworth (2014).

There are also cross-mode relationships in high pass data, which are more complex (reflecting transient wave-mean flow interaction and baroclinic life cycles) and tend to be of opposite sign to those at lower frequencies. Thus, combining low and high pass data leads to a confusing picture as it combines different kinds of behavior that can exhibit some cancellation between them (as shown by Sparrow et al. 2009).

In summary, this Chapter has shown that the nature and extent of the coupling between barotropic and baroclinic modes of extratropical atmospheric variability depends strongly on the timescale of variability. On synoptic timescales there is negative coupling through the baroclinic life cycle (Simmons and Hoskins, 1978); on quasi-steady timescales (periods longer than 50 days) there is positive coupling through the baroclinic feedback mechanism (Robinson, 2000); and on

intermediate timescales there is a decoupling, with purely baroclinic variability that can manifest itself in a baroclinic oscillator (Thompson and Barnes, 2014), consistent with weakly nonlinear models of baroclinic instability (Pedlosky, 1970). In the quasi-steady limit the pulsating modes of variability and their correlations depend sensitively on the model climatology. This could have implications for the modeled circulation response to climate change.

4

Baroclinic and Barotropic Mean Flows in Storm Tracks

4.1 Introduction

The previous Chapter focused on the zonally homogeneous EKE budget and its link to the barotropic momentum equation, however it has not discussed the baroclinic equation that was also derived in Chapter 2, nor has it discussed the planetary scale wave influence on the atmospheric flow. The multiscale asymptotic theory (Chapter 2) also includes the case of forced planetary scale waves (in addition to the zonal mean flow and the synoptic eddies) and suggests that the planetary scale heat fluxes are more important for the zonal mean flow dynamics than the synoptic scale heat fluxes. It also suggests that under our assumptions the synoptic and planetary scales interact only through the zonal mean flow or the source-sink terms (frictional and diabatic processes), and that the baroclinic and barotropic parts of the zonal flow are linked through the planetary scale dynamics (planetary scale heat fluxes appear in both equations). The theory also predicts the inefficiency of the synoptic scale heat fluxes for forcing of baroclinicity (meridional temperature gradient) at lower frequencies, which was also pointed out in Blanco-Fuentes and Zurita-Gotor (2011) and Zurita-Gotor (2017), based on zonally averaged Southern Hemisphere (SH) reanalysis data. Here we examine the relative importance of planetary and synoptic scale heat fluxes for the baroclinic and barotropic parts of the zonal flow, locally and in the zonal mean. This Chapter thus rounds out the analysis of the asymptotic theory (Chapter 2).

The outline of this Chapter is as follows. Section 4.1 provides further background theory on baroclinic and barotropic flows as well as teleconnections and Rossby wave trains that are related to barotropic flows, section 4.2 describes the methodology used in this Chapter, and the following sections of this Chapter address the theoretical predictions of Chapter 2 that were not analysed in Chapter 3. Firstly, section 4.3 discusses the impact of different localised diabatic processes for storm tracks to test the prediction of Chapter 2 that planetary and synoptic waves interact via the diabatic processes. Section 4.4 analyses the variability of the baroclinic zonal mean flow in different zonally homogeneous model configurations using cross-spectrum analysis to test the baroclinic budget (2.28c). Section 4.5 extends the cross-spectrum analysis of section 4.4 to zonally inhomogeneous flows with forced planetary waves to determine the relative importance of planetary and synoptic waves in driving the baroclinic and barotropic mean flows both locally and in a zonal mean (extending the analysis of the theory from Chapter 2 to include planetary waves), and also links the barotropic flows in storm track regions to teleconnection patterns and Rossby wave-trains using regression analysis. Section 4.5.3 addresses the barotropic time mean flow momentum flux forcing from planetary and synoptic waves as well as transient and stationary waves, rounding out the analysis of the barotropic flow on different temporal and spatial scales. Conclusions of this Chapter are given in section 4.6. Additional material on the model used in this Chapter, additional figures, and suggestions for future work on asymptotic methods are given in Appendices I-L.

4.1.1 Baroclinic and barotropic equations

Although, as noted above, the baroclinicity equation has been examined in the SH zonally averaged reanalysis data, it has not been examined for the Northern Hemisphere (NH) observations, or in model simulations. As the asymptotic theory predicts influences from both planetary and synoptic scale heat fluxes on baroclinicity locally (2.19), we examine the zonal mean and up- and down-stream parts of the storm tracks and the relative importance of the planetary and synoptic scale waves, as well as their interactions (see section 4.5). The asymptotic theory further suggests that under synoptic scale averaging the synoptic scale heat fluxes do not affect the mean baroclinic flow (2.20) at leading order, which is tested below (see sections 4.4, 4.5). Similarly the theory predicts that both synoptic and planetary scale momentum fluxes are important for the barotropic mean flow (2.18), both locally and in a zonal mean, and that synoptic

scale momentum fluxes do not vanish under synoptic scale averaging, which is also tested below (see sections 4.4, 4.5).

The vertically averaged equation for baroclinicity is (for zonal mean see, e.g., Zurita-Gotor 2017)

$$\frac{\partial \langle b \rangle}{\partial t} + \frac{\partial}{\partial y} \nabla \cdot (\langle \mathbf{u}^* \theta^* \rangle) = -\frac{\langle b \rangle}{\tau_b} \tag{4.1}$$

where $b = \partial\theta/\partial y$ is baroclinicity, θ is potential temperature, $\mathbf{u} = (u, v)$ is horizontal velocity vector, $\nabla\cdot$ is horizontal divergence, the other terms (e.g. diabatic processes and the mean meridional circulation) are represented as damping $-\langle b \rangle/\tau_b$ with τ_b a constant, asterisk (*) represents perturbation from zonal mean, and angle brackets ($\langle . \rangle$) represent vertical average. The heat flux term can be further split into contributions from the synoptic and planetary scale waves

$$\underbrace{\mathbf{u}^*\theta^*}_{\text{full}} = \underbrace{\mathbf{u}_s^*\theta_s^*}_{\text{synoptic}} + \underbrace{\mathbf{u}_p^*\theta_p^*}_{\text{planetary}} + \underbrace{\mathbf{u}_s^*\theta_p^* + \mathbf{u}_p^*\theta_s^*}_{\text{interaction terms}} \tag{4.2}$$

where subscript s denotes synoptic scale waves and subscript p denotes planetary scale waves. Equation (4.1) can then be averaged zonally and meridionally in a particular sector of a storm track or over the full zonal extent. Locally both zonal and meridional heat fluxes play an important role, whereas in a full zonal mean, only the meridional heat fluxes are important (i.e. the derivatives with respect to longitude vanish), and the interaction terms also vanish.

Similarly, the vertically averaged barotropic zonal momentum equation is (for zonal mean see, e.g., Lorenz and Hartmann 2001)

$$\frac{\partial \langle u \rangle}{\partial t} + \nabla \cdot (\langle \mathbf{u}^* u^* \rangle) = -\frac{\langle u \rangle}{\tau} \tag{4.3}$$

where u is zonal velocity, and the friction is represented as damping $-\langle u \rangle/\tau$ with τ a constant. The momentum flux term can be further split into contributions from the synoptic and planetary scale waves

$$\underbrace{\mathbf{u}^*u^*}_{\text{full}} = \underbrace{\mathbf{u}_s^*u_s^*}_{\text{synoptic}} + \underbrace{\mathbf{u}_p^*u_p^*}_{\text{planetary}} + \underbrace{\mathbf{u}_s^*u_p^* + \mathbf{u}_p^*u_s^*}_{\text{interaction terms}} \tag{4.4}$$

Equation (4.3) can then also be averaged zonally and meridionally in a particular sector of a storm track or over a full zonal extent. Locally both zonal and meridional momentum fluxes play an important role, whereas in the full zonal mean, only the meridional momentum fluxes are important, and the interactions terms vanish (as mentioned above for the baroclinic equation).

Note that the zonal momentum equation generally includes a longitudinal geopotential (or pressure) gradient which can affect the zonal flow locally (and vanishes under the zonal mean), but is here included in the damping term in (4.3).

In both equations (4.1, 4.3), the terms involving zonal-mean-zonal-perturbation interactions (e.g. $[u]v^*$ or $[u]\theta^*$) were omitted, and can be considered as part of the damping term. The cross-spectra results (sections 4.4, 4.5) demonstrate that in terms of variability (the imaginary part of the cross-spectra) these terms do not contribute much.

4.1.2 Teleconnection patterns in the NH observations

To better understand the barotropic flow (4.3, 4.4) in the storm track regions, links with teleconnection patterns are established.

Teleconnection patterns are planetary scale low-frequency patterns of variability that exist in preferred locations (e.g. where sea surface temperature fluctuations are large), and have remote impacts (James, 1994). Often they link the tropical or subtropical and midlatitude transients, and can thus be linked to Rossby wave-trains. However, these modes rarely exhibit the perfect 'sinusoidal' oscillatory behaviour, and are hence often described as 'irregular switching' between two different circulation states (James, 1994). These patterns are usually identified through empirical orthogonal function analysis (EOF; discussed in Chapter 3 and in Appendix G). They can be persistent and as they occur on longer timescales, they can also provide a source of subseasonal-to-interannual predictability.

The dominant modes of variability in the midlatitudes are the annular modes (discussed in Chapters 1,3), however these are often based on zonal mean indices. As the northern hemisphere has many asymmetries (e.g. continents, orography, land-sea contrasts etc.), more localised modes emerge (which can sometimes be linked to the hemispheric-scale annular modes, e.g. Ambaum et al. 2001). Such localised modes are then linked to the north-south shifts of the jet stream in different regions, and hence affect the storm-track-paths as well, which affects the regional weather.

The teleconnection patterns that are considered here are those that are strongly linked to the storm track regions in the northern hemisphere (e.g. Wallace and Gutzler 1981; Barnston and Livezey 1987): North Atlantic Oscillation (NAO), Pacific/North-American pattern (PNA), and the West and East Pacific Oscillations (WPO and EPO, respectively). Their structures are given in Fig. 4.1. The NAO, WPO and EPO show clear north-south dipolar patterns

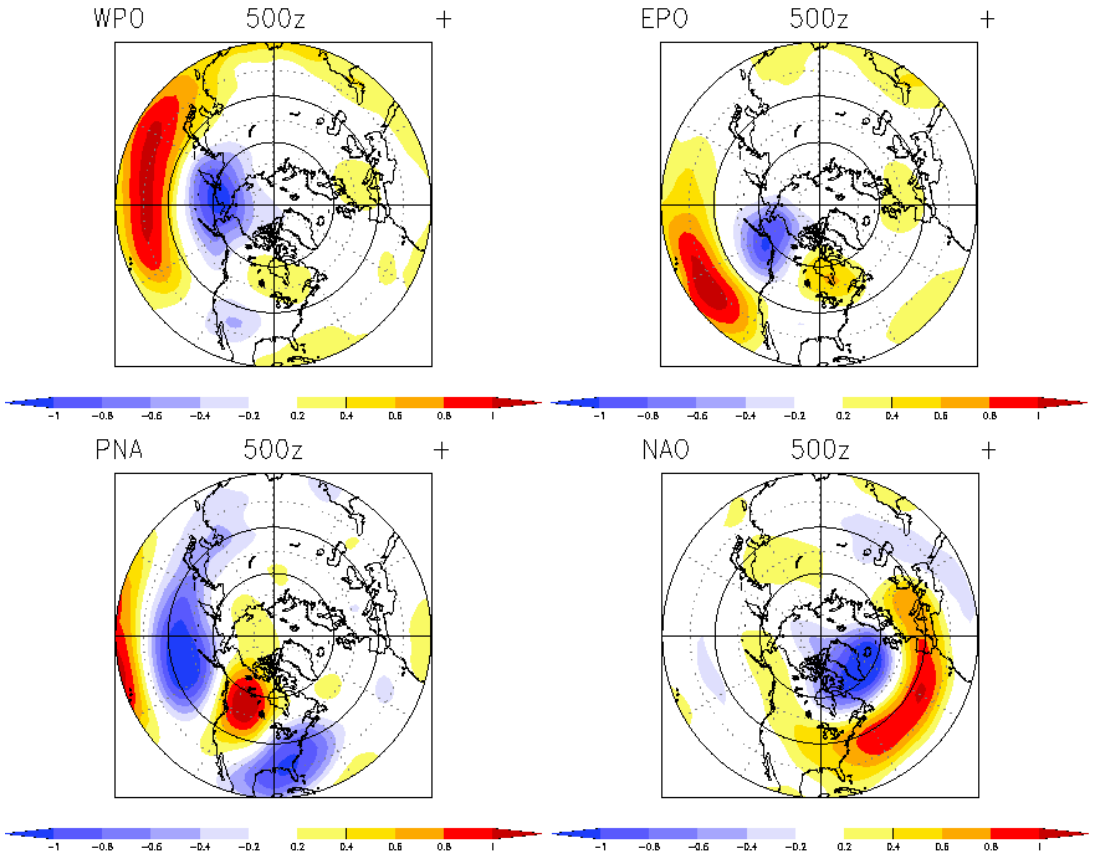

Figure 4.1: Northern Hemisphere teleconnection patterns (positive phases) based on geopotential height anomalies of the 500 hPa surface. - West Pacific Oscillation (WPO) [top left panel], East Pacific Oscillation (EPO) [top right panel], Pacific/North-American pattern (PNA) [bottom left panel], and North Atlantic Oscillation (NAO) [bottom right panel]. Images were provided by the NOAA/OAR/ESRL PSD, from their Web site: http://www.esrl.noaa.gov/psd/.

suggesting shifting of the jet stream north-south in their regions. The WPO is further linked to the Aleutian low (area of low pressure around the Aleutian islands in the Pacific), whereas the NAO is linked to the Icelandic low (area of low pressure around Iceland in the Atlantic) (Wallace and Gutzler, 1981). The PNA, on the other hand, resembles wave-trains emanating from the tropical Pacific that travel across North America into the North Atlantic, providing a link between the two regions. Note that the Pacific indices are linked to the El Nino Southern Oscillation and Pacific Decadal Oscillation (e.g. Rodionov et al. 2005; Drouard et al. 2015), and both the Atlantic and Pacific indices can also be linked to the Arctic oscillation (e.g. Ambaum et al. 2001) as mentioned above, however these links are not a subject of this study.

Another pattern that has been associated with the barotropic variability in the North At-

lantic is the East Atlantic (EA) pattern (e.g. Woollings et al. 2010). As the correlations in the Atlantic region with this pattern are substantially lower than the correlations with other indices (only 0.24 compared to at least 0.80 for other indices; see section 4.5.2), the EA is not considered further.

4.1.3 Wave-trains in the NH observations

Another way of visualising and better understanding the barotropic flow is through Rossby wave-trains, which link remote regions of the Earth (as mentioned above), providing further teleconnection links. The preferred paths of these wave trains have been identified in numerous studies, e.g. Wallace et al. (1988), Hoskins and Ambrizzi (1993), Ambrizzi et al. (1995), Chang and Yu (1999), and Chang (2005).

The most prominent paths for these wave-trains are the so-called waveguides (Hoskins and Ambrizzi, 1993), which are usually linked to the strong jet streams in the midlatitudes (North Atlantic, North African-South Asian, and Southern Hemisphere jet streams), which are able to trap waves and hence provide low-loss propagation pathways (shown in Fig. 4.2 with hatched arrows). Other teleconnection pathways (thick black arrows in Fig. 4.2) are related to other ray path refractions (e.g. Fig. 2 in Hoskins and Ambrizzi 1993) and depend on flow properties. Two paths that are important for further discussion in this chapter are: the North-Asian path that continues from the North Atlantic jet stream along the great circle into the Pacific, and the path across North America, which resembles the PNA pattern. Another path (not evident in Fig. 4.2) across central North America was also identified in other studies (e.g. Ambrizzi et al. 1995; Chang and Yu 1999). Other paths in Fig. 4.2 involve midlatitude-tropical connections and Southern Hemispheric pathways, which are not a subject of this study.

4.2 Methodology

4.2.1 Data

The numerical model used for this chapter is the aquaplanet model configuration of the Met Office Unified Model (version 8.6) with QOBS sea surface temperature profile (Neale and Hoskins, 2000) and different localised forcings (see Appendix I for more details). For the majority of this study the SH800 configuration with constant localised sensible heat flux forcing is used, as it produces strong planetary scale waves. This is not the case with the other configurations which

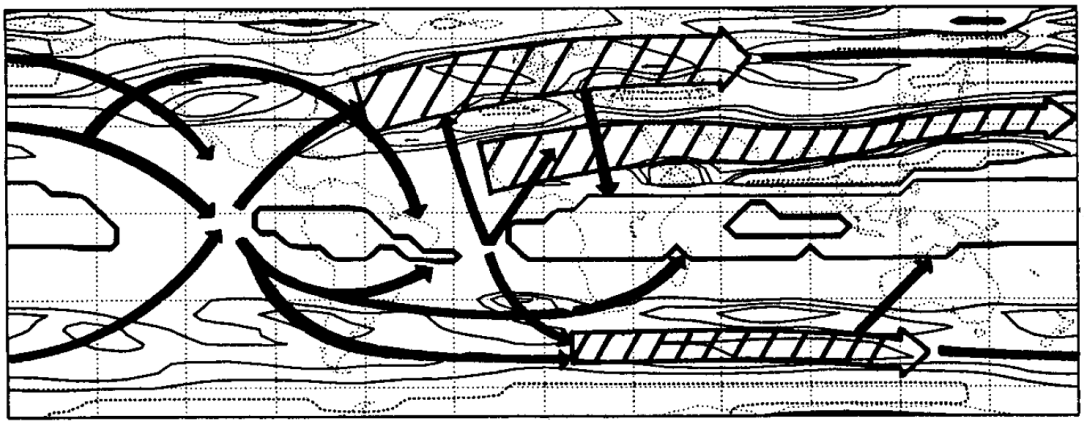

Figure 4.2: The waveguides (hatched arrows) and preferred teleconnection pathways (thick black arrows) in the boreal winter. - Source: Hoskins and Ambrizzi (1993), Fig. 13.

have the localised forcing dependent on latent heat flux and/or frictional velocity (20Moist, 2MoistHighVel, SH80HighVel). The vertically averaged eddy kinetic energy for different model configurations is shown in Fig. 4.3b-e, which shows the average storm track propagation (if planetary/stationary waves are strong it exhibits some tilt, see next section for details). The black dashed boxes denote the localised forcing region, whereas the black solid boxes denote upstream and downstream of the storm track (where applicable). All model configurations have an unperturbed Southern Hemisphere, which can be analysed as the control (zonally homogeneous) configuration.

The SH800 model configuration is run at climate model resolution (N96L85) and for 10800 days, of which the first 1440 days are taken as a spin-up period. The output is analysed at 6-hourly resolution on 15 vertical pressure levels (from 925 to 100 hPa). For further details see Appendix I.

The model output (NH of SH800 model configuration) is then compared to the Northern Hemisphere of the ERA-Interim observational reanalysis dataset from the European Centre for Medium-Range Weather Forecasts (Dee et al., 2011). The Southern Hemisphere (SH) of ERA-Interim, as well as the SH of the SH800 model configuration (as control simulation), are also used for the comparison in the zonal mean perspective. ERA-Interim data are analysed at 0.7^{o} resolution, on 27 pressure levels between 1000 and 100 hPa, and at 6-hourly resolution between 1 January 1981 and 31 December 2010 (10957 days). No specific season was chosen as the temporal anomalies are formed by removing the seasonal cycle (see next section for more details). The vertically averaged EKE for ERA-Interim is shown in Fig. 4.3a, which shows two localised

storm tracks in the NH (Pacific and Atlantic) denoted with black solid boxes (upstream and downstream of storm tracks), and a zonally homogeneous storm track in the SH (comparable to the model's SH in Fig. 4.3b-e).

Note that the upstream and downstream regions of the storm tracks (Fig. 4.3) are determined by the maxima in the time mean vertically averaged EKE (upstream of the EKE maximum for the upstream of the storm track and downstream of the EKE maximum for the downstream of the storm track). The upstream and downstream regions for different storm tracks are defined in Table 4.1, and are also shown with black solid boxes in Fig. 4.3a,b (as mentioned above).

Table 4.1: The upstream and downstream regions of localised storm tracks in ERA-Interim and SH800 model configuration.

	North Atlantic	North Pacific	SH800 NH
upstream	40°N-60°N, 280°E-320°E	35°N-55°N, 165°E-205°E	35°N-55°N, 85°E-125°E
downstream	40°N-60°N, 320°E-360°E	35°N-55°N, 205°E-245°E	35°N-55°N, 125°E-165°E

The timeseries are obtained by averaging within the box over the upstream and downstream of the storm tracks as defined above, averaging over the full storm track (average over both the upstream and the downstream of the storm track), and also by taking a zonal mean between two latitudes as defined in Table 4.2.

Table 4.2: The latitudinal extents for zonal mean storm tracks in ERA-Interim and SH800 model configuration.

	ERA-Interim NH	ERA-Interim SH	SH800 NH	SH800 SH
latitudinal extent	40°N-60°N	35°S-55°S	35°N-55°N	30°S-50°S

Correlations with teleconnection patterns are computed as well, since the regression analysis reveals similar patterns (section 4.5.2). The daily teleconnection data for WPO, EPO, PNA and NAO are provided by the NOAA/OAR/ESRL PSD, from their Web site (http://www.esrl.noaa.gov/psd/), which is based on the NCAR/NCEP reanalysis data (Kalnay et al., 1996). Since the data for the teleconnection patterns are produced by a different reanalysis dataset, smaller correlations could be expected between the fields obtained from ERA-Interim and teleconnection indices from NCEP reanalysis. The indices are identified as in Wallace and

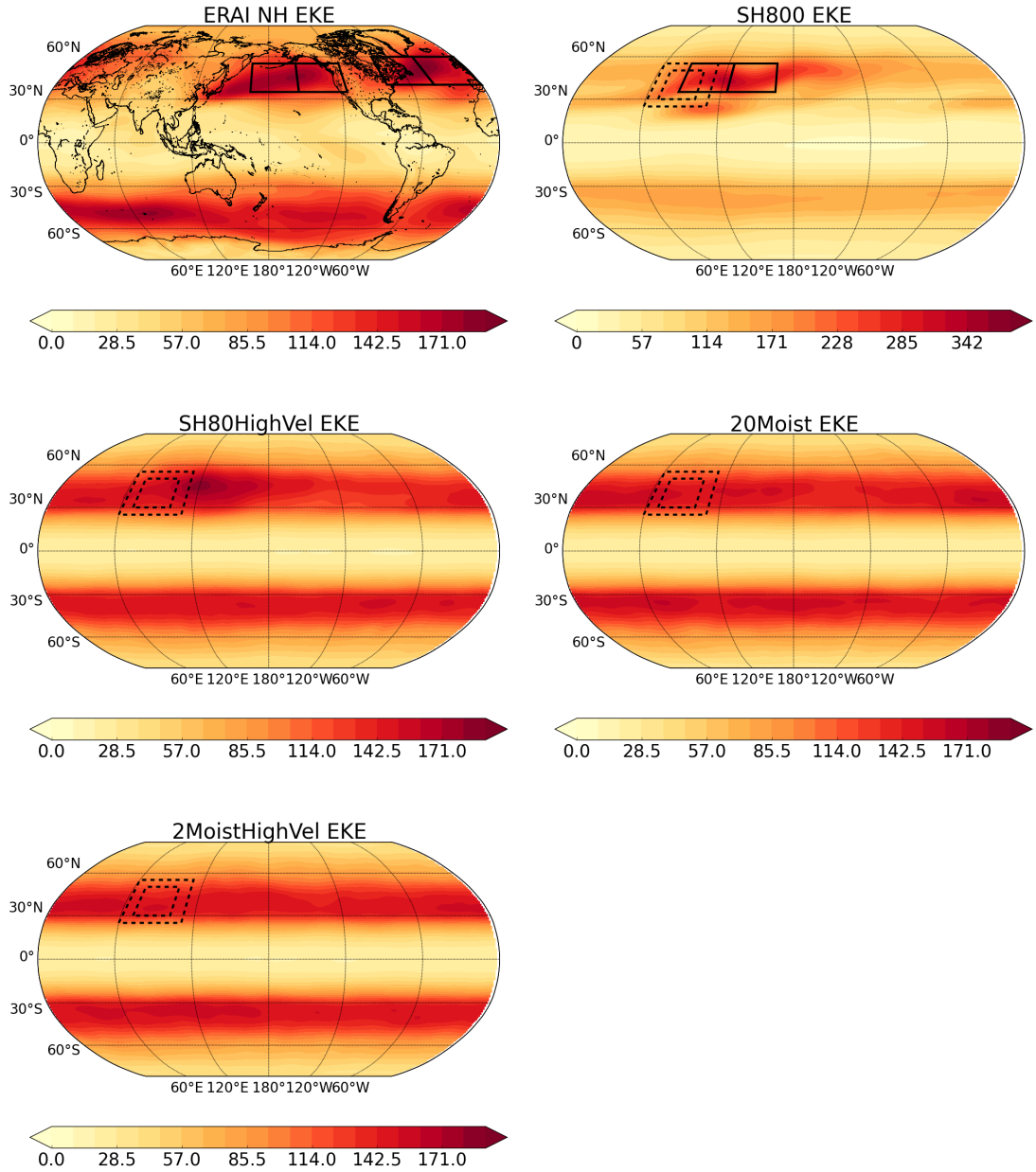

Figure 4.3: Time-vertical mean eddy kinetic energy for ERA-Interim and different model configurations (as labeled; see Appendix I for details). - Units are $m^2\ s^{-2}$. Dashed thick black lines denote the area of forcing (with outer box denoting tapering off of the forcing), thick solid black lines denote the up- and down-stream of storm tracks (see text for more details). Note that the colour-bar of the SH800 model configuration is different due to strong forcing and consequently stronger EKE in this configuration.

Gutzler (1981) and Barnston and Livezey (1987), and are calculated from 500 hPa geopotential height (Φ) as:

$$\text{WPO} = \Phi(\text{25-40N, 140E-150W}) - \Phi(\text{50-70N, 140E-150W}) \tag{4.5}$$

$$\text{EPO} = \Phi(\text{20-35N, 160W-125W}) - \Phi(\text{55-65N, 160W-125W}) \tag{4.6}$$

$$\begin{aligned}\text{PNA} = {} & \Phi(\text{15-25N, 180-140W}) - \Phi(\text{40-50N, 180-140W}) \\ & + \Phi(\text{45-60N, 125W-105W}) - \Phi(\text{25-35N, 90W-70W})\end{aligned} \tag{4.7}$$

$$\text{NAO} = \Phi(\text{35-45N, 70W-10W}) - \Phi(\text{55-70N, 70W-10W}). \tag{4.8}$$

Fig. 4.1 shows the centres of action with similar extents as seen in the above equations (4.5-4.8).

4.2.2 Spectral analysis and time filtering

The relationships (4.1, 4.3) are tested using cross-spectrum analysis (Lorenz and Hartmann, 2001; Zurita-Gotor, 2017) as was previously done for the EKE and zonal mean zonal wind (Chapter 3). The Fourier transform of (4.3) is given in (3.5). A similar equation can be obtained for the Fourier transform of (4.1):

$$\frac{B^c H}{B^c B} = i\omega + \frac{1}{\tau_b} \tag{4.9}$$

where B is the the Fourier transform of baroclinicity, H is the Fourier transform of the gradient of divergence of the heat flux (and can be further split into contributions from planetary and synoptic waves), ω is angular frequency and the superscript c denotes complex conjugate. If this relationship holds, the imaginary part of the cross-spectrum ($B^c H / B^c B$) is proportional to ω and the real part is constant. Note that in this Chapter, EOF analysis is not performed on the data, hence the timeseries are computed by regional horizontal averaging in storm track regions or in the zonal mean.

To calculate the cross-spectra, the timeseries are first split into sections (length varies between 256 and 512 days), overlapped by a half-length (between 128 and 256 days), which provides more degrees of freedom (Lorenz and Hartmann, 2001). The same procedure was used in Chapter 3.

The spectral analysis is performed on the full momentum flux divergence and on the gradient of divergence of the full heat flux, as well as on the planetary and synoptic contributions to them. To compute the planetary and synoptic wave contributions to the heat and momentum fluxes (4.2, 4.4), each component (e.g. u, v or θ) is first split according to zonal wavenumber k, and

then multiplied to find the fluxes (e.g. $\mathbf{u}_s^* u_s^*$). The planetary waves are the waves with $1 \leq k \leq 3$, whereas the synoptic waves have $k \geq 4$ (note that waves smaller than synoptic are not well-resolved at the model/reanalysis resolution used in this study). The interaction terms in (4.2, 4.4), representing the interactions between synoptic and planetary waves, are computed as the residual between the full momentum (or heat) flux and the sum of the synoptic and planetary components. Afterwards a seasonal cycle is removed from these fluxes for ERA-Interim data, and the time mean is removed for the model data, before computing the cross-spectra. However, a different order of operations is used for time filtering (see below). Note that for the time mean fields, the seasonal cycle is not removed (unless time-filtering is involved as below).

Further understanding of the synoptic and planetary waves can be gained by filtering the eddies also in time (using the Lanczos filter, Duchon 1979). Here, the filtering is again performed on each component separately, i.e. first filter u, v and θ before multiplying them to find the fluxes. The cut-off period between high and low frequency waves is 10 days (which is a typical timescale of baroclinic life cycles; e.g. Hoskins et al. 1983). Note that before filtering the data in time, the seasonal cycle was removed (daily climatology is removed from each 6-hourly data slice), hence no specific season is analysed and the seasonal cycle can partly be filtered out. Any of the fluxes can be split into contributions from different waves using the temporal filter as

$$\mathbf{u}^*\theta^* = \underbrace{\mathbf{u}^*_{seas}\theta^*_{seas}}_{\text{quasi-stationary}} + \underbrace{\underbrace{\mathbf{u}_h'^*\theta_h'^*}_{\text{high}} + \underbrace{\mathbf{u}_l'^*\theta_l'^*}_{\text{low}} + \underbrace{\mathbf{u}_h'^*\theta_l'^* + \mathbf{u}_l'^*\theta_h'^*}_{\text{high-low interaction}}}_{\text{transient}} + \underbrace{\mathbf{u}_{l,h}'^*\theta^*_{seas} + \mathbf{u}^*_{seas}\theta_{l,h}'^*}_{\text{stationary-transient interaction}} \tag{4.10}$$

$$\mathbf{u}^*u^* = \underbrace{\mathbf{u}^*_{seas}u^*_{seas}}_{\text{quasi-stationary}} + \underbrace{\underbrace{\mathbf{u}_h'^*u_h'^*}_{\text{high}} + \underbrace{\mathbf{u}_l'^*u_l'^*}_{\text{low}} + \underbrace{\mathbf{u}_h'^*u_l'^* + \mathbf{u}_l'^*u_h'^*}_{\text{high-low interaction}}}_{\text{transient}} + \underbrace{\mathbf{u}_{l,h}'^*u^*_{seas} + \mathbf{u}^*_{seas}u_{l,h}'^*}_{\text{stationary-transient interaction}} \tag{4.11}$$

where the asterisk denotes perturbation from the zonal mean, prime denotes perturbation from the seasonal cycle (transients) which can be further split into low (subscript l) and high (subscript h) frequency components, and subscript *seas* denotes the contributions from the slowly evolving seasonal cycle. The fluxes in (4.10, 4.11) can be further split into contributions from planetary, synoptic and interaction terms as in (4.2, 4.4). Note that under time averaging the stationary-transient interaction terms on the right-hand-side of (4.10, 4.11) vanish. In the model, where a seasonal cycle is not present, the time mean is removed before filtering instead of the seasonal cycle.

Note that the heat and momentum fluxes are first filtered at 6-hourly resolution and then multiplied and afterwards daily averaged, where applicable. This retains the diurnal cycle.

Lastly, the fields are averaged vertically within the troposphere (for ERA-Interim this is between 1000 hPa and 100 hPa; for the aquaplanet model between 925 hPa and 100 hPa) in the same way as in Chapter 3.

4.3 Diabatic forcing of planetary waves in the aquaplanet model

The different aquaplanet model configurations described in Appendix I and the previous section provide a framework for studying the effect of localised diabatic processes on the atmospheric flow. If the localised forcing is strong enough, it can generate forced planetary scale waves that tilt the storm tracks and localise their position (as in ERA-Interim, Fig. 4.3a).

The asymptotic theory predicts that the interaction between the planetary and synoptic waves is primarily through the source-sink terms and through the zonal mean flow. To test the first part of this hypothesis, model simulations with localised forcing dependent on frictional velocity and with constant forcing are performed (see Appendix I for details). If the hypothesis holds, the velocity-dependent localised forcing (linked to eddies) would lead to stationary waves and a tilted storm track that can immediately be seen in the EKE field. Fig. 4.3b-e shows vertically averaged EKE for different model configurations. While all configurations show some localisation and tilting in the EKE field, there are large differences between the different configurations.

The SH800 model configuration with strong constant localised sensible heat flux forcing clearly shows an enhanced localised storm track with a clear planetary/stationary wave structure (Fig. 4.3b), consistent with previous work done with similar forcing (e.g. Kaspi and Schneider 2011, 2013). When the localised sensible heat flux depends on the frictional velocity (forcing by eddies) with maximum value similar to the SH800 model configuration (SH80HighVel in Fig. 4.3c), it still produces a tilted storm track implying the eddies are forcing the stationary wave, but it is much weaker than in the constant forcing case.

When the forcing depends on the latent heat flux that is calculated through the parametrisation schemes, the stationary wave forcing becomes very weak. The 20Moist model configuration multiplies the latent heat flux locally by a constant, which leads to a weak tilting and localisation (Fig. 4.3d), but it is a lot weaker than the above-described cases. When the localised forcing

depends on both latent heat flux (produced by the model) and frictional velocity (2MoistHighVel, Fig. 4.3e), the tilting and localisation vanish, i.e. are not distinguishable from the control simulation (in the SH of the same model configuration). Some tilting was present in the lower troposphere (not shown), however upon vertically averaging data it vanished.

Note that the configurations with the locally increased latent heat flux show that when storms enter regions of enhanced moisture availability (such as when a cyclone travels from land to sea) it can produce planetary waves, though weaker than those forced by constant forcings.

While many of these configurations show tilting of the storm tracks and could support the asymptotic theory, it is worth mentioning that the forcings used are the strongest possible (or stronger than realistic sensible and latent heat fluxes in the atmosphere would be) for each configuration, which means that under more realistic forcing this tilting of storm tracks might vanish. This means that while there could be excitation of planetary waves through synoptic diabatic forcing, it is likely to be weak. Additionally, when performing the local cross-spectrum analysis in these model configurations we find strong influences from the planetary scale waves only in the SH800 model configuration, hence other configurations are omitted for further analysis in this chapter (they do not differ from the control configuration in the zonal mean or locally).

4.4 Baroclinic flow in zonal mean storm tracks with weak planetary waves

In the zonal mean framework of the baroclinic equation (4.1), only the meridional heat fluxes play an important role for baroclinicity. Fig. 4.4 shows the cross spectrum analysis between the full meridional heat flux and baroclinicity following (4.1, 4.9) for different set-ups with weak planetary waves (equinox, summer and winter Held-Suarez model configurations, SH of SH800 (control) aquaplanet model configuration and ERA-Interim SH), which all show a suppression of the role of heat fluxes for forcing baroclinicity at lower frequencies (periods longer than 25 days) in the real part of the cross spectrum. This is consistent with Zurita-Gotor (2017), and shows that the result is robust to different model configurations. Zurita-Gotor (2017) has further shown that this suppression is a result of the cancellation between the synoptic and planetary heat fluxes, with damping of the baroclinicity due to the synoptic heat fluxes and forcing due to the planetary heat fluxes, which is further confirmed in the following sections.

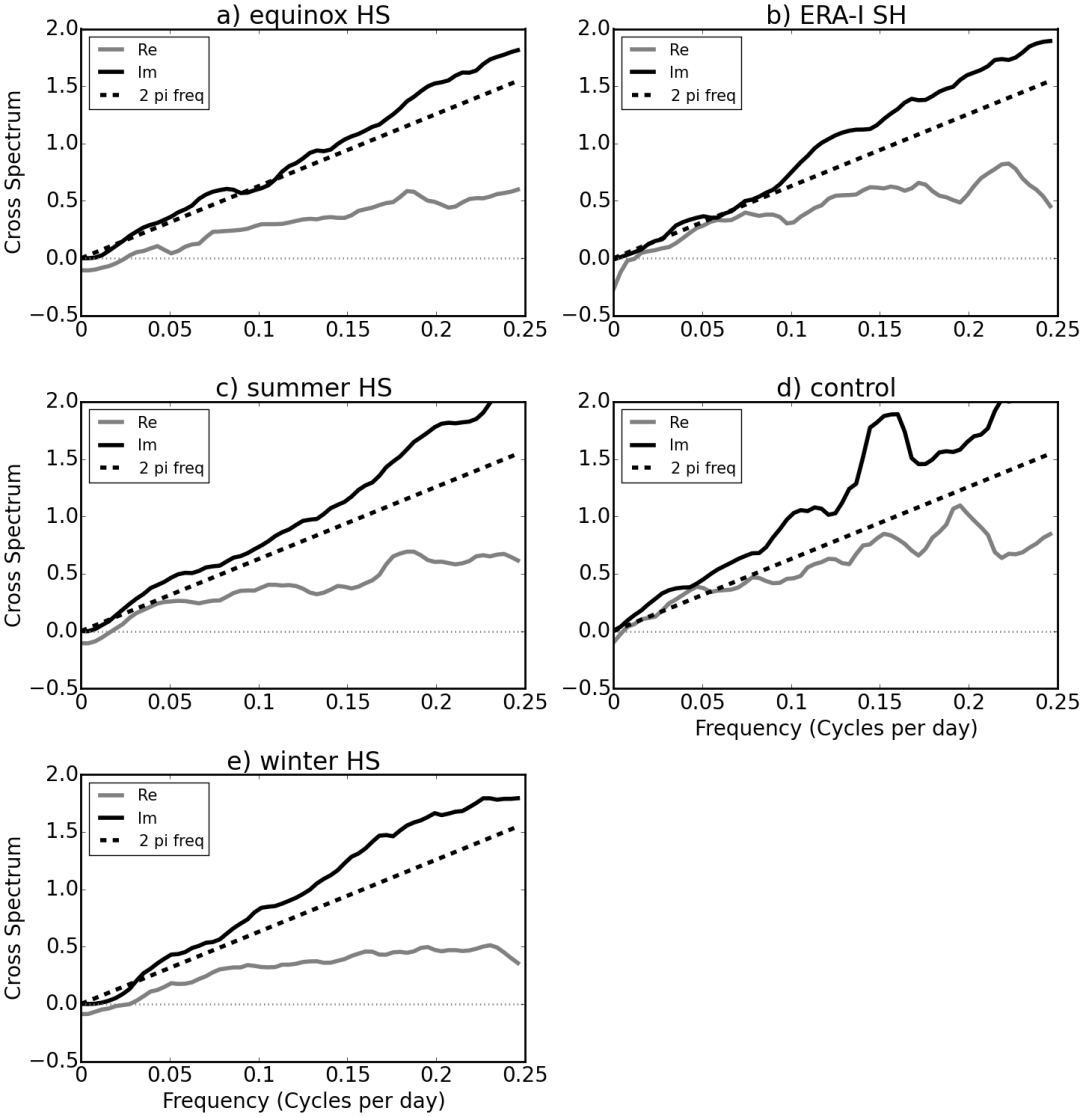

Figure 4.4: Cross spectrum analysis of the zonal mean baroclinic equation (4.1) for the cases of weak planetary waves. - a) equinox, c) summer and e) winter Held-Suarez model configurations, b) ERA-Interim SH and d) SH of SH800 (control) aquaplanet model configuration. Note that the peaks are not robust to different sampling (not significant).

In Fig. 4.4 the heat flux suppression is dominated by synoptic heat fluxes, hence a negative (damping) contribution can be seen at lower frequencies. Zurita-Gotor (2017) further argued that the driving of the baroclinicity at lower frequencies is mainly due to diabatic processes and the mean meridional circulation. This is consistent with the asymptotic theory, where the baroclinic equation was averaged over synoptic meridional and temporal scales, leading to a

lack of synoptic scale heat fluxes at lower frequencies (2.28c). Note that the suppression of heat fluxes at lower frequencies only means that the linear damping in the simple relationship (4.1,4.9) breaks down (is not constant at lower frequencies). The latter also means that the quasi-steady limit of the simple relationship (4.1) cannot be determined (i.e. more terms in the baroclinicity equation which were subsumed into the damping term must play a role, such as diabatic forcing and the mean meridional circulation as mentioned above). Hence, the lower frequency regime in this Chapter is analogous to the intermediate frequency regime of Chapter 3.

The imaginary part of the cross-spectrum for the full heat flux reasonably closely follows the angular frequency line, suggesting that the variability at higher frequencies is indeed driven by the heat fluxes. The following sections take advantage of this relationship to examine the relative contributions of planetary and synoptic waves to the full fluxes for different longitudinal averages (similarly for barotropic flows).

Note that the barotropic flow in a zonal mean storm track with weak planetary waves was discussed in Lorenz and Hartmann (2001) and in Chapter 3 and is hence not repeated here. The barotropic zonal mean zonal wind is closely related to eddy momentum fluxes at all timescales, as equation (4.3) suggests.

4.5 Baroclinic and barotropic flows in storm tracks with strong planetary waves

When the planetary scale waves are strong (as in the NH of the SH800 model configuration or in the NH of ERA-Interim), further insight into the variability can be gained by splitting the momentum fluxes into synoptic- and planetary-wave contributions. Therefore, this section focuses on the importance of planetary and synoptic waves for the baroclinic and barotropic mean flows in storm tracks under different longitudinal averages (zonal mean and within storm track regions). First, the storm track in the NH of the SH800 aquaplanet model configuration is analysed using cross-spectrum analysis, followed by comparison to the North Atlantic and North Pacific storm tracks in the ERA-Interim data. The ERA-Interim data are also analysed using a regression analysis which links the storm track regions to teleconnection patterns and Rossby wave-trains.

4.5.1 Cross-spectrum analysis

Model storm track (SH800)

Baroclinic flow

Zonal mean and average over a full storm track

As shown in the previous section, there is a low frequency suppression of the heat flux contribution to the zonal mean baroclinic flow (Zurita-Gotor, 2017). Thus, Fig. 4.5a,b shows the imaginary and real parts, respectively, of the cross spectrum for the SH800 aquaplanet model configuration. The heat flux was split into contributions from the planetary, synoptic and interaction terms (4.1). The real part of the cross spectrum clearly demonstrates the low frequency suppression of the full heat flux (Fig. 4.5b), with planetary and synoptic scale heat flux cancellation, where planetary scale heat fluxes force the baroclinicity and synoptic scale heat fluxes damp it, consistent with Zurita-Gotor (2017). This is also consistent with the asymptotic theory which suggests forcing of the baroclinicity at lower frequencies by planetary scale waves and other diabatic processes [see (2.20)], but does not capture the damping by the synoptic scale heat fluxes.

However, the imaginary part of the cross spectrum (Fig. 4.5a) shows that the eddy heat fluxes are responsible for the variability in the zonal mean baroclinicity, and are dominated by the synoptic scale heat fluxes at all frequencies. The relative importance of planetary scale waves is minimal in this zonal mean framework in the SH800 aquaplanet model configuration.

The average over the storm track (Fig. 4.5c,d) shows a similar picture to the zonal mean, except for the interaction term becoming more important than the planetary scale heat fluxes themselves, while the synoptic scale heat fluxes still dominate the baroclinic variability. There is also a weaker relationship between the baroclinicity and heat fluxes at lower frequencies (imaginary part of cross-spectra, Fig. 4.5c), which is especially pronounced when only the transient waves from (4.10) are considered (Fig. J.1b).

When only transient waves from (4.10) are considered, it can further be shown that the baroclinic variability in the SH800 model configuration is dominated by the transient waves, as Figs. 4.5 and J.1 closely resemble each other. This means that stationary-transient interactions from (4.10) are not important for the baroclinic variability in the model. A further split into the high and low frequency transient components (not shown) shows that the high-frequency variability is dominated by high frequency waves and the interactions between the high and

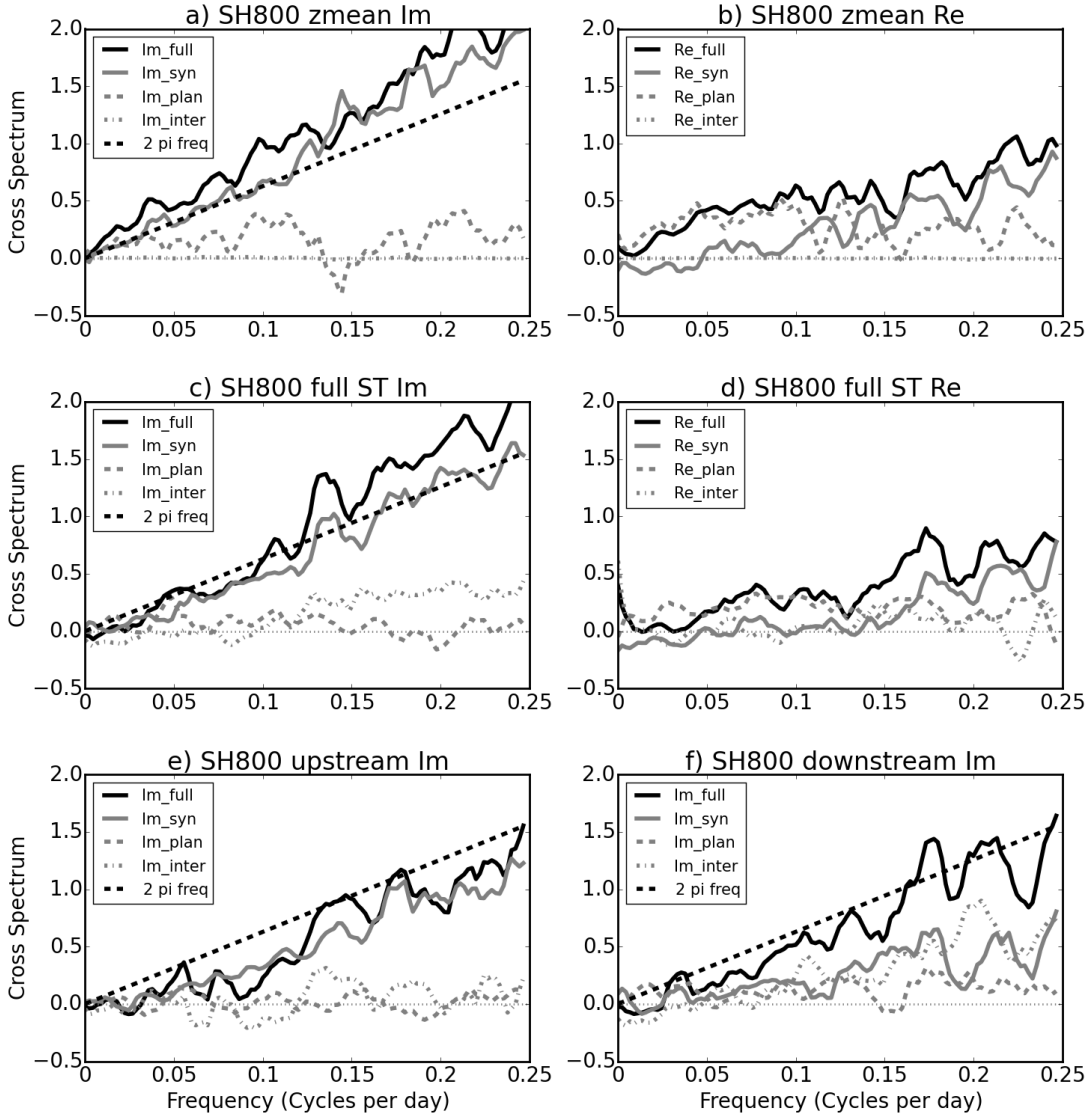

Figure 4.5: Cross spectrum analysis of baroclinic equation (4.1) in the SH800 aquaplanet model configuration. - a) imaginary, and b) real parts for the cross spectrum for the zonal mean case, c) imaginary, and d) real parts for the cross spectrum for the average over the full storm track, and imaginary part of the cross spectrum for e) upstream and f) downstream of the storm track. Different lines in panels denote contributions from full (solid black line), synoptic (solid grey line), planetary (dashed grey line) and interaction (grey dash-dotted line) heat fluxes (4.2), as well as the angular frequency line (black dashed line) where applicable.

low frequency waves, consistent with frequency triads (through Fourier analysis). Similarly, it can be shown that the low-frequency behaviour is linked to low (planetary) and high (synoptic) frequency waves, with the damping by the synoptic scale heat fluxes at lower frequencies in

the real part of the cross-spectra (e.g. Fig. 4.5b,d) dominated by the contribution from high frequency synoptic waves (not shown).

Up- and down-stream of storm track

While in the zonal mean and when averaged over the storm track the synoptic waves dominate the variability in baroclinicity, it is not necessarily the case upstream or downstream of storm tracks. Fig. 4.5e,f shows the imaginary part of the cross spectrum for upstream and downstream of the storm track, respectively. While upstream of the storm track is still dominated by the synoptic scale heat fluxes with weak influence from the planetary waves and the interaction term, downstream of the storm track is influenced by both planetary and synoptic eddies as well as their interaction, i.e. synoptic scale heat fluxes alone are not enough to explain the covariability of the baroclinicity and the heat fluxes. This suggests a contribution from both planetary and synoptic eddies (and their interactions) in the high frequency limit, implying that the synoptic eddies alone may not be sufficient to describe the high frequency variability. This is even more pronounced in the ERA-Interim data (section 4.5.1). Note that in a time mean, the synoptic fluxes are dominated by the high frequency components as is often implied in the literature (see section 4.5.3).

Note that the real part of the cross spectrum is not shown here (for brevity) as it shows similar behaviour as in the zonal mean case.

The dominance of the synoptic scale heat fluxes in the upstream region could be potentially linked to the oscillator model of Ambaum and Novak (2014), but this is less clear in the ERA-Interim data (section 4.5.1). Note that Ambaum and Novak (2014) used the term 'transient eddies', which could be combining contributions from waves with different wavenumbers (planetary and synoptic) as noted above. The increased importance of planetary scale heat fluxes (and their interaction with synoptic eddies) downstream is consistent with Kaspi and Schneider (2011, 2013), who found important contributions of stationary wave sensible and latent heat fluxes for the downstream forcing and damping of baroclinicity in a time mean framework.

As in the zonal mean and the average over the storm track, the transient waves from (4.10) dominate the covariability of baroclinicity and heat fluxes also upstream and downstream of the model storm track (Fig. J.1c,d), i.e. stationary-transient interactions are negligible. This is not necessarily inconsistent with Kaspi and Schneider (2013) as they analysed the time mean framework where stationary planetary scale waves are very important locally, whereas here the

transient regime is considered and as mentioned before the (transient) planetary waves are still important for the baroclinic variability.

The asymptotic theory for the baroclinic mean flow (discussed in Chapter 2) is only valid at lower frequencies (average over synoptic time and spatial scales), hence at higher frequencies (eliminated in the synoptic scale average) we expect both planetary and synoptic scale heat fluxes to affect baroclinicity, especially locally as seen above. Note that the meridional spatial average (over a 20-degree latitudinal band) did not reduce the influence of the synoptic scale heat fluxes (especially at higher frequencies), suggesting the asymptotic theory does not hold well in this case. A theory allowing similar synoptic and planetary meridional scales is most likely necessary to address this case [see Appendix L and Dolaptchiev (2008) for further suggestions].

Barotropic flow

Zonal mean and average over a full storm track

The barotropic budget (4.3) is now analysed in a similar way as the baroclinic budget in the previous section for the SH800 aquaplanet model configuration. Fig. 4.6a,b shows the imaginary and real parts of the cross spectra, respectively, for the zonal mean momentum flux divergence [split into contributions from planetary and synoptic waves, as in (4.4)] and zonal mean zonal wind. While the real part of the cross spectrum remains constant at all frequencies and the contributions of different waves are similar, the imaginary part is more interesting as it shows that the synoptic scale momentum fluxes dominate the variability in zonal mean zonal wind, however the contribution from the planetary scale waves is also large at all frequencies. This is consistent with the barotropic budget of the asymptotic theory (2.18), which predicts the influence of both planetary and synoptic scale momentum fluxes onto the zonal mean flow.

The imaginary part of the cross spectrum for the average over the storm track (Fig. 4.6c) shows that the influence of synoptic waves on the zonal flow is reduced locally at the expense of the interaction between the synoptic and planetary waves (the planetary scale momentum fluxes retain a similar influence), in contrast to the zonal mean case. The real part of the cross spectrum (Fig. 4.6d) becomes noisier, but remains consistent with the zonal mean picture and is hence not shown for the up- and down-stream cases.

A further insight into the barotropic variability can be gained through the analysis of the transient waves from (4.11) as was previously done for the baroclinic budget. Fig. J.2a shows that the zonal mean barotropic budget is well-explained by the transient waves alone, i.e. it

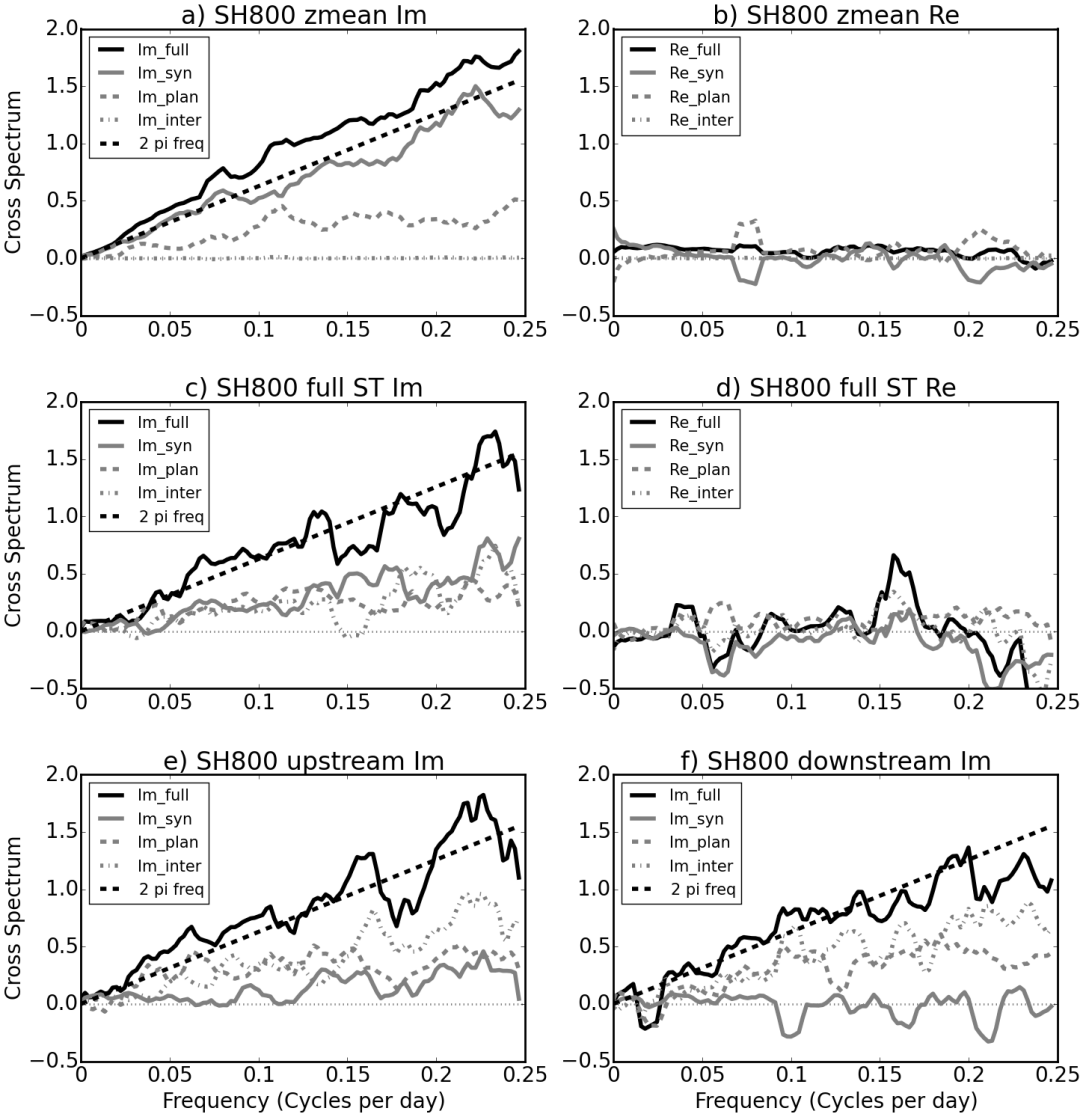

Figure 4.6: As in Fig. 4.5, but for the barotropic equation (4.3, 4.4).

closely resembles Fig. 4.6a. However, Fig. J.2b shows that locally (averaged over the storm track) the stationary-transient interactions are important (unlike in the baroclinic budget), especially for the planetary waves and the interaction term (the cross spectra of the synoptic momentum fluxes and zonal wind are dominated by the transient eddies as the solid gray lines in Figs. 4.6c and J.2b closely resemble each other).

The importance of the stationary-transient interactions for the planetary waves could be understood as fluctuations of the same wave, i.e. the stationary component of the planetary

wave and its temporal fluctuations could project onto planetary stationary-transient interactions as shown in Fig. 4.7. The importance of the stationary-transient interaction for the planetary-synoptic wave interaction could be understood as the stationary planetary wave 'steering' the transient synoptic eddies as shown in Fig. 4.8, which is often the case in the storm track regions (tilted storm tracks) or for Rossby wave trains (section 4.5.2). In both cases an interaction between a stationary and transient (independently propagating) wave is possible as well; other interpretations are also not excluded.

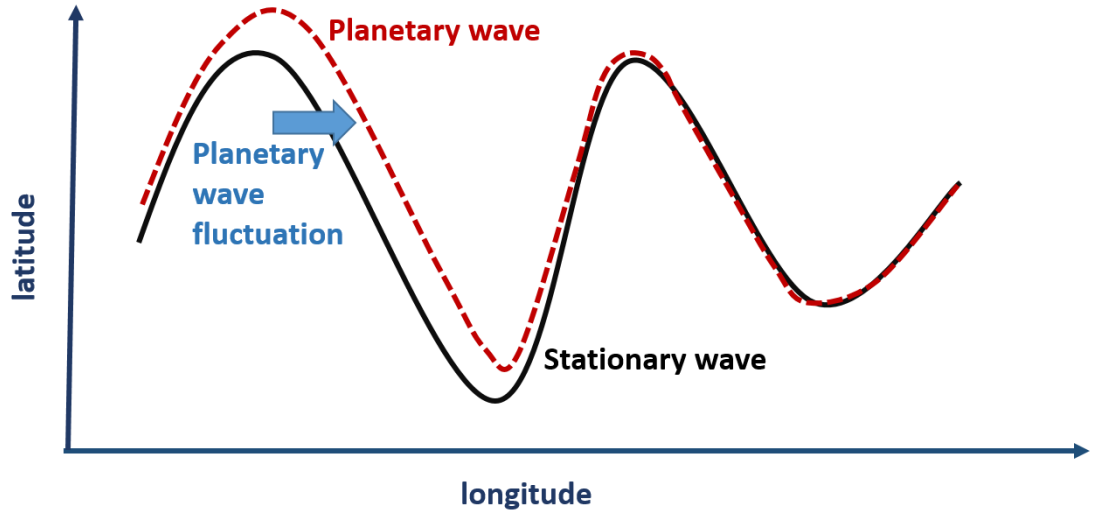

Figure 4.7: An example of a schematic showing a stationary-transient planetary wave interaction. - The stationary and transient planetary waves may be the same physical feature with the transient planetary wave representing fluctuations from the climatological state (e.g. changes in the tilt of the wave), which results in increased momentum flux divergence. The black solid line represents the stationary wave, the red dashed line is the transient planetary wave, and the blue arrow represents the transient fluctuations of the planetary wave.

Up- and down-stream of storm track

Splitting the storm track into upstream and downstream contributions can further elucidate the variability of the storm tracks. Fig. 4.6e,f thus shows the imaginary part of the cross spectrum between the momentum flux divergence (and the relative contributions from planetary and synoptic waves) and the zonal flow for the upstream and downstream of the storm track, respectively, for the SH800 aquaplanet model configuration. This analysis shows that the synoptic scale momentum fluxes alone, both up- and down-stream of the storm track, have only a small influence on the zonal flow, however their contribution is still present through the interaction

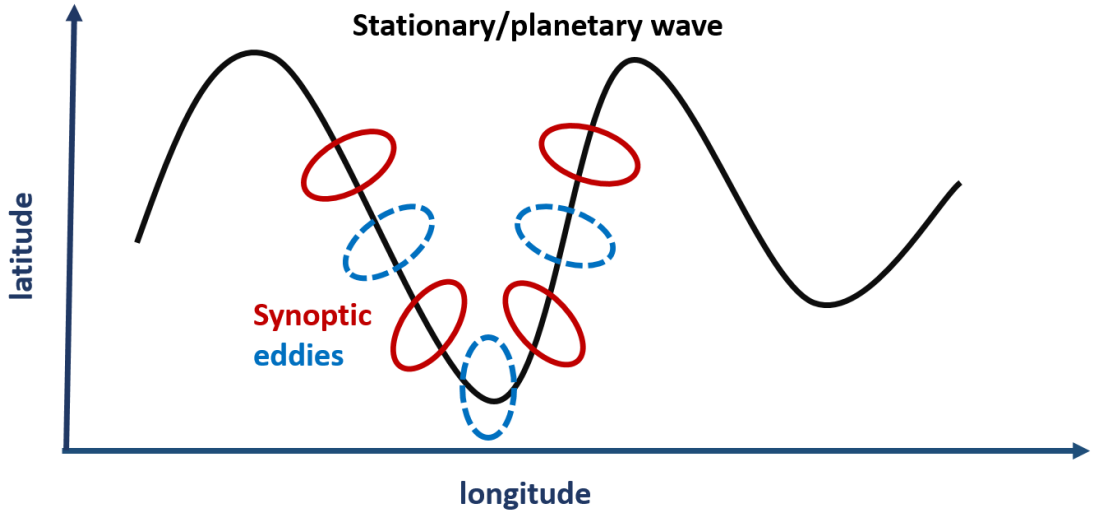

Figure 4.8: An example of a schematic showing the planetary wave 'steering' the synoptic eddies. - The black solid line represents the stationary/planetary wave, and the red solid and blue dashed circles represent the synoptic eddies (positive and negative values of e.g. vorticity, respectively) that follow the planetary (stationary) wave.

term. The planetary scale waves and their interactions with synoptic eddies dominate this local barotropic budget.

It can further be shown (Fig. J.2c,d) that also in the upstream and downstream regions of the model storm track both the transient waves as well as their interactions with stationary waves are necessary to explain the full barotropic variability, especially at higher frequencies.

This analysis thus shows that (especially) high frequency variability in storm track regions is not driven by transients alone, nor is it driven by the synoptic eddies alone. To represent the full barotropic (and baroclinic) variability, both planetary and synoptic waves are important as well as their stationary and transient components.

ERA-Interim NH storm tracks

Zonal mean storm track

Baroclinic flow

The real part of the cross spectrum for the zonal mean baroclinic flow in the ERA-Interim NH has similar characteristics as in the aquaplanet model (SH800), i.e. low frequency suppression of the full heat fluxes, with a cancellation between the synoptic and planetary scale heat fluxes

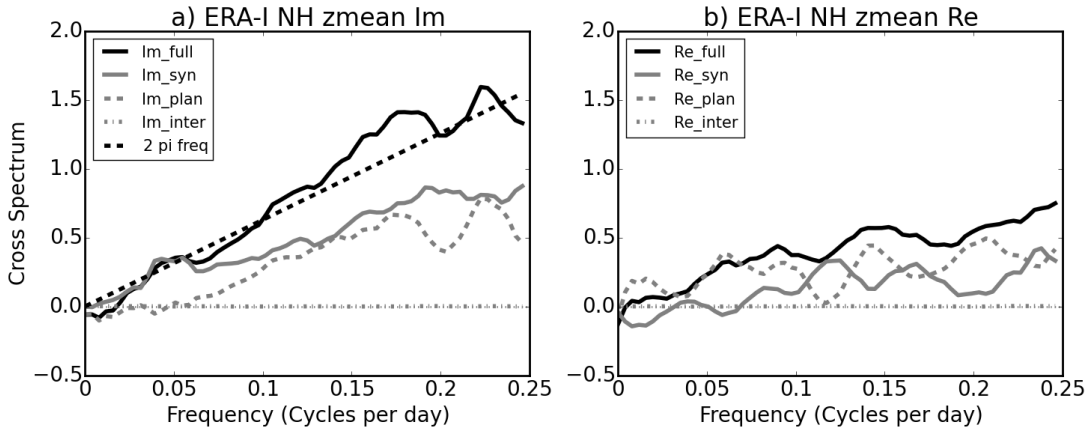

Figure 4.9: Cross spectrum analysis of the baroclinic equation (4.1) in ERA-Interim NH. - a) imaginary, and b) real parts of the cross spectrum for the zonal mean case. The different lines in panels are the same as in Fig. 4.5.

(Fig. 4.9b). However, the imaginary part of the cross spectrum shows that planetary scale waves are more important in ERA-Interim, especially at higher frequencies, whereas at lower frequencies only the synoptic scale heat fluxes are contributing to the full heat flux and its forcing of baroclinicity. While the low frequency dominance of synoptic eddies could be suggestive of the low-frequency baroclinic feedback, further analysis shows that it is hardly distinguishable from the seasonal cycle and it is only seen in the zonal mean.

As in the model storm track, the zonal mean baroclinic budget is dominated by the transient eddies, though here the planetary waves and their stationary component are contributing as well (Fig. J.3a shows a slightly lower contribution from the transient planetary heat fluxes compared with the full planetary heat flux contribution in Fig. 4.9a, suggesting that transient-stationary interactions matter here).

Barotropic flow

The zonal mean barotropic budget in the ERA-Interim NH shows similar characteristics as the barotropic budget in the SH800 aquaplanet model simulation, i.e. both planetary and synoptic waves matter for the zonal mean barotropic flow (Fig. 4.10; the similarity is especially clear through the imaginary part of the cross spectrum in panel a). When only the transient components of the momentum fluxes are considered, the picture looks very similar (i.e. Fig. 4.10a and Fig. J.4a closely resemble each other), with some contribution from the planetary quasi-stationary wave interactions with transients as was the case also in the zonal mean baroclinic

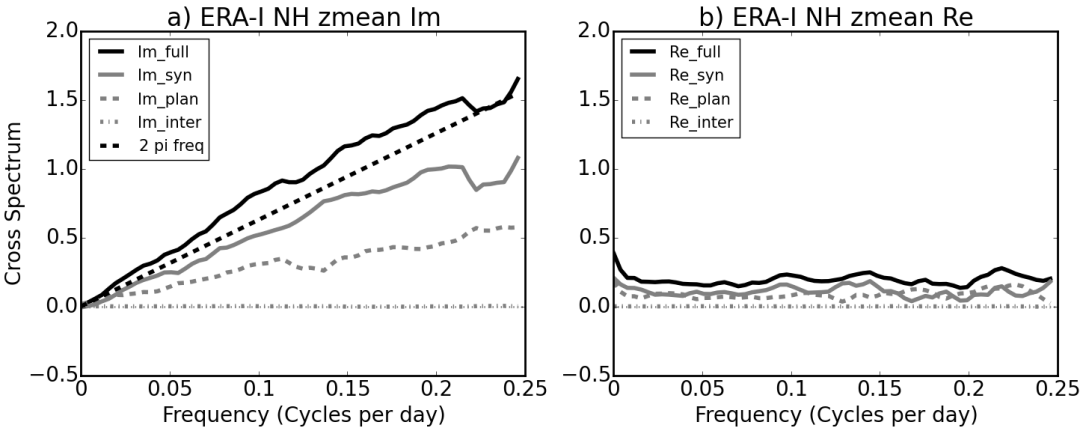

Figure 4.10: As in Fig. 4.9 but for the barotropic equation (4.1).

budget in ERA-Interim.

A similar budget was analysed in Lorenz and Hartmann (2003) (although here the effects of the mountain torque have not been removed), however they did not split the momentum fluxes into the contributions from the planetary and synoptic eddies in terms of wavenumber. Instead, they analysed the feedbacks on the zonal mean flow from the transient and lower frequency eddies, however these different frequency bands can include influences from both planetary and synoptic waves (in terms of wavenumber) as mentioned above (unless planetary waves are weak). Lorenz and Hartmann (2003) found that both transient (waves with periods shorter than 15 days) and quasi-stationary (waves with periods longer than 40 days) waves reinforce the zonal mean zonal wind, whereas the waves coming from the intermediate frequencies (periods between 15 and 40 days) acted to damp the zonal flow, which they associated with external Rossby waves (Held et al., 1985). It is shown in section 4.5.3 that low frequency planetary and interaction momentum fluxes [coming from the waves with periods longer than 10 days and shorter than the seasonal cycle/quasi-stationary timescale, i.e. Lorenz and Hartmann (2003)'s intermediate frequency waves] damp the time mean zonal flow only in the upstream regions of the storm tracks, consistent with Hoskins et al. (1983). Lorenz and Hartmann (2003) also found that the transient eddies dominate the positive feedbacks at longer lead-times, as in Lorenz and Hartmann (2001) for the SH.

North Atlantic storm track

In the Earth's Northern Hemisphere the zonal mean perspective can be misleading, given the asymmetries due to orography, continents, localised heating etc. that give rise to localised and tilted storm tracks and zonal flows. Thus, it is important to look at the Atlantic (and the Pacific) storm tracks in more details locally.

Baroclinic flow

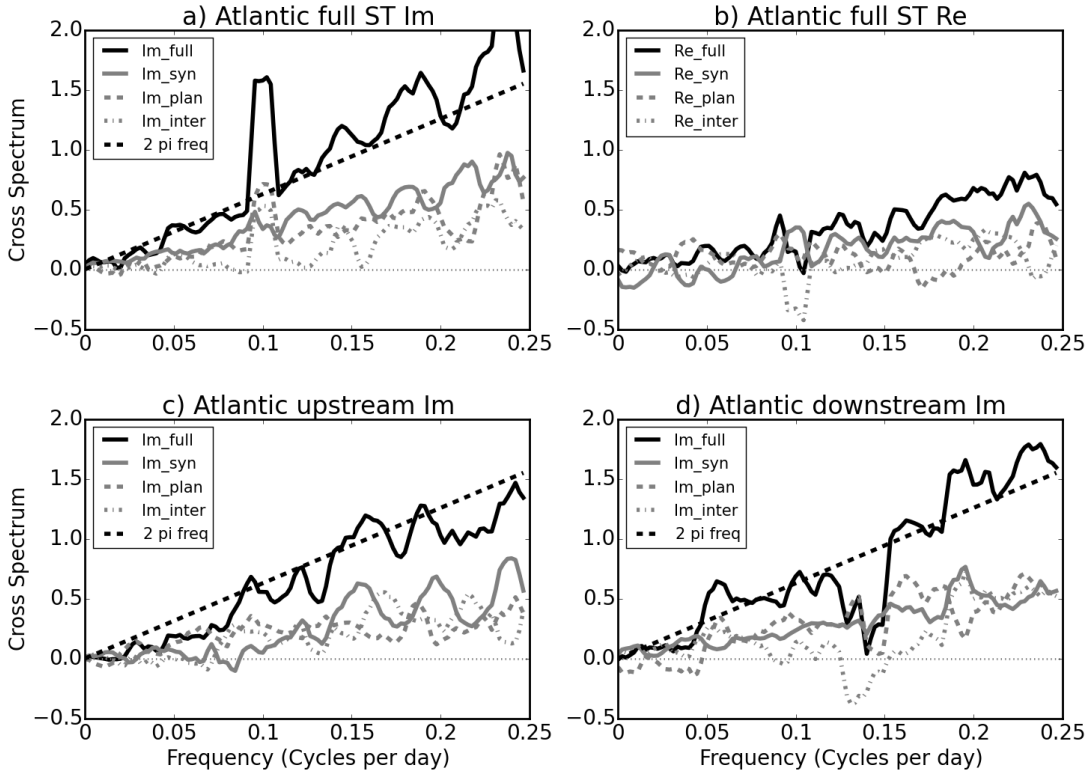

Figure 4.11: Cross spectrum analysis of the baroclinic equation (4.1) in ERA-Interim North Atlantic sector. - a) imaginary, and b) real parts of the cross spectrum for the average over the North Atlantic storm track, and imaginary part of the cross spectrum for c) upstream and d) downstream of the storm track. The different lines in panels are the same as in Fig. 4.5. Note that the peaks in the spectra are not robust to subsampling (artificial).

Fig. 4.11 shows the cross spectra from the baroclinic budget (4.1), averaged over the whole storm track and separately for up- and downstream of the Atlantic storm track. The real part of the cross spectrum for the average over the full storm track (Fig. 4.11b) again shows the suppression of heat fluxes at low frequencies (Zurita-Gotor, 2017), consistent with previous

analysis of the baroclinic budget. The imaginary part of the cross spectrum for all cases (Fig. 4.11a,c,d) shows the importance of both planetary and synoptic waves in forcing baroclinicity as well as the importance of the interaction between planetary and synoptic waves, consistent with the SH800 model storm track, but the importance of planetary waves is more pronounced in the Atlantic storm track, especially downstream.

As in the zonal mean baroclinic flow in ERA-Interim and in the model storm track, the transient waves explain the majority of the baroclinic variability also in the Atlantic storm track (Fig. J.3b-d), with minor contributions from stationary-transient interactions.

Barotropic flow

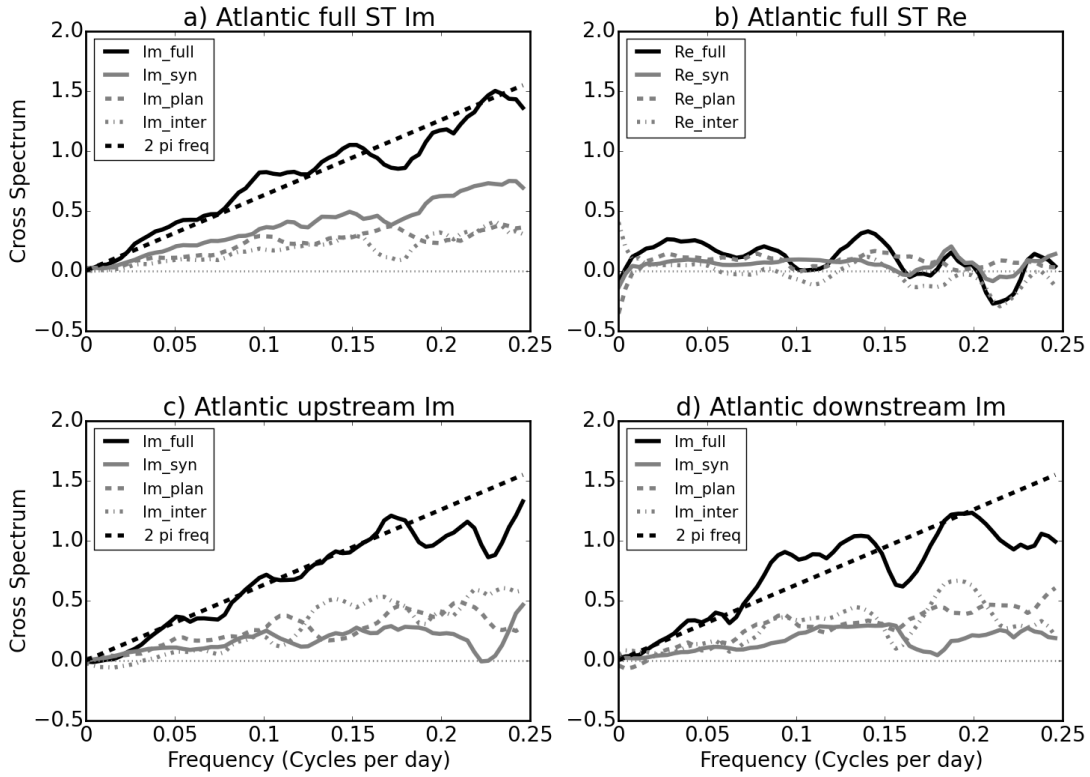

Figure 4.12: As in Fig. 4.11, but for the barotropic budget (4.3).

Fig. 4.12 shows the cross spectra from the barotropic budget (4.3), averaged over the whole Atlantic storm track and separately for upstream and downstream of this storm track. The panels in Fig. 4.12 are largely consistent with the SH800 barotropic budget (i.e. inefficiency of synoptic eddies for the upstream and downstream forcing of the barotropic flow, and a relatively

larger importance of planetary scale waves and their interaction with synoptic eddies). Similarly, the transient eddies also here cannot account for the full barotropic variability (Fig. J.4b-d), i.e. there is strong influence from the quasi-stationary interactions with transient waves for the momentum flux contributions from planetary waves and planetary-synoptic wave-interactions.

North Pacific storm track

In the Earth's Northern Hemisphere there is also a localised storm track in the North Pacific, which is generally less tilted than the Atlantic storm track (Fig. 4.3a), is located further equatorward, and the EKE maximises further east of the Asian coast (i.e. storms can propagate further and/or get reinforced further downstream). Therefore, the up- and downstream regions of the Pacific storm track are in the middle-east Pacific rather than further west. These characteristics of the Pacific storm track can lead to different variability in the baroclinic and barotropic flows associated with them.

Baroclinic flow

Fig. 4.13 shows the cross-spectra from the baroclinic budget (4.1), averaged over the whole Pacific storm track and separately for up- and downstream of the Pacific storm track. The average over the full storm track shows the importance of heat fluxes due to synoptic, planetary and interaction components (Fig. 4.13a,b), consistent with the Atlantic and SH800 storm tracks. While the imaginary cross-spectrum also shows the dominance of the synoptic scale heat fluxes in driving baroclinicty at lower frequencies (periods longer than 20 days), as was also seen in the zonal mean NH baroclinic budget, this feature is only robust at the seasonal timescales.

The imaginary part of the cross spectrum for up- and downstream of the Pacific storm track (Fig. 4.13c,d) shows a weaker influence of the synoptic eddies in the downstream region compared to the upstream region and that again all components of the heat fluxes matter, consistent with the Atlantic and SH800 storm tracks. Note that in the Pacific the full heat flux influence on the baroclinicity downstream is also reduced (i.e. the imaginary part of the cross spectrum is below the angular frequency line, Fig. 4.13d). This suggests that the relationship between the baroclinicity and heat fluxes is not as clear in the downstream region of the Pacific storm track as it is in its upstream region.

When only transient waves are considered (Fig. J.3e-g), the picture remains similar to the Atlantic storm track, i.e. the quasi-stationary interactions with transient waves for the planetary

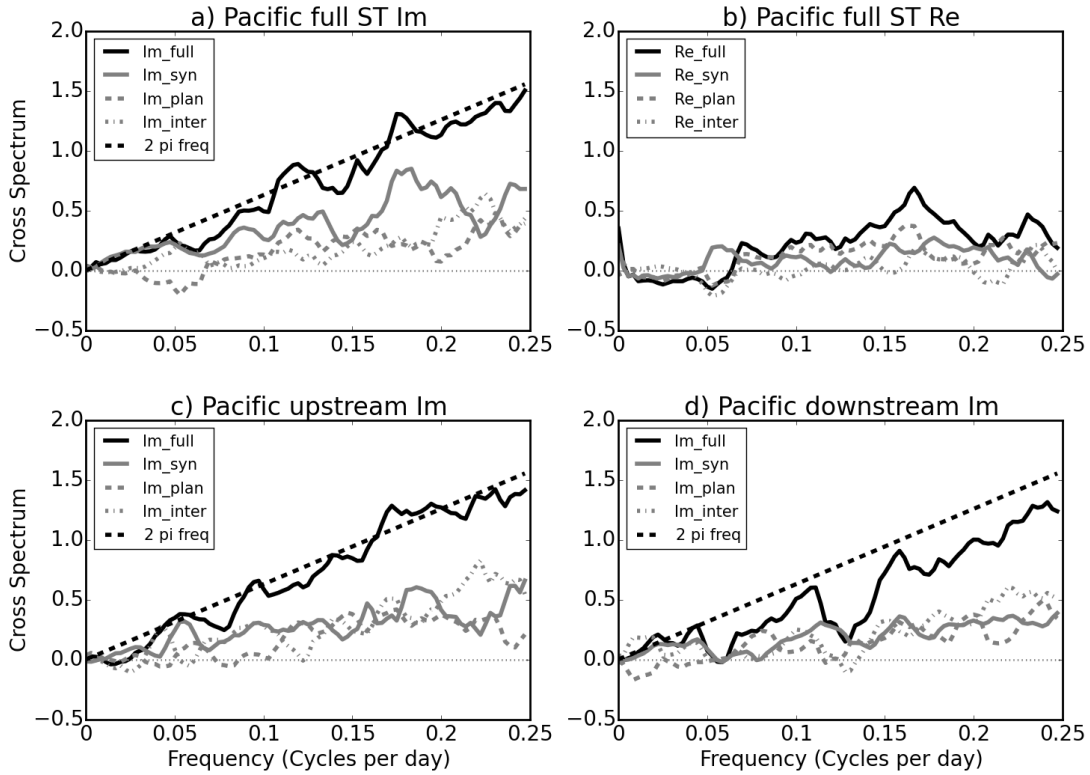

Figure 4.13: As in Fig. 4.11 but for ERA-Interim North Pacific sector. - Note that the abrupt increase at the lowest frequency in (b) is not robust to subsampling (artificial).

waves and planetary-synoptic wave-interactions are important, whereas the synoptic eddies are dominated by the transient component.

Barotropic flow

Fig. 4.14 shows the cross-spectra from the barotropic budget (4.3), averaged over the whole Pacific storm track and separately for up- and downstream of the Pacific storm track. The average over the full storm track shows the importance of momentum fluxes due to synoptic, planetary and interaction components (Fig. 4.13a,b), consistent with the Atlantic and SH800 storm tracks. However, the imaginary parts of the cross-spectra for up- and downstream of the Pacific storm track (Fig. 4.13c,d) are slightly different from the Atlantic. There is a dominance of the planetary scale momentum fluxes at low frequencies (periods longer than 20 days) which is only robust on seasonal timescales.

Further insight into the barotropic variability in the Pacific storm track can be gained by

considering the transient waves only. Fig. J.4f-g shows similar features as the barotropic flows in the Atlantic and model storm tracks (i.e. importance of quasi-stationary planetary waves and their interactions with transients), and also shows that the apparent low frequency dominance of planetary waves is mainly due to transient waves, but is less pronounced here.

The storm track regions can be linked to the teleconnection patterns (WPO, EPO, NAO and PNA) that are mainly associated with the planetary momentum fluxes, which are dominated by quasi-stationary and low-frequency variability (see next sections for further details).

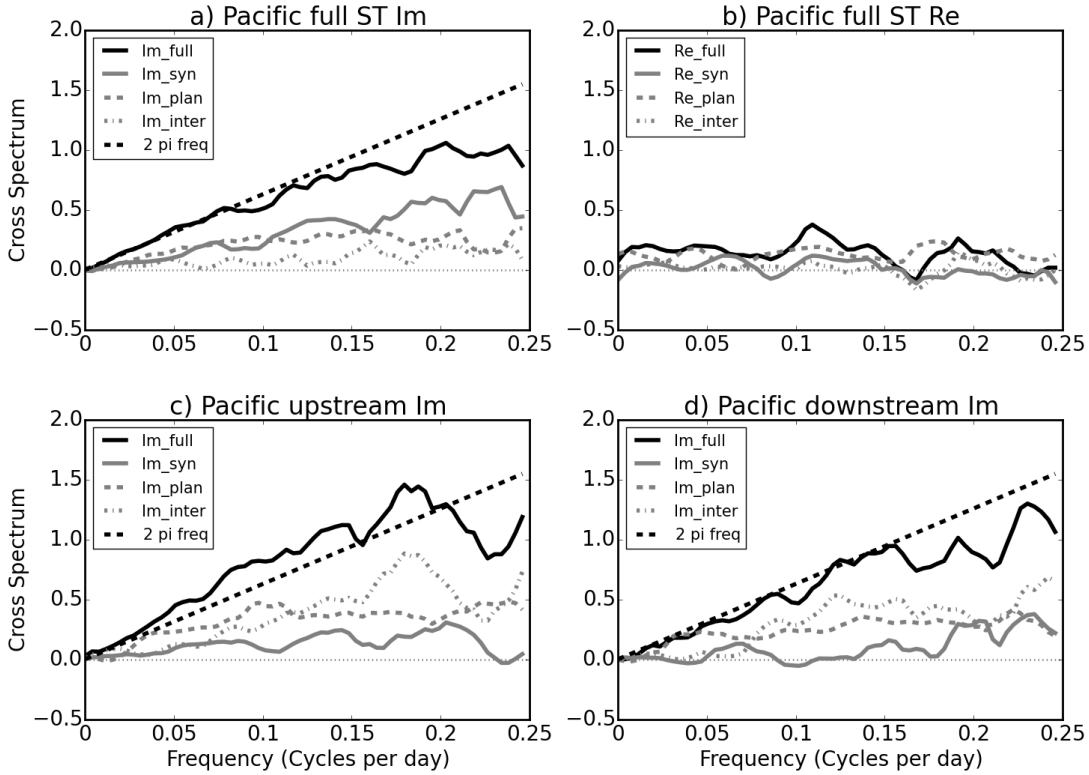

Figure 4.14: As in Fig. 4.12 but for ERA-Interim North Pacific sector.

In summary, the cross-spectrum analysis has revealed that both the synoptic and planetary waves play a vital role for the baroclinic and barotropic variability in the storm track regions at all timescales, hence care must be taken when relating the transient (high frequency) variability to synoptic eddies, as it may include planetary scale waves (similarly for low frequency variability). Similarly, it can be shown that locally the transient eddies alone are not suffient to explain the co-variability of momentum fluxes with the zonal flow; the stationary-transient interactions are necessary as well. These cross-spectra provide an explicit measure of the relative importance

of planetary and synoptic waves for the atmospheric variability, which can help us further understand the variability at different timescales. The main caveat of this approach is that the planetary and synoptic eddies can represent the same physical feature (similarly for transient and stationary waves) and hence their transient variability potentially cannot be distinguished (see schematics in Figs. 4.7, 4.8). Donohoe and Battisti (2009) argued that temporal filtering is better than spatial filtering for feature tracking as it removes the time mean component of the fields, however the transients alone cannot explain the full barotropic variability as mentioned above, but can largely explain the baroclinic variability (especially in the model storm track), and they dominate the synoptic scale variability.

4.5.2 Regression analysis of the barotropic flow in NH observations

In order to visualise the above cross-spectra, a regression analysis of vertically averaged zonal and meridional winds on the momentum flux divergence (split into synoptic, planetary and interaction components) is performed for upstream and downstream of the Pacific and Atlantic storm tracks. The patterns that emerge are then further linked to teleconnection patterns (e.g. Wallace and Gutzler 1981; Barnston and Livezey 1987) and Rossby-wave trains (e.g. Wallace et al. 1988; Hoskins and Ambrizzi 1993; Ambrizzi et al. 1995; Chang and Yu 1999; Chang 2005).

Zonal wind regressions and teleconnection patterns

North Pacific

Fig. 4.15 shows the regressions of vertically averaged zonal wind on the full momentum flux divergence, as well as on the synoptic, planetary and interaction contributions to the momentum flux divergence, for the upstream Pacific storm track, complementing Fig. 4.14c. The regression on the full momentum flux divergence in this region is dominated by the planetary and interaction components with a smaller and opposing influence from the synoptic momentum flux divergence as also suggested by Fig. 4.14c. The regression of $\langle u \rangle$ on the full and planetary momentum fluxes resembles its regression on the WPO (Fig. K.1a) and the WPO itself (Fig. 4.1), which is even clearer when the planetary component of $\langle u \rangle$, $\langle u_p \rangle$, is regressed on the same momentum flux divergence (Fig. K.3). That the planetary momentum flux divergence picks up the WPO pattern (or any other teleconnection pattern) is not surprising given that planetary waves and teleconnection patterns occur at lower frequencies and that the planetary waves tend to be zonally elongated (e.g. Hoskins et al. 1983). The relationship between the upstream region

of the Pacific storm track and the WPO is further confirmed by the correlation between $\langle u \rangle$ in this region and the WPO index, reaching 0.87. The correlation with the PNA pattern is only 0.26, however the correlation of $\langle v \rangle$ in this region with the PNA is 0.51, suggesting that the PNA links to the meridional wind instead of the zonal wind. This is consistent with the PNA pattern which resembles a wave-train structure (Fig. 4.1), which the meridional velocities show (see next section).

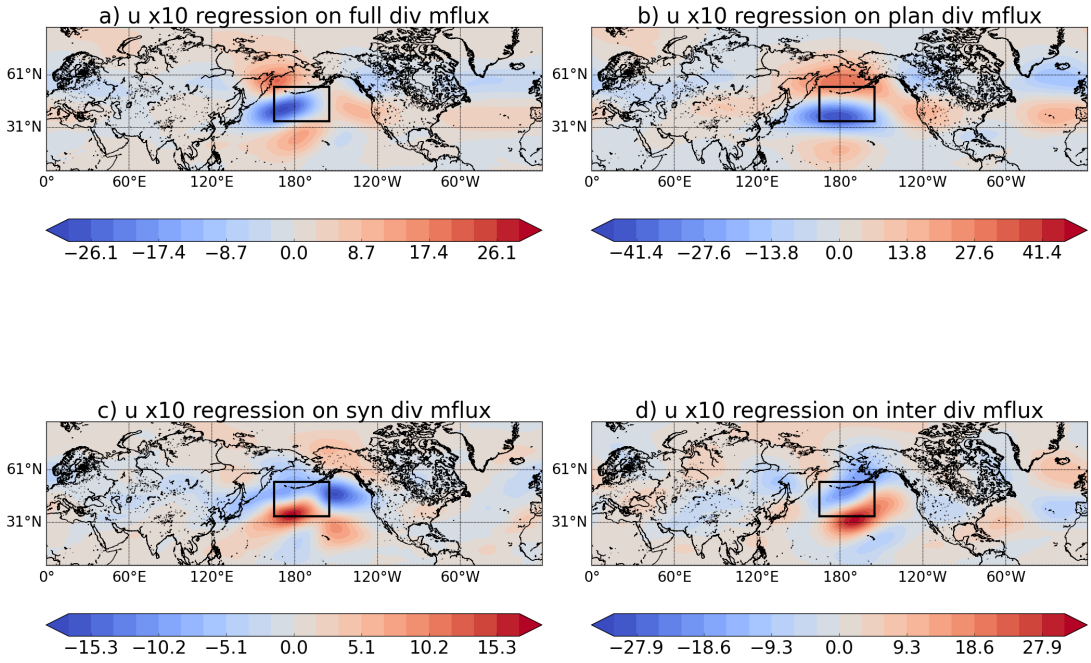

Figure 4.15: Regression of the vertically integrated zonal wind on normalised momentum flux divergence. - For (a) full momentum flux divergence, (b) planetary, (c) synoptic, and (d) interaction contributions to the momentum flux divergence for upstream of the Pacific storm track. Units are m s^{-1} (multiplied by 10). The momentum flux divergence was first averaged over the box shown and normalised by its standard deviation then the wind fields were regressed. Note that the colourbars are not the same, in order to show the different features more clearly.

Fig. 4.16 shows the regressions of vertically averaged zonal wind on the full momentum flux divergence, as well as on the synoptic, planetary and interaction contributions to the momentum flux divergence, for the downstream of the Pacific storm track, complementing Fig. 4.14d. The regression on the full momentum flux divergence resembles a combination of the planetary and interaction components of the momentum flux divergence, with the synoptic momentum flux divergence showing a different and opposing impact on $\langle u \rangle$ (as was the case also in the upstream region), which is again consistent with Fig. 4.14d. The regression of $\langle u \rangle$ on the full and planetary

momentum flux divergence resembles its regression on the EPO (Fig. K.1b) and the EPO itself (Fig. 4.1), which is even clearer when $\langle u_p \rangle$ is regressed on the same momentum flux divergence (Fig. K.4). The correlation between the EPO and $\langle u \rangle$ downstream of the Pacific storm track is 0.89, whereas the correlation with the PNA in the same region is only 0.07. However, the correlation of $\langle v \rangle$ in this region with the PNA is 0.82 (and the regression of $\langle v \rangle$ on the PNA, Fig. K.2c, resembles the PNA index, Fig. 4.1), again suggesting a link between the wave-train in that region with the PNA (see next section).

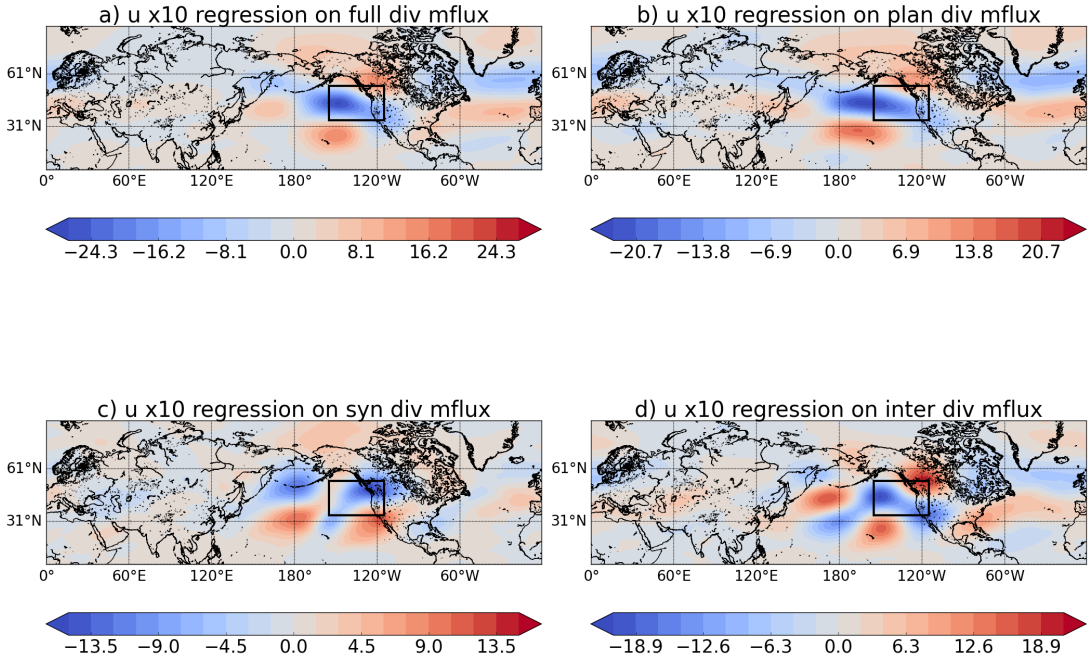

Figure 4.16: As in Fig. 4.15, but for downstream of the Pacific storm track.

North Atlantic

While the North Pacific storm track shows links with three different teleconnection patterns (WPO, EPO and PNA), the North Atlantic storm track's vertically averaged zonal wind is well correlated with the NAO both upstream (0.79) and downstream (0.80), hence there is no reason for correlating it with other patterns that occur over Europe and Asia (further east). Comparing $\langle u \rangle$ (Figs. 4.17, 4.18) and $\langle u_p \rangle$ (Figs. K.5, K.6) regressions on the upstream and downstream (planetary) momentum flux divergence in the Atlantic indeed reveals the NAO-like pattern (Fig. 4.1, K.1d), which is clearer in the downstream region. Unlike in the Pacific, the

synoptic momentum flux divergence contributes to the regressions of $\langle u \rangle$ on the momentum flux divergence in the Atlantic storm track, consistent with Fig. 4.12c,d, i.e. all different components of the momentum fluxes contribute (equally) to the variability in the Atlantic storm track. However, as in the Pacific storm track, also in the Atlantic the regressions on the synoptic scale momentum flux divergence generally oppose those on the interaction and planetary components.

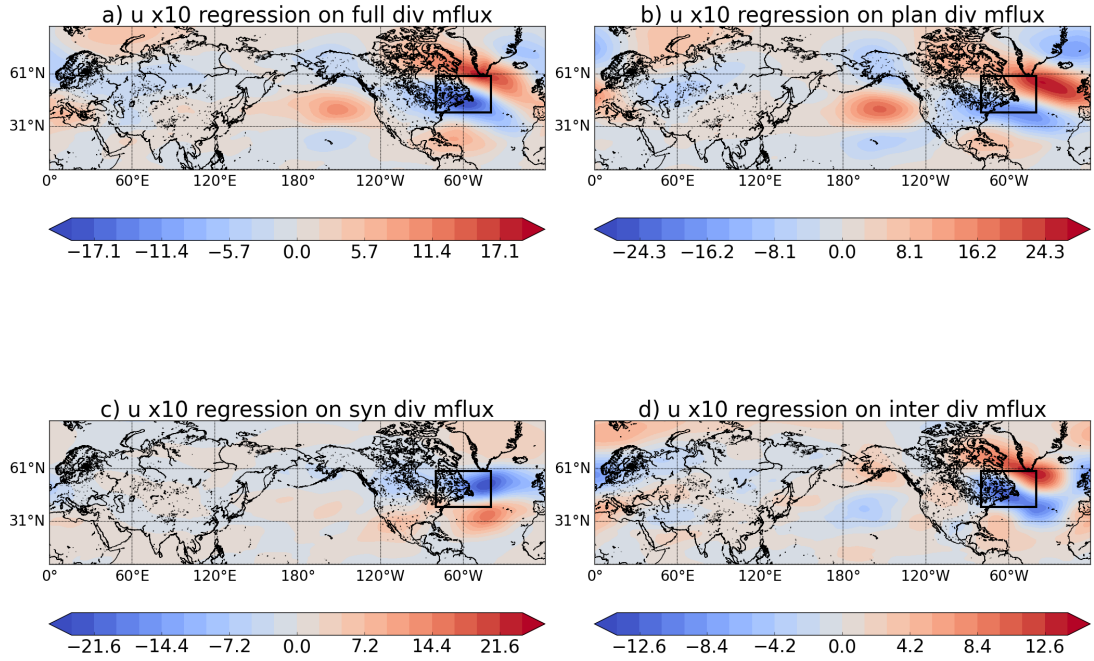

Figure 4.17: As in Fig. 4.15, but for the upstream of the Atlantic storm track.

The robust opposing effects of the synoptic and planetary momentum fluxes is consistent with Hoskins et al. (1983) and Cai et al. (2007), who found opposing forcings of the zonal flow by the planetary and synoptic waves, a consequence of the different orientations of the synoptic (meridional orientation) and planetary (zonal orientation) waves.

Luo et al. (2007) have also shown that the NAO phase (i.e. its pattern) depends on the planetary wave-forcing (consistent with Figs. 4.17-4.18), whereas the life cycle of the NAO is linked to the synoptic wave-forcing (not directly addressed in this study). This could be the case in the Pacific sector for the WPO and EPO as well.

Note that the correlations between different teleconnections are small, except for the correlation between EPO and WPO which reaches 0.40. Similarly, the correlations between the Atlantic and Pacific storm tracks are small, although the regression of $\langle u \rangle$ on the momentum flux divergence in the downstream Pacific storm track shows a weak signal in the North Atlantic

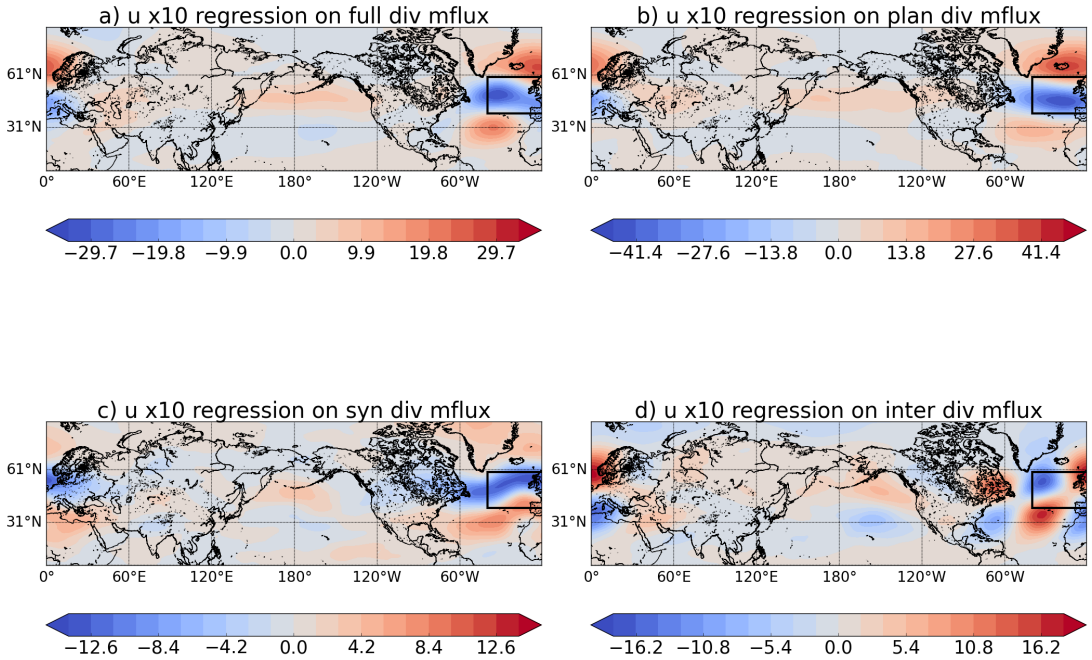

Figure 4.18: As in Fig. 4.15, but for the downstream of the Atlantic storm track.

(Fig. 4.16), and similarly the regression of $\langle u \rangle$ on the momentum flux divergence in the upstream Atlantic storm track shows a signal in the west Pacific (Fig. 4.17), suggesting a link between these two regions. Previous studies have found a link between the two regions through wave trains (e.g. via PNA) and through the Aleutian Low - Icelandic Low seesaw (see e.g. Honda et al. 2001; Honda and Nakamura 2001; Honda et al. 2007; Drouard et al. 2015).

Meridional wind regressions and Rossby wave-trains

In addition to teleconnection patterns that can be identified through the zonal velocity (except for PNA), the regressions of vertically averaged meridional wind on momentum flux divergence provide another perspective on the storm track dynamics, the so-called Rossby wave-trains (see Fig. 4.2 for more details). These regressions are dominated by regressions of the synoptic meridional velocity $\langle v_s \rangle$, hence any conclusions about the full meridional velocity will mainly involve the behaviour of the synoptic component, despite the different momentum flux forcings. The dominance of synoptic meridional velocity can be expected as the synoptic eddies tend to be meridionally elongated (Hoskins et al., 1983), whereas planetary waves (as mentioned above) are zonally elongated and thus dominate the zonal velocity (though to a lesser extent).

North Pacific

Figs. 4.19, 4.20 show the zero-lag regressions of $\langle v \rangle$ on different momentum flux divergence components for the upstream and downstream regions of the Pacific storm track, respectively. Additional figures are provided in Appendix K for lags of ± 2 days for the regressions on the planetary and interaction momentum flux divergence (Fig. K.7), as these two components dominate the regressions (Figs. 4.19, 4.20), consistent with cross-spectra and regressions of the zonal velocity.

The regressions on the upstream Pacific storm track's planetary momentum flux divergence (Figs. 4.19b, K.7a,c) reveal a wave-train coming from northern Eurasia into the Pacific storm track with a north-west to south-east tilt, and out of the storm track region with a south-west to north-east tilt continuing across northern North America back into Eurasia. These fluxes are related to the wave trains into North America, which is also seen in the regressions on the full momentum flux in the eastern Pacific (Fig. 4.19a). Note that from this analysis one cannot infer the causal relation between the momentum fluxes and $\langle v \rangle$.

The regressions on the interaction momentum flux divergence in the upstream region of the Pacific storm track (Figs. 4.19d, K.7b,d) show a wave-train coming from Eurasia (much like in the case of the planetary momentum flux divergence), however, in this case they are related to the wave-train southwards along the eastern Pacific coast towards the subtropics. A part of this is evident in the regressions of $\langle v \rangle$ on the full momentum flux divergence (Fig. 4.19a), where the southward propagating wave-train in the western Pacific resembles the regression on the interaction momentum flux divergence (Fig. 4.19d).

The regressions on the synoptic momentum flux divergence largely show the opposite behaviour to the interaction and planetary components and seem overwhelmed by the latter two, and are hence not discussed further (similar results are found for other regressions mentioned below).

These wave-trains resemble the north Eurasian pathway previously discussed in Wallace et al. (1988), Hoskins and Ambrizzi (1993), Chang and Yu (1999), and Chang (2005). While this pathway is considered secondary compared to the south Asian waveguide, it appears of primary importance in these regressions. Similar results were found for v at 300 hPa, even though Chang and Yu (1999) argued that the south Asian path can only be seen in the upper troposphere due to the high orography in that region. Hoskins and Ambrizzi (1993) pointed out that the north Eurasian pathway is one of the preferred paths between the different waveguides

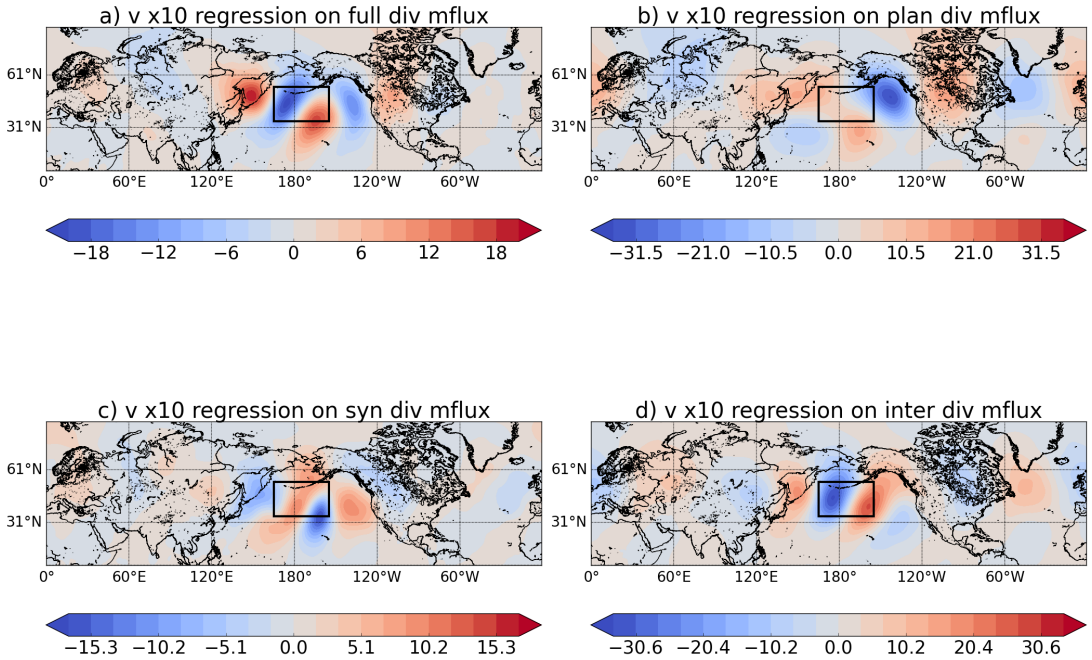

Figure 4.19: Regression of the vertically integrated meridional wind on normalised momentum flux divergence. - For (a) full momentum flux divergence, (b) planetary, (c) synoptic, and (d) interaction contributions to the momentum flux divergence for upstream of the Pacific storm track. Units are m s^{-1} (multiplied by 10). The momentum flux divergence was first averaged over the box shown and normalised by its standard deviation then the wind fields were regressed. Note that the colourbars are not the same, in order to show the different features more clearly.

(see also Fig. 4.2). Here, this path is mainly linked to the interaction momentum flux divergence of the upstream Pacific storm track. A path across northern North America ('starting' in the mid-Pacific), identified through the planetary momentum flux divergence in the upstream region, is also shown in Hoskins and Ambrizzi (1993).

Similar analysis of the downstream region of the Pacific storm track (Figs. 4.20, K.7e-h) reveals a wave-train, related to the downstream planetary momentum flux divergence, across northern North America, similar to the one identified through the upstream region, although here the negative lags show a propagation southwards along the eastern Pacific coast and turning across northern North America with positive lags. The regressions on the interaction momentum fluxes show a west-to-east wave-train propagation across central North America without any clear steering, starting from the upstream region of the Pacific storm track. This brings wave-trains to the beginning of the Atlantic storm track on the eastern coast of North America. Such a path was identified in Ambrizzi et al. (1995) and Chang and Yu (1999). In the Atlantic

these wave-trains (related to the interaction momentum fluxes) have a south-eastward direction, perhaps suggesting they could be joining the south-Asian waveguide as in Chang and Yu (1999).

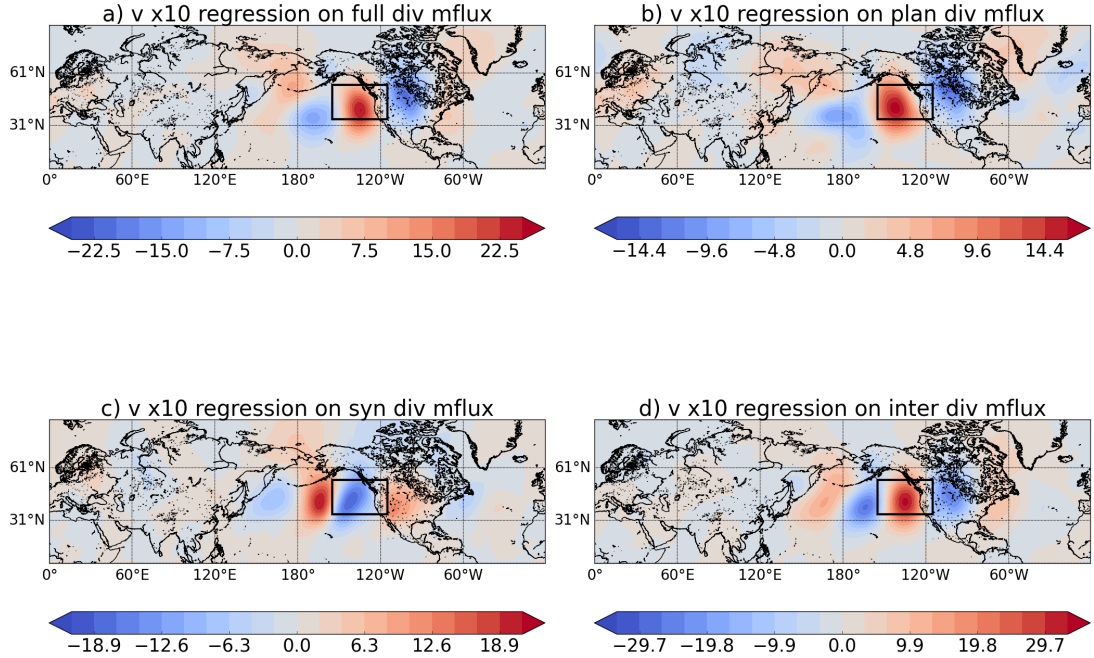

Figure 4.20: As in Fig. 4.19, but for downstream of the Pacific storm track.

Notice that these regressions resemble the PNA pattern discussed above. Indeed, the regression of $\langle v \rangle$ on the downstream (Pacific storm track) planetary and interaction momentum flux convergence (Fig. 4.20b,d) resembles the regressions of $\langle v \rangle$ on the PNA pattern (Fig. K.2c). The correlation between $\langle v \rangle$ in the downstream region of the Pacific storm track and the PNA index is correspondingly high (0.82); slightly lower but still high correlations (0.51) were found for the upstream region of the Pacific storm track as well (as mentioned above).

North Atlantic

Figs. 4.21, 4.22 show the zero-lag regressions of $\langle v \rangle$ on different momentum flux divergence components for the upstream and downstream regions of the Atlantic storm track, respectively. Additional figures are provided in Appendix K for lags of ± 2 days for the regressions on the planetary and interaction momentum flux divergence (Fig. K.8), as these two components dominate the regressions (Figs. 4.21, 4.22), consistent with cross-spectra and regressions of the zonal velocity.

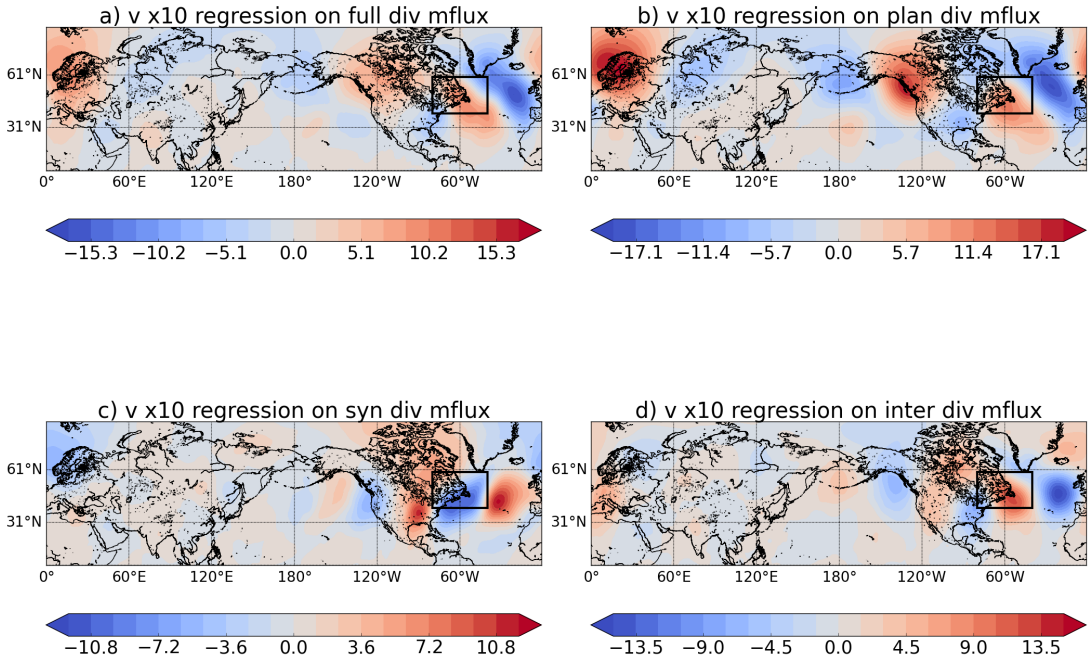

Figure 4.21: As in Fig. 4.19, but for upstream of the Atlantic storm track.

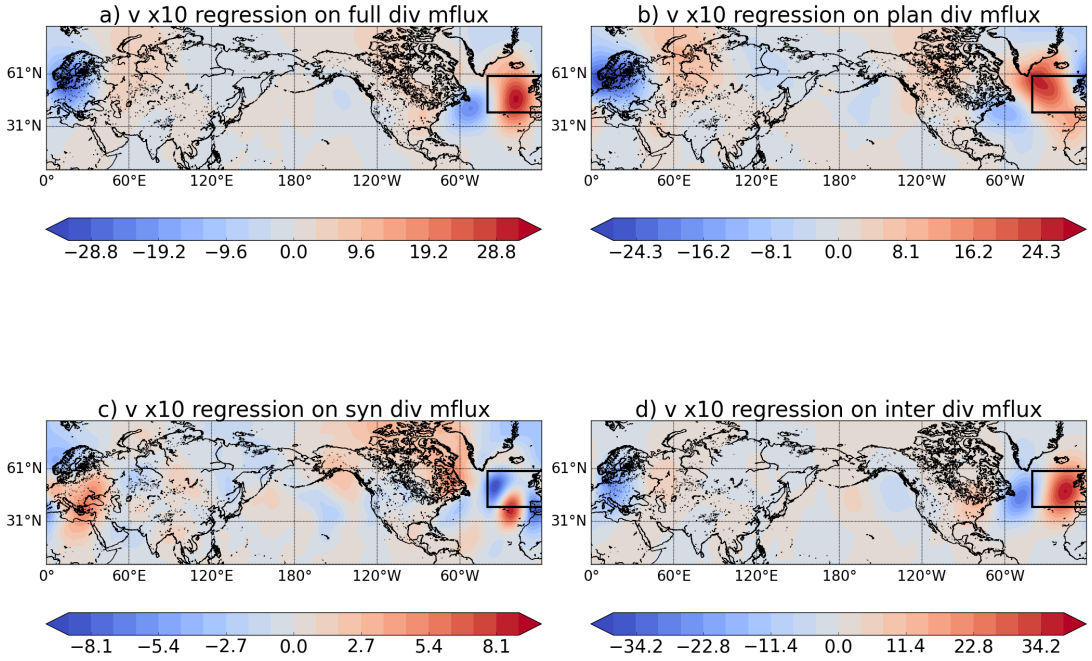

Figure 4.22: As in Fig. 4.19, but for downstream of the Atlantic storm track.

The regressions on the upstream planetary momentum flux divergence (Figs. 4.21b, K.8a,c) are reminiscent of the wave-trains identified in the Pacific storm track region, i.e. a wave-train travelling from the mid-Pacific across northern North America into the Atlantic, where they are primarily related to the wave-train propagation north-eastward. This can also be seen in the regressions on the downstream Atlantic planetary momentum flux convergence (Figs. 4.22b, K.8e,g). A similar teleconnection pathway was identified in Ambrizzi et al. (1995).

The regressions on the interaction momentum flux divergence, both upstream (Figs. 4.21d, K.8b,d) and downstream (Figs. 4.22d, K.8f,h) of the Atlantic storm track, are also reminiscent of similar regressions in the Pacific. The wave trains first propagate southwards along the eastern Pacific coast, then across central North America and at first south-eastward towards the south-Asian wave guide, but later on turn eastwards and north-eastwards together with the wave trains related to the planetary momentum flux divergence, joining the north Asian pathway. Although these regressions suggest a south-Asian pathway, there is only little evidence of it: the +2-day lags (Fig. K.8d,h) show a boomerang-like shape across Eurasia, which could suggest that the interaction momentum fluxes are related to the wave-train propagation into both Asian pathways; another piece of evidence can be seen at -2-day lag regressions on the upstream Pacific interaction momentum flux divergence (Fig. K.7b), where a weak regression in the south-Asian region suggests some influence from the south Asian pathway.

Note that here the synoptic momentum flux divergence influence on the wave trains is overwhelmed by the planetary and interaction components, in contrast to the regressions of $\langle u \rangle$, where all three components played an important role (in the north Atlantic storm track). Their influence is still opposing the dominant pattern in the region.

Overall, these results point to the importance of the planetary and interaction momentum fluxes for the barotropic flow in storm tracks, consistent with the cross-spectra. They also link the storm track regions to previously identified Rossby wave-trains as well as teleconnection patterns. The planetary 'steering' of the synoptic waves is a well-known feature (e.g. Branstator 1995), though a better understanding of wave-trains may be possible through the analysis of the interaction and planetary momentum fluxes, e.g. elucidating which pathways come from or are affected by planetary-only forcing in the storm track regions, and which from/by the planetary-synoptic interaction as demonstrated above (though arguably they both represent interactions as $\langle v \rangle$ is dominated by $\langle v_s \rangle$); it is, of course, also possible for the wave-trains to affect these momentum fluxes. Similarly, a better understanding of the storm track links to teleconnections through the planetary momentum flux forcing is suggested. Note that these

conclusions only provide information about the influence of the momentum fluxes in the storm track regions on the barotropic flow (and/or vice versa) and not about an individual storm. To link the momentum fluxes to individual storms (or a composite of them) in the upstream and downstream regions, one would have to use, for example, a cyclone-tracking algorithm (e.g. Hoskins and Hodges 2002).

4.5.3 Time mean barotropic flow in the NH observations

The previous sections have focused on the variability of the baroclinic and barotropic mean flows in the storm track regions and in the zonal mean. This section provides additional insight into the barotropic flow in the ERA-Interim NH storm tracks from a time mean perspective, which might not explain the variability and relative contributions from different waves seen in the previous sections, but provides additional information for the time mean (climatological) barotropic behaviour. Note that similar results can also be found in the SH800 model; those results are omitted for brevity.

Fig. 4.23 shows the vertically averaged time mean momentum flux convergence (and its different contributions from planetary and synoptic waves, as well as their interactions) and the zonal and meridional flow. Note that negative momentum flux divergence implies convergent momentum fluxes and hence acceleration of the zonal flow (the opposite is true for positive values). While the synoptic scale momentum flux divergence is of similar magnitude in both sectors, a few clear differences between the North Atlantic and North Pacific sectors can be identified: *(i)* the zonal flow in the Atlantic is weaker than in the Pacific; *(ii)* the planetary scale momentum flux convergence is much stronger in the Pacific than in the Atlantic; and *(iii)* the momentum flux divergence due to the interaction between the synoptic and planetary waves is stronger in the Pacific than in the Atlantic and is of opposite sign to the planetary and synoptic scale momentum flux divergence (consistent with, e.g., Cai and Mak 1990), and hence acts to decelerate the time mean flow in both regions. The stronger planetary scale momentum flux divergence in the Pacific can be linked to the Aleutian low, where the correlation between the WPO and the zonal flow upstream of the Pacific storm track is high in the time period analysed (section 4.5.2).

To elucidate which waves (in terms of frequency) contribute to the time mean behaviour of planetary, synoptic, interaction and full momentum flux divergence, a further split into stationary, time perturbation, high pass and low pass contributions (4.11) is shown in Figs. 4.24, 4.25.

Note that the time perturbation (transients) is a sum of low and high frequency components and that the stationary component includes the slowly varying seasonal cycle as defined in (4.11).

These figures clearly show a dominance of the high frequency component for the time mean synoptic momentum flux divergence (Fig. 4.25a-d), and a dominance of the stationary component for the planetary momentum flux divergence (Fig. 4.24e-h), as suggested by previous studies (e.g. Hoskins et al. 1983; Cai et al. 2007). While the former can be linked to the two storm track regions and suggests an influence from baroclinic life cycles, the latter can be linked to the Aleutian (AL) and Icelandic (IL) lows (regions of low pressure in the Pacific and Atlantic sectors, respectively), where the AL is significantly stronger. The upstream region of the Pacific storm track is located where the strong negative stationary planetary momentum flux divergence is present (AL), however in the Atlantic both the upstream and downstream regions lie slightly to the south of the negative stationary planetary momentum flux divergence (IL). Some studies have identified a link between the two lows, called the AL-IL seesaw (Honda et al., 2001; Honda and Nakamura, 2001; Honda et al., 2007), which occurs via a stationary Rossby wave pattern accross North America, which could also be linked to the wave-train pattern found for the upstream Pacific and Atlantic planetary momentum flux divergence (as already mentioned in section 4.5.2; Figs. 4.19b, 4.21b, K.7a,c, and K.8a,c).

While there is a strong negative stationary planetary momentum flux divergence in the Pacific, it is largely balanced by the positive stationary momentum flux divergence due to the interaction between the synoptic and planetary waves (Fig. 4.25e), although the strong stationary component in the Pacific and Atlantic is still present when the contributions from stationary planetary, synoptic and interaction momentum flux divergence are added together (Fig. 4.24a).

The momentum flux divergence due to low frequency planetary scale waves shows a contrast between upstream and downstream of the storm tracks, namely positive values in the upstream region and negative values further downstream evident in both storm tracks (Fig. 4.24g). Similar influence is shown from the low frequency interaction momentum flux divergence (Fig. 4.25g). The low frequency synoptic waves contribute less (Fig. 4.25c), hence the overall low pass momentum flux divergence resembles a combination of planetary and interaction contributions (Fig. 4.24c).

The high frequency contributions of the planetary and interaction components are much weaker compared to the synoptic component (Figs. 4.24h, 4.25d,h), hence a sum of all these

components for higher frequency waves (Fig. 4.24d) resembles the synoptic momentum flux divergence, which is similar both upstream and downstream of both storm tracks (Fig. 4.25d).

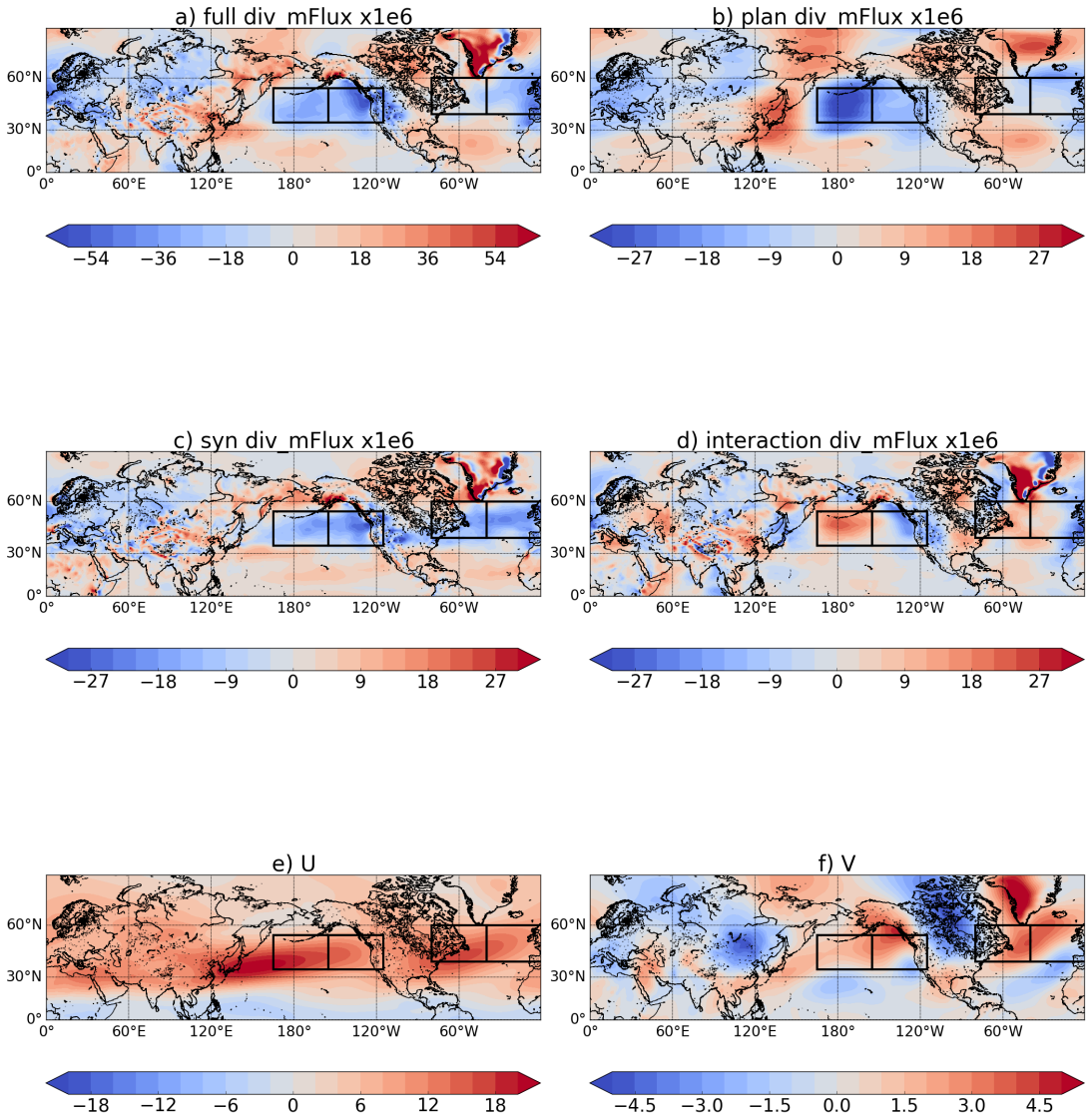

Figure 4.23: Time mean barotropic budget (4.3) for the ERA-Interim NH. - The different panels show: (a) full momentum flux divergence, (b) planetary, (c) synoptic, and (d) interaction contributions to momentum flux divergence (all in m s^{-2}, multiplied by 10^6). The bottom panels show the mean flow in the northern hemisphere: (e) vertically averaged zonal wind $\langle u \rangle$, (f) vertically averaged meridional wind $\langle v \rangle$ (both in m s^{-1}). Note that the colourbars are not the same, in order to show the different features more clearly.

These results are consistent with Hoskins et al. (1983), who showed that high frequency waves force westerly zonal flow in the upstream and middle part of the storm track, whereas

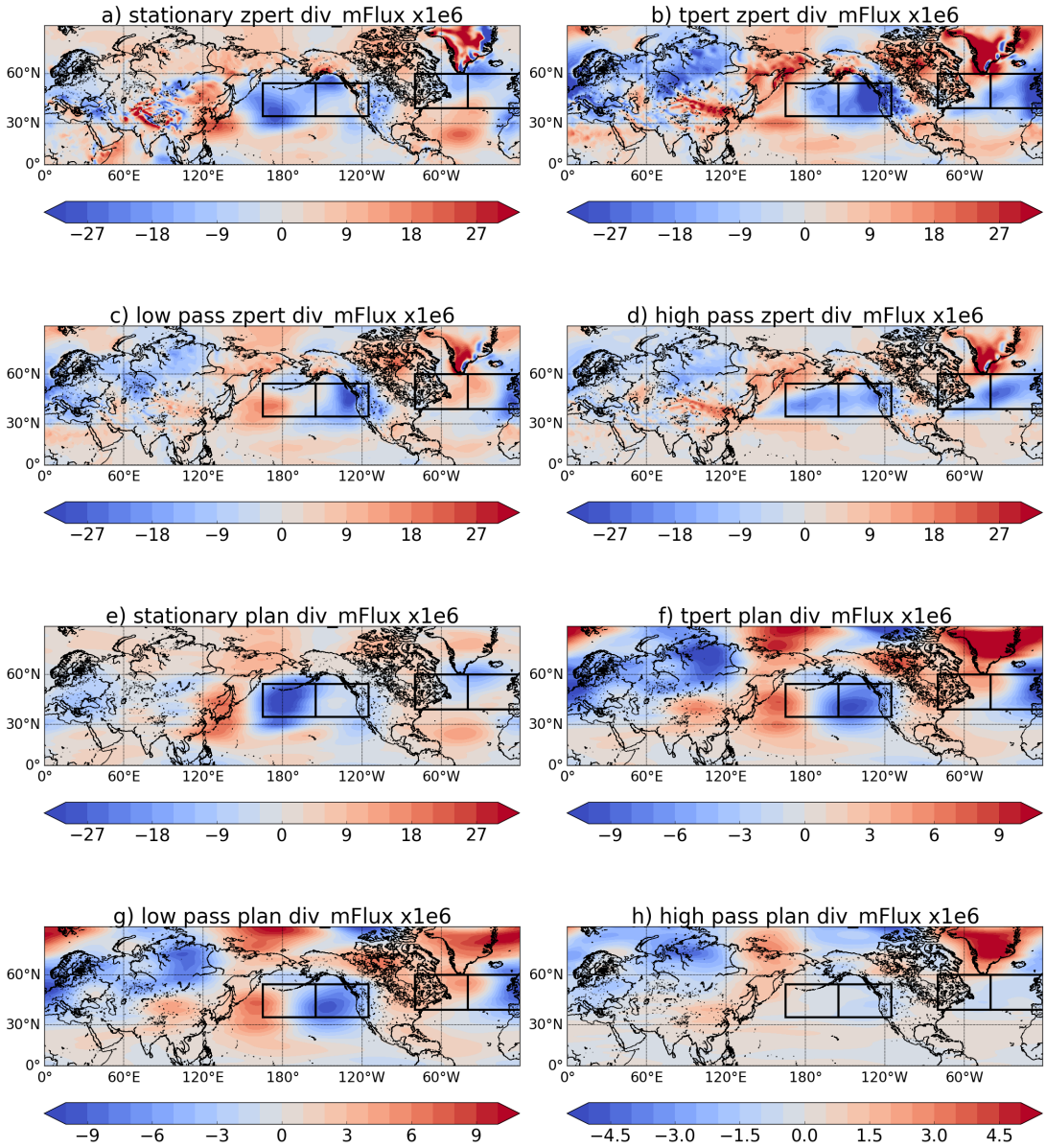

Figure 4.24: Time mean barotropic budget (4.3) with time filtering (4.11) for the ERA-Interim NH. - The different panels show: (a) seasonal cycle (stationary) component, (b) time perturbation component, (c) low pass filtered component, and (d) high pass filtered component of full momentum flux divergence (all in m s^{-2}, multiplied by 10^6); (e) seasonal cycle (stationary) component, (f) time perturbation component, (g) low pass filtered component, and (h) high pass filtered component of planetary momentum flux divergence (all in m s^{-2}, multiplied by 10^6). Note that the colourbars are not the same, in order to show the different features more clearly.

low frequency waves force easterly zonal flow in the upstream of the storm tracks and force

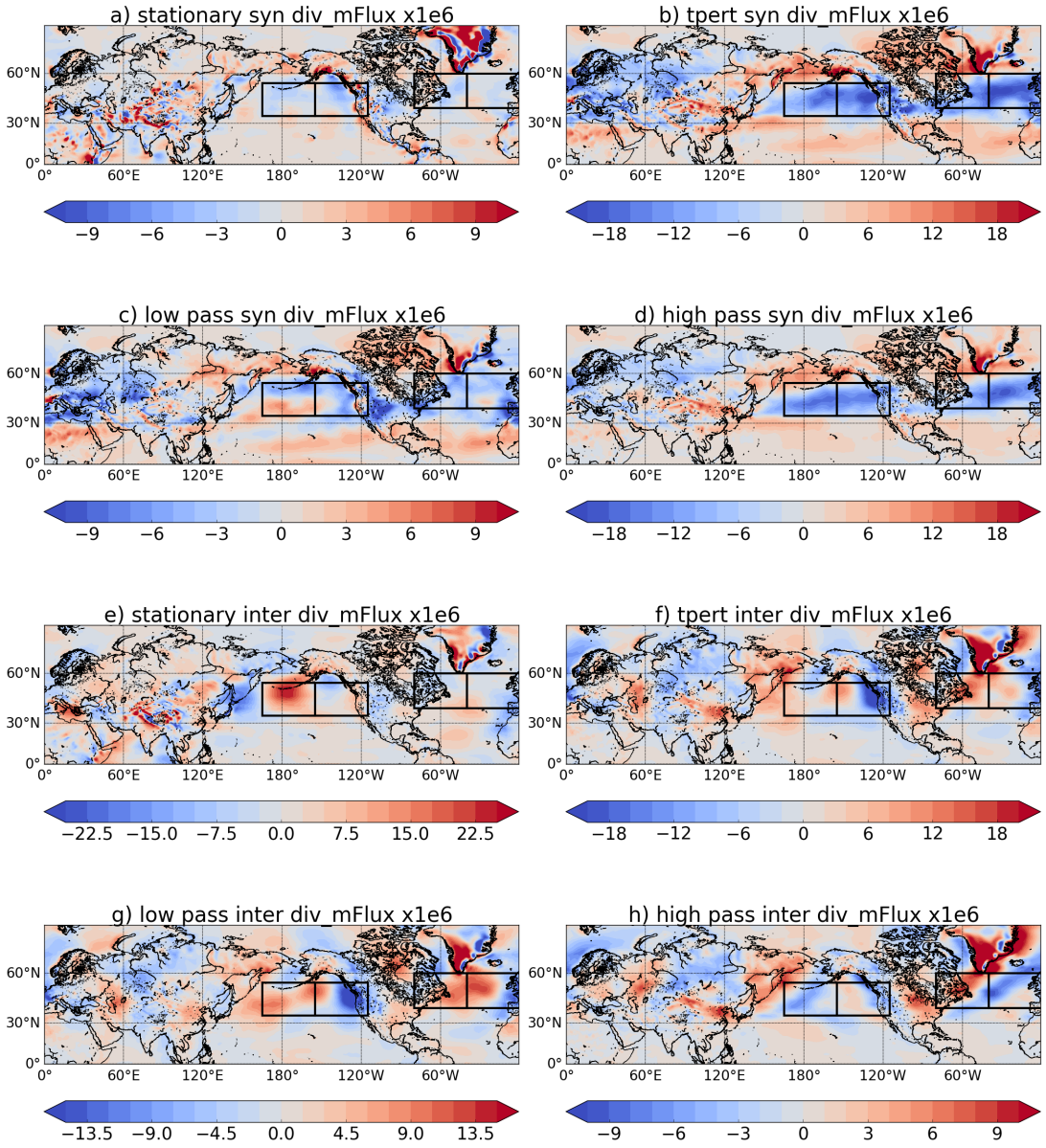

Figure 4.25: As in Fig. 4.24, but for time filtered synoptic momentum flux divergence (a-d), and for time filtered interaction momentum flux divergence (e-h).

westerly zonal flow downstream. The westerly forcing by low frequency planetary and interaction momentum flux divergence is especially evident downstream and over the continent beyond the downstream region (North America in Pacific, Europe in Atlantic) (Figs. 4.24g, 4.25g). Note that the upstream stationary planetary wave forcing (Fig. 4.24e) is in the opposite sense to the upstream low frequency planetary wave forcing (Fig. 4.24g), which stresses the different

behaviour of stationary and low frequency planetary waves; not to mention the interaction between the planetary and synoptic waves, which counteracts the stationary planetary forcing but is similar to the low frequency planetary forcing.

A better understanding of the interplay between planetary and synoptic waves at different timescales is important for wave-forcing of the zonal flow under climate change (Simpson et al., 2014). While both Atlantic and Pacific basins have similar high frequency synoptic wave forcing and low frequency planetary wave forcing, the forcing from the stationary planetary waves and interactions between the synoptic and planetary waves can differ significantly between the two storm tracks (both forcings are much stronger in the Pacific than Atlantic), hence different responses to climate change in the Atlantic and Pacific could be expected. Simpson et al. (2014) have found that the downstream Pacific jet stream will shift equatorwards under climate change, whereas the upstream Pacific and whole Atlantic jet streams would shift polewards. The poleward shift was mainly associated with high frequency transient eddies, whereas the equatorward shift in the Pacific was linked to stationary waves (Simpson et al., 2014). Hence, a better understanding of stationary waves is crucial also for climate change studies (van Niekerk et al., 2017).

4.6 Conclusions

This Chapter has addressed the variability of the baroclinic and barotropic mean flows on different spatial and temporal scales through analyses of cross-spectra, regression analysis and time mean perspective. The interplay of planetary and synoptic waves was studied through the contributions of the planetary, synoptic and interaction heat and momentum fluxes, as well as their transient and stationary components, to the baroclinic (4.1, 4.2, 4.10) and barotropic (4.3, 4.4, 4.11) budgets. The results are summarised below.

The cross-spectrum analysis of the zonal mean flow showed that the zonal mean barotropic flow is influenced by both planetary and synoptic waves at all frequencies for both the SH800 aquaplanet model and for ERA-Interim, consistent with the asymptotic theory. On the other hand, the zonal mean baroclinic flow in the SH800 aquaplanet model revealed a dominant influence from synoptic eddies with minor influence from planetary waves, whereas the baroclinic flow in the ERA-Interim NH revealed influence from both planetary and synoptic waves, with the synoptic eddies dominating for periods longer than 20 days. However no baroclinic feedback with timescales distinguishable from the seasonal cycle was found. While the planetary waves in the

SH800 aquaplanet model seem unimportant from the zonal mean baroclinic budget perspective, they nevertheless significantly contribute to the zonal mean barotropic budget, which reveals an interesting dynamical regime that could be explored in the future. Generally, the planetary waves play a larger role in the barotropic budget than in the baroclinic budget (also locally).

The cross-spectrum analysis of the local variability in barotropic and baroclinic flows revealed that both planetary and synoptic waves matter (if not themselves then through the interaction between the planetary and synoptic waves), with synoptic eddies having a weaker influence downstream of the storm tracks than upstream, whereas for planetary waves the opposite is true (consistent with e.g. Kaspi and Schneider 2011, 2013). Since both planetary and synoptic eddies matter at all frequencies (in the majority of studied cases), associating the transient (high frequency) behaviour with synoptic eddies alone would be misleading. Note also that low and high frequency transients, low-high frequency interactions and transient-stationary interactions all contribute to (especially) the barotropic variability, i.e. transients alone cannot explain the full barotropic variability. The transients, on the other hand, dominate the synoptic variability as well as the baroclinic variability, and the zonal mean budgets.

While the cross-spectra provide a useful tool for assessing the relative importance of synoptic and planetary waves (as well as stationary and transient eddies) for the variability, it is hard to distinguish between separate features, i.e. the transient variability of the synoptic and planetary waves may be coming from the same physical feature (e.g. planetary waves 'steering' synoptic waves or the quasi-stationary and transient planetary wave interactions representing fluctuations of the same physical wave; see Figs. 4.8, 4.7, respectively).

The barotropic variability in the different regions in observations can also be linked to the teleconnection patterns: *(i)* upstream and downstream of the Atlantic storm track are linked to NAO; *(ii)* upstream of the Pacific storm track is linked to WPO and also weakly linked to PNA; and *(iii)* downstream of the Pacific storm track is strongly linked to both EPO and PNA. The links to the teleconnection patterns are evident through the correlations of u or v with teleconnection indices, as well as through the regressions of u and v on the planetary momentum flux convergence in the different regions. That the regressions on the planetary scale momentum fluxes depict these patterns can be expected as planetary waves tend to be zonally oriented and vary on longer timescales.

The barotropic variability in the storm track regions can be further linked to Rossby wave-trains. In the Pacific, the planetary momentum flux divergence was, for example, linked to wave trains coming from northern Eurasia and continuing over northern North America, whereas the

momentum flux divergence due to interactions between the synoptic and planetary waves was linked to a wave train coming from northern Eurasia and continuing equatorwards along the east Pacific coast. Similar wave-trains were found for other studied regions as well. Note that the synoptic momentum flux divergence was generally weaker, in the opposite sense to the other two components, and was linked to more localised wave-trains.

Apart from the variability in the storm track regions, one can also analyse the time mean budget. The time mean barotropic flow in the NH of ERA-Interim exhibits the different forcing of the planetary low frequency and synoptic high frequency flows, consistent with Hoskins et al. (1983): *(i)* westerly barotropic forcing by high frequency synoptic eddies throughout the storm track; *(ii)* easterly barotropic forcing by low frequency planetary waves in the upstream regions of the storm tracks; and *(iii)* westerly barotropic forcing by low frequency planetary waves in the downstream regions of the storm tracks. Note that the interactions between low frequency synoptic and planetary waves had a similar signal to low frequency planetary waves. The time mean barotropic flow also exhibits opposing effects of the stationary planetary wave forcing and the stationary forcing due to interactions between the synoptic and planetary waves, which was especially pronounced in the Pacific (in the region of the Aleutian low). The stationary planetary waves have opposing impacts on the mean flow in the storm track regions compared with the low frequency planetary waves, and dominate the time mean planetary wave forcing of the mean flow.

The asymptotic theory (Chapter 2) suggested weak interactions between the synoptic and planetary waves, however here it is shown that these interactions are very strong and are relevant at all timescales. Hence, further improvements of the theory could be achieved through relaxing the small amplitude approximation for the waves and/or by relaxing the assumption on scale separation between the planetary and synoptic waves in the meridional direction (Dolaptchiev, 2008). See Appendix L for further suggestions. Further understanding of the planetary and synoptic wave interplay is also important for better understanding the jet stream response to climate change (e.g. Simpson et al. 2014, van Niekerk et al. 2017). The above results suggest that both wavenumber decomposition and temporal filtering provide insight into the behaviour of this interplay.

5

Conclusions and Future Work

5.1 Conclusions

This thesis addressed the role of the planetary and synoptic waves for baroclinic and barotropic processes and their forcing of the zonal mean flow. The analysis included: *(i)* a theoretical framework for planetary and synoptic wave-mean flow interaction using multiscale asymptotic methods (Chapter 2); *(ii)* a baroclinic and barotropic annular mode framework within an idealised zonally homogeneous model as well as SH reanalysis (Chapter 3); and *(iii)* a framework of planetary and synoptic wave forcing of the baroclinic and barotropic mean flows on various temporal and spatial scales (Chapter 4). This section concludes the thesis with a summary of the previous chapters as well as suggestions for future work.

In Chapter 2 a multiscale asymptotic theory for the planetary and synoptic wave interaction with the zonal mean flow was derived for the first time. The theory includes wave activity equations for planetary and synoptic waves, the baroclinic and barotropic equations for the zonal mean flow, angular momentum conservation, and the non-acceleration theorem. The equations take a form of planetary geostrophy for the planetary waves and of quasi-geostrophy for the synoptic waves, with the background PV gradient resembling that of planetary geostrophy as well, implying the importance of baroclinic processes for eddy generation. The theory has further shown that under synoptic scale averaging (within the assumptions used) the planetary scale waves and diabatic and frictional processes link the baroclinic and barotropic processes, and that the planetary and synoptic waves interact via the source-sink terms or the zonal mean flow to leading order. When the planetary scale waves are weak (in a zonally homogeneous framework),

the baroclinic and barotropic processes can be decoupled with the eddy heat fluxes forcing wave activity and the eddy momentum fluxes forcing the zonal mean barotropic flow, whereas the baroclinic flow is mainly diabatically driven (again under the synoptic scale average).

As the decoupling of the baroclinic and barotropic processes implied in Chapter 2 is consistent with the decoupling of the baroclinic and barotropic annular modes (Thompson and Woodworth, 2014), Chapter 3 explored this counterintuitive result using different annular modes of variability in a model with different climatologies as well as in SH observations. This revealed three different timescales of variability: *(i)* a synoptic timescale with baroclinic life cycles (midlatitude storms grow via eddy heat fluxes and decay via eddy momentum fluxes, which leads to zonal mean flow acceleration; i.e. the baroclinic and barotropic processes are linked [Simmons and Hoskins 1978]); *(ii)* an intermediate timescale where the baroclinic and barotropic annular modes are decoupled (baroclinic processes are linked to eddy heat fluxes only, as in a baroclinic oscillator model [Thompson and Barnes 2014], whereas barotropic processes are linked to eddy momentum fluxes only, as in barotropic dynamics [Vallis et al. 2004]); and *(iii)* a quasi-steady limit with the positive baroclinic feedback mechanism (baroclinic zones with storm tracks move with jet shifts, again linking the baroclinic and barotropic processes [Robinson 2000]). This means that the decoupling, which is robust to different model climatologies, can occur, but is frequency dependent. This analysis also revealed that monopolar (BAM1) and tripolar (SAM2, BAM3) modes of variability and their coupling as well as BAM1's timescale depend on the model climatology, which could have implications for climate studies.

Chapter 4 extended the analysis of the theoretical framework (Chapter 2) to the baroclinic mean flow as well as to the zonally inhomogeneous framework where planetary scale waves are explicitly represented. The relative importance of planetary and synoptic waves in forcing the baroclinic and barotropic mean flows was tested in an aquaplanet model with forced planetary waves as well as in NH observations. This analysis revealed that the baroclinic zonal mean flow in the aquaplanet model is dominated by the synoptic scale heat fluxes, whereas in the NH observations both planetary and synoptic waves contribute to the baroclinic variability (except for timescales longer than 20 days). On the other hand, the zonal mean barotropic flow is affected by both planetary and synoptic momentum fluxes in both the aquaplanet model and NH observations. Note that the barotropic and baroclinic zonal mean variability is dominated by transient waves.

A local perspective for different storm tracks (North Atlantic, North Pacific and model storm tracks) revealed that both synoptic and planetary waves as well as their interactions are

important for the variability in the mean flows. The planetary waves contributed significantly especially in the downstream regions of storm tracks. The planetary wave interactions with the synoptic eddies are dominated by the stationary-transient interactions, the planetary waves are linked to both transient and stationary-transient interactions, whereas the synoptic eddies are predominantly transient. The planetary scale momentum fluxes were then further linked to the barotropic mean flow that is associated with teleconnection patterns (NAO, WPO, EPO, PNA) and with Rossby wave trains, where the planetary-synoptic scale interactions also played an important role.

The time mean barotropic flow revealed strong stationary planetary scale forcing of the mean flow in the regions of the Aleutian and Icelandic lows, which was balanced by the forcing from stationary planetary-synoptic scale interactions. The transient synoptic eddies act to accelerate the zonal flow throughout the storm track regions, whereas the low frequency planetary waves act to decelerate the flow in the upstream regions of the storm tracks and to accelerate it downstream, consistent with Hoskins et al. (1983). Chapter 4 therefore shows that direct planetary-synoptic scale interactions are important for driving the baroclinic and barotropic mean flows and hence a different theoretical framework to Chapter 2 should be considered in this case (e.g. Appendix L).

Overall this study showed that the theory (Chapter 2) can explain the decoupling between the baroclinic and barotropic flows (Chapter 3), but further theoretical frameworks should be developed for cases where the planetary and synoptic waves exhibit strong interactions (Chapter 4), which then force the mean flow. This analysis also showed that both planetary and synoptic waves matter for the baroclinic and barotropic variability on various timescales, hence neither should be neglected in zonally inhomogeneous frameworks.

5.2 Future Work

This thesis has addressed planetary and synoptic wave-mean flow interaction and the baroclinic and barotropic processes related to it. However, many questions also arise from this thesis and are hence suggested for future work in this field.

Chapter 2 derived leading order wave activity and mean flow equations for small amplitude isotropic waves in the presence of a zonal mean flow. Further extension of this theory to higher order approximations would help in closing the non-acceleration theorem for the barotropic

mean flow (Appendix D) as well as provide a framework for direct interactions of the planetary and synoptic waves that was absent at the leading order.

The theory of Chapter 2 for the zonally homogeneous case and under synoptic scale averaging predicted a relationship between the wave activity and eddy heat fluxes (vertical EP flux) only, suggesting a decoupling of the baroclinic eddy and barotropic mean flow dynamics. However, in Chapter 3 eddy kinetic energy was used as a proxy for wave activity [to test Thompson and Woodworth (2014)'s BAM1], which showed a decoupling of the baroclinic and barotropic modes of variability at intermediate timescales, but the relationship between eddy heat fluxes and wave activity would be more defensible (less approximations necessary than for the EKE budget), and could be tested in the future.

While Chapter 3 analysed an idealised EKE budget (EKE and heat flux relationship only), further insight into the EKE variability at different timescales can be gained by analysing the full EKE budget, i.e. without approximations. This can be achieved by replacing the empirical parameter α_{EKE} by the terms multiplying the eddy heat flux in EKE budget as well as by adding the momentum flux (and EKE flux) terms, which would strengthen the results of Chapter 3.

The baroclinic variability between the EKE and heat flux and its decoupling from the barotropic variability was robust to different model climatologies and was present in the SH reanalysis as well (Chapter 3). As the timescale of BAM1 (which is related to this decoupling) is about 30 days and EKE at those timescales has an empirical relationship with eddy heat fluxes, there could be implications for subseasonal predictability of eddy activity and associated impacts (e.g. precipitation related to storms) in the SH.

While the decoupling (above) is robust to different settings, the relationships between the monopolar and tripolar modes of variability as well as BAM1's timescale are dependent on the model configuration (Chapter 3). In the idealised model, the largest difference was between the winter hemisphere (with strong polar vortex and jet stream located further poleward) and the other configurations. This could imply that there is a stratospheric influence on the tropospheric pulsating modes of variability, or that a poleward shift of the jet stream and eddy activity (as in the seasonal cycle or under climate change, e.g. Wang et al. 2018) could lead to a change (increase) in the timescale of BAM1 or to a change in its links to barotropic modes, which could be explored further (e.g. via hierarchies of models).

Further insight can also be gained for the local storm track dynamics (Chapter 4), which was explored over limited regions for various scales of waves and their interactions, but the type of interactions necessary to account for the variability found in the storm track regions was

not explored (only examples were provided). It would be interesting to see whether the waves of different wavenumbers are propagating eastwards, westwards or are stationary in the storm track regions, which can be achieved by computing phase speeds of waves, further elucidating the type of interactions present. A comparison of transient and full flux covariability with the mean flow has already provided some insight into the planetary-synoptic scale interactions that are largely related to stationary-transient interactions, but further work is necessary.

Chapter 4 provided insight into the variability in the storm track regions and related it to particular waves, however to link the eddy momentum or heat fluxes to the variability of a single storm (or a composite of them) one would need to track the storms (e.g. Hoskins and Hodges 2002) and test which waves contribute to the variability for a particular storm in its upstream and downstream development.

The theory (Chapter 2) provided a framework for explaining the decoupling of the baroclinic and barotropic dynamics (Chapter 3), however Chapter 4 has shown that the direct interactions between the planetary and synoptic waves can be large, especially locally, which is inconsistent with the theory's prediction of weak coupling between the planetary and synoptic waves. The theoretical framework should therefore be extended to a case where the meridional scale separation is relaxed or to a finite amplitude approximation, allowing for synoptic and planetary waves to directly interact. Suggestions for such cases are provided in Appendix L, which include a finite amplitude version of the theory from Chapter 2, and the so-called anisotropic finite and small amplitude cases where the meridional scale separation is relaxed. The examples provided in Appendix L include partial theories only (wave activity equations for eddies only), hence further derivations of the mean flow dynamics as well as the links between the eddies and the mean flow (e.g. TEM or non-acceleration theorem) are necessary to complete those theories. Note that these and other regimes were also discussed in Dolaptchiev (2008).

While Chapter 4 discussed the baroclinic and barotropic mean flows and their forcing via heat and momentum fluxes from planetary and synoptic waves, it has not discussed the local (storm track) variability in EKE or wave activity, which are also a part of the theory (Chapter 2). Therefore, the analysis of Chapter 4 could be extended to the local planetary and synoptic wave activity theory (e.g. Huang and Nakamura 2017).

Appendix A

The Multiscale Asymptotic Version of the Primitive Equations

Using the assumptions from section 2.2.2 the momentum, thermodynamic, continuity, hydrostatic and thermal wind balance equations at different orders ($\mathcal{O}(i)$) can be derived following DK09, DK13.

Hydrostatic balance

The hydrostatic balance for density and pressure up to the 4^{th} order is:

$$\rho^{(i)} = -\frac{\partial p^{(i)}}{\partial z} \quad ; \quad i = 0, ..., 4. \tag{A.1}$$

By using this hydrostatic balance (A.1), ideal gas law (2.1f) and the assumption for θ-expansion (2.3), it can be shown that $p^{(0)}(z) = \exp(-z)$ and $p^{(1)} = 0$ [for details of the derivation see DK09, equations (37)-(46)]. Via (A.1) follows that the expressions for density are the same as for pressure for these two orders: $\rho^{(0)}(z) = \exp(-z)$ and $\rho^{(1)} = 0$.

Similarly, there is also a relationship between p and θ via (2.1f) and (A.1) as also defined in (47) in DK09:

$$\frac{\partial \pi^{(i)}}{\partial z} = \theta^{(i)} \quad ; \quad i = 2, 3, 4 \tag{A.2}$$

where $\pi^{(i)} = p^{(i)}/\rho^{(0)}$. This identity at the fourth order only holds if $\frac{\partial}{a\partial\phi_s}$ of θ is taken (and this relationship will only be used in this case).

Using (A.2) and (A.1) one gets a relationship between ρ, p and θ:

$$\rho^{(i)} = p^{(i)} - \rho^{(0)}\theta^{(i)} \quad ; \quad i = 2, 3 \tag{A.3}$$

where recall that $\rho^{(0)} = \exp(-z)$ and $\rho^{(1)} = 0$.

Momentum equations

Below is the list of all momentum equations up to 5th order. Note that we derive the PV and wave activity equations from the 3rd order momentum equation, and we obtain a barotropic equation for the mean flow from the 5th order momentum equation.

$\mathcal{O}(\varepsilon^1)$ - geostrophic balance for zonal mean wind:

$$f\mathbf{e}_r \times \mathbf{u}^{(0)} = f\mathbf{e}_r \times \mathbf{u}_m^{(0)} = -\nabla_p \pi^{(2)} = -\frac{\partial}{\partial y_p}\pi^{(2)}\mathbf{e}_\phi \tag{A.4}$$

where subscript m refers to the mean flow - $\mathbf{u}^{(0)}$ is related to the zonal mean zonal velocity. Note that $v^{(0)} = 0$.

$\mathcal{O}(\varepsilon^2)$ - geostrophic balance for 1st order wind (planetary and synoptic scale perturbations to zonal mean):

$$f\mathbf{e}_r \times \mathbf{u}^{(1)} = -\left(\nabla_p \pi^{(3)} + \nabla_s \pi^{(4)}\right) \tag{A.5}$$

where $\mathbf{u}^{(1)} = \mathbf{u}_p^{(1)} + \mathbf{u}_s^{(1)}$ (with subscripts p and s referring to planetary and synoptic waves, respectively), such that $f\mathbf{e}_r \times \mathbf{u}_p^{(1)} = -\nabla_p \pi^{(3)}$ and $f\mathbf{e}_r \times \mathbf{u}_s^{(1)} = -\nabla_s \pi^{(4)}$.

$\mathcal{O}(\varepsilon^3)$ - the first order that includes a time derivative, used to derive PV equations:

$$\frac{\partial \mathbf{u}^{(1)}}{\partial t_s} + \mathbf{u}^{(0)} \cdot \nabla_s \mathbf{u}^{(1)} + f\mathbf{e}_r \times \mathbf{u}^{(2)} + \mathbf{e}_\phi \frac{u^{(0)} u^{(0)} \tan\phi_p}{a} = -\nabla_p \pi^{(4)} + \frac{\rho^{(2)}}{\rho^{(0)}} \nabla_p \pi^{(2)} - \nabla_s \pi^{(5)} + \mathbf{S}_u^{(3)} \tag{A.6}$$

$\mathcal{O}(\varepsilon^4)$ - we require only the u-momentum equation:

$$\frac{\partial u^{(2)}}{\partial t_s} + \frac{\partial u^{(1)}}{\partial t_p} + \mathbf{u}^{(1)} \cdot \nabla_s u^{(1)} + \frac{\partial}{\partial \tilde{x}_s}\left(u^{(0)}u^{(2)}\right) + \frac{\partial}{\partial \tilde{x}_p}\left(u^{(0)}u^{(1)}\right) + v^{(1)}\frac{\partial}{\partial y_p}u^{(0)} + w^{(4)}\frac{\partial}{\partial z}u^{(0)} - fv^{(3)} - \frac{u^{(0)}v^{(1)}\tan\phi_p}{a} = -\frac{\partial}{\partial x_p}\pi^{(5)} + \frac{\partial}{\partial x_p}\left(\frac{\rho^{(2)}}{\rho^{(0)}}\pi^{(3)}\right) - \frac{\partial}{\partial x_s}\pi^{(6)} + \frac{\partial}{\partial x_s}\left(\frac{\rho^{(2)}}{\rho^{(0)}}\pi^{(4)}\right) + S_u^{(4)} \tag{A.7}$$

$\mathcal{O}(\varepsilon^5)$ - again we require only the u-momentum equation, used to derive the barotropic pressure equation (equation for the zonal mean zonal flow):

$$\frac{\partial u^{(0)}}{\partial t_m} + \frac{\partial u^{(3)}}{\partial t_s} + \frac{\partial u^{(2)}}{\partial t_p} + \mathbf{u}^{(1)} \cdot \nabla_s u^{(2)} + \mathbf{u}^{(2)} \cdot \nabla_s u^{(1)} + \frac{\partial}{\partial \tilde{x}_s}\left(u^{(0)}u^{(3)}\right) + \frac{\partial}{\partial \tilde{x}_p}\left(u^{(0)}u^{(2)}\right) + \mathbf{u}^{(1)} \cdot \nabla_p u^{(1)} + v^{(2)}\frac{\partial}{\partial y_p}u^{(0)} + w^{(4)}\frac{\partial}{\partial z}u^{(1)} + w^{(5)}\frac{\partial}{\partial z}u^{(0)} - fv^{(4)} - \frac{u^{(0)}v^{(2)}\tan\phi_p}{a} - \frac{u^{(1)}v^{(1)}\tan\phi_p}{a} + w^{(4)}\cos\phi_p = -\frac{\partial}{\partial x_p}\pi^{(6)} + \frac{\partial}{\partial x_p}\left(\frac{\rho^{(2)}}{\rho^{(0)}}\pi^{(4)}\right) + \frac{\rho^{(3)}}{\rho^{(0)}}\frac{\partial}{\partial x_p}\pi^{(3)} - \frac{\partial}{\partial x_s}\pi^{(7)} + \frac{\partial}{\partial x_s}\left(\frac{\rho^{(2)}}{\rho^{(0)}}\pi^{(5)}\right) + \frac{\partial}{\partial x_s}\left(\frac{\rho^{(3)}}{\rho^{(0)}}\pi^{(4)}\right) + S_u^{(5)} \tag{A.8}$$

where in all equations $\frac{\partial}{\partial y_{p,s}} = \frac{1}{a}\frac{\partial}{\partial \phi_{p,s}}$, $\frac{\partial}{\partial \tilde{y}_{p,s}} = \frac{1}{a\cos\phi_p}\frac{\partial \cos\phi_p}{\partial \phi_{p,s}}$, $\frac{\partial}{\partial \tilde{x}_{p,s}} = \frac{\partial}{\partial x_{p,s}} = \frac{1}{a\cos\phi_p}\frac{\partial}{\partial \lambda_{p,s}}$, ∇_p and ∇_s are the horizontal gradients in a spherical coordinate system (with the above x and y coordinates, tilde is used when ∇ is used as curl or divergence), and $\mathbf{e}_\phi$ and $\mathbf{e}_r$ are the unit vectors in the latitudinal and vertical directions respectively. Here $\mathbf{S}_u^{(i)}$ represent frictional processes at different orders (with no specific assumptions imposed). The vertical velocities $w^{(i=0,1,2,3)}$ are not present in the above equations as the continuity (A.13) and thermodynamic (A.10) budgets below imply that $w^{(i=0,1,2,3)} = 0$.

Thermal wind balance

Using (A.5) and (A.2):

$$\frac{\partial}{\partial z}u^{(0)} = -\frac{1}{f}\frac{\partial\theta^{(2)}}{\partial y_p}, \tag{A.9a}$$

$$\frac{\partial}{\partial z}\mathbf{u}^{(1)} = \frac{1}{f}\mathbf{e}_r \times \left(\nabla_p\theta^{(3)} + \nabla_s\theta^{(4)}\right). \tag{A.9b}$$

Thermodynamic (θ) equations

Below is the list of all needed thermodynamic equations. Note that all orders below $\mathcal{O}(\varepsilon^5)$ give nothing [and $w^{(i=0,1,2)} = 0$ via (A.13)], thus the first order that appears below is $\mathcal{O}(\varepsilon^5)$.

$\mathcal{O}(\varepsilon^5)$:

$$w^{(3)} = \frac{S_\theta^{(5)}}{\partial\theta^{(2)}/\partial z} = 0 \tag{A.10}$$

$\mathcal{O}(\varepsilon^6)$:

$$\frac{\partial\theta^{(3)}}{\partial t_p} + \frac{\partial\theta^{(4)}}{\partial t_s} + \frac{\partial}{\partial\tilde{x}_p}\left(u^{(0)}\theta^{(3)}\right) + \frac{\partial}{\partial\tilde{x}_s}\left(u^{(0)}\theta^{(4)}\right) + v^{(1)}\frac{\partial\theta^{(2)}}{\partial y_p} + w^{(4)}\frac{\partial\theta^{(2)}}{\partial z} = S_\theta^{(6)} \tag{A.11}$$

$\mathcal{O}(\varepsilon^7)$:

$$\begin{aligned}\frac{\partial\theta^{(4)}}{\partial t_p} + \frac{\partial\theta^{(5)}}{\partial t_s} + \frac{\partial\theta^{(2)}}{\partial t_m} + \frac{\partial}{\partial\tilde{x}_p}\left(u^{(0)}\theta^{(4)}\right) + \mathbf{u}^{(1)}\cdot\nabla_p\theta^{(3)} + \mathbf{u}^{(1)}\cdot\nabla_s\theta^{(4)} \\ + \frac{\partial}{\partial\tilde{x}_s}\left(u^{(0)}\theta^{(5)}\right) + v^{(2)}\frac{\partial\theta^{(2)}}{\partial y_p} + w^{(4)}\frac{\partial\theta^{(3)}}{\partial z} + w^{(5)}\frac{\partial\theta^{(2)}}{\partial z} = S_\theta^{(7)}\end{aligned} \tag{A.12}$$

Continuity equations

This is the set of all continuity equations (also the trivial ones as they give us information about vertical velocities).

$\mathcal{O}(\varepsilon^0)$, $\mathcal{O}(\varepsilon^1)$ & $\mathcal{O}(\varepsilon^2)$:

$$\frac{\partial\rho^{(0)}w^{(i)}}{\partial z} = 0 \quad ; \quad i = 0,1,2 \tag{A.13}$$

Since $\rho^{(0)} = \exp(-z)$ and $\rho^{(1)} = 0$ (as mentioned above), $w^{(i)}$ can either be $\exp(z)$ or 0. The former is unphysical, hence the latter is chosen, i.e. $w^{(i)} = 0$ for $i = 0, 1, 2$.

$\mathcal{O}(\varepsilon^3)$ (here note that $w^{(3)} = 0$ from the thermodynamic equation (A.10) and that $\nabla_s \cdot \mathbf{u}^{(1)} = 0$ by definition):

$$\nabla_p \cdot \mathbf{u}^{(0)} = 0 \tag{A.14}$$

$\mathcal{O}(\varepsilon^4)$:

$$\nabla_p \cdot \left(\mathbf{u}^{(1)}\rho^{(0)}\right) + \nabla_s \cdot \left(\mathbf{u}^{(2)}\rho^{(0)}\right) + \frac{\partial}{\partial z}\left(w^{(4)}\rho^{(0)}\right) = 0 \tag{A.15}$$

$\mathcal{O}(\varepsilon^5)$:

$$\nabla_p \cdot \left(\mathbf{u}^{(2)}\rho^{(0)}\right) + \nabla_s \cdot \left(\mathbf{u}^{(3)}\rho^{(0)}\right) + \frac{\partial}{\partial z}\left(w^{(5)}\rho^{(0)}\right) = 0 \tag{A.16}$$

$\mathcal{O}(\varepsilon^6)$:

$$\begin{aligned} \frac{\partial \rho^{(3)}}{\partial t_p} + \frac{\partial \rho^{(4)}}{\partial t_s} + \nabla_p \cdot \left(\mathbf{u}^{(3)}\rho^{(0)} + \mathbf{u}^{(1)}\rho^{(2)} + \mathbf{u}^{(0)}\rho^{(3)}\right) + \\ \nabla_s \cdot \left(\mathbf{u}^{(4)}\rho^{(0)} + \mathbf{u}^{(2)}\rho^{(2)} + \mathbf{u}^{(0)}\rho^{(4)} - \mathbf{u}^{(1)}\rho^{(0)}\frac{z}{a}\right) + \frac{\partial}{\partial z}\left(w^{(4)}\rho^{(2)} + w^{(6)}\rho^{(0)}\right) = 0 \end{aligned} \tag{A.17}$$

$\mathcal{O}(\varepsilon^7)$:

$$\begin{aligned} \frac{\partial \rho^{(2)}}{\partial t_m} + \frac{\partial \rho^{(4)}}{\partial t_p} + \frac{\partial \rho^{(5)}}{\partial t_s} + \nabla_p \cdot \left(\mathbf{u}^{(4)}\rho^{(0)} + \mathbf{u}^{(2)}\rho^{(2)} + \mathbf{u}^{(1)}\rho^{(3)} + \mathbf{u}^{(0)}\rho^{(4)} - \mathbf{u}^{(1)}\rho^{(0)}\frac{z}{a}\right) \\ + \nabla_s \cdot \left(\mathbf{u}^{(5)}\rho^{(0)} + \mathbf{u}^{(3)}\rho^{(2)} + \mathbf{u}^{(2)}\rho^{(3)} + \mathbf{u}^{(1)}\rho^{(4)} + \mathbf{u}^{(0)}\rho^{(5)} - \mathbf{u}^{(2)}\rho^{(0)}\frac{z}{a}\right) \\ + \frac{\partial}{\partial z}\left(w^{(4)}\rho^{(3)} + w^{(5)}\rho^{(2)} + w^{(7)}\rho^{(0)}\right) = 0 \end{aligned} \tag{A.18}$$

where terms with z/a come from corrections to the shallow-atmosphere approximation at higher orders. Note that these terms vanish in the zonal mean and/or synoptic scale average.

Vorticity Equation

To derive the vorticity equation, take $\nabla_s \times \mathcal{O}(\varepsilon^3)$ momentum equation (A.6), and note that terms with $\nabla_s \times \nabla_s$ and synoptic scale derivatives of terms (π, ρ, θ) that do not depend on

synoptic scales (up to 3^{rd} order) are zero. This yields (following DK13):

$$\frac{\partial}{\partial t_s}\boldsymbol{\zeta}^{(1)} + \nabla_s \times \left(\mathbf{u}^{(0)} \cdot \nabla_s \mathbf{u}^{(1)}\right) + \nabla_s \times \left(f\mathbf{e}_r \times \mathbf{u}^{(2)}\right) = -\nabla_s \times \nabla_p \pi^{(4)} + \nabla_s \times \mathbf{S}_u^{(3)} \qquad \text{(A.19)}$$

where $\nabla_s = \left((a\cos\phi_p)^{-1}\partial/\partial\lambda_s, a^{-1}\partial/\partial\phi_s\right)$, $\nabla_p = \left((a\cos\phi_p)^{-1}\partial/\partial\lambda_p, a^{-1}\partial/\partial\phi_p\right)$, the numbers in superscripts denote orders of variables, $\mathbf{u} = (u, v)$ is horizontal velocity, $\pi = p/\rho$, $\boldsymbol{\zeta}^{(1)} = \nabla_s \times \mathbf{u}^{(1)}$ is relative vorticity, and as ∇_s and $\mathbf{u}^{(1)}$ have only horizontal components $\boldsymbol{\zeta}^{(1)} = \zeta^{(1)}\mathbf{e}_r$. The source term $S_u^{(3)}$ represents frictional processes. Note that $\nabla_s \times \nabla_p \pi^{(4)} = (0, 0, \nabla_p \cdot (f\mathbf{u}_s^{(1)}))$. Taking $\mathbf{e}_r \cdot$ of (A.19) and applying the vector identities as in DK09 and DK13, we get:

$$\frac{\partial}{\partial t_s}\zeta^{(1)} + \mathbf{u}^{(0)} \cdot \nabla_s \zeta^{(1)} + f\nabla_s \cdot \mathbf{u}^{(2)} = -\nabla_p \cdot (f\mathbf{u}_s^{(1)}) + \mathbf{e}_r \cdot \nabla_s \times \mathbf{S}_u^{(3)} \qquad \text{(A.20)}$$

where $S_\zeta = \mathbf{e}_r \cdot \nabla_s \times \mathbf{S}_u^{(3)}$ and $\nabla_p \cdot (f\mathbf{u}^{(1)}) = f\nabla_p \cdot \mathbf{u}^{(1)} + v^{(1)}\cos\phi_p/a$ with $a^{-1}\cos\phi_p = a^{-1}\partial f/\partial\phi_p = \beta$. Since $\mathbf{u}^{(2)}$ is not known, we use the $\mathcal{O}(\varepsilon^4)$ continuity equation (A.15) to obtain the vorticity equation:

$$\frac{\partial}{\partial t_s}\zeta^{(1)} + \mathbf{u}^{(0)} \cdot \nabla_s \zeta^{(1)} - \frac{f}{\rho^{(0)}}\frac{\partial}{\partial z}\left(\rho^{(0)} w^{(4)}\right) + \beta v^{(1)} = S_\zeta \qquad \text{(A.21)}$$

where $w^{(4)}$ is known from the $\mathcal{O}(\varepsilon^6)$ thermodynamic equation (A.11), which can be used to derive the potential vorticity equation. This vorticity equation resembles the QG vorticity equation (e.g. Holton 2004), but now there are different scales represented in the equation.

Appendix B

Derivation of the Mean Flow Equations

B.1 Barotropic equation

This section shows the steps in deriving the barotropic pressure equation - combining the correct thermodynamic, hydrostatic, thermal wind, momentum and continuity equations (see Appendix A) with the $\mathcal{O}(\varepsilon^5)$ momentum equation (A.8) averaged over t_s, λ_s, ϕ_s, t_p, λ_p, z (denoted with overline). Note that the vertical mean assumes $w = 0$ at the top and bottom boundaries. This section modifies the momentum (A.8) and thermodynamic (A.12) equations, which can then be used to derive the barotropic equations in section 2.4.2 (following DK13).

First average the flux forms of all equations mentioned:

Momentum Equations at $\mathcal{O}(\varepsilon^3)$, $\mathcal{O}(\varepsilon^4)$, $\mathcal{O}(\varepsilon^5)$:

$$\overline{v^{(2)}} = -\frac{\overline{S_u^{(3)}}^{s,p,z}}{f}, \tag{B.1a}$$

$$\overline{v^{(3)}} = -\frac{\overline{S_u^{(4)}}^{s,p,z}}{f}, \tag{B.1b}$$

$$\frac{\partial \overline{u^{(0)}\rho^{(0)}}^{s,p,z}}{\partial t_m} + \frac{\partial}{\partial \tilde{y}_p}\left(\overline{v^{(1)}u^{(1)}\rho^{(0)}}^{s,p,z} + \overline{v^{(2)}u^{(0)}\rho^{(0)}}^{s,p,z}\right)$$
$$-\frac{\tan\phi_p}{a}\left(\overline{v^{(1)}u^{(1)}\rho^{(0)}}^{s,p,z} + \overline{v^{(2)}u^{(0)}\rho^{(0)}}^{s,p,z}\right) - \overline{\rho^{(0)}v^{(4)}f}^{s,p,z}$$
$$+\rho^{(0)}\overline{w^{(4)}}^{s,p,z}\cos\phi_p = \overline{\rho^{(3)}\frac{\partial \pi^{(3)}}{\partial x_p}}^{s,p,z} + \overline{\rho^{(0)}S_u^{(5)}}^{s,p,z}. \tag{B.1c}$$

Continuity equations at $\mathcal{O}(\varepsilon^4)$, $\mathcal{O}(\varepsilon^5)$, $\mathcal{O}(\varepsilon^6)$, $\mathcal{O}(\varepsilon^7)$:

$$\frac{\partial}{\partial \tilde{y}_p}\left(\overline{v^{(1)}\rho^{(0)}}^{s,p,z}\right) = 0, \tag{B.2a}$$

$$\frac{\partial}{\partial \tilde{y}_p}\left(\overline{v^{(2)}\rho^{(0)}}^{s,p,z}\right) = 0, \tag{B.2b}$$

$$\frac{\partial}{\partial \tilde{y}_p}\left(\overline{v^{(3)}\rho^{(0)}}^{s,p,z}\right) = 0, \tag{B.2c}$$

$$\frac{\partial \overline{\rho^{(2)}}^{s,p,z}}{\partial t_m} + \frac{\partial}{\partial \tilde{y}_p}\left(\overline{v_p^{(1)}\rho^{(3)}}^{s,p,z} + \overline{v^{(2)}\rho^{(2)}}^{s,p,z} + \overline{v^{(4)}\rho^{(0)}}^{s,p,z}\right) = 0. \tag{B.2d}$$

Thermodynamic equations at $\mathcal{O}(\varepsilon^6)$, $\mathcal{O}(\varepsilon^7)$:

$$\overline{w^{(4)}}^{s,p,z} = \frac{\overline{S_\theta^{(6)}}^{s,p,z}}{\partial\theta^{(2)}/\partial z}, \tag{B.3a}$$

$$\frac{\partial \overline{\rho^{(0)}\theta^{(2)}}^{s,p,z}}{\partial t_m} + \frac{\partial}{\partial \tilde{y}_p}\left(\overline{v_p^{(1)}\rho^{(0)}\theta^{(3)}}^{s,p,z} + \overline{v^{(2)}\rho^{(0)}\theta^{(2)}}^{s,p,z}\right) = \overline{S_\theta^{(7)}\rho^{(0)}}^{s,p,z}. \tag{B.3b}$$

Hydrostatic balance at $\mathcal{O}(\varepsilon^2)$

$$\overline{\rho^{(2)}}^{s,p,z} = -\overline{\rho^{(0)}\theta^{(2)}}^{s,p,z} + \overline{p^{(2)}}^{s,p,z}. \tag{B.4}$$

Equations (B.1a,B.1b) show that $\overline{v^{(2)}}^{s,p,z}$ and $\overline{v^{(3)}}^{s,p,z}$ are related to source-sink terms, thus in the equations below they will be replaced by them. Note that $\rho^{(3)}\partial\pi^{(3)}/\partial x_p = f\rho^{(3)}v_p^{(1)}$ (via (A.5)). Taking the hydrostatic balance equation (B.4), using it to substitute $\rho^{(2)}$ in the continuity equation (B.2d) and matching the $\partial\overline{\rho^{(0)}\theta^{(2)}}^{s,p,z}/\partial t_m$ term in the thermodynamic equation (B.3b)

yields

$$\frac{\partial \overline{p^{(2)}}^{s,p,z}}{\partial t_m} + \frac{\partial}{\partial \tilde{y}_p}\left(\overline{v_p^{(1)}\rho^{(0)}\theta^{(3)}}^{s,p,z} + \overline{v_p^{(1)}\rho^{(3)}}^{s,p,z} + \overline{v^{(4)}\rho^{(0)}}^{s,p,z}\right) = \overline{\rho^{(0)}S_\theta^{(7)}}^{s,p,z} + \frac{\partial}{\partial \tilde{y}_p}\left(\overline{\left(\rho^{(2)} + \rho^{(0)}\theta^{(2)}\right)\frac{S_u^{(3)}}{f}}^{s,p,z}\right). \tag{B.5}$$

Rewriting the momentum equation then gives:

$$\begin{aligned}\frac{1}{f}\frac{\partial \overline{u^{(0)}\rho^{(0)}}^{s,p,z}}{\partial t_m} + \frac{1}{f}\frac{\partial}{\partial \tilde{y}_p}\left(\overline{v^{(1)}u^{(1)}\rho^{(0)}}^{s,p,z}\right) - \frac{1}{f}\frac{\tan\phi_p}{a}\left(\overline{v^{(1)}u^{(1)}\rho^{(0)}}^{s,p,z}\right) \\ -\overline{\rho^{(0)}v^{(4)}}^{s,p,z} - \overline{\rho^{(3)}v_p^{(1)}}^{s,p,z} = \frac{1}{f}\overline{\rho^{(0)}S_u^{(5)}}^{s,p,z} + \frac{1}{f}\frac{\partial}{\partial \tilde{y}_p}\left(\overline{\frac{S_u^{(3)}}{f}u^{(0)}\rho^{(0)}}^{s,p,z}\right) \\ -\frac{1}{f}\frac{\tan\phi_p}{a}\left(\overline{\frac{S_u^{(3)}}{f}u^{(0)}\rho^{(0)}}^{s,p,z}\right) - \frac{\rho^{(0)}\overline{S_\theta^{(6)}}^{s,p,z}\cos\phi_p}{f\partial\theta^{(2)}/\partial z}.\end{aligned} \tag{B.6}$$

The latter two equations are then used in section 2.4.2 to derive the barotropic pressure equation (2.17) or (2.18).

B.2 Baroclinic equation

This section shows the steps in deriving the baroclinic mean flow equation, which is derived through the $\mathcal{O}(\varepsilon^7)$ thermodynamic equation (A.12) using the continuity and momentum equations averaged over t_s, λ_s, t_p, λ_p (denoted with an overbar). The averaged equations are:

Thermodynamic equations at $\mathcal{O}(\varepsilon^6)$, $\mathcal{O}(\varepsilon^7)$:

$$\overline{w^{(4)}}^{t_s,\lambda_s,p} = \frac{\overline{S_\theta^{(6)}}^{t_s,\lambda_s,p}}{\partial\theta^{(2)}/\partial z}, \tag{B.7a}$$

$$\frac{\partial\overline{\rho^{(0)}\theta^{(2)}}^{t_s,\lambda_s,p}}{\partial t_m}+\frac{\partial}{\partial\tilde{y}_p}\left(\overline{v_p^{(1)}\rho^{(0)}\theta^{(3)}}^{t_s,\lambda_s,p}+\overline{v^{(2)}\rho^{(0)}\theta^{(2)}}^{t_s,\lambda_s,p}\right)$$
$$+\frac{\partial}{\partial\tilde{y}_s}\left(\overline{v_s^{(1)}\rho^{(0)}\theta^{(4)}}^{t_s,\lambda_s,p}+\overline{v^{(2)}\rho^{(0)}\theta^{(3)}}^{t_s,\lambda_s,p}-\overline{v^{(2)}\frac{\tilde{z}}{a}}^{t_s,\lambda_s,p}\right)$$
$$+\frac{\partial}{\partial z}\left(\overline{w^{(4)}\rho^{(0)}\theta^{(3)}}^{t_s,\lambda_s,p}-\overline{w^{(4)}\frac{\tilde{z}}{a}}^{t_s,\lambda_s,p}\right)+\overline{\rho^{(0)}w^{(5)}}^{t_s,\lambda_s,p}\frac{\partial\theta^{(2)}}{\partial z}=\overline{S_\theta^{(7)}\rho^{(0)}}^{t_s,\lambda_s,p}, \tag{B.7b}$$

where terms with z/a come from corrections to the shallow-atmosphere approximation.

Continuity equations at $\mathcal{O}(\varepsilon^4)$, $\mathcal{O}(\varepsilon^5)$:

$$\frac{\partial}{\partial\tilde{y}_p}\left(\overline{v^{(1)}\rho^{(0)}}^{t_s,\lambda_s,p}\right)+\frac{\partial}{\partial\tilde{y}_s}\left(\overline{v^{(2)}\rho^{(0)}}^{t_s,\lambda_s,p}\right)+\frac{\partial}{\partial z}\left(\overline{w^{(4)}\rho^{(0)}}^{t_s,\lambda_s,p}\right)=0, \tag{B.8a}$$

$$\frac{\partial}{\partial\tilde{y}_p}\left(\overline{v^{(2)}\rho^{(0)}}^{t_s,\lambda_s,p}\right)+\frac{\partial}{\partial\tilde{y}_s}\left(\overline{v^{(3)}\rho^{(0)}}^{t_s,\lambda_s,p}\right)+\frac{\partial}{\partial z}\left(\overline{w^{(5)}\rho^{(0)}}^{t_s,\lambda_s,p}\right)=0. \tag{B.8b}$$

Momentum equations at $\mathcal{O}(\varepsilon^3)$, $\mathcal{O}(\varepsilon^4)$:

$$\overline{v^{(2)}}^{t_s,\lambda_s,p}=-\frac{\overline{S_u^{(3)}}^{t_s,\lambda_s,p}}{f}, \tag{B.9a}$$

$$\overline{v^{(3)}}^{t_s,\lambda_s,p}=-\frac{\overline{S_u^{(4)}}^{t_s,\lambda_s,p}}{f}+\frac{\partial}{\partial\tilde{y}_s}\left(\frac{\overline{u_s^{(1)}v_s^{(1)}}^{t_s,\lambda_s,p}}{f}\right)+\frac{\overline{w^{(4)}}^{t_s,\lambda_s,p}}{f}\frac{\partial u^{(0)}}{\partial z}. \tag{B.9b}$$

Here note that terms with $v_p^{(1)}\theta^{(3)}$ or $w^{(4)}\theta^{(3)}$, $v_p^{(1)}$ and $w^{(4)}$ cannot simply be averaged over λ_p and t_p - we need to average $v_p^{(1)}\theta^{(3)}$ or $w^{(4)}\theta^{(3)}$ together as also $\theta^{(3)}$ depends on planetary scales. This means that, in order to replace the $w^{(4)}$ and $v_p^{(1)}$ terms in equation (B.7b), the $\mathcal{O}(\varepsilon^6)$ thermodynamic equation and $\mathcal{O}(\varepsilon^3)$ momentum equation have to first be multiplied by $\theta^{(3)}$ and then averaged over $\lambda_s, t_s, \lambda_p, t_p$. For the $\mathcal{O}(\varepsilon^3)$ momentum equation this gives

$$\overline{\theta^{(3)}v^{(2)}}^{t_s,\lambda_s,p}=-\frac{\overline{\theta^{(3)}S_u^{(3)}}^{t_s,\lambda_s,p}}{f}+\overline{\frac{\theta^{(3)}}{f}\frac{\partial\pi^{(4)}}{\partial x_p}}^{t_s,\lambda_s,p}. \tag{B.10}$$

Multiplying equation (B.10) by $\rho^{(0)}$ and taking $\partial/\partial\tilde{y}_s$ of it yields

$$\frac{\partial}{\partial\tilde{y}_s}\left(\overline{\rho^{(0)}\theta^{(3)}v^{(2)}}^{t_s,\lambda_s,p}\right) = -\frac{\partial}{\partial\tilde{y}_s}\left(\frac{\overline{\rho^{(0)}\theta^{(3)}S_u^{(3)}}^{t_s,\lambda_s,p}}{f}\right) + \overline{\rho^{(0)}u_s^{(1)}\frac{\partial\theta^{(3)}}{\partial x_p}}^{t_s,\lambda_s,p} \tag{B.11}$$

where $u_s^{(1)} = -f^{-1}\partial\pi^{(4)}/\partial y_s$ was used. However, it is more complicated for the thermodynamic equation - here is a short derivation: First multiply (A.11) by $\theta^{(3)}$

$$\begin{aligned}\frac{1}{2}\frac{\partial\theta^{(3)^2}}{\partial t_p} + \frac{\partial\theta^{(3)}\theta^{(4)}}{\partial t_s} + \frac{1}{2}\frac{\partial}{\partial\tilde{x}_p}\left(u^{(0)}\theta^{(3)^2}\right) + \frac{\partial}{\partial\tilde{x}_s}\left(\theta^{(3)}u^{(0)}\theta^{(4)}\right)\\ +\theta^{(3)}v^{(1)}\frac{\partial\theta^{(2)}}{\partial y_p} + \theta^{(3)}w^{(4)}\frac{\partial\theta^{(2)}}{\partial z} = \theta^{(3)}S_\theta^{(6)},\end{aligned} \tag{B.12}$$

then average it over $\lambda_s, t_s, \lambda_p, t_p$:

$$\overline{\theta^{(3)}w^{(4)}}^{t_s,\lambda_s,p} = -\overline{\theta^{(3)}v^{(1)}}^{t_s,\lambda_s,p}\frac{\partial\theta^{(2)}/\partial y_p}{\partial\theta^{(2)}/\partial z} + \frac{\overline{\theta^{(3)}S_\theta^{(6)}}^{t_s,\lambda_s,p}}{\partial\theta^{(2)}/\partial z}. \tag{B.13}$$

We can derive an equation for $\overline{w^{(5)}\rho^{(0)}}^{t_s,\lambda_s,p}$ by integrating (B.8b) over z and using (B.9a) and (B.9b). This yields:

$$\overline{w^{(5)}\rho^{(0)}}^{t_s,\lambda_s,p} = -\int_0^{z_{max}}\rho^{(0)}\frac{\partial}{\partial\tilde{y}_s}\left(\frac{\partial}{\partial\tilde{y}_s}\left(\frac{\overline{v_s^{(1)}u_s^{(1)}}^{t_s,\lambda_s,p}}{f}\right)\right)\mathrm{d}z + S_{w5} \tag{B.14}$$

with

$$S_{w5} = -\int_0^{z_{max}}\left[\frac{\partial}{\partial\tilde{y}_s}\left(\rho^{(0)}\left\{\frac{\overline{S_\theta^{(6)}}^{t_s,\lambda_s,p}}{f}\frac{\partial u^{(0)}/\partial z}{\partial\theta^{(2)}/\partial z} - \frac{\overline{S_u^{(4)}}^{t_s,\lambda_s,p}}{f}\right\}\right) - \frac{\partial}{\partial\tilde{y}_p}\left(\rho^{(0)}\frac{\overline{S_u^{(3)}}^{t_s,\lambda_s,p}}{f}\right)\right]\mathrm{d}z.$$

These equations are then used in section 2.4.3 to derive the final baroclinic equation for the mean flow (2.19, 2.20).

Appendix C

Derivation of the Angular Momentum Equation

This Appendix shows the derivation of angular momentum conservation for the zonal mean flow ($u^{(0)}$) equation, following from the $\mathcal{O}(\varepsilon^5)$ momentum equation (A.8). Note that similar systems can be derived for higher order velocities as well and at all asymptotic orders, but are omitted for brevity.

Deriving an angular momentum equation for the mean flow means that something that corresponds to the fifth order momentum equation (A.8) must be used. This means that, for example, Du/Dt has to be of fifth order, which overall makes the angular momentum equation (2.24) a second order equation, thus the rest of the terms in the equation must follow that pattern.

Using these statements and noting that $\phi = \phi_p$, the angular momentum equation (2.24) becomes

$$\varepsilon^{-3}\varepsilon^5\frac{\mathrm{D}M}{\mathrm{D}t_m} = \varepsilon^{-3}\varepsilon^5 a\cos\phi_p\frac{\mathrm{D}u^{(0)}}{\mathrm{D}t_m} - (u^{(0)}+\varepsilon u^{(1)}+\varepsilon^2u^{(2)}+...)(\varepsilon v^{(1)}+\varepsilon^2v^{(2)}+...)\sin\phi_p \\ -\varepsilon^{-2}f(v^{(0)}+\varepsilon v^{(1)}+\varepsilon^2v^{(2)}+...)a\cos\phi_p, \quad \text{(C.1)}$$

where $v^{(0)} = 0$ because the zonal mean flow is geostrophic to leading order (A.4). In this form, angular momentum is not conserved. To get a conservative form of this equation, multiply (C.1)

by $\rho = \rho^{(0)} + \varepsilon^2\rho^{(2)} + ...$

$$\begin{aligned}\varepsilon^2\rho\frac{\mathrm{D}M}{\mathrm{D}t_m} &= \varepsilon^2 a\cos\phi_p(\rho^{(0)} + \varepsilon^2\rho^{(2)} + ...)\frac{\mathrm{D}u^{(0)}}{\mathrm{D}t_m} \\ &- (\rho^{(0)} + \varepsilon^2\rho^{(2)} + ...)(u^{(0)} + \varepsilon u^{(1)} + \varepsilon^2 u^{(2)} + ...)(\varepsilon v^{(1)} + \varepsilon^2 v^{(2)} + ...)\sin\phi_p \\ &- \varepsilon^{-2} f(\rho^{(0)} + \varepsilon^2\rho^{(2)} + ...)(\varepsilon v^{(1)} + \varepsilon^2 v^{(2)} + ...)a\cos\phi_p \end{aligned} \tag{C.2}$$

and taking the same orders together, yields the second order angular momentum equation (omit ε everywhere)

$$\begin{aligned}\rho\frac{\mathrm{D}M}{\mathrm{D}t_m} = a\cos\phi_p\rho^{(0)}\frac{\mathrm{D}u^{(0)}}{\mathrm{D}t_m} &- (\rho^{(0)}u^{(1)}v^{(1)} + \rho^{(0)}u^{(0)}v^{(2)})\sin\phi_p \\ &- f(\rho^{(0)}v^{(4)} + \rho^{(2)}v^{(2)} + \rho^{(3)}v^{(1)})a\cos\phi_p. \end{aligned} \tag{C.3}$$

Note that since an angular momentum equation for the mean flow is derived, (C.3) can be averaged over synoptic scales (t_s, λ_s, ϕ_s) and planetary time scale (t_p), which simplifies it. To get the angular momentum conservation equation, the continuity equations (A.14-A.16) are needed, which can be written together as

$$\nabla_p \cdot (\overline{\rho^{(0)}\mathbf{u}^{(i)}}^{s,t_p}) + \frac{\partial(\overline{\rho^{(0)}w^{(i+3)}})^{s,t_p}}{\partial z} = 0 \tag{C.4}$$

where overline denotes average over $(t_s, t_p, \lambda_s, \phi_s)$, and $i = 0, 1, 2$ (where for $i = 0$, $w^{(3)} = 0$). This equation can then be written in a shorter form as

$$\nabla_p^{3D} \cdot (\overline{\rho^{(0)}\mathbf{u}_{3D}^{(i)}}^{s,t_p}) = 0 \tag{C.5}$$

where

$$\nabla_p^{3D}\cdot = \left(\frac{1}{a\cos\phi_p}\frac{\partial}{\partial\lambda_p}, \frac{1}{a\cos\phi_p}\frac{\partial\cos\phi_p}{\partial\phi_p}, \frac{\partial}{\partial z}\right)$$

now includes the vertical derivative and $\mathbf{u}_{3D}^{(i)} = (u^{(i)}, v^{(i)}, w^{(i+3)})$ is the three-dimensional velocity

field. Note that in general the continuity equation can be used to simplify expression (C.3), using

$$\begin{aligned}\rho\frac{\mathrm{D}G}{\mathrm{D}t} &= \frac{\mathrm{D}\rho G}{\mathrm{D}t} - G\frac{\mathrm{D}\rho}{\mathrm{D}t} \\ &= \frac{\partial(\rho G)}{\partial t} + \nabla^{3D}\cdot(G\rho\mathbf{u}_{3D})\end{aligned} \tag{C.6}$$

where G is an arbitrary scalar, and $\mathbf{u}_{3D}$ is three-dimensional velocity; noting that mass is conserved for every order, the continuity equation for each order in general takes the form $\mathrm{D}\rho/\mathrm{D}t = -\rho\nabla^{3D}\cdot\mathbf{u}_{3D}$, where $\partial\rho/\partial t$ is mainly zero as $\rho^{(0)}$ only depends on the vertical coordinate.

Using (C.6) for $\rho\mathrm{D}M/\mathrm{D}t_m$ and (C.5, for $\rho^{(0)}\mathrm{D}u^{(0)}/\mathrm{D}t_m$ gives

$$\begin{aligned}\frac{\partial\overline{(\rho M)}^{s,t_p}}{\partial t_m} + \nabla_p^{3D}\cdot\overline{(M\rho\mathbf{u}_{3D})}^{s,t_p} &= a\cos\phi_p\frac{\partial\overline{(\rho^{(0)}u^{(0)})}^{s,t_p}}{\partial t_m} \\ +a\cos\phi_p\nabla_p^{3D}\cdot\left(\overline{u^{(2)}\rho^{(0)}\mathbf{u}_{3D}^{(0)}}^{s,t_p} + \overline{u^{(1)}\rho^{(0)}\mathbf{u}_{3D}^{(1)}}^{s,t_p} + \overline{u^{(0)}\rho^{(0)}\mathbf{u}_{3D}^{(2)}}^{s,t_p}\right) \\ -(\overline{\rho^{(0)}u^{(1)}v^{(1)}}^{s,t_p} + \overline{\rho^{(0)}u^{(0)}v^{(2)}}^{s,t_p})\sin\phi_p - f(\overline{\rho^{(0)}v^{(4)}}^{s,t_p} + \overline{\rho^{(2)}v^{(2)}}^{s,t_p} + \overline{\rho^{(3)}v^{(1)}}^{s,t_p})a\cos\phi_p.\end{aligned} \tag{C.7}$$

Note that the orders of separate terms on the right hand side are not given as they do not play an important role in the further derivation (for simplicity), however note that overall $\overline{\rho M}^{s,t_p}$ and $\overline{M\rho\mathbf{u}_{3D}}^{s,t_p}$ are of the second order.

From (A.8) multiplied by $\rho^{(0)}$ it follows that

$$\begin{aligned}\overline{\rho^{(0)}\frac{Du^{(0)}}{Dt_m}}^{s,t_p} &= f(\overline{v^{(4)}\rho^{(0)}}^{s,t_p} + \overline{v^{(1)}\rho^{(3)}}^{s,t_p} + \overline{v^{(2)}\rho^{(2)}}^{s,t_p}) \\ +\frac{\tan\phi_p}{a}\left(\overline{v^{(2)}u^{(0)}\rho^{(0)}}^{s,t_p} + \overline{v^{(1)}u^{(1)}\rho^{(0)}}^{s,t_p}\right) + \overline{\rho^{(0)}S_u^{(5)}}^{s,t_p} - \frac{\partial}{\partial x_p}\left(\overline{\pi^{(6)}\rho^{(0)}}^{s,t_p}\right) \\ -\overline{\frac{\cos\phi_p}{\partial\theta^{(2)}/\partial z}S_\theta^{(6)}}^{s,t_p} + \overline{\rho^{(2)}S_u^{(3)}}^{s,t_p} + \frac{\partial}{\partial x_p}\left[\frac{\cos\phi_p}{\partial\theta^{(2)}/\partial z}\left(\overline{u^{(0)}\theta^{(3)}\rho^{(0)}}^{s,t_p} + \overline{\frac{\rho^{(0)}\pi^{(3)}}{f}\frac{\partial\theta^{(2)}}{\partial y_p}}^{s,t_p}\right)\right]\end{aligned} \tag{C.8}$$

where the last two terms come from the $w^{(4)}\cos\phi_p$ term using the thermodynamic equation (A.11) averaged over synoptic scales and t_p, $fv^{(1)}\rho^{(3)} = \rho^{(3)}\partial\pi^{(3)}/\partial x_p$ (via (A.5)), and $\overline{fv^{(2)}\rho^{(2)}}^{s,t_p} = \overline{\pi^{(4)}\rho^{(2)}}^{s,t_p} + \overline{\rho^{(2)}S_u^{(3)}}^{s,t_p}$ (via (A.6)). Notice that the first two terms on the right-hand-side of (C.8) resemble the terms involving $\sin\phi_p$ and $fa\cos\phi_p$ in (C.7), and lead to a cancellation after combining (C.7) and (C.8). The terms that remain in the equation can all

be integrated over a volume V_p (λ_p, ϕ_p, z). Following Gauss' theorem[1], assuming no source-sink terms and assuming there is no orography (for simplicity) yields angular momentum conservation

$$\iiint_{Vp} \frac{\partial \overline{(\rho M)}^{s,t_p}}{\partial t_m} \mathrm{d}V_p = 0. \tag{C.9}$$

The angular momentum equation can be linked to the barotropic pressure equation (2.18) using (C.7), dividing it first by $a\cos\phi_p$, then integrating it over a longitude-height slice (over area A_p, which effectively gives additional averaging over λ_p and z) and using the Gauss' theorem again which gives

$$\begin{aligned}
\frac{1}{a\cos\phi_p}\left[\frac{\partial \overline{(\rho M)}^{s,p,z}}{\partial t_m} + \frac{\partial}{\partial \tilde{y}_p}\overline{(M\rho v)}^{s,p,z}\right] &= \frac{\partial \overline{\rho^{(0)}u^{(0)}}^{s,p,z}}{\partial t_m} \\
+\frac{\partial}{\partial \tilde{y}_p}\left(\overline{u^{(1)}\rho^{(0)}v^{(1)}}^{s,p,z} + \overline{u^{(0)}\rho^{(0)}v^{(2)}}^{s,p,z}\right) - (\overline{\rho^{(0)}u^{(1)}v^{(1)}}^{s,p,z} + \overline{\rho^{(0)}u^{(0)}v^{(2)}}^{s,p,z})\frac{\tan\phi_p}{a} \\
-f(\overline{\rho^{(0)}v^{(4)}}^{s,p,z} + \overline{\rho^{(2)}v^{(2)}}^{s,p,z} + \overline{\rho^{(3)}v^{(1)}}^{s,p,z}).
\end{aligned} \tag{C.10}$$

Here the overbar denotes an average over $t_s, t_p, \lambda_s, \lambda_p, \phi_s, z$ and note that $v^{(2)}$ is proportional to a source term under such an average (B.1a). Now divide (C.10) by f, take $\partial/\partial\tilde{y}_p$ of it, and finally multiply it by f. This yields

$$\begin{aligned}
\mathcal{L}\left\{\frac{1}{a\cos\phi_p}\left[\frac{\partial \overline{\rho M}^{s,p,z}}{\partial t_m} + \frac{\partial}{\partial \tilde{y}_p}\left(\overline{Mv}^{s,p,z}\right)\right]\right\} &= \mathcal{L}\left\{\frac{\partial \overline{\rho^{(0)}u^{(0)}}^{s,p,z}}{\partial t_m}\right\} \\
+\mathcal{L}\left\{\frac{\partial}{\partial \tilde{y}_p}\left(\overline{u^{(1)}\rho^{(0)}v^{(1)}}^{s,p,z}\right) - (\overline{\rho^{(0)}u^{(1)}v^{(1)}}^{s,p,z})\frac{\tan\phi_p}{a}\right\} \\
-f\frac{\partial}{\partial \tilde{y}_p}\left(\overline{\rho^{(0)}v^{(4)}}^{s,p,z} + \overline{\rho^{(2)}v^{(2)}}^{s,p,z} + \overline{\rho^{(3)}v^{(1)}}^{s,p,z}\right),
\end{aligned} \tag{C.11}$$

where source terms were omitted for simplicity, the left-hand-side can be simplified to

$$\mathcal{L}\left\{\overline{\frac{\rho}{a\cos\phi_p}\frac{DM}{Dt_m}}^{s,p,z}\right\}$$

[1]Gauss' theorem generally states $\iiint_V \nabla\cdot\mathbf{G}\mathrm{d}V = \iint_{\partial V}\mathbf{G}\cdot\mathbf{n}\mathrm{d}S$, where $\mathbf{G}$ is a three-dimensional vector, $\mathbf{n}$ is a normal vector on surface S, and ∂V is the surface around the volume V of interest. Note that in the case of $\mathbf{G} = \rho M\mathbf{u}$ the $\iint_{\partial V}\mathbf{G}\cdot\mathbf{n}\mathrm{d}S = 0$ as $\mathbf{u}\cdot\mathbf{n} = 0$ at the lower boundary and $\rho \to 0$ at the upper boundary.

with

$$\mathcal{L} = \frac{\partial}{\partial \tilde{y}_p} - \frac{\beta}{f},$$

and the last term in the equation can be simplified to $+f\partial\rho^{(2)}/\partial t_m$ via (B.2d). Notice how all but the last term on the right-hand-side resemble terms in the barotropic pressure equation (2.18). This means that (2.18) can be rewritten using the angular momentum equation as

$$\mathcal{L}\left\{\overline{\frac{\rho}{a\cos\phi_p}\frac{DM}{Dt_m}}^{s,p,z}\right\} - f\frac{\partial\overline{\rho^{(2)}}^{s,p,z}}{\partial t_m} = -f\frac{\partial\overline{p^{(2)}}^{s,p,z}}{\partial t_m} - f\frac{\partial}{\partial\tilde{y}_p}\left(\overline{\rho^{(0)}v_p^{(1)}\theta^{(3)}}^{s,p,z}\right) \tag{C.12}$$

where $\rho^{(2)} = p^{(2)} - \rho^{(0)}\theta^{(2)}$ via (B.4), which further simplifies it. This now gives a clear link between the barotropic equation for the mean flow and the angular momentum.

Appendix D

The Non-acceleration Theorem

This Appendix shows the derivation of the non-acceleration theorem for the given asymptotic set of equations. To derive this, a Transformed Eulerian Mean (TEM) (Andrews and McIntyre, 1976; Edmon et al., 1980) version of the zonal mean (averaged over λ_p, λ_s, denoted by [.]) momentum and thermodynamic equations is necessary. From the zonal mean continuity ($\mathcal{O}(\varepsilon^4, \varepsilon^5)$), thermodynamic ($\mathcal{O}(\varepsilon^6, \varepsilon^7)$) and momentum equations ($\mathcal{O}(\varepsilon^3, \varepsilon^4, \varepsilon^5)$) at different asymptotic orders, we can identify the residual meridional circulation ($v_r^{(i)}$, $w_r^{(i)}$ with subscript r representing residual velocity and i represents its order)

$$[\rho^{(0)} v_r^{(2)}] = [\rho^{(0)} v^{(2)}] - \frac{\partial}{\partial z}\left[\frac{v_p^{(1)}\theta^{(3)}\rho^{(0)}}{\partial\theta^{(2)}/\partial z}\right] \tag{D.1}$$

$$[\rho^{(0)} w_r^{(4)}] = [\rho^{(0)} w^{(4)}] + \frac{\partial}{\partial \tilde{y}_s}\left[\frac{v_p^{(1)}\theta^{(3)}\rho^{(0)}}{\partial\theta^{(2)}/\partial z}\right] = [\rho^{(0)} w^{(4)}] \tag{D.2}$$

$$[\rho^{(0)} v_r^{(3)}] = [\rho^{(0)} v^{(3)}] - \frac{\partial}{\partial z}\left[\frac{v_s^{(1)}\theta^{(4)}\rho^{(0)}}{\partial\theta^{(2)}/\partial z}\right] \tag{D.3}$$

$$[\rho^{(0)} w_r^{(5)}] = [\rho^{(0)} w^{(5)}] + \frac{\partial}{\partial \tilde{y}_p}\left[\frac{v_p^{(1)}\theta^{(3)}\rho^{(0)}}{\partial\theta^{(2)}/\partial z}\right] + \frac{\partial}{\partial \tilde{y}_s}\left[\frac{v_s^{(1)}\theta^{(4)}\rho^{(0)}}{\partial\theta^{(2)}/\partial z}\right], \tag{D.4}$$

which satisfy continuity equations at different orders.

Using the residual velocities (D.1-D.4), the zonal mean momentum equations at $\mathcal{O}(\varepsilon^3, \varepsilon^4)$

(A.6, A.7) become

$$\frac{\partial[\rho^{(0)}u^{(1)}]}{\partial t_s} - f[\rho^{(0)}v_r^{(2)}] = [\rho^{(0)}S_u^{(3)}] + \frac{\partial}{\partial z}\left[\frac{v_p^{(1)}\theta^{(3)}\rho^{(0)}}{\partial\theta^{(2)}/\partial z}\right], \tag{D.5}$$

$$\begin{aligned}&\frac{\partial[\rho^{(0)}u^{(2)}]}{\partial t_s} + \frac{\partial[\rho^{(0)}u^{(1)}]}{\partial t_p} + [\rho^{(0)}w_r^{(4)}]\frac{\partial u^{(0)}}{\partial z} - f[\rho^{(0)}v_r^{(3)}]\\ &= [\rho^{(0)}S_u^{(4)}] - \frac{\partial}{\partial\tilde{y}_s}\left[\rho^{(0)}u_s^{(1)}v_s^{(1)}\right] + \frac{\partial}{\partial z}\left[\frac{v_s^{(1)}\theta^{(4)}\rho^{(0)}}{\partial\theta^{(2)}/\partial z}\right],\end{aligned} \tag{D.6}$$

which can both be linked to the zonal mean wave activity equations on planetary (2.14) and synoptic (2.13) scales, respectively, through their respective zonal mean EP flux divergences ($[\nabla_p^{3D}\cdot\mathbf{F}_p]$, $[\nabla_s^{3D}\cdot\mathbf{F}_s]$) that appear on the right-hand-side of (D.5, D.6). Thus, (D.5, D.6) can be rewritten in terms of wave activities as

$$\frac{\partial[\rho^{(0)}u^{(1)}]}{\partial t_s} + \frac{\partial[\mathcal{A}_p]}{\partial t_p} = f[\rho^{(0)}v_r^{(2)}] + [\rho^{(0)}S_u^{(3)}] + [S_p^{wa}], \tag{D.7}$$

$$\frac{\partial[\rho^{(0)}u^{(2)}]}{\partial t_s} + \frac{\partial[\rho^{(0)}u^{(1)}]}{\partial t_p} + \frac{\partial[\mathcal{A}_s]}{\partial t_s} = f[\rho^{(0)}v_r^{(3)}] - [\rho^{(0)}w_r^{(4)}]\frac{\partial u^{(0)}}{\partial z} + [\rho^{(0)}S_u^{(4)}] + [S_s^{wa}], \tag{D.8}$$

which, under synoptic scale averaging (ϕ_s, t_s), for steady eddies (wave activity tendencies vanish), and in the absence of source-sink terms, satisfy the non-acceleration theorem, i.e. the tendencies of the zonal mean velocities vanish. These equations also show that planetary wave activity affects the zonal mean flow evolution on synoptic timescales, and that the synoptic wave activity (linked to synoptic heat and momentum fluxes) affects the zonal mean flow evolution on planetary timescales. However, the latter relationship vanishes under synoptic scale averaging, leaving only the residual circulation terms and source-sink terms affecting the evolution of $u_p^{(1)}$ in (D.8). This means that an evolution equation for $p^{(3)}$ (related to $u_p^{(1)}$), which can be derived in a similar manner as the barotropic equation (evolution equation for $p^{(2)}$; Appendix B, section 2.4.2) using $\mathcal{O}(\varepsilon^4)$ u-momentum equation, $\mathcal{O}(\varepsilon^6)$ thermodynamic equation, $\mathcal{O}(\varepsilon^6)$ continuity equation, and hydrostatic balance for $p^{(3)}$ averaged over synoptic scales and vertically, is only affected by the source-sink terms

$$\left(\frac{\partial}{\partial\tilde{y}_p}\frac{1}{f}\frac{\partial}{\partial y_p} - \frac{\beta}{f^2}\frac{\partial}{\partial y_p} - f\right)\frac{\partial\overline{p^{(3)}}^{\lambda_p,s,z}}{\partial t_p} = -\overline{f\rho^{(0)}S_\theta^{(6)}}^{\lambda_p,s,z} - \left(\frac{\partial}{\partial\tilde{y}_p} - \frac{\beta}{f}\right)\left(\overline{\rho^{(0)}S_u^{(4)}}^{\lambda_p,s,z}\right). \tag{D.9}$$

This evolution equation suggests that a higher order momentum equation is needed to find the

dynamic influences on the mean flow on planetary spatial scales (averaged over synoptic scales) and longer time scales (t_m) - see barotropic pressure equation (2.17).

Note that (D.7,D.8) provide equations for zonal mean flow variations on shorter timescales (synoptic and planetary), which have dynamical importance for higher frequency atmospheric flow (e.g. baroclinic life cycles or barotropic annular modes with timescales of 10 days or less). Upon averaging over these scales, the slower variations in the mean flow (t_m) emerge (as in the barotropic equation for the mean flow).

The TEM version of the $\mathcal{O}(\varepsilon^5)$ zonal momentum equation can also be derived using the same residual velocities (with the same procedure), however, here we only show an equation averaged over $t_s, t_p, \lambda_s, \lambda_p, \phi_s, z$ as this was the averaging performed to derive the barotropic equation for the mean flow (2.18). This yields

$$\begin{aligned}\frac{\partial\overline{\rho^{(0)}u^{(0)}}^{p,s,z}}{\partial t_m} + \overline{\rho^{(0)}v_r^{(2)}\frac{\partial u^{(0)}}{\partial \tilde{y}_p}}^{p,s,z} + \overline{\rho^{(0)}w_r^{(5)}\frac{\partial u^{(0)}}{\partial z}}^{p,s,z} + \overline{\rho^{(0)}w_r^{(4)}}^{p,s,z}\cos\phi_p \\ -f\overline{\rho^{(0)}v^{(4)}}^{p,s,z} - \overline{f\rho^{(3)}v_p^{(1)}}^{p,s,z} = \overline{\rho^{(0)}S_u^{(5)}}^{p,s,z} + \frac{\partial\overline{F^y}^{p,s,z}}{\partial\tilde{y}_p}\end{aligned} \tag{D.10}$$

with

$$F^y = -\rho^{(0)}u^{(1)}v^{(1)}\cos\phi_p + \frac{\partial u^{(0)}}{\partial z}\frac{v_p^{(1)}\theta^{(3)}\rho^{(0)}}{\partial\theta^{(2)}/\partial z} \tag{D.11}$$

where $a^{-1}\tan\phi_p\overline{\rho^{(0)}u^{(1)}v^{(1)}}^{p,s,z}$ was absorbed into F^y through $\cos\phi_p$. As in section 2.4.2, many terms in (D.10) can be related to source-sink terms, $v^{(4)}$ can be eliminated via the continuity and thermodynamic equations, and $f\rho^{(3)}v_p^{(1)}$ is related to meridional heat flux on planetary scales. To link (D.10) to the wave activity tendency, a higher order wave activity approximation would be needed, and due to the planetary scale heat fluxes in (D.10), also a boundary wave activity may be needed, which are not the subject of this thesis (only the leading order approximations are of interest). Hence a non-acceleration theorem for this order of the momentum equation is yet to be determined, but is expected to hold as is the case at lower orders.

The $\mathcal{O}(\varepsilon^7)$ thermodynamic equation within the TEM framework (under a $t_s, t_p, \lambda_s, \lambda_p, \phi_s$

average) is

$$\frac{\partial \overline{\rho^{(0)}\theta^{(2)}}^{s,p}}{\partial t_m} + \overline{\rho^{(0)} v_r^{(2)}}^{s,p} \frac{\partial \theta^{(2)}}{\partial y_p} + \overline{\rho^{(0)} w_r^{(5)}}^{s,p} \frac{\partial \theta^{(2)}}{\partial z} = \overline{\rho^{(0)} S_\theta^{(7)}}^{s,p} - \frac{\partial}{\partial z} \left(\frac{\overline{S_\theta^{(6)} \theta^{(3)} \rho^{(0)}}^{s,p}}{\partial \theta^{(2)} / \partial z} \right), \quad \text{(D.12)}$$

which completes the TEM version of the equations. Note that the $\mathcal{O}(\varepsilon^6)$ thermodynamic equation remains unchanged within the TEM framework and is hence not repeated here.

Appendix E

Dimensionalisation of Asymptotic Equations

This section addresses dimensionalising of the asymptotic theory that was based on the non-dimensional equations. This can help us relate the theory to the model data (see Appendix H and Chapters 3 and 4).

E.1 Parameters used for dimensionalisation

This section gives a list of terms in nondimensional equations and how they can be dimensionalised in general (e.g. nondimensional z becomes z_{dim}/h_{sc}). For simplicity, the nondimensional parameters are written with asterix (*) and dimensional parameters without it for this appendix only (so all the parameters from this chapter in the nondimensional set of equations now get an asterix). The zonal mean is then denoted by overline and the perturbations therefrom are denoted by prime (again for this appendix only).

- $\frac{\partial}{\partial t_m^*} \rightarrow \frac{t_{ref}}{\varepsilon^5}\frac{\partial}{\partial t}$ with $t_{ref} = \frac{hsc}{u_{ref}}$;
- $\frac{\partial}{\partial t_p^*} \rightarrow \frac{t_{ref}}{\varepsilon^3}\frac{\partial}{\partial t}$;
- $\frac{\partial}{\partial t_s^*} \rightarrow \frac{t_{ref}}{\varepsilon^2}\frac{\partial}{\partial t}$;
- $\frac{\partial}{\partial x_p^*} = \frac{\partial}{\partial \tilde{x}_p^*} = \frac{\partial}{a^* \cos\phi_p \partial\lambda_p} \rightarrow \frac{h_{sc}}{\varepsilon^3}\frac{\partial}{a\cos\phi\partial\lambda} = \frac{h_{sc}}{\varepsilon^3}\frac{\partial}{\partial x} = \frac{h_{sc}}{\varepsilon^3}\frac{\partial}{\partial \tilde{x}}$;

E. DIMENSIONALISATION OF ASYMPTOTIC EQUATIONS

- $\frac{\partial}{\partial x_s^*} = \frac{\partial}{\partial \tilde{x}_s^*} = \frac{\partial}{a^* \cos\phi_p \partial\lambda_s} \rightarrow \frac{h_{sc}}{\varepsilon^2} \frac{\partial}{a\cos\phi\partial\lambda} = \frac{h_{sc}}{\varepsilon^2}\frac{\partial}{\partial x} = \frac{h_{sc}}{\varepsilon^2}\frac{\partial}{\partial \tilde{x}}$;
- $\frac{\partial}{\partial y_p^*} = \frac{\partial}{a^*\partial\phi_p} \rightarrow \frac{h_{sc}}{\varepsilon^3}\frac{\partial}{a\partial\phi} = \frac{h_{sc}}{\varepsilon^3}\frac{\partial}{\partial y}$;
- $\frac{\partial}{\partial y_s^*} = \frac{\partial}{a^*\partial\phi_s} \rightarrow \frac{h_{sc}}{\varepsilon^2}\frac{\partial}{a\partial\phi} = \frac{h_{sc}}{\varepsilon^2}\frac{\partial}{\partial y}$;
- $\frac{\partial}{\partial \tilde{y}_p^*} = \frac{\partial \cos\phi_p}{a^* \cos\phi_p \partial\phi_p} \rightarrow \frac{h_{sc}}{\varepsilon^3}\frac{\partial\cos\phi}{a\cos\phi\partial\phi} = \frac{h_{sc}}{\varepsilon^3}\frac{\partial}{\partial\tilde{y}}$;
- $\frac{\partial}{\partial \tilde{y}_s^*} = \frac{\partial \cos\phi_p}{a^* \cos\phi_p \partial\phi_s} \rightarrow \frac{h_{sc}}{\varepsilon^2}\frac{\partial\cos\phi}{a\cos\phi\partial\phi} = \frac{h_{sc}}{\varepsilon^2}\frac{\partial}{\partial\tilde{y}}$;
- $\frac{\partial}{\partial z^*} \rightarrow h_{sc}\frac{\partial}{\partial z}$;
- $\theta_{ref} = T_{ref} = \frac{p_{ref}}{\rho_{ref} R} \approx 280K$ where $R = 287\frac{J}{kgK}$;
- Coriolis parameter: $f^* = \frac{f}{2\Omega}$ and beta-parameter: $\beta^* = \frac{h_{sc}}{\varepsilon^3 2\Omega}\frac{\partial f}{\partial y} = \frac{h_{sc}}{\varepsilon^3 2\Omega}\beta$;
- Dimensionalising "background":
  - $\theta_o \rightarrow \theta_{ref} \cdot 1$;
  - $p_o \rightarrow p_{ref} p^{(0)}(z^*)$;
  - $\rho_o \rightarrow \rho_{ref}\rho^{(0)}(z^*)$;
- Dimensionalising "zonal mean" (bar denotes zonal mean):
  - $\bar{\theta} \rightarrow \varepsilon^2\theta_{ref}\theta^{(2)}(y_p^*, z^*, t_m^*)$;
  - $\bar{p} \rightarrow \varepsilon^2 p_{ref} p^{(2)}(y_p^*, z^*, t_m^*)$;
  - $\bar{u} \rightarrow u_{ref} u_m^{(0)}(y_p^*, z^*, t_m^*) = \frac{1}{f\rho_o}\frac{\partial\bar{p}}{\partial y}$
- Dimensionalising "planetary scale perturbation" (prime denotes planetary scale perturbation):
  - $\theta' \rightarrow \varepsilon^3\theta_{ref}\theta^{(3)}(x_p^*, y_p^*, z^*, t_p^*)$;
  - $p' \rightarrow \varepsilon^3 p_{ref} p^{(3)}(x_p^*, y_p^*, z^*, t_p^*)$;
  - $\mathbf{u}' = \frac{1}{f\rho_o}\mathbf{e}_r \times \nabla p' \rightarrow \varepsilon u_{ref}\mathbf{u}_p^{(1)}(x_p^*, y_p^*, z^*, t_p^*)$ where $\nabla = \left(\frac{\partial}{\partial x}, \frac{\partial}{\partial y}\right)$ and $\mathbf{e}_r$ is unit vector in z-direction;
- Dimensionalising "synoptic scale perturbation" (double prime denotes synoptic scale perturbation):
  - $\theta'' \rightarrow \varepsilon^4\theta_{ref}\theta^{(4)}(x_s^*, y_s^*, t_s^*, x_p^*, y_p^*, z^*, t_p^*)$;

- $p'' \to \varepsilon^4 p_{ref} p^{(4)}(x_s^*, y_s^*, t_s^*, x_p^*, y_p^*, z^*, t_p^*)$;
- $\mathbf{u}'' = \frac{1}{f\rho_o}\mathbf{e}_r \times \nabla p'' \to \varepsilon u_{ref} \mathbf{u}_s^{(1)}(x_s^*, y_s^*, t_s^*, x_p^*, y_p^*, z^*, t_p^*)$;

- Vertical velocities: $w_a \to \varepsilon^5 u_{ref} w^{(5)}$, $w \to \varepsilon^4 u_{ref} w^{(4)}$;

- Additionally, the scaling parameters (Rossby, Froude and Mach numbers) and the relationships between different reference values are used to cancel out different ε that occur during dimensionalisation process.

Note that the equations for the mean tend to be averaged over many dimensions, like $x_s^*, y_s^*, t_s^*, x_p^*, z^*, t_p^*$ for barotropic or $x_s^*, t_s^*, x_p^*, t_p^*$ for baroclinic (where baroclinic can additionally be averaged over y_s^* and z^*). Below are examples of dimensionalised equations for the mean flow without a presence of forced planetary scale waves.

E.2 Dimensionalised equations for the mean flow

Baroclinic equation - weak planetary scale waves

Using equations (2.19) and (B.14) without planetary scale heat fluxes and all dimensionalisation above, yields

$$\frac{\partial}{\partial t}\left(\overline{f\rho_o \frac{\partial \bar{u}}{\partial z}}\right) = \frac{R}{h_{sc}}\frac{\partial}{\partial y}\left[\frac{\partial}{\partial \tilde{y}}\left(\overline{\rho_o v'' \theta''}\right) + \frac{\partial \bar{\theta}}{\partial z}\overline{\rho_o w_a}\right] + S_{terms} \tag{E.1}$$

where long overline denotes averages present in the baroclinic equation, $\overline{w_a \rho_o} = -\frac{1}{f}\int_0^{z_{max}} \frac{\partial}{\partial \tilde{y}}\frac{\partial}{\partial \tilde{y}}\left(\overline{\rho_o v'' u''}\right) \mathrm{d}z$, $\frac{R}{h_{sc}} = \frac{g}{\theta_{ref}}$ (what we expect from thermal wind balance), and if we average over y_s we get:

$$\frac{\partial}{\partial t}\left(\overline{f\rho_o \frac{\partial \bar{u}}{\partial z}}\right) = S_{terms} \tag{E.2}$$

Note that through thermal wind balance $f\frac{\partial \bar{u}}{\partial z} = -\frac{R}{h_{sc}}\frac{\partial \bar{\theta}}{\partial y}$ we can see that there is the same factor $\frac{R}{h_{sc}}$ as in the equation (E.1), implying consistency.

Barotropic equation - weak planetary scale waves

Using equation (2.28b) and all dimensionalisation above, yields

$$\left(\frac{\partial}{\partial\tilde{y}}-\frac{\beta}{f}\right)\frac{\partial\overline{\rho_o\bar{u}}}{\partial t}+\frac{\rho_{ref}}{p_{ref}}f\overline{\frac{\partial\bar{p}}{\partial t}}+\left(\frac{\partial}{\partial\tilde{y}}-\frac{\beta}{f}\right)\left[\frac{\partial}{\partial\tilde{y}}\overline{(\rho_o v''u'')}-\frac{\tan\phi}{a}\overline{(\rho_o v''u'')}\right]=S_{terms} \tag{E.3}$$

where long overline denotes averages present in the barotropic equation, and $\frac{\rho_{ref}}{p_{ref}}=\frac{1}{gh_{sc}}$.

Appendix F

Held-Suarez configuration in the Unified Model

The numerical model used in this Chapter is the dry dynamical core version of the UK Met Office Unified Model (UM) version 8.6 with ENDGame semi-Lagrangian dynamical core (Walters et al., 2014). The model configuration followsHeld and Suarez (1994) with some modifications, namely the perpetual equinox (Held and Suarez, 1994), and perpetual solstice (Polvani and Kushner, 2002; Sheshadri et al., 2015) configurations[1] (described in detail below). The model resolution used is N96L63 with a model top at 32 km (1.875^o in longitude, 1.25^o in latitude and varying vertical resolution - from approximately 200 m in the lower troposphere to approximately 1000 m in the stratosphere) and is run for 10800 days, of which the first 1440 days are taken as a spin-up period. The output is analysed at daily resolution and in height coordinates. These configurations have no orography or other longitudinal asymmetries (such as land-sea contrast) that would give rise to forced stationary planetary waves.

F.1 Equinox configuration

The equinox configuration follows Held and Suarez (1994), where the temperature field is relaxed to the equillibrium temperature profile, and has linear frictional and thermal damping. These processes are the only non-conservative processes in this type of model. The source-sink term in

[1]To reproduce these model configurations in the UM, copy the following jobs: xlyyt for the equinox configuration, and xmxic for the solstice configuration.

the momentum equations is $\mathbf{S_u} = -k_v\mathbf{u}$ (with k_v frictional damping coeficient, $\mathbf{u}$ the 3D velocity vector), which is only applied close to the surface. The source-sink term in the thermodynamic equation is $S_T = -k_T(T - T_{eql})$ (with k_T thermal damping coeficient, T temperature, T_{eql} the equillibrium temperature profile).

The damping coefficients are

$$k_v = k_f \max\left(0, \frac{\sigma - \sigma_b}{1 - \sigma_b}\right) \tag{F.1}$$

$$k_T = k_a + (k_s - k_a)\max\left(0, \frac{\sigma - \sigma_b}{1 - \sigma_b}\right)\cos^4\phi \tag{F.2}$$

where $k_f = 1$ day^{-1}, $k_a = 1/40$ day^{-1}, $k_s = 1/4$ day^{-1}, ϕ is latitude, $\sigma = p/p_s$ is the σ-coordinate, p is pressure, p_s is instantaneous surface pressure, and $\sigma_b = 0.7$ is the top σ-level for damping effects, confining them close to the surface.

The equillibrium temperature profile (in K) is

$$T_{eql} = \max\left[200\text{ K}, \left(315\text{ K} - \Delta T_y \sin^2\phi - \Delta\theta_z \ln\left(\frac{p}{p_o}\right)\cos^2\phi\right)\left(\frac{p}{p_o}\right)^{\kappa}\right] \tag{F.3}$$

where $\Delta T_y = 60$ K, $\Delta\theta_z = 10$ K, $p_o = 1000$ hPa, $\kappa = R/c_p = 2/7$, $R = 287$ J kg^{-1} K^{-1} is gas constant, and $c_p = 1004$ J kg^{-1} K^{-1} is specific heat at constant pressure. The equillibrium temperature profile of this equinox Held-Suarez model configuration is shown in Fig. F.1 (left panel), which shows that the temperature decreases towards the pole and is constant in the stratosphere, i.e. no stratospheric variability such as polar vortex is imposed. To obtain the potential temperature, θ, use $\theta = T(p_o/p)^{\kappa}$ (e.g. Ambaum 2010).

Figs. F.2, F.3 (left panels) show the climatological zonal mean temperature and zonal wind of the equinox configuration, respectively. The temperature profile is similar to the equillibrium temperature profile, whereas the zonal wind shows an eddy-driven jet centred around 40$^{\text{o}}$ latitude in the troposphere of each hemisphere. Note that the troposphere-only zonal mean zonal wind profiles are given in Fig. 3.1.

F.2 Solstice configuration

The solstice configuration follows Polvani and Kushner (2002)'s strong polar vortex forcing ($\Gamma_{pv} = 4$ K km^{-1}) with a troposphere to stratosphere transition at 200 hPa (as in Sheshadri

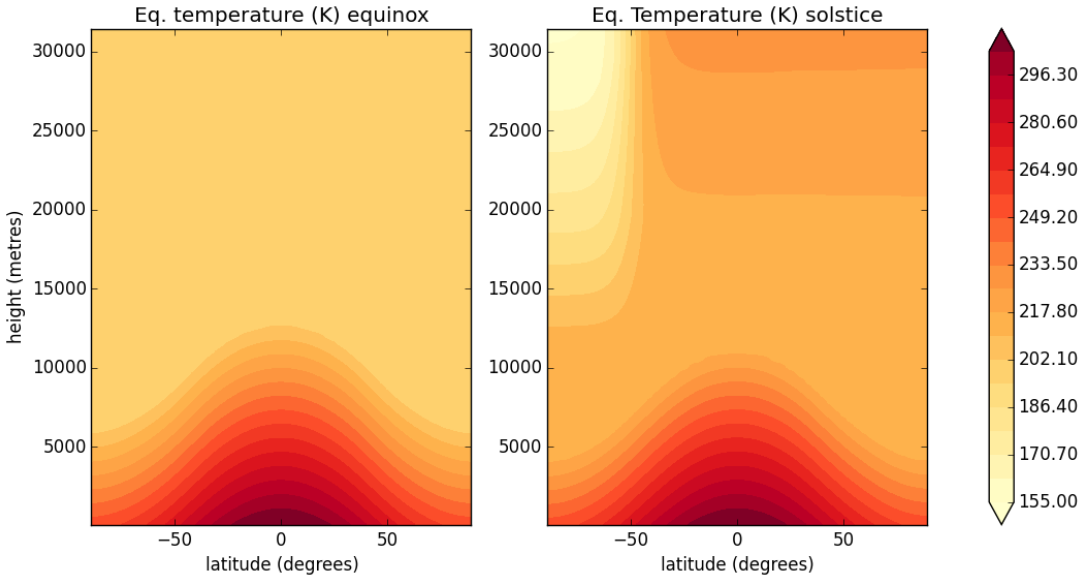

Figure F.1: The equillibrium temperature profile (in K). - For the equinox (left panel) and solstice (right panel) model configurations.

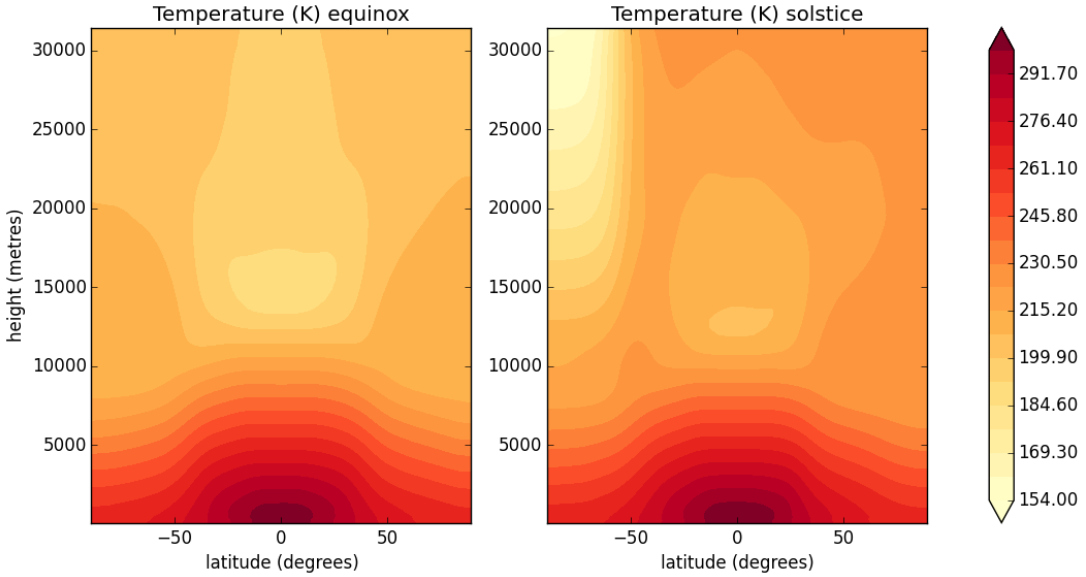

Figure F.2: The climatological zonal mean temperature profile (in K). - For the equinox (left panel) and solstice (right panel) model configurations.

et al. 2015) and only the stratospheric equillibrium temperature profile is modified. The strong polar vortex is in the SH of this model configuration (winter hemisphere), whereas the NH of the model configuration has a warmer stratosphere (summer hemisphere). The damping coefficients

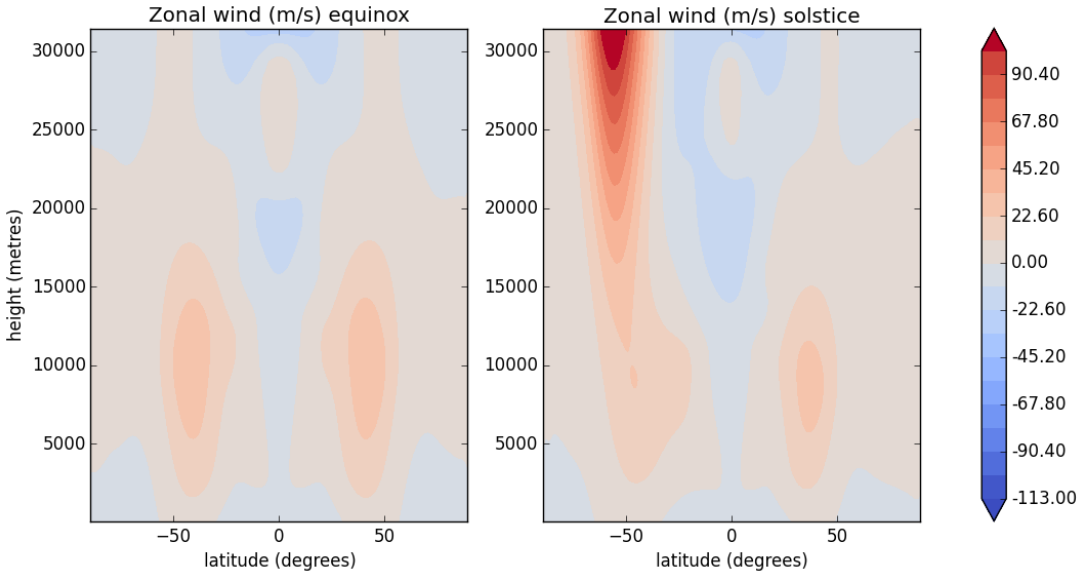

Figure F.3: The climatological zonal mean zonal wind profile (in m/s). - For the equinox (left panel) and solstice (right panel) model configurations.

were not changed, only the equillibrium temperature profile.

To change the equillibrium profile, Polvani and Kushner (2002) used the U.S. Standard Atmosphere (NASA, 1976) as background temperature profile from tropopause upwards. Here, it is defined as (see also Ambaum 2010)

$$T_{us} = \begin{cases} 216.65 \text{ K} & ; \quad 200 \text{ hPa} > p \geq 55 \text{ hPa} \\ T_{oo}\left(\frac{p}{p_{oo}}\right)^{\Gamma R/g}, \text{ with } \Gamma = -1 \text{ K km}^{-1}, & ; \quad 55 \text{ hPa} > p \geq 8.5 \text{ hPa} \\ T_{oo} = 216.65 \text{ K}, \, p_{oo} = 55 \text{ hPa} & \\ T_{oo}\left(\frac{p}{p_{oo}}\right)^{\Gamma R/g}, \text{ with } \Gamma = -2.8 \text{ K km}^{-1}, & ; \quad p < 8.5 \text{ hPa} \\ T_{oo} = 228.65 \text{ K}, \, p_{oo} = 8.5 \text{ hPa} & \end{cases} \tag{F.4}$$

where Γ denotes lapse rate in a given atmospheric layer, $g = 9.81$ is gravitational acceleration and other notation is as defined or as used before.

Combining the above T_{us} profile and the Held and Suarez (1994)'s tropospheric temperature profile with slight warming yields the equillibrium temperature profile

$$T_{eql} = \begin{cases} \max\left[216.65 \text{ K}, \left(315 \text{ K} - \Delta T_y \sin^2\phi - \Delta\theta_z \ln\left(\frac{p}{p_o}\right)\cos^2\phi\right)\left(\frac{p}{p_o}\right)^{\kappa}\right] & ; \quad p \geq 200 \text{ hPa} \\ (1 - W(\phi))T_{us} + W(\phi)T_{pv} & ; \quad p < 200 \text{ hPa} \end{cases} \tag{F.5}$$

where $T_{pv} = T_{us}\,(p/p_T)^{\Gamma_{pv}R/g}$, $p_T = 200$ hPa, $\Gamma_{pv} = 4$ K km^{-1} is the lapse rate defining the strength of the polar vortex (i.e. the cooling of the polar stratosphere), $W(\phi) = 0.5\,[1 - \tanh\,((\phi - \phi_{oo})/\Delta\phi)]$ is the weighting function defining the location of the stratospheric cooling (i.e. polar stratosphere), $\phi_{oo} = -5\pi/18$, and $\Delta\phi = \pi/18$. This equillibrium temperature profile is given in Fig. F.1 (right panel), which clearly shows strong cooling in the polar stratosphere in the SH and a warmer stratosphere in NH.

Figs. F.2, F.3 (right panels) show the climatological zonal mean temperature and zonal wind of the solstice configuration, respectively. The temperature profile is similar to the equillibrium temperature profile, whereas the zonal wind shows tropospheric eddy-driven jets centred around 35°N (summer hemisphere) and 45°S (winter hemisphere), as well as a strong polar vortex in the SH stratosphere centered around 60°S. Again note that the troposphere-only zonal mean zonal wind profiles are given in the main text.

Appendix G

Empirical Orthogonal Function and Regression Analysis

G.1 Empirical Orthogonal Function

As mentioned in section 3.2.2, the data are first averaged vertically and zonally, as well as weighted by $\sqrt{\cos\phi}$ (where ϕ is latitude), before calculating empirical orthogonal function (EOF). The data can now be represented as a latitude-time matrix $\mathbf{X}(t, \phi)$, which is then used in the EOF analysis.

Since the spatial dimension (for data between 20 and 70 degrees latitude at about 1 degree resolution) is considerably smaller than time dimension (with over 9000 points), it is more efficient to first calculate the spatial eigenvectors (usually referred to as EOFs) and from them then calculate principal components (PCs) or temporal eigenvectors.

First, calculate the covariance matrix $\mathbf{S}$ (Ambaum, 2004)

$$\mathbf{S} = \frac{1}{n-1}\mathbf{X}^T\mathbf{X} \tag{G.1}$$

where n is the number of points in time dimension, $\mathbf{S}$ is of size $m \times m$, m is the number of points in spatial dimension, and ^{T} denotes the transpose of the matrix. From $\mathbf{S}$ eigenvectors $\mathbf{\Psi}$ and eigenvalues λ can be calculated using eigenvalue decomposition

$$\mathbf{S}\mathbf{\Psi}_i = \lambda_i\mathbf{\Psi}_i \tag{G.2}$$

where i denotes index of eigenvector. These eigenvectors satisfy orthogonality relationship

$$(\lambda_i - \lambda_j)\mathbf{\Psi}_i \cdot \mathbf{\Psi}_j = 0 \tag{G.3}$$

where $i \neq j$ with i and j, two indices to two different eigenvectors of the same covariance matrix. This means that by construction two eigenvectors must be orthogonal with respect to one another, which can sometimes lead to unphysical or misleading results (Ambaum et al., 2001). Nonetheless, the EOFs are still used for the analysis here as they usually provide a physically consistent picture at least for the leading modes of variability (leading modes of variability or eigenvectors are the ones with the largest eigenvalues), e.g. latitudinal shifting of the jet stream (annular modes).

The eigenvectors are then normalised for easier further comparison of results (such as regressions on various PC timeseries discussed below) using (Ambaum, 2004)

$$|\mathbf{\Psi}_i|^2 = \mathbf{\Psi}_i \cdot \mathbf{\Psi}_i = \lambda_i \tag{G.4}$$

from which the normalisation constant $\alpha_i = \frac{\lambda_i}{|\mathbf{\Psi}_i|^2}$ can be defined, which helps rescaling the eigenvectors as

$$\mathbf{EOF}_i = \mathbf{\Psi}_i\sqrt{\alpha_i} \tag{G.5}$$

where the normalised spatial eigenvector is now called EOF.

As the temporal variance of the field is also of interest, the temporal eigenvectors $\mathbf{P}$ from these spatial eigenvectors are calculated as (Ambaum, 2004)

$$\mathbf{P}_i = \frac{1}{\lambda_i}\mathbf{X}\mathbf{\Psi}_i. \tag{G.6}$$

These can be further normalised using

$$|\mathbf{P}_i|^2 = \mathbf{P}_i \cdot \mathbf{P}_i = n - 1 \tag{G.7}$$

as the normalisation procedure, which gives another normalisation constant $\beta_i = \frac{n-1}{|\mathbf{P}_i|^2}$, which can be used to rescale the temporal eigenvector to obtain principal component timeseries (PCs):

$$\mathbf{PC}_i = \mathbf{P}_i\sqrt{\beta_i}. \tag{G.8}$$

With this analysis the EOFs (spatial eigenvectors) and PCs (temporal eigenvectors) of a given field were obtained. Note that a combination of these eigenvators can recover the initial field and can also be used for reducing the dimensions (useful for large datasets) as only the first few EOFs/PCs usually explain most of the variance in the field.

Note that EOFs/PCs have arbitrariness of sign, thus for consistency, the PCs and EOFs with opposite sign to the chosen one (according to previous literature) were multiplied by (-1).

The explained variance by a certain EOF/PC is reflected in eigenvalues of the above eigenvalue decomposition. The variance is defined as the ratio between the eigenvalue of the i-th eigenvector, divided by the sum of all eigenvalues

$$var_i = \frac{\lambda_i}{\sum_{j=0}^{N} \lambda_j} \tag{G.9}$$

where N is the total number of eigenvalues, and var_i is the variance explained for i-th eigenvector.

G.2 Regression Analysis

To find the magnitude of temporal correlation between a variable and the PC timeseries of another/same variable, the regression analysis is used. This means that for each latitude and height of zonal mean field (or e.g. vertical mean field) a linear regression coefficient between the given timeseries of the field and the PC timeseries is computed. The linear regression is the best fit to the given data and its coefficient is what is ultimately plotted in the regression figures. Linear regression is defined as

$$fit(\mathbf{PC}_i) = kk\mathbf{PC}_i + nn \tag{G.10}$$

where fit represents the best fit of the data with respect to given PC timeseries $\mathbf{PC}_i$, kk is the regression coefficient, and nn is the interception (where the best fit line intercepts y-axis). An example is shown in Fig. G.1 for a regression of zonal mean momentum flux ($[u^*v^*]$) onto the first PC of zonal mean zonal wind. The red circles in the figure denote all time points for the momentum flux at 11.5 km and 45° latitude in the equinox Held-Suarez model run, whose values are shown on y-axis, the x-axis shows the PC timeseries, and the blue solid line shows the best linear regression fit to the given data points. The coefficient in this case is approximately 15 m^2 s^{-2} as the chosen point is near the maximum of the momentum flux influence onto the zonal mean wind. The same methodology was used in Thompson and Woodworth (2014).

While this methodology is linear by construction (thus not capturing nonlinearities), it still provides a leading order response of the fields to given timeseries.

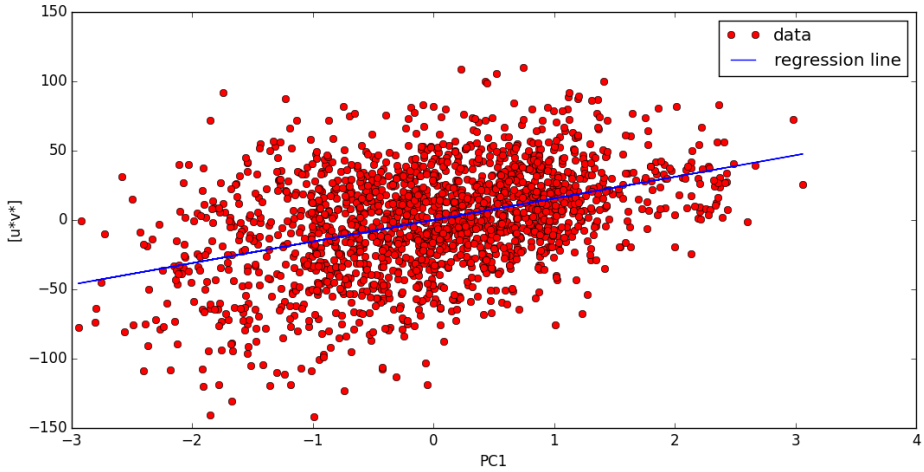

Figure G.1: The regression of zonal mean momentum flux timeseries at 45 degrees latitude and 11.5 km height on PC1 of zonal mean zonal wind. - The momentum flux $[u^*v^*]$ timeseries (in $\mathrm{m}^2\ \mathrm{s}^{-2}$) is shown by red dots and the best fit using linear regression analysis is shown by blue solid line. The data is for a 5-year-long section of the equinox Held-Suarez model configuration.

Appendix H

Visualising Multiscale Asymptotic Primitive Equations

This appendix tests how well the different orders of the asymptotic model from Appendix A [Chapter 2] hold in an idealised model (equinox Held-Suarez model as described in Appendix F). The tests are performed for the case without planetary scale waves (i.e. terms involving $\pi^{(3)}$ vanish), in a time mean framework (all $\partial/\partial t$ terms vanish) and zonal mean ($\partial/\partial x$ terms vanish), but the average over the synoptic meridional scale (ϕ_s) is not performed in order to show the meridional structure.

As the model does not have built-in multi-scale asymptotic methods, we do not separate different scales (synoptic/mean flow) and we test different orders through merging equations at different orders as there is, for example, only one ageostrophic velocity in the model (not several). In other words, the condition is that if the sum of the terms at particular order is much smaller than the individual terms in that equation (at that order), the asymptotic order has good agreement with reality. We then add this sum to the next order approximation and find a new residual etc.

Another step was taken when calculating the terms in the equation. All the equations in Appendix A [Chapter 2] can be multiplied by $\rho^{(0)}$ (balances take a clearer flux form - also for vertical averaging), which represents a problem as it (in a sense) represents the mean density. While in the idealised asymptotic model this is a good approximation, the problems arise when calculating it in the model as the full density is needed in order to close the budgets (as shown below). The density is needed as everything is defined and calculated in geometric height (z)

coordinates instead of the conventional pressure coordinates (where density is included in the pressure coordinate and thus causes no problems). Note also that the UM is formulated in geometric coordinates (the UM's vertical coordinate is terrain-following, but in the Held-Suarez framework there is no topography so this reduces to altitude above sea level).

We first test the accuracy of the vertically averaged primitive equation budget in the height coordinates, and define the so-called density weighted velocities, before calculating the terms at different asymptotic orders.

H.1 Density Weighted Velocities

The density plays an important role in the geometric height primitive equation system (as mentioned above), and the terms can differ significantly from the conventional pressure primitive equation system. To demonstrate this, we first look at the vertically averaged time-zonal mean full continuity equation, and then apply similar logic to the thermodynamic and momentum equations.

The time-zonal mean continuity equation in height coordinates is

$$\frac{\partial}{\partial \tilde{y}} \left(\overline{[\rho][v]}^{t,x} + \overline{\rho^* v^*}^{t,x} \right) + \frac{\partial}{\partial z} \left(\overline{[\rho][w]}^{t,x} + \overline{\rho^* w^*}^{t,x} \right) = 0 \tag{H.1}$$

where square brackets denote zonal mean, asterisk denotes perturbations therefrom, the overline denotes zonal and time average, and under the vertical average the $\partial/\partial z$ terms vanish. An analogous continuity equation in the pressure coordinates is

$$\frac{\partial}{\partial \tilde{y}} \left(\overline{[v]}^{t,x} \right) + \frac{\partial}{\partial p} \left(\overline{[\omega_p]}^{t,x} \right) = 0 \tag{H.2}$$

where ω_p is the vertical velocity in pressure coordinates. It is immediately obvious that there are extra terms in (H.1) compared with (H.2). To demonstrate this difference, the vertically averaged (H.1) is shown in Fig. H.1. Note that the vertical average here is up to the model top (32 km). This shows that the terms $\frac{\partial}{\partial \tilde{y}} \left(\overline{[\rho][v]}^{t,x} \right)$ and $\frac{\partial}{\partial \tilde{y}} \left(\overline{\rho^* v^*}^{t,x} \right)$ balance each other out, rather than each of them integrating to zero as is the case for the $\frac{\partial}{\partial \tilde{y}} \left(\overline{[v]}^{t,x} \right)$ in pressure coordinates.

We thus define density weighted velocities: $U_\rho = \rho u$, $V_\rho = \rho v$, $W_\rho = \rho w$ (in figure labels, subscript m is used instead of subscript ρ), that bring the continuity equation (and similarly

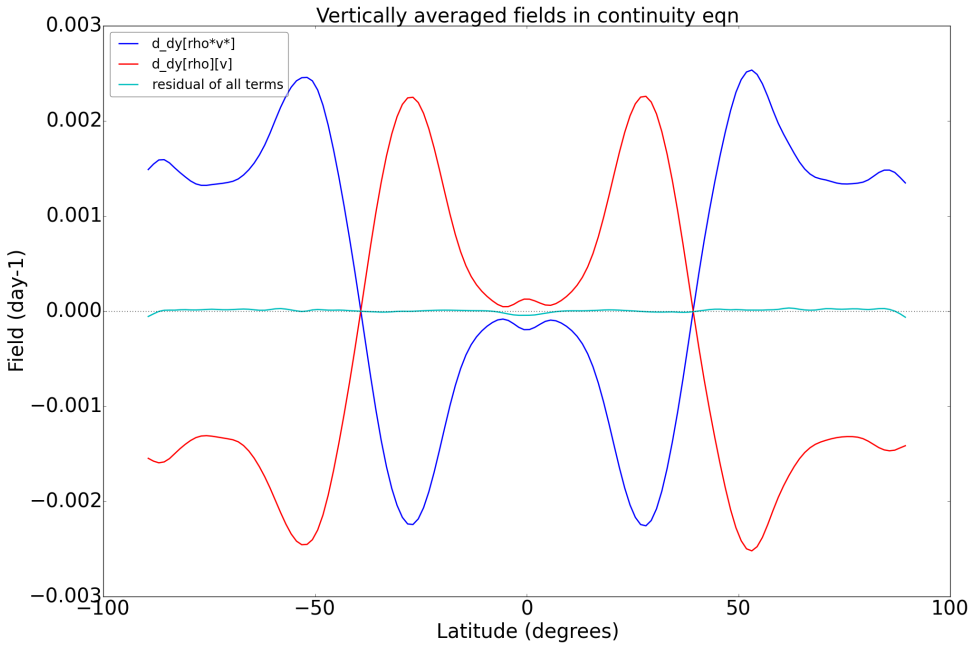

Figure H.1: The vertically averaged continuity equation (H.1). - The blue solid line shows $\frac{\partial}{\partial \tilde{y}}\left(\overline{\rho^* v^*}^{t,x,z}\right)$, the red solid line shows $\frac{\partial}{\partial \tilde{y}}\left(\overline{[\rho][v]}^{t,x,z}\right)$, and the cyan solid line shows the residual of all terms in the continuity equation. The other terms are small. The units are day^{-1}.

also momentum and thermodynamic equation below) closer to the pressure coordinate version (H.2) of it:

$$\frac{\partial}{\partial \tilde{y}}\left(\overline{[V_\rho]}^{t,x}\right) + \frac{\partial}{\partial z}\left(\overline{[W_\rho]}^{t,x}\right) = 0 \tag{H.3}$$

where $[V_\rho] = [v][\rho] + [v^*\rho^*]$, and similarly $[W_\rho] = [w][\rho] + [w^*\rho^*]$. Now the vertical average of (H.3) brings the residual close to zero (i.e. $\frac{\partial}{\partial \tilde{y}}\left(\overline{[V_\rho]}^{t,x}\right)$ integrates to zero as in the pressure coordinates), and is hence not shown. This facilitates a physical interpretation similar to that in the pressure coordinates (as seen below), and is also consistent with the typical density weighting in the isentropic coordinates (e.g. Andrews et al. 1987).

Similarly, the thermodynamic equation in geometric height coordinates is

$$\begin{aligned}&\frac{\partial}{\partial \tilde{y}}\left(\overline{[\rho][\theta][v]}^{t,x} + \overline{[\rho]\theta^* v^*}^{t,x} + \overline{\rho^*\theta^*[v]}^{t,x} + \overline{\rho^* v^*[\theta]}^{t,x} + \overline{\rho^* v^*\theta^*}^{t,x}\right)\\ +&\frac{\partial}{\partial z}\left(\overline{[\rho][\theta][w]}^{t,x} + \overline{[\rho]\theta^* w^*}^{t,x} + \overline{\rho^*\theta^*[w]}^{t,x} + \overline{\rho^* w^*[\theta]}^{t,x} + \overline{\rho^* w^*\theta^*}^{t,x}\right) = \overline{\rho S_\theta}^{t,x}\end{aligned} \tag{H.4}$$

which can be rewritten using the density weighted velocities as

$$\frac{\partial}{\partial \tilde{y}}\left(\overline{[\theta][V_\rho]}^{t,x}+\overline{\theta^* V_\rho^*}^{t,x}\right)+\frac{\partial}{\partial z}\left(\overline{[\theta][W_\rho]}^{t,x}+\overline{\theta^* W_\rho^*}^{t,x}\right)=\overline{\rho S_\theta}^{t,x} \tag{H.5}$$

where S_θ are the diabatic source-sink terms. Equation (H.5) now closely resembles the thermodynamic equation in pressure coordinates. Figs. H.2, H.3 compare the vertically averaged budgets (H.4) and (H.5), respectively.

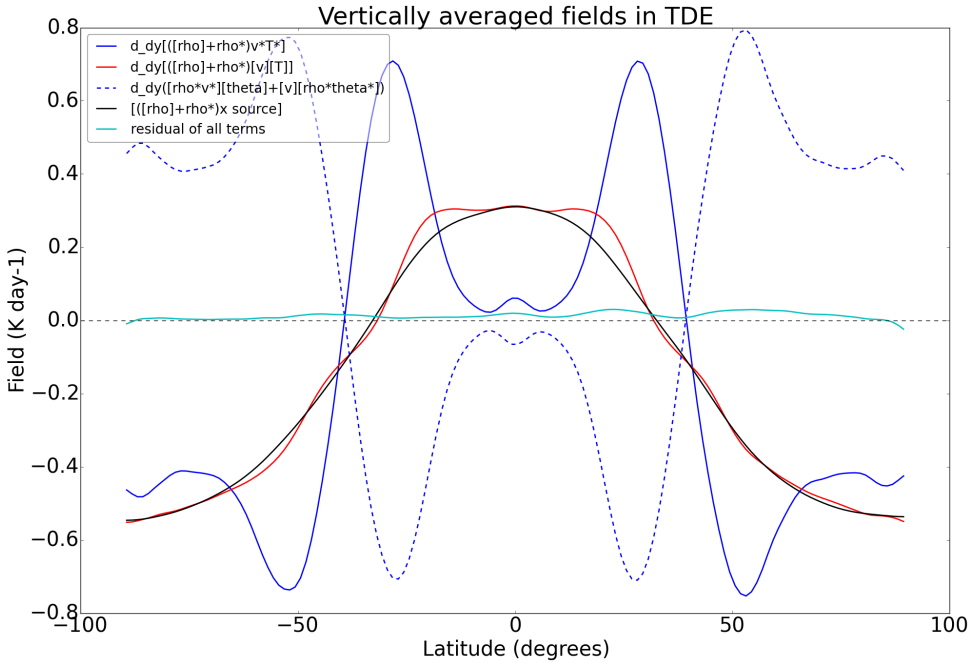

Figure H.2: The vertically averaged thermodynamic equation (H.4). - The blue solid line shows $\frac{\partial}{\partial \tilde{y}}\left(\overline{([\rho]+\rho^*)\theta^* v^*}^{t,x,z}\right)$, the red solid line shows $\frac{\partial}{\partial \tilde{y}}\left(\overline{([\rho]+\rho^*)[\theta][v]}^{t,x,z}\right)$, the blue dashed line shows $\frac{\partial}{\partial \tilde{y}}\left(\overline{\rho^*\theta^*[v]}^{t,x}+\overline{\rho^* v^*[\theta]}^{t,x}\right)$, the black solid line is the source-sink term $\overline{([\rho]+\rho^*)S_\theta}$, and the cyan solid line shows the residual of all terms in the thermodynamic equation. The other terms are small. The units are K day^{-1}.

Fig. H.2 shows that in the vertical average the following terms in thermodynamic equation (H.4) balance each other out: $\frac{\partial}{\partial \tilde{y}}\left(\overline{([\rho]+\rho^*)[\theta][v]}^{t,x,z}\right) \approx \overline{([\rho]+\rho^*)S_\theta}^{t,x,z}$ (the mean meridional flux term closely follows the diabatic heating term) and $\frac{\partial}{\partial \tilde{y}}\left(\overline{([\rho]+\rho^*)\theta^* v^*}^{t,x,z}+\overline{\rho^*\theta^*[v]}^{t,x,z}+\overline{\rho^* v^*[\theta]}^{t,x,z}\right) \approx 0$ (this is due to ρ^* and θ^* being related through the ideal gas law) where the term with $\rho^*\theta^*[v]$ is much smaller than the rest. Notice how the additional terms (those including ρ^*) balance the eddy heat flux term, implying that

the eddy heat fluxes are not important for the atmospheric energy budget in the midlatitudes. This is counter-intuitive as we would expect the mean terms of thermodynamic equation to be more important in the tropics and the eddy terms to be more important in the extratropics from the more familiar pressure coordinate system, but here the eddy terms cancel out and the mean term is balanced by the source term.

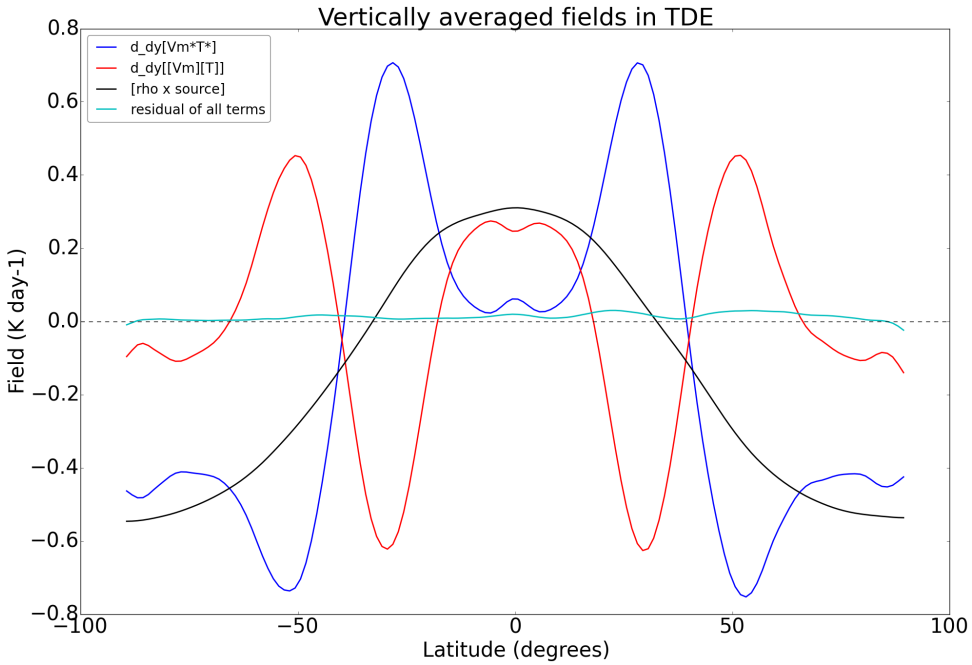

Figure H.3: The vertically averaged thermodynamic equation (H.5). - The blue solid line shows $\frac{\partial}{\partial \tilde{y}}\left(\overline{V_\rho^* \theta^*}^{t,x,z}\right)$, the red solid line shows $\frac{\partial}{\partial \tilde{y}}\left(\overline{[V_\rho][\theta]}^{t,x,z}\right)$, the black solid line is the source-sink term $[\rho S_\theta]$, and the cyan solid line shows the residual of all terms in the thermodynamic equation. The other terms are small. The units are K day^{-1}.

The latter problem vanishes when the density weighted velocities are used. Fig. H.3 shows the terms in the vertically averaged thermodynamic equation (H.5), which shows that this approach restores a more familiar picture (e.g. from pressure coordinate system): the mean term is balancing out the diabatic heating in the tropics, while the eddy terms are larger in the extratropics, largely balanced by the mean terms and their residual is balanced by the source term.

Finally, following the logic for the thermodynamic and continuity equations we now compare the momentum equation in the geometric height coordinates with and without the density

weighted velocities. The momentum equation is

$$\begin{aligned}
&\frac{\partial}{\partial \tilde{y}}\left(\overline{[\rho][v][u]}^{t,x}+\overline{[\rho]v^*u^*+}^{t,x}+\overline{\rho^*u^*[v]}^{t,x}+\overline{\rho^*v^*[u]}^{t,x}+\overline{\rho^*v^*u^*}^{t,x}\right)\\
+&\frac{\partial}{\partial z}\left(\overline{[\rho][u][w]}^{t,x}+\overline{[\rho]u^*w^*}^{t,x}+\overline{\rho^*u^*[w]}^{t,x}+\overline{\rho^*w^*[u]}^{t,x}+\overline{\rho^*w^*u^*}^{t,x}\right)\\
-&\frac{\tan\phi}{a}\left(\overline{[\rho][v][u]}^{t,x}+\overline{[\rho]v^*u^*+}^{t,x}+\overline{\rho^*u^*[v]}^{t,x}+\overline{\rho^*v^*[u]}^{t,x}+\overline{\rho^*v^*u^*}^{t,x}\right)\\
&-\overline{f([\rho][v]+\rho^*v^*)}^{t,x}=\overline{(\rho^*+[\rho])S_u}^{t,x}
\end{aligned}\tag{H.6}$$

which can be reqritten using the density weighted velocities as

$$\frac{\partial\left(\overline{[V_\rho][u]+V_\rho^*u^*}^{t,x}\right)}{\partial\tilde{y}}+\frac{\partial\left(\overline{[W_\rho][u]+W_\rho^*u^*}^{t,x}\right)}{\partial z}-\frac{\tan\phi}{a}\left(\overline{[V_\rho][u]+V_\rho^*u^*}^{t,x}\right)-\overline{f[V_\rho]}^{t,x}=\overline{\rho S_u}^{t,x}\tag{H.7}$$

where S_u is the momentum (frictional) source-sink term. Figs. H.4 and H.5 show the vertically averaged terms from equations (H.6) and (H.7), respectively.

As for the thermodynamic and continuity equations we can see some clear cancellations of terms also for the momentum equation (H.6) in Fig. H.4: the two Coriolis terms ($-\overline{f([\rho][v]+\rho^*v^*)}^{t,x}$) cancel out due to mass conservation (as for the continuity equation (H.1)), the eddy terms (involving eddy momentum fluxes $([\rho]+\rho^*)u^*v^*$) closely follow the frictional term (ρS_u) and largely balance it out, with some help from the mean terms (involving zonal mean momentum fluxes $([\rho]+\rho^*)[u][v]$ or meridional circulation $[\rho][v]$ terms) and the additional terms (other terms involving ρ^*v^*).

Fig. H.5, where the density weighted velocities are used, again recovers the more familiar picture (from pressure coordinates: see, e.g., Fig. 8a of Haigh et al. 2005). Here the eddies (terms involving $V_\rho^*u^*$) dominate the extratropics and are mainly balanced by the frictional (ρS_u) source term (as in Fig. H.4), and their residual is balanced by the sum of the mean terms (terms involving $[V_\rho][u]$). The Coriolis term ($-f[V_\rho]$) is zero in the vertical average as is the case in the pressure coordinates. The final residual in both figures is small (budgets are well-closed), and closely resemble each otehr (approaches are complementary).

These density weighted velocities recover a more familiar picture (as in pressure coordinates), and also a more accurate picture as we then use the full density ($\rho=[\rho]+\rho^*$) instead of just zonal (or global) mean density ($[\rho]$) that was suggested by the asymptotic theory ($\rho^{(0)}$) in Chapter 2.

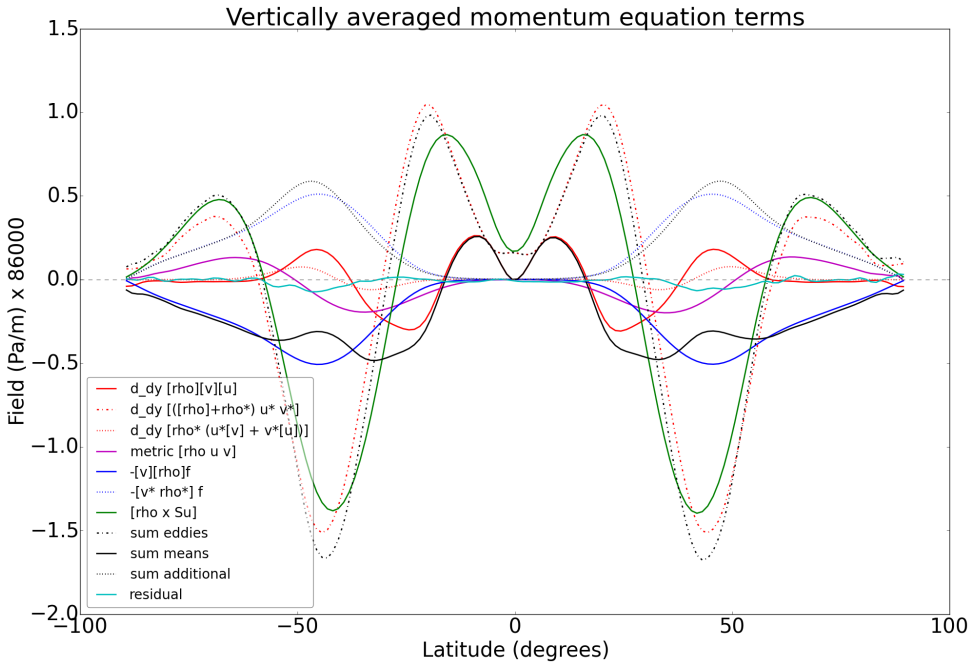

Figure H.4: The vertically averaged momentum equation (H.6). - The red dash-dotted solid line shows $\frac{\partial}{\partial \tilde{y}}\left(\overline{([\rho]+\rho^*)v^*u^*}^{t,x,z}\right)$, the red solid line shows $\frac{\partial}{\partial \tilde{y}}\left(\overline{([\rho]+\rho^*)[v][u]}^{t,x,z}\right)$, the red dotted line shows $\frac{\partial}{\partial \tilde{y}}\left(\overline{\rho^*u^*[v]+\rho^*v^*[u]}^{t,x,z}\right)$, the green solid line is the source-sink term $\overline{([\rho]+\rho^*)S_u}^{t,x,z}$, the blue solid line is the mean Coriolis term $(-\overline{f[v][\rho]}^{t,x,z})$, the blue dotted line is the additional Coriolis term $(-\overline{fv^*\rho^*}^{t,x,z})$, the purple solid line shows the sum of all metric terms (involving $\tan\phi/a$), the black dash-dotted line shows the sum of all eddy terms (involving v^*u^*), black solid line shows the sum of all mean terms (involving $[v][u]$ and Coriolis term $-\overline{f[v][\rho]}^{t,x,z}$), black dotted line shows the sum of additional terms (those involving ρ^*v^* and ρ^*u^*), and the cyan solid line shows the residual of all terms in the momentum equation. The other terms are small. The units are kg m^{-2} s^{-1} day^{-1}.

Therefore, to test the equations at different asymptotic orders, we use density weighted velocities for the remainder of this section.

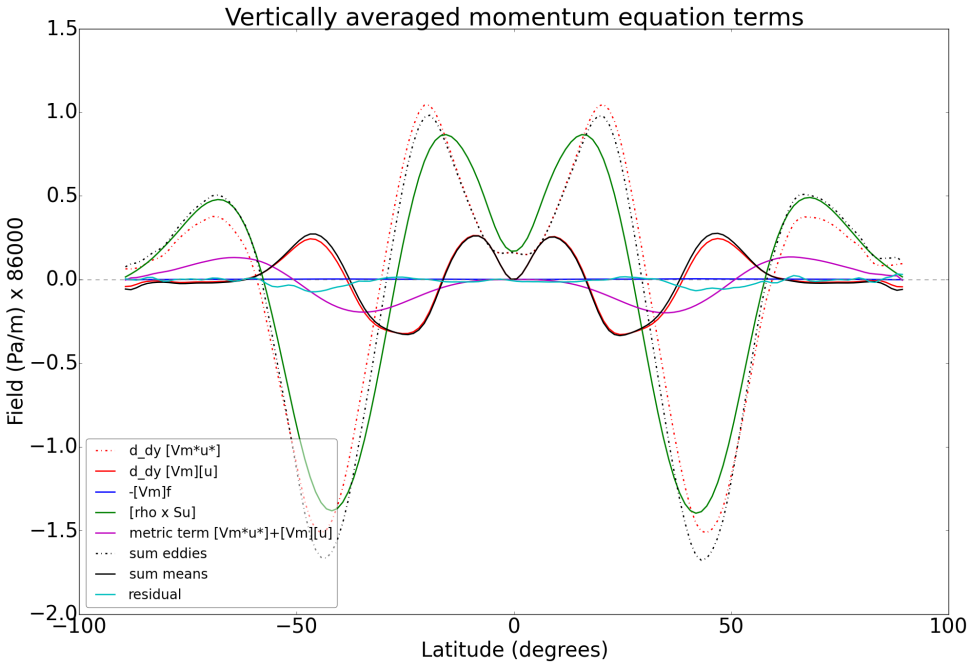

Figure H.5: The vertically averaged momentum equation (H.7). - The red dash-dotted solid line shows $\frac{\partial}{\partial \bar{y}}\left(\overline{V_\rho^* u^*}^{t,x,z}\right)$, the red solid line shows $\frac{\partial}{\partial \bar{y}}\left(\overline{[V_\rho][u]}^{t,x,z}\right)$, the green solid line is the source-sink term $\overline{\rho S_u}^{t,x,z}$, the blue solid line is the Coriolis term $(-\overline{f[V_\rho]}^{t,x,z})$, the purple solid line shows the sum of all metric terms (involving $\tan\phi/a$), the black dash-dotted line shows the sum of all eddy terms (involving $V_\rho^* u^*$), black solid line shows the sum of all mean terms (involving $[V_\rho]$) and the cyan solid line shows the residual of all terms in the momentum equation. The other terms are small. The units are kg m^{-2} s^{-1} day^{-1}.

H.2 Different asymptotic orders

In order to apply the equations from the asymptotic theory in Appendix A [Chapter 2] to the model output, we need to recognise which terms in the primitive equations correspond to the terms in the asymptotic system (A.4 - A.18). In the primitive equations we usually split the terms into zonal mean and perturbation from this mean (as done above), and here we use the density weighted velocities (as established above): $u = u^* + [u]$ (for u-momentum equation), $U_\rho = [U_\rho] + U_\rho^*$ (for geostrophic balance), $V = V_\rho^* + [V_\rho]$, $\theta = \theta^* + [\theta]$, $\rho = \rho^* + [\rho]$, and $W_\rho = W_\rho^* + [W_\rho]$, which can be related to the terms in the equations (A.4 - A.18) to leading order as:

- zonal mean zonal velocity: $[u] \Leftrightarrow u^{(0)}$,
- density weighted zonal mean zonal velocity: $[U_\rho] \Leftrightarrow \rho^{(0)} u^{(0)}$,
- zonally perturbed zonal velocity: $u^* \Leftrightarrow u^{(1)*}$,
- zonally perturbed density weighted meridional velocity: $V_\rho^* \Leftrightarrow \rho^{(0)} v^{(1)*}$,
- zonal mean pressure: $[p] \Leftrightarrow p^{(2)}$,
- zonal mean potential temperature: $[\theta] \Leftrightarrow [\theta^{(2)}]$,
- zonally perturbed potential temperature: $\theta^* \Leftrightarrow \theta^{(4)*}$,
- ageostrophic meridional velocity: $[V_\rho] \Leftrightarrow \rho^{(0)}[v^{(2)}]$,
- ageostrophic vertical velocity: $[W_\rho] \Leftrightarrow \rho^{(0)}[w^{(4)}]$,
- zonally perturbed density weighted vertical velocity: $W_\rho^* \Leftrightarrow \rho^{(0)} w^{(4)*}$, and
- density: $\rho \Leftrightarrow \rho^{(0)}$ (full density is used for accuracy).

Here note that W_ρ^* is not present in the asymptotic equations where planetary waves are weak. Also, higher asymptotic orders of terms considered above follow similar logic and are hence not repeated.

Continuity and Thermodynamic Equations

Applying the above relations, the continuity equation (A.15) under time average predicts

$$\frac{\partial}{\partial \tilde{y}}\left(\overline{[V_\rho]}^{t,x}\right)+\frac{\partial}{\partial z}\left(\overline{[W_\rho]}^{t,x}\right)=0 \tag{H.8}$$

and (A.16) (or any higher orders) is just a higher order correction to (A.15). Equation (A.11) predicts that

$$\frac{\partial}{\partial \tilde{y}}\left(\overline{[V_\rho][\theta]}^{t,x}\right)+\frac{\partial}{\partial z}\left(\overline{[W_\rho][\theta]}^{t,x}\right)=\overline{\rho S_\theta}^{t,x} \tag{H.9}$$

while the sum of (A.11) and (A.12) predicts:

$$\frac{\partial}{\partial \tilde{y}}\left(\overline{[V_\rho][\theta]}^{t,x}+\overline{V_\rho^*\theta^*}^{t,x}\right)+\frac{\partial}{\partial z}\left(\overline{[W_\rho][\theta]}^{t,x}\right)=\overline{\rho S_\theta}^{t,x}. \tag{H.10}$$

These equations suggest that for thermodynamic and continuity equations at the leading order only the mean fluxes are important, while the eddy fluxes enter at higher orders. This was tested in the equinox Held-Suarez model output on both the continuity (Fig. H.6) and thermodynamic equations (Fig. H.7), where it is clear that the terms in the continuity equation as well as the mean heat fluxes in the thermodynamic equation largely cancel out (Figs. H.6a-b, H.7a-b), leaving only a small residual (Figs. H.6c, H.7c). Note that the residual shows some numerical discretisation errors in the tropics which hides the smaller residual in the extratropics. Equation (H.9) also suggests that the diabatic heating (Fig. H.7d) would help reducing the residual, which is indeed shown in Fig. H.7g.

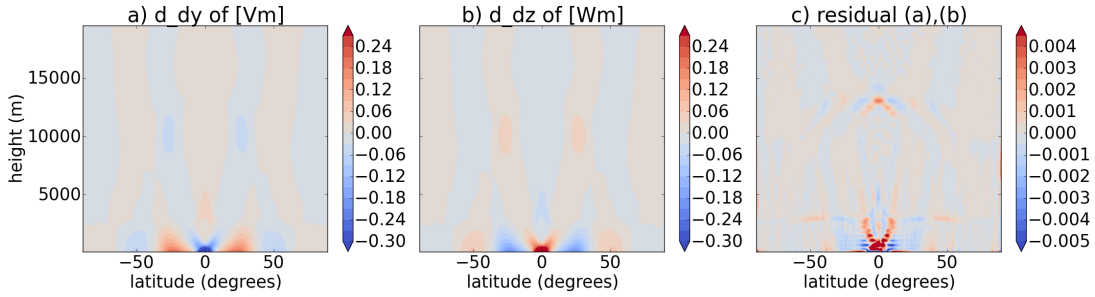

Figure H.6: Meridional-vertical cross section of the continuity equation (H.8) terms. - (a) $\frac{\partial}{\partial \tilde{y}}\left(\overline{[V_\rho]}^{t,x}\right)$, (b) $\frac{\partial}{\partial z}\left(\overline{[W_\rho]}^{t,x}\right)$, and (c) the residual of the continuity equation. The units are kg m^{-3} day^{-1}. Note that the colourbars are not the same.

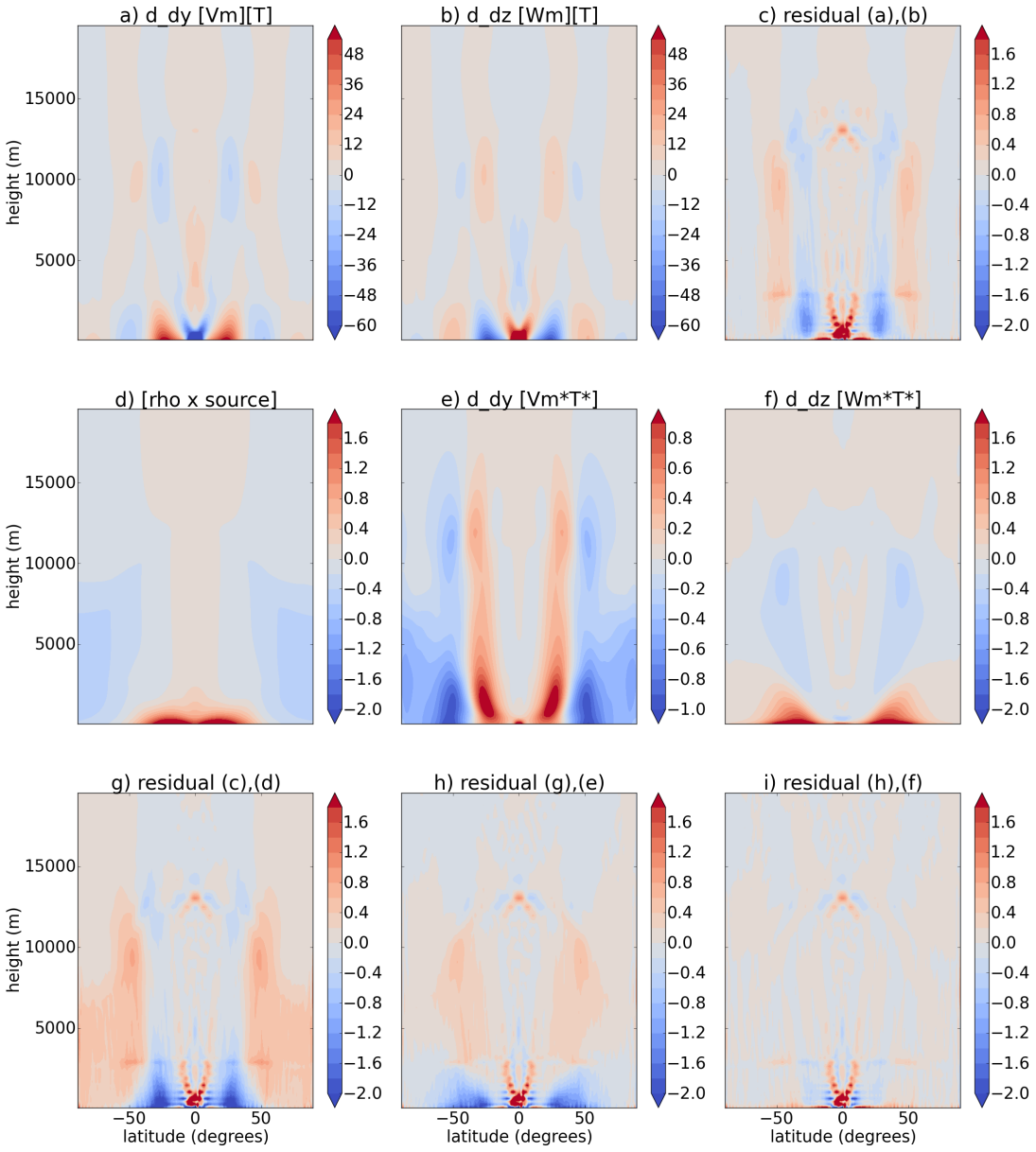

Figure H.7: Meridional-vertical cross section of the terms in the thermodynamic equations (H.9) and (H.10). - a) $\frac{\partial}{\partial \tilde{y}}\left(\overline{[V_\rho][\theta]}^{t,x}\right)$, b) $\frac{\partial}{\partial z}\left(\overline{[W_\rho][\theta]}^{t,x}\right)$, c) the residual of the terms in (a) and (b), d) $\overline{\rho S_\theta}^{t,x}$, e) $\frac{\partial}{\partial \tilde{y}}\left(\overline{V_\rho^* \theta^*}^{t,x}\right)$, f) $\frac{\partial}{\partial z}\left(\overline{W_\rho^* \theta^*}^{t,x}\right)$, g) the residual of the terms in (a), (b), and (d) [equation (H.9)], h) the residual of the terms in (a), (b), (d), and (e) [equation (H.10)], and i) the residual of the thermodynamic equation (H.5), i.e. adding the term in (f) to the residual in (h). The units are kg K m^{-3} day^{-1}. Note that the colourbars are not the same.

Fig. (H.7e) shows the term with the meridional eddy heat fluxes, which is much smaller than the mean heat flux terms, confirming the above statements. Notice that the term with the vertical eddy heat fluxes (Fig. H.7f) does not enter (H.9) or (H.10) (as it is also the case in the quasi-geostrophic system). However, the vertical eddy heat flux term turns out to be comparable in magnitude to the diabatic heating, and also concentrated near the surface, something that is not represented in the asymptotic theory. This suggests that it should perhaps be considered as a part of the diabatic heating from the perspective of the theory. The residuals of (H.10) and (H.5) are given in Fig. H.7h-i for comparison.

Momentum Equation

The leading order momentum equations (A.4)-(A.5) in the asymptotic theory predict a zonal mean geostrophic balance:

$$\overline{fU_\rho}^{t,x} = -\frac{\partial \overline{p}^{t,x}}{\partial y}. \tag{H.11}$$

Fig. H.8 shows the geostrophic balance (H.11) for the zonal wind, demonstrating that the balance between the Coriolis and pressure gradient forces is a leading order balance with the residual (Fig. H.8c) two orders of magnitude smaller than the individual terms in the balance (Fig. H.8a,b). Note that this leading order balance occurs only in the v-momentum equation (zonal geostrophic wind) under zonal mean.

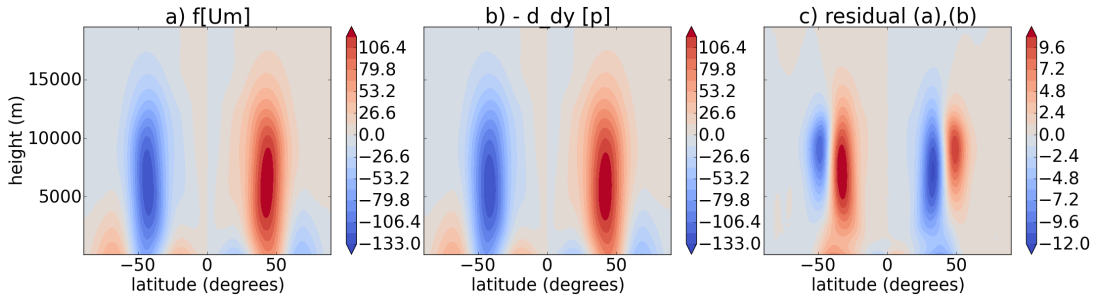

Figure H.8: Meridional-vertical cross section of the geostrophic balance (H.11) terms. - (a) $\overline{fU_\rho}^{t,x}$, (b) $-\frac{\partial \overline{p}^{t,x}}{\partial y}$, and (c) the residual of the geostrophic balance. The units are kg m^{-2} s^{-1} day^{-1}. Note that the colourbars are not the same.

The higher asymptotic order approximations of the momentum equation (A.6)-(A.8) are:

$$3^{rd} \text{ order}$$

$$-\overline{fV_\rho}^{t,x} = \overline{\rho S_u}^{t,x} \tag{H.12}$$

$$4^{rd} \text{ order}$$

$$\frac{\partial\left(\overline{[V_\rho][u]+V_\rho^* u^*}^{t,x}\right)}{\partial\tilde{y}} + \frac{\partial\left(\overline{[W_\rho][u]}^{t,x}\right)}{\partial z} - \overline{fV_\rho}^{t,x} = \overline{\rho S_u}^{t,x} \tag{H.13}$$

$$5^{rd} \text{ order}$$

$$\frac{\partial\left(\overline{[V_\rho][u]+V_\rho^* u^*}^{t,x}\right)}{\partial\tilde{y}} + \frac{\partial\left(\overline{[W_\rho][u]+W_\rho^* u^*}^{t,x}\right)}{\partial z} - \frac{\tan\phi}{a}\left(\overline{[V_\rho][u]+V_\rho^* u^*}^{t,x}\right)$$
$$-\overline{fV_\rho}^{t,x} + \overline{\cos\phi W_\rho}^{t,x} = \overline{[\rho S_u]}^{t,x}. \tag{H.14}$$

Here, only the time-zonal mean u-momentum budget is given, which is analysed in more detail in Chapters 2-4. Fig. H.9 shows the terms in equations (H.12)-(H.14) and the residuals of each order. Notice how the leading order terms from (H.12) in Fig. H.9a,b are of similar magnitude to the residual of the geostrophic wind, which is two orders of magnitude smaller than the geostrophic balance, consistent with the asymptotic orders (i.e. geostrophic balance appears at the first order, (H.12) respresents the third order).

The third asymptotic order (H.12) shows the balance between the Coriolis force and the frictional term, which both maximise close to the surface (Fig. H.9a,b), and balance each other out (Fig. H.9c). The upper-level part of the Coriolis term is much weaker and balances out the momentum fluxes at higher orders. This suggests that the asymptotic theory also distinguishes between the different parts of the domain as well. This would indicate that the usual Ferell cell picture (e.g. Vallis 2006, Fig. 11.15) would have a stronger lower-tropospheric branch than the upper-tropospheric one.

The fourth asymptotic order (H.13) adds the meridional and vertical momentum flux divergence to the balance, except for the vertical eddy momentum flux divergence ($\partial\left(\overline{W_\rho^* u^*}^{t,x}\right)/\partial z$). This order now represents the upper-tropospheric balance, but its residual (Fig. H.9h) is of similar order to the individul terms in (H.13), however once the vertical eddy momentum flux divergence (Fig. H.9g) is added to the residual (Fig. H.9i) the values reduce significantly. This means that the fourth asymptotic order would be closed better if the vertical eddy momentum flux divergence were added (this is the case when planetary scale waves are considered), and

suggests that at this order the asymptotic theory is less correct.

The fifth asymptotic order (H.14) incorporates the vertical eddy momentum flux divergence, as well as the metric terms (involving $\tan\phi/a$, Fig. H.9j,k). This budget is then well closed with the residual (Fig. H.9l) much smaller than the individual terms. There is another term that is present in (H.14), $\overline{\cos\phi W_\rho}^{t,x}$, which is of similar magnitude as the residual (not shown), and should become relevant at the next order, but is already present in the fifth order, again suggesting that the asymptotic theory is less correct in this case. Note that the residual of the fifth order (Fig. H.9l) is likely at the limit of the discretisation accuracy used here (centred-in-space scheme).

The majority of the balances described in this appendix are consistent with the conventional dimensional analysis (e.g. Holton 2004), with minor discrepancies in the asymptotic theory as described above. This means that the asymptotic methods reproduce the balances expected from dimensional analysis reasonably well. An interesting balance is the one at the third order that shows stronger lower-tropospheric balance compared to the upper-tropospheric one at the fourth order, having implications for the Ferell cell. We also find that the geometric height primitive equations with the density weighted velocities have a more familiar physical interpretation (similar to the pressure coordinates), and were hence used for the majority of this section.

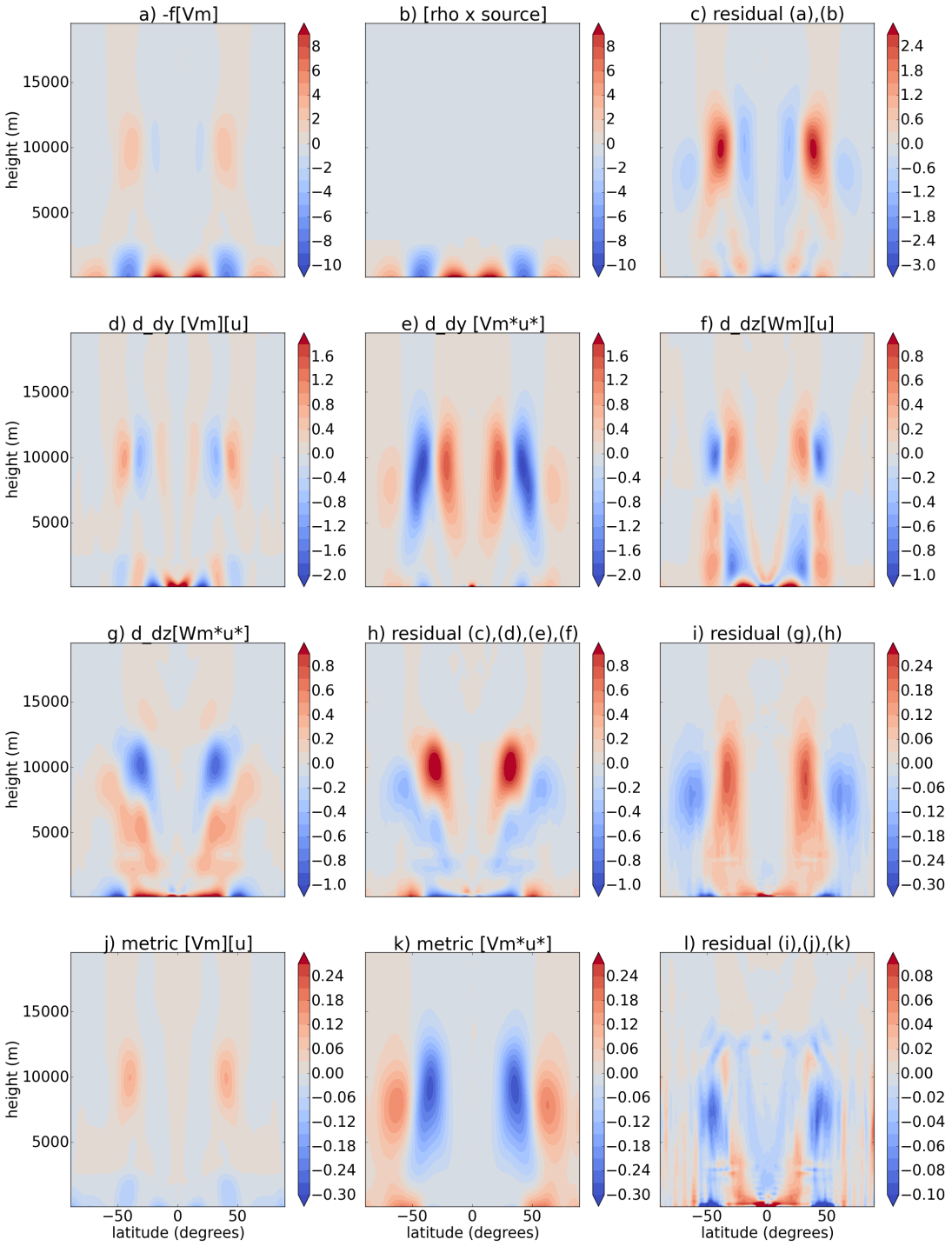

Figure H.9: Meridional-vertical cross section of the u-momentum budget (H.12)-(H.14) terms. - a) $-\overline{fV_\rho}^{t,x}$, b) $\overline{\rho S_u}^{t,x}$, c) the residual of the third order momentum equation (H.12), d) $\frac{\partial\left(\overline{[V_\rho][u]}^{t,x}\right)}{\partial\tilde{y}}$, e) $\frac{\partial\left(\overline{V_\rho^* u^*}^{t,x}\right)}{\partial\tilde{y}}$, f) $\frac{\partial\left(\overline{[W_\rho][u]}^{t,x}\right)}{\partial z}$, g) $\frac{\partial\left(\overline{W_\rho^* u^*}^{t,x}\right)}{\partial z}$, h) residual of the fourth order momentum equation (H.13), i) residual between (h) and (g), j) $-\frac{\tan\phi}{a}\left(\overline{[V_\rho][u]}^{t,x}\right)$, k) $-\frac{\tan\phi}{a}\left(\overline{V_\rho^* u^*}^{t,x}\right)$, l) residual of the fifth order momentum equation (H.14). The units are kg m^{-2} s^{-1} day^{-1}. Note that the colourbars are not the same.

Appendix I

Aquaplanet configuration in the Unified Model

The prescribed sea-surface-temperature (SST) and perpetual equinox aquaplanet configuration of the Met Office Unified Model (UM), vn. 8.6, is used in this chapter (as mentioned in the main text). The horizontal resolution (N96) of this model configuration is the same as for the Held-Suarez model configuration (previous chapter), however the aquaplanet model is run with 85 vertical levels (with top level at 85 km) and varying vertical resolution (from approximately 30 m at the surface to approximately 5 km near the model top). The output is analysed on 15 vertical pressure levels between 925 hPa and 100 hPa at 6-hourly resolution.

This configuration is different from the Held-Suarez model used in the previous chapter, in that it includes complex parametrisations schemes of the general circulation models (GCMs), including full moisture parametrisation. The latter is important for midlatitude storms, and its influence on the time mean storm track path was also examined here (section 4.3), in addition to the analysis of the baroclinic and barotropic flows.

The aquaplanet model is generally zonally homogeneous, however local zonal asymmetries can be introduced through different components (e.g. by adding orography, locally increasing temperature or sensible/latent heat fluxes etc.; see, e.g., Brayshaw et al. 2009; Kaspi and Schneider 2011). The different configurations mentioned in Chapter 4 are described below in more detail.

I.1 Zonally homogeneous configuration (control)

The zonally homogeneous configuration of the UM uses QOBS-SST (Fig. I.1; Neale and Hoskins 2000)

$$T_{QOBS} = \begin{cases} \frac{T_{max}}{2}\left[2 - \sin^4\left(\frac{3\phi}{2}\right) - \sin^2\left(\frac{3\phi}{2}\right)\right] & ; \quad -60^o \leq \phi \leq 60^o \\ 0^oC & ; \quad \text{otherwise} \end{cases} \tag{I.1}$$

where $T_{max} = 27^oC$, and T_{QOBS} is considered the most realistic SST configuration.

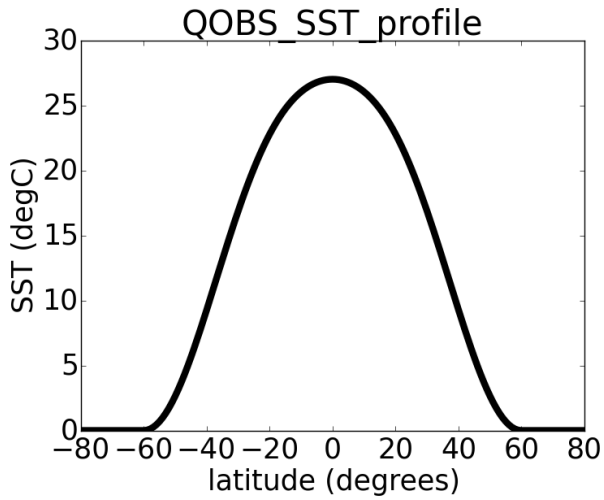

Figure I.1: QOBS sea surface temperature profile (I.1), after Neale and Hoskins (2000).

This model produces zonal mean temperature (Figs. I.2, I.3) and zonal wind profiles (Figs. I.4, I.5) consistent with the Aquaplanet Experiment (APE) (Williamson et al., 2013). The values of temperaure and zonal wind in the troposphere are within the standard deviation of the APE multi-model intercomparison (Figs. I.3, I.5), however there are larger differences in the stratosphere, which could be a consequence of lower model top/vertical resolution or different parametrisation schemes in APE intercomparison compared with the UM.

The aquaplanet model used in this study also exhibits a realistic quasi-biennial oscillation (QBO) (Fig. I.6), which comes from the non-orographic gravity wave drag parametrisation (and disappears upon switching it off). The UM aquaplanet configuration has a single Intertropical-Convergence-Zone (ITCZ) bias, seen in the zonal mean precipitation distribution (Fig. I.7), where the APE multimodel mean peak at the Equator is significantly reduced (and wider in latitude) due to a subset of models with a double-ITCZ bias (Williamson et al., 2013).

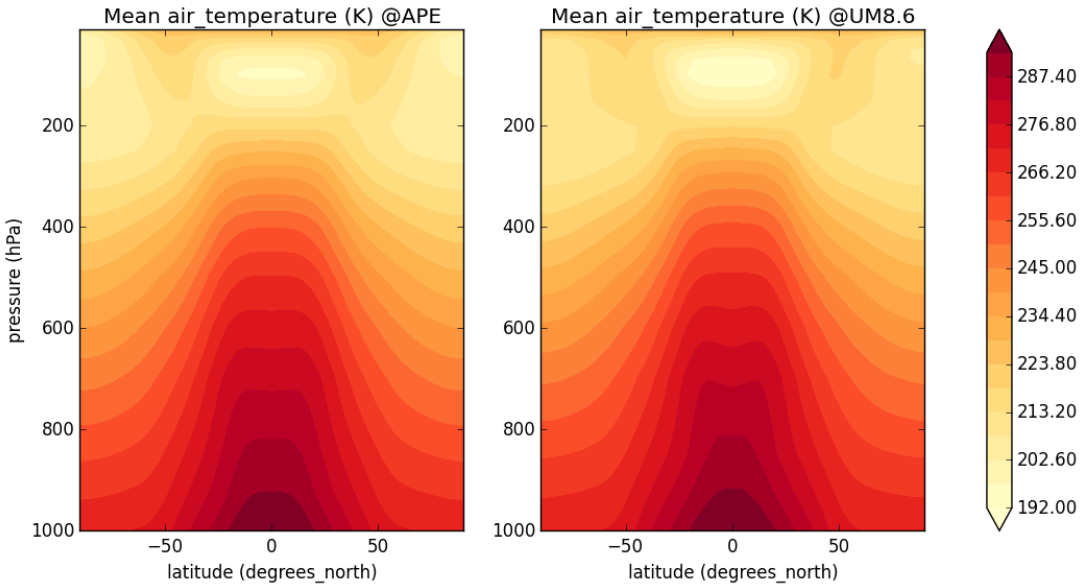

Figure I.2: Zonal mean temperature (in K) profile from APE (left) and the Unified Model used here (right).

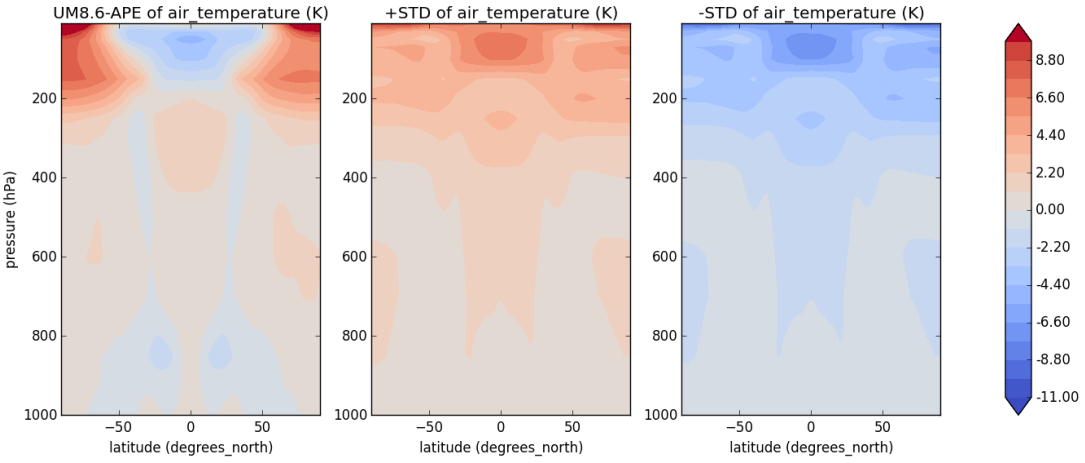

Figure I.3: The difference between the zonal mean temperature (in K) profiles of APE and the Unified Model used here (left panel). - For comparison, the ± standard deviations (STD) of the multimodel mean of APE are given in the middle and right panels.

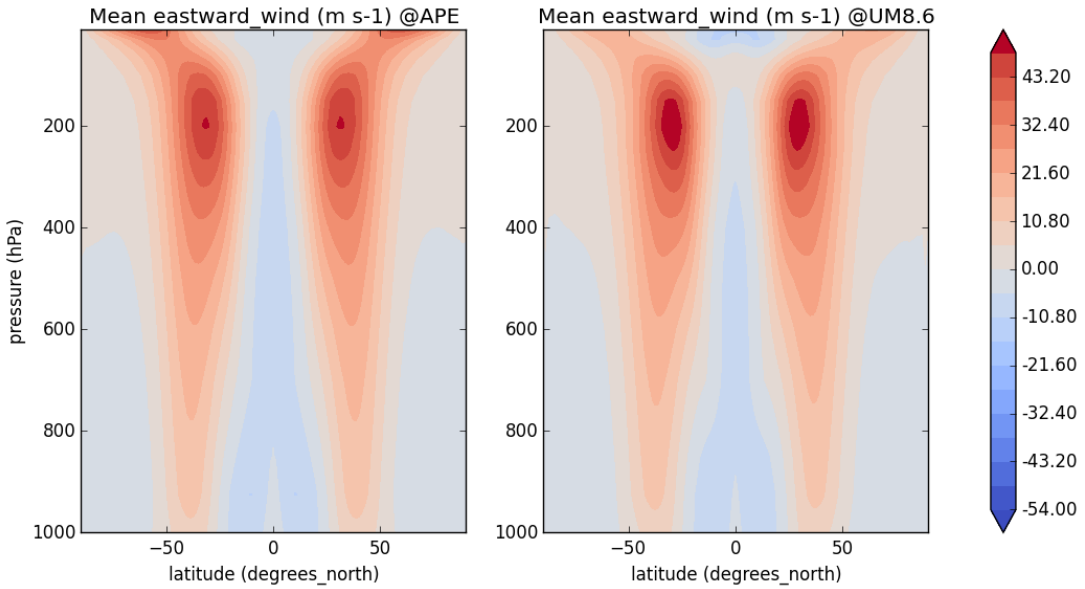

Figure I.4: Zonal mean zonal wind (in m/s) profile from APE (left) and the Unified Model used here (right).

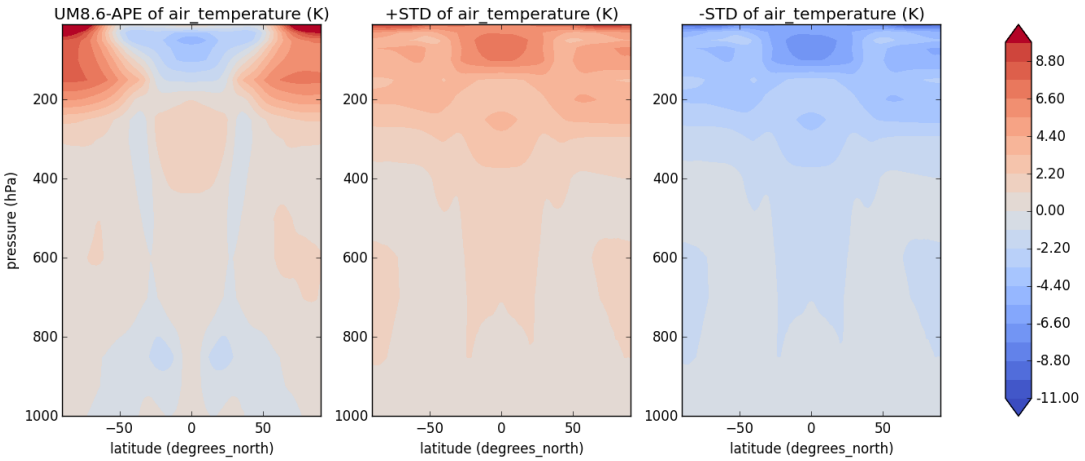

Figure I.5: The difference between the zonal mean zonal wind (in m/s) profiles of APE and the Unified Model used here (left panel). - For comparison, the ± standard deviations (STD) of the multimodel mean of APE are given in the middle and right panels.

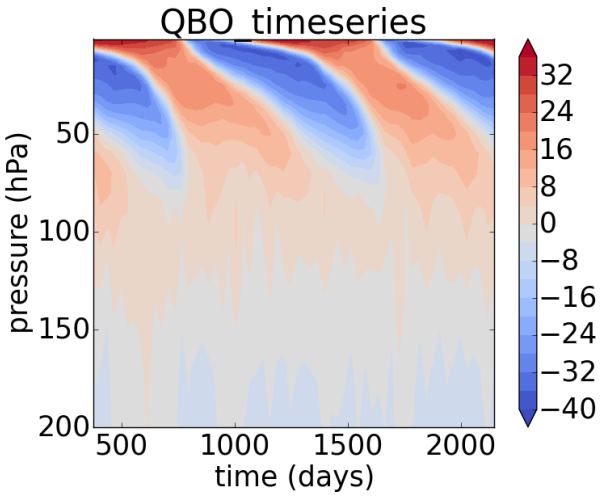

Figure I.6: Zonal mean zonal wind at the Equator above 200 hPa level (in m/s) in the aquaplanet configuration of the Unified Model.

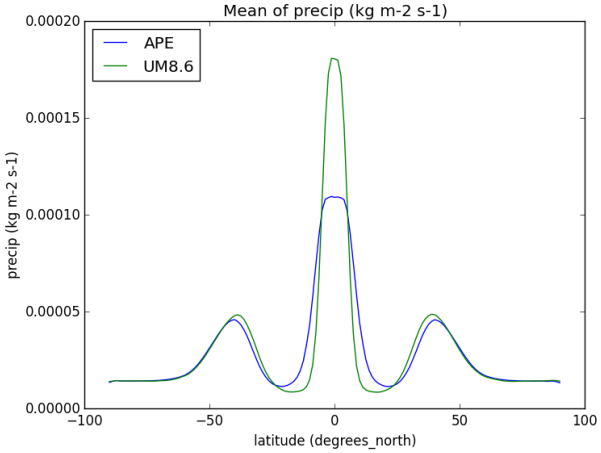

Figure I.7: Zonal mean precipitation rate in the aquaplanet configuration of the Unified Model (green solid line) and APE multimodel mean (blue solid line). - Units are kg m^{-2} s^{-1}.

I.2 Zonally inhomogeneous configuration

The zonally inhomogeneous aquaplanet model configuration is used to force planetary scale waves in the midlatitude region. This is achieved by locally increasing latent (moisture) or sensible heat fluxes. These model configurations are run as the asymptotic theory (Chapter 2) predicts that the interaction between the planetary and synoptic eddies primarily occurs via the zonal mean flow or frictional and diabatic processes, which is further discussed in Chapter 4.

The localised forcing is imposed between 70° and 100° longitude and 30° and 50° latitude (inner black dashed box in Fig. 4.3b-e). The forcing is linearly tapered off between 60° and 70° and 100° and 110° longitude, and between 25° and 30° and 50° and 55° latitude (outer black dashed box in Fig. 4.3b-e):

$$F_{loc} = \begin{cases} F_{new} & ; \quad 70^{\circ} \leq \lambda \leq 100^{\circ}, 30^{\circ} \leq \phi \leq 50^{\circ} \\ F_1 = F_{old} + \frac{F_{new} - F_{old}}{\pi/18} (\lambda - \pi/3) & ; \quad 60^{\circ} \leq \lambda \leq 70^{\circ}, 30^{\circ} \leq \phi \leq 50^{\circ} \\ F_2 = F_{new} + \frac{F_{old} - F_{new}}{\pi/18} (\lambda - 5\pi/9) & ; \quad 100^{\circ} \leq \lambda \leq 110^{\circ}, 30^{\circ} \leq \phi \leq 50^{\circ} \\ F_3 = F_{old} + \frac{F_{new} - F_{old}}{\pi/36} (\phi - 5\pi/36) & ; \quad 70^{\circ} \leq \lambda \leq 100^{\circ}, 25^{\circ} \leq \phi \leq 30^{\circ} \\ F_4 = F_{new} + \frac{F_{old} - F_{new}}{\pi/36} (\phi - 5\pi/18) & ; \quad 70^{\circ} \leq \lambda \leq 100^{\circ}, 50^{\circ} \leq \phi \leq 55^{\circ} \\ \min(F_1, F_3) & ; \quad 60^{\circ} \leq \lambda \leq 70^{\circ}, 25^{\circ} \leq \phi \leq 30^{\circ} \\ \min(F_2, F_3) & ; \quad 100^{\circ} \leq \lambda \leq 110^{\circ}, 25^{\circ} \leq \phi \leq 30^{\circ} \\ \min(F_1, F_4) & ; \quad 60^{\circ} \leq \lambda \leq 70^{\circ}, 50^{\circ} \leq \phi \leq 55^{\circ} \\ \min(F_2, F_4) & ; \quad 100^{\circ} \leq \lambda \leq 110^{\circ}, 50^{\circ} \leq \phi \leq 55^{\circ} \\ F_{old} & ; \quad \text{otherwise} \end{cases} \tag{I.2}$$

where F_{loc} is localised forcing in latent or sensible heat flux, F_{new} is the forcing within the inner box (Fig. 4.3b-e), F_{old} is generally the value outside the outer box (Fig. 4.3b-e), λ is longitude in radians, ϕ is latitude in radians, and π here is the Archimedes' constant. While F_{old} is calculated via the model's parametrisation schemes, different model configurations (as named in Fig. 4.3) use different F_{new}[1]:

- SH800: $F_{new} = 800$ in W m^{-2} (constant sensible heat flux within the localised region);
- SH80HighVel: $F_{new} = 1 + 80 \left(\frac{v_f}{0.3}\right)^2$ in W m^{-2}, such that the maximum value does not exceed 800 W m^{-2} [sensible heat flux depending on frictional velocity (v_f; with values up to 1 m s^{-1}, and typical value 0.3 m s^{-1}, Holton 2004) of the parametrisation schemes within the localised region];

[1]To reproduce these model configurations in the UM, copy the following jobs: xnlwv for SH800, xnlwt for SH80HighVel, xnlwp for 20Moist, xnlwq for 2MoistHighVel, and xnlwn for a separate control simulation.

- 20Moist: $F_{new} = 20F_{old}$ (increase the latent heat flux within the localised region; see also Boutle et al. 2011);
- 2MoistHighVel: $F_{new} = F_{old}\left(1 + 2\left(\frac{v_f}{0.3}\right)^2\right)$ (increase latent heat flux within the localised region, depending on the frictional velocity).

The dependence on the frictional velocity is used in order to increase the values in the latent or sensible heat fluxes for the high velocity regime only, which would largely correspond to eddy forcing rather than the mean flow. This allows for a study of eddy diabatic effects on forcing the planetary scale waves, which was suggested by the asymptotic theory (Chapter 2). This is further discussed in Chapter 4, where also the vertically integrated eddy kinetic energy (EKE) figures for each of these configurations are given (colours in Fig. 4.3b-e). Note that the control simulation (zonally homogeneous configuration) was performed separately, but ultimately the SH of the SH800 model configuration was used for the analysis in Chapter 4.

Appendix J

Cross-spectra for transient waves

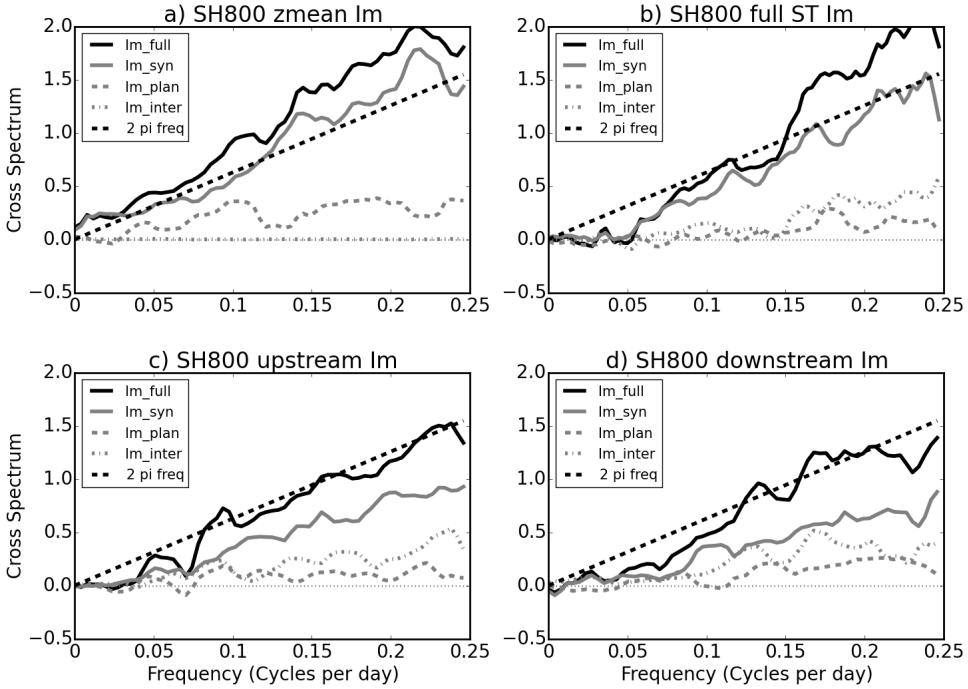

Figure J.1: Imaginary parts of the cross-spectra for the baroclinic flow (4.1,4.2) with transient heat fluxes only (from (4.10)), for different zonal averages. - a) zonal mean, b) average over the storm track, c) average over the upstream region of the storm track, and d) average over the downstream region of the storm track. The lines are as in Fig. 4.5. The data is from the NH of the SH800 model configuration.

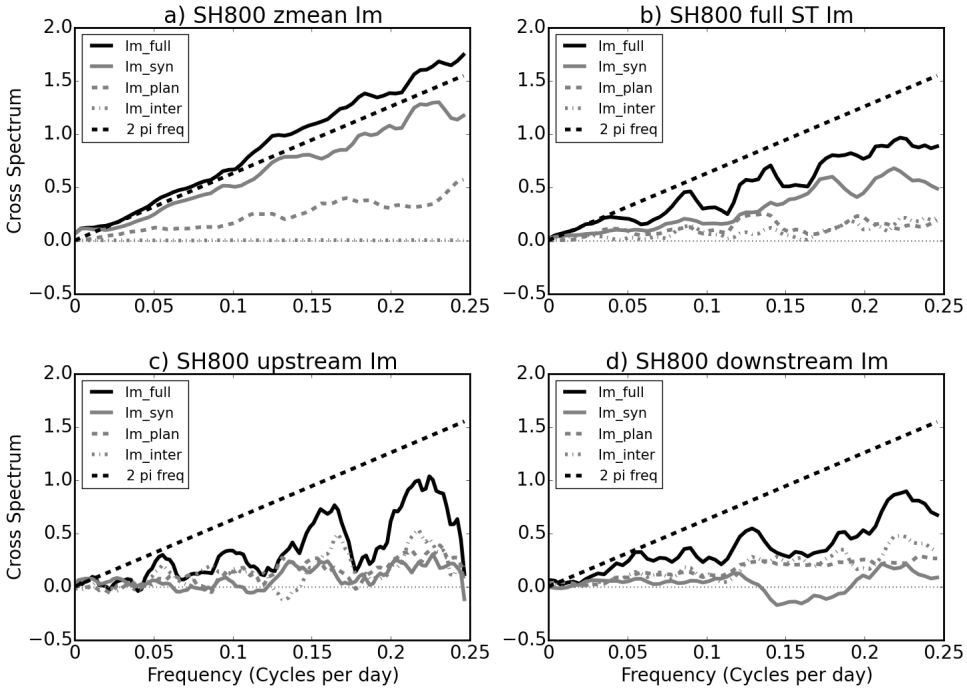

Figure J.2: As in Fig. J.1 but for the barotropic flow (4.3, 4.4) with transient momentum fluxes only (from (4.11)).

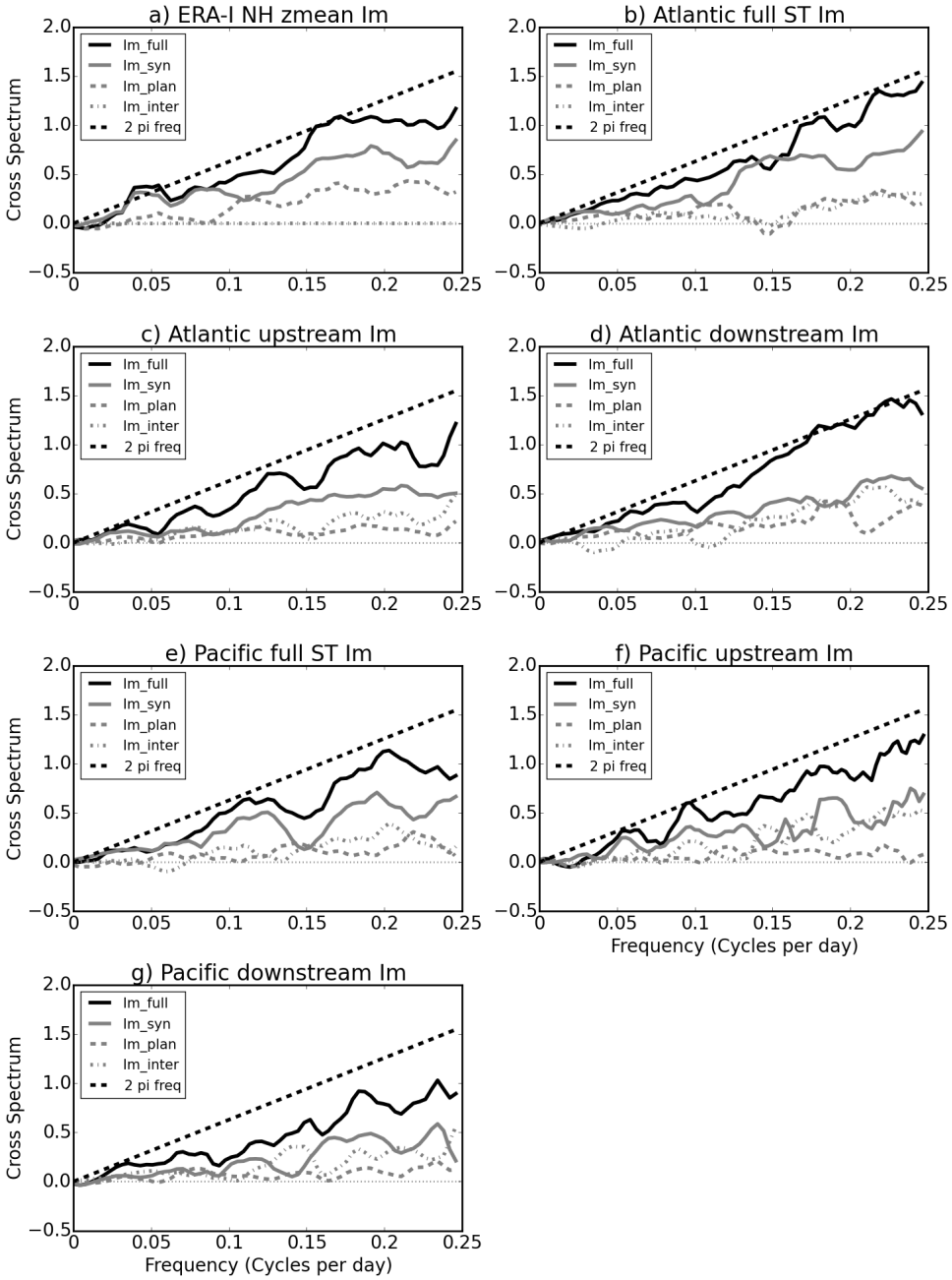

Figure J.3: Imaginary parts of the cross-spectra for the baroclinic flow (4.1,4.2) with transient heat fluxes only (from (4.10)), for different zonal averages. - a) zonal mean, b) average over the Atlantic storm track, c) average over the upstream region of the Atlantic storm track, d) average over the downstream region of the Atlantic storm track, e) average over the Pacific storm track, f) average over the upstream region of the Pacific storm track, and g) average over the downstream region of the Pacific storm track. The lines are as in Fig. 4.5. The data is from the NH of ERA-Interim data.

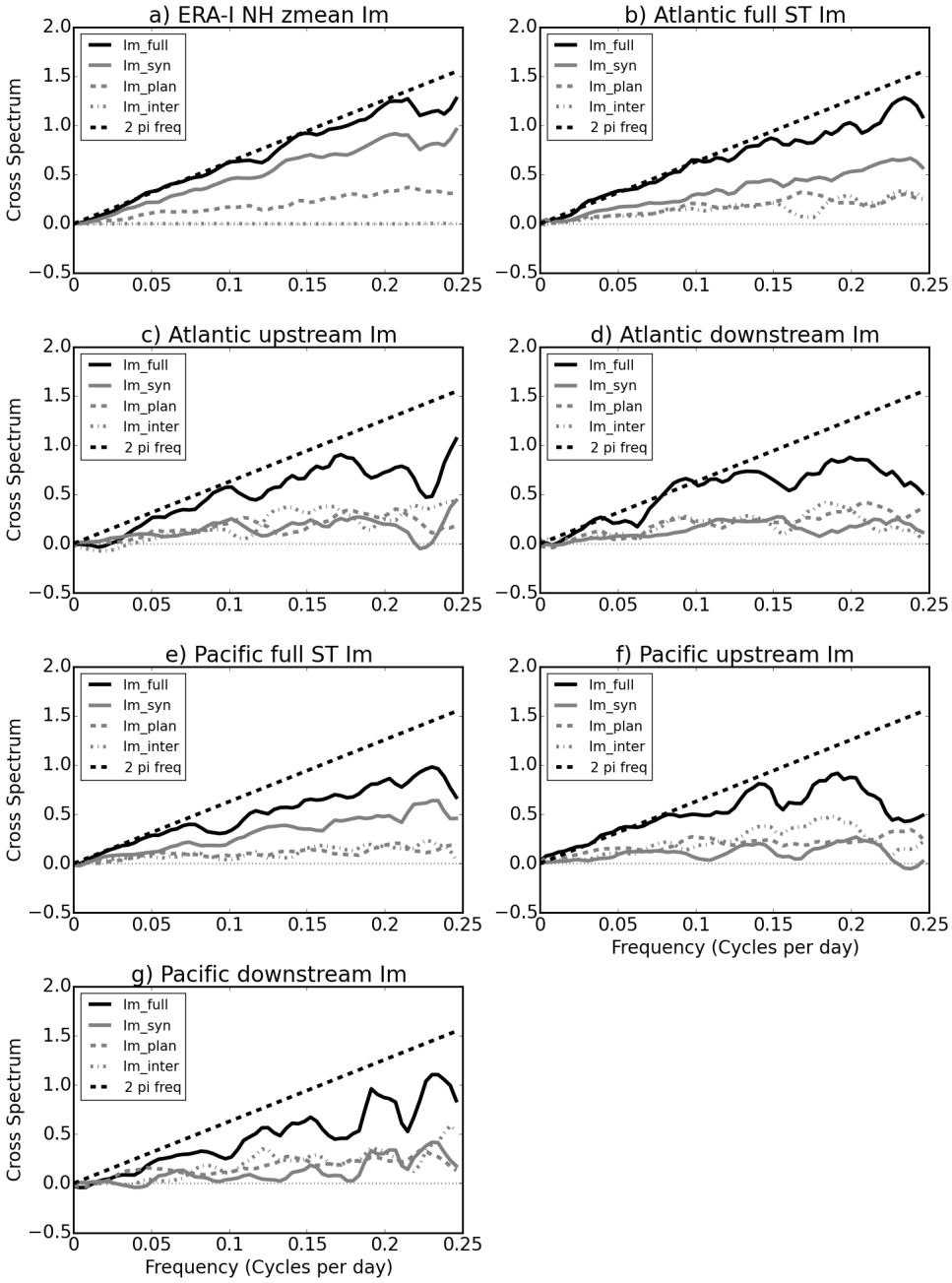

Figure J.4: As in Fig. J.3 but for the barotropic flow (4.3, 4.4) with transient momentum fluxes only (from (4.11)).

Appendix K

Additional regression analysis

K.1 Regressions on teleconnection patterns

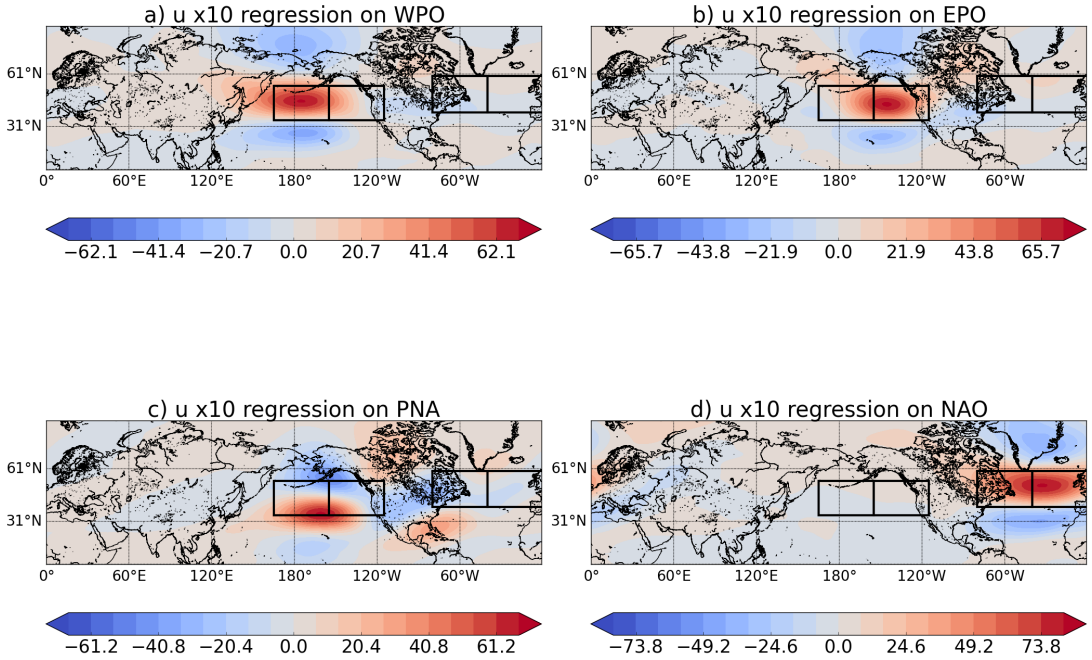

Figure K.1: Regression of the vertically integrated zonal wind on normalised teleconnection patterns. - (a) west Pacific oscillation (WPO), (b) east Pacific oscillation (EPO), (c) Pacific/North-American pattern (PNA), and (d) North Atlantic oscillation (NAO). Units are m s^{-1} (multiplied by 10). Note that the colourbars are not the same, in order to show different features more clearly.

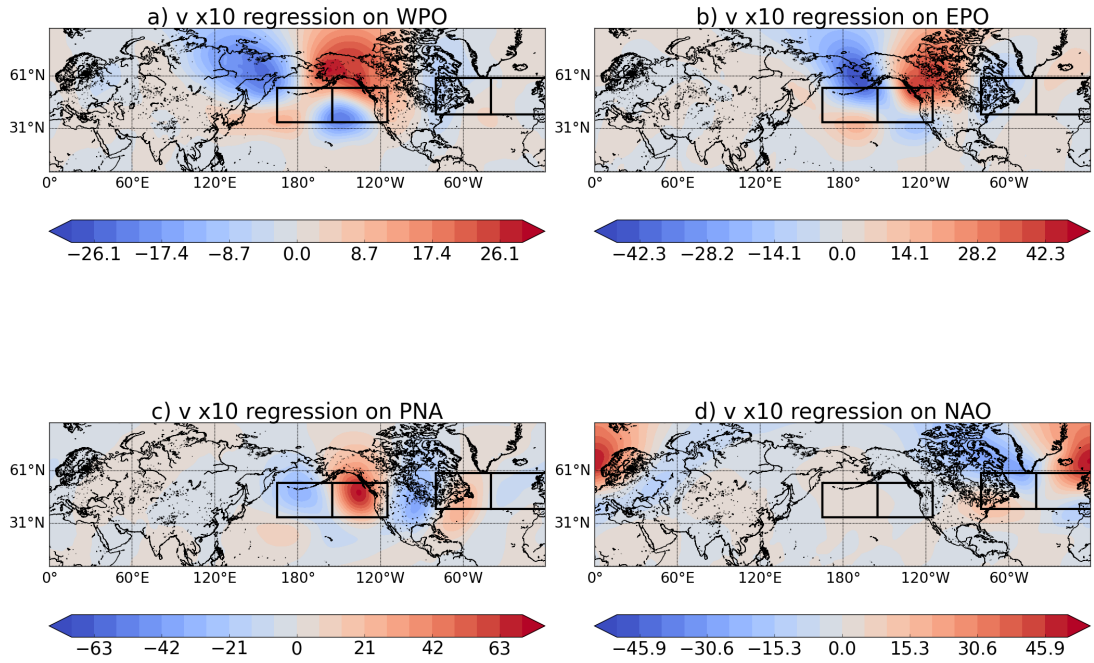

Figure K.2: As in Fig. K.1, but for the regression of the vertically integrated meridional wind.

K.2 Planetary zonal wind regressions

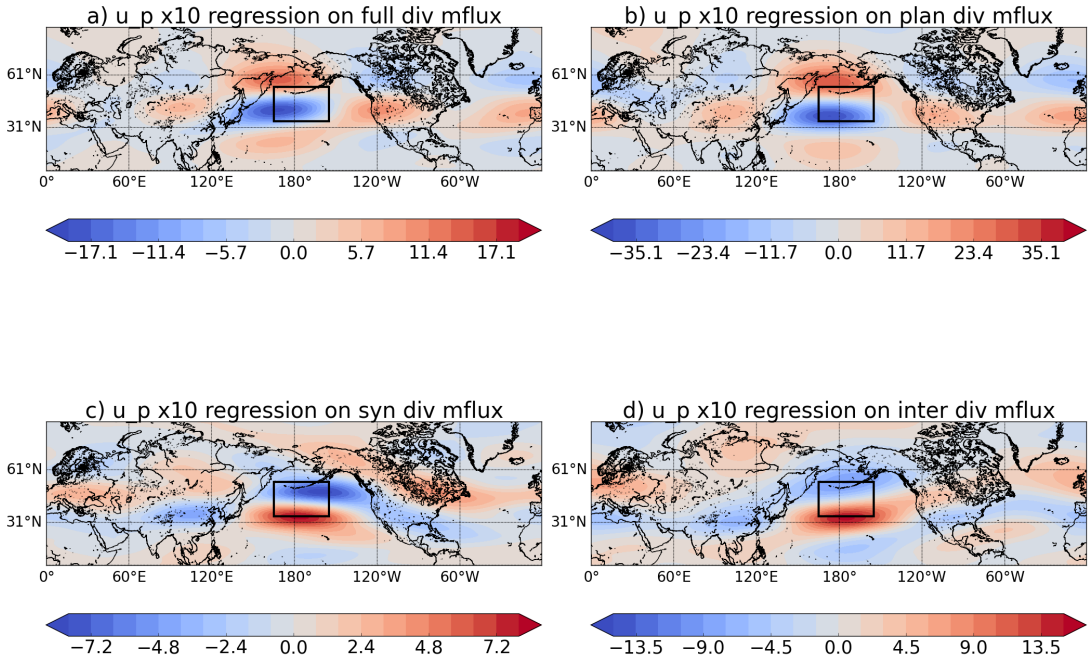

Figure K.3: Regression of the vertically integrated planetary component of zonal wind on normalised momentum flux divergence. - (a) full momentum flux divergence, (b) planetary, (c) synoptic, and (d) interaction contributions to the momentum flux divergence for upstream of the Pacific storm track. Units are m s^{-1}, (multiplied by 10). Note that the colourbars are not the same, in order to show different features more clearly.

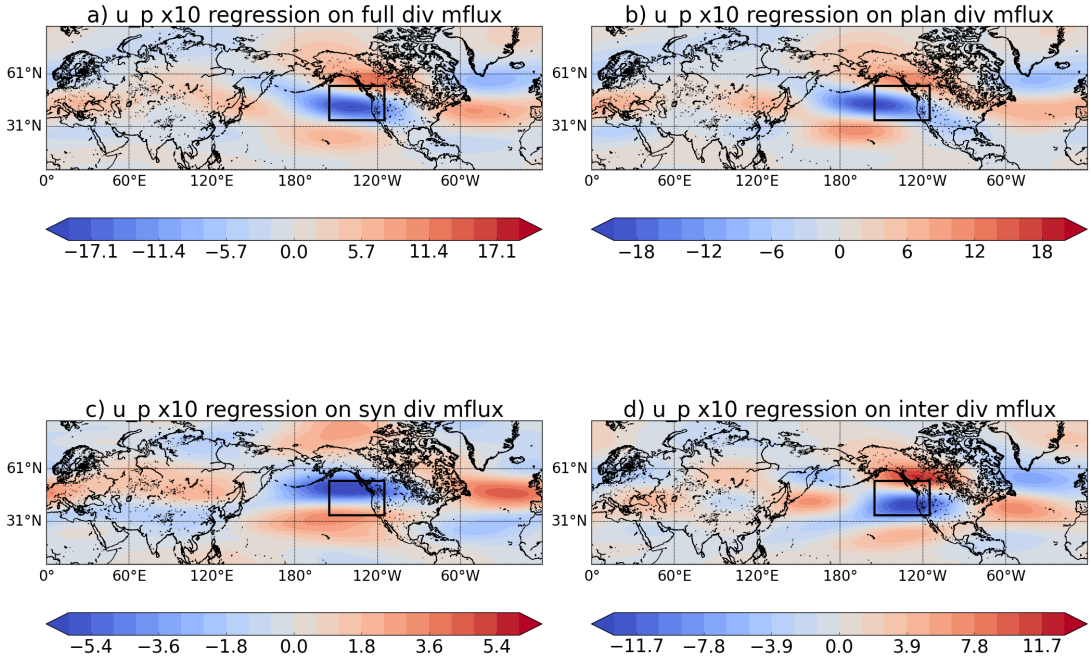

Figure K.4: As in Fig. K.3, but for downstream of the Pacific storm track.

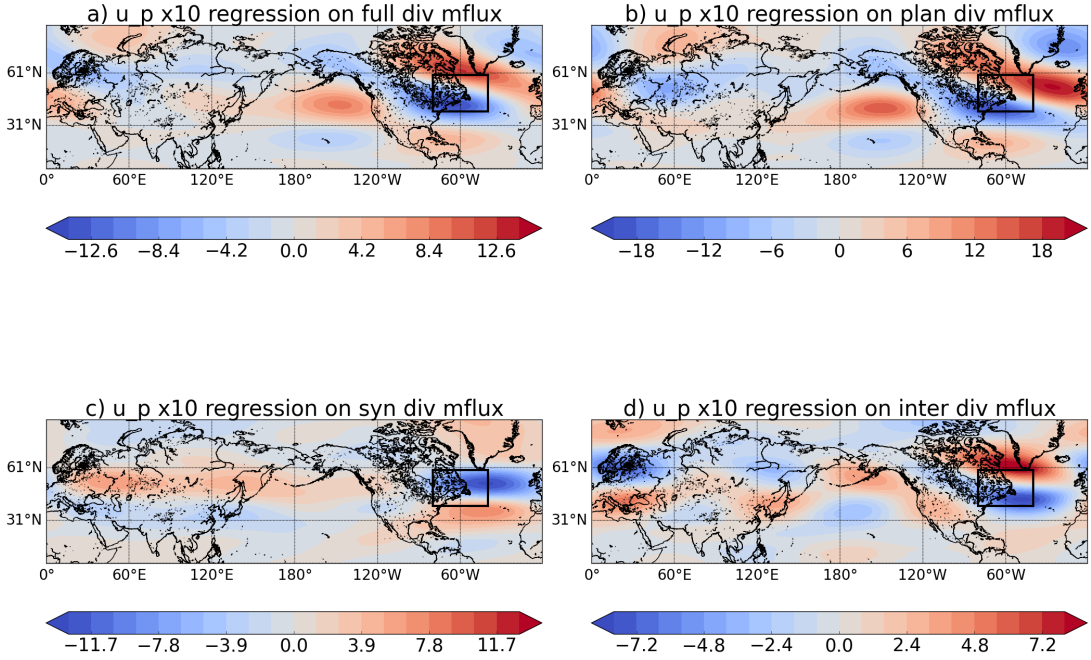

Figure K.5: As in Fig. K.3, but for upstream of the Atlantic storm track.

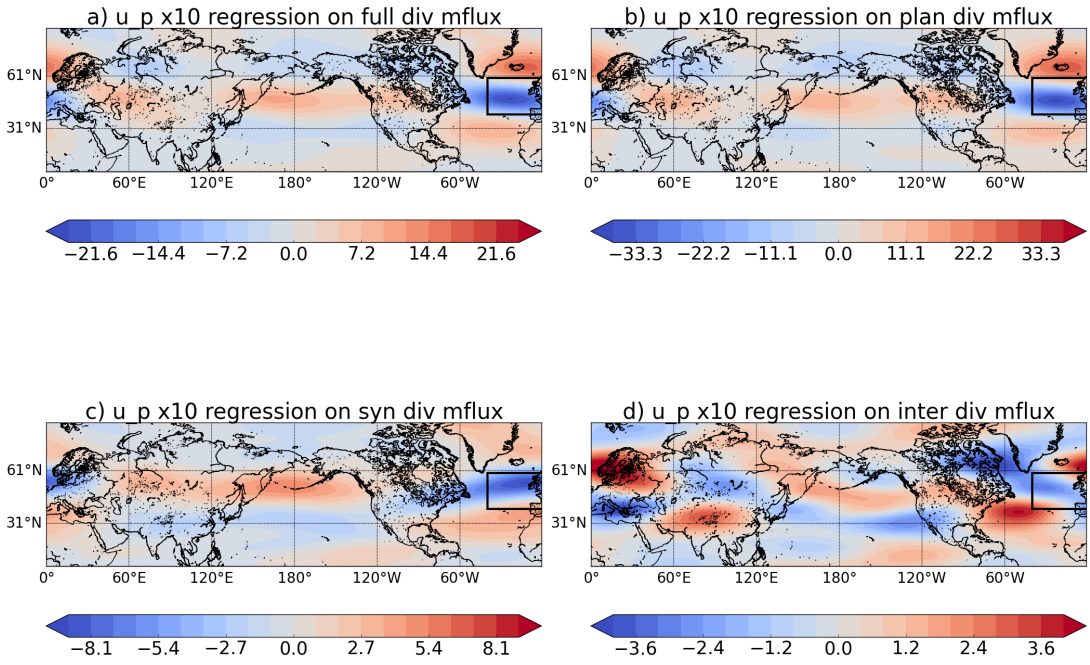

Figure K.6: As in Fig. K.3, but for downstream of the Atlantic storm track.

K.3 Lag regressions of meridional wind

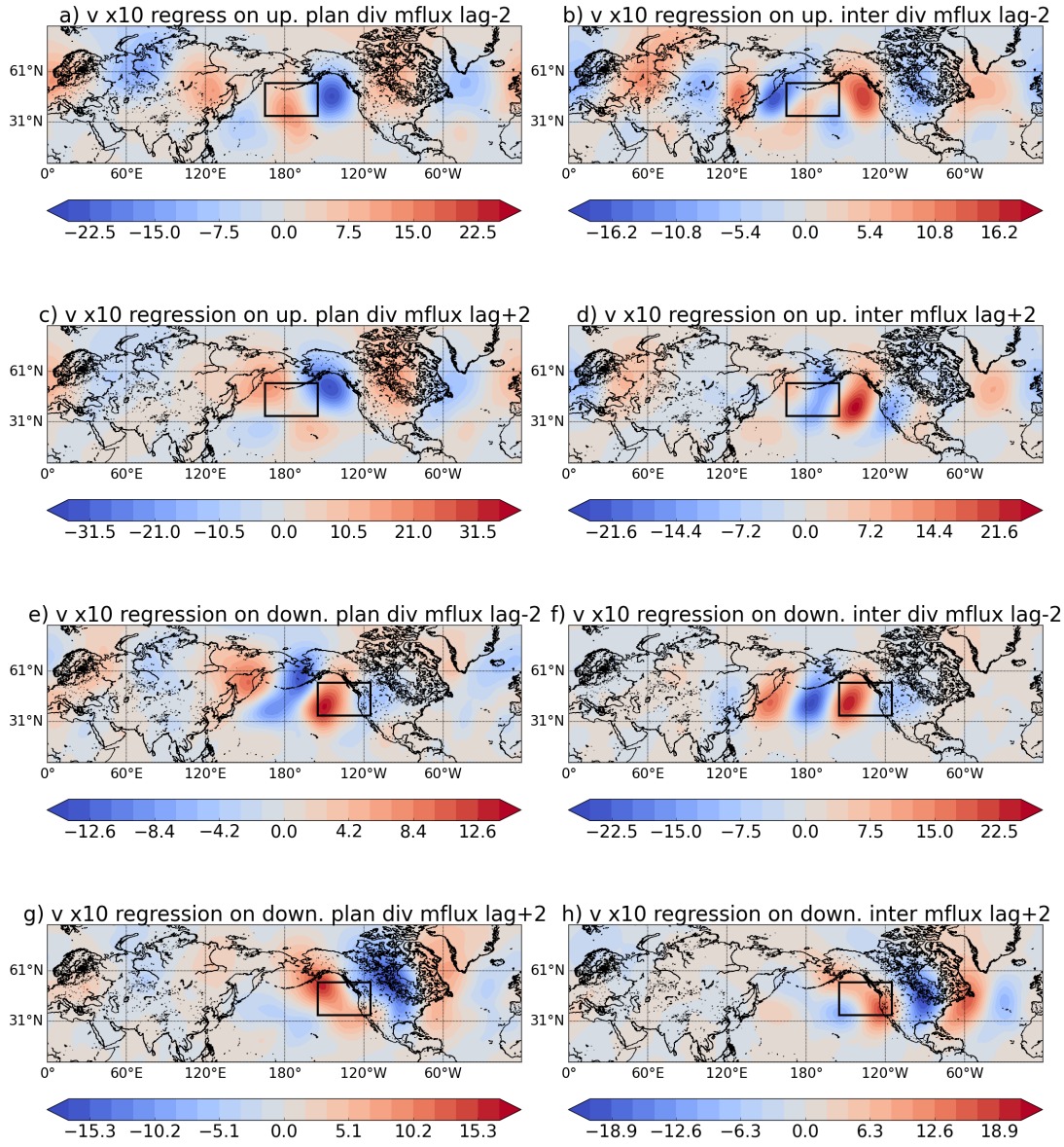

Figure K.7: Regression of the vertically integrated meridional wind on normalised momentum flux divergence. - (a) planetary momentum flux divergence at lag -2 days, (b) interaction momentum flux divergence at lag -2, (c) planetary momentum flux divergence at lag +2 days, and (d) interaction momentum flux divergence at lag +2 for the upstream of the Pacific storm track; (e) to (h) are the corresponding regressions for the downstream region of the Pacific storm track (in the same order). Units are m s^{-1} (multiplied by 10). Note that the colourbars are not the same, in order to show different features more clearly.

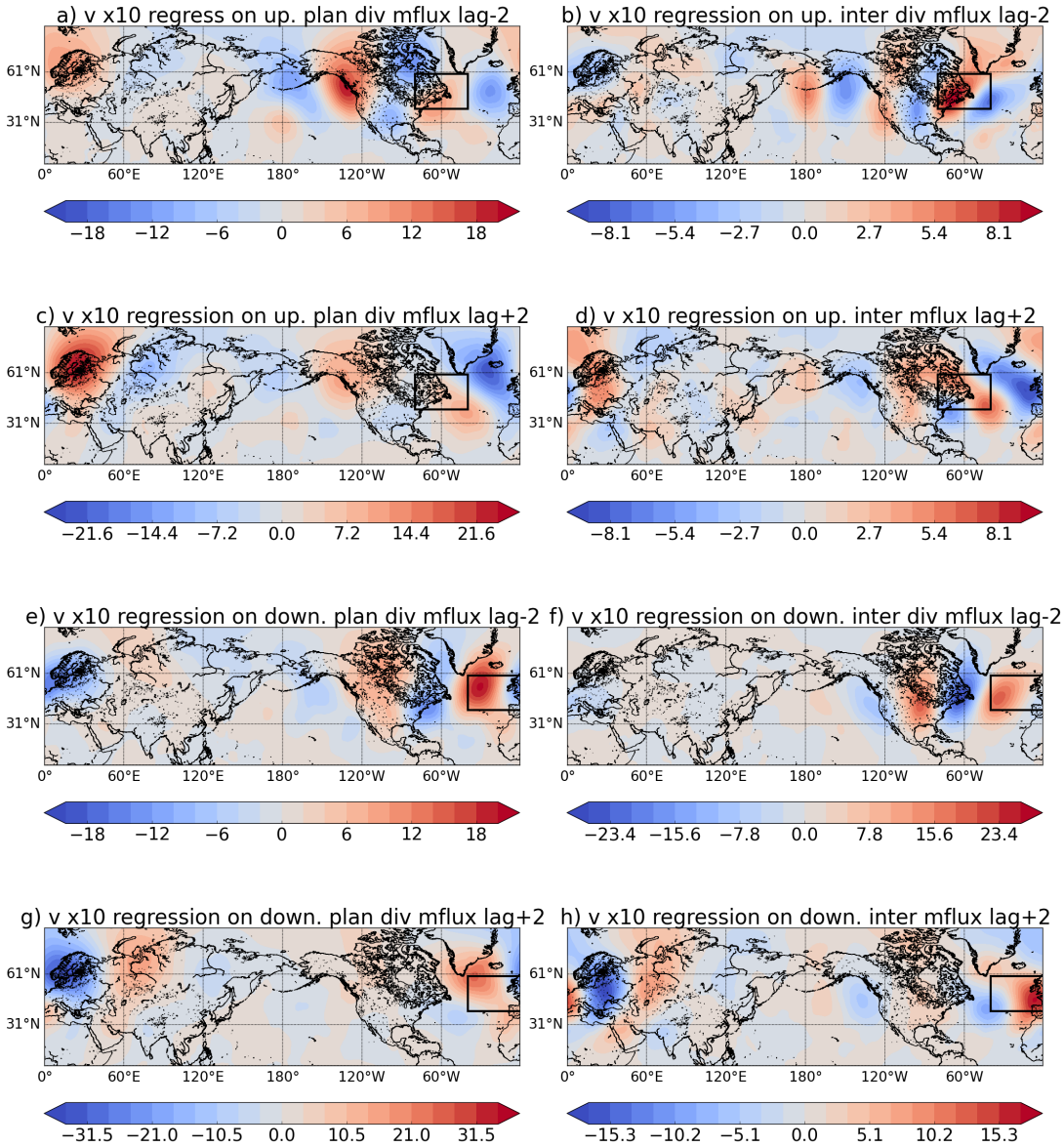

Figure K.8: As in Fig. K.7, but for upstream and downstream of the Atlantic storm track.

Appendix L

Other multiscale asymptotic regimes and wave activity theory

L.1 Finite Amplitude Isotropic Regime

The finite amplitude isotropic regime refers to the system of equations derived in DK13, where the planetary and synoptic wave interaction was studied (without the presence of the zonal mean flow - this was further analysed in Dolaptchiev 2008 and is not considered here). They considered the interaction between synoptic and planetary waves through the PV budget, but have not derived the wave activity budget for it. The wave activity for that system is presented here. The wave amplitude in this case is larger than in Chapter 2 as the planetary and synoptic waves enter the asymptotic series at a lower order. An example of the asymptotic series is given for the potential temperature [see (13) in DK13]

$$\theta = 1 + \varepsilon^2 \theta^{(2)}(\lambda_p, \phi_p, z, t_p) + \varepsilon^3 \theta^{(3)}(\lambda_p, \phi_p, \lambda_s, \phi_s, z, t_p, t_s) + ... \tag{L.1}$$

where the notation is as in Chapter 2 and the scale separation is similar, with the only difference in the temporal scale separation: $\lambda = \lambda_p = \varepsilon\lambda_s$, $\phi = \phi_p = \varepsilon\phi_s$, $t = \varepsilon^{-3} t_p = \varepsilon^{-2} t_s$.

DK13 then derived the PV equations for planetary and synoptic waves, as well as the barotropic pressure equation (barotropic equation for zonal mean flow), which are given in (40) - (47) of DK13.

L. OTHER MULTISCALE ASYMPTOTIC REGIMES AND WAVE ACTIVITY THEORY

PV equations

The synoptic scale PV is used to derive the wave activity equation, whereas the planetary scale PV is essentially representing the background PV equation. Here, the synoptic scale PV equation (44) from DK13 is used, however instead of the planetary scale PV equation (40) from DK13, the right-hand-side of equation (A5) from DK13 is used to avoid vertical velocity, as in Chapter 2. Furthermore, thermal wind balance [e.g. (57) in DK09] $\left(\frac{\partial \mathbf{u}^{(0)}}{\partial z} = f^{-1}\mathbf{e}_r \times \nabla\theta^{(2)}\right)$ is used to derive the final version of the planetary scale PV equation seen below. The PV equations are then

Planetary scale

$$\left(\frac{\partial}{\partial t_p} + \mathbf{u}_p^{(0)} \cdot \nabla_p\right) Q = S_{\partial\theta/\partial z} = \frac{\mathrm{D}_p Q}{\mathrm{D}_p t_p} \tag{L.2a}$$

Synoptic scale

$$\left(\frac{\partial}{\partial t_s} + (\underline{\underline{\mathbf{u}_p^{(0)}}} + \mathbf{u}_s^{(0)}) \cdot \nabla_s\right) q_s^{(3)} + \mathbf{u}_s^{(0)} \cdot \underline{\underline{\nabla_p Q}} = S_q \tag{L.2b}$$

with

$$q_s^{(3)} = \frac{1}{f}\nabla_s^2 \pi^{(3)} + \frac{f}{\rho^{(0)}}\frac{\partial}{\partial z}\left(\frac{\rho^{(0)}\theta^{(3)}}{\partial\theta^{(2)}/\partial z}\right) \tag{L.3a}$$

$$\frac{\partial Q}{\partial t_p} = \frac{\partial f(\phi_p)}{\partial t_p} + \frac{f}{\rho^{(0)}}\frac{\partial}{\partial z}\frac{\frac{\partial(\rho^{(0)}\theta^{(2)})}{\partial t_p}}{\partial\theta^{(2)}/\partial z} \tag{L.3b}$$

$$\nabla_p Q = \nabla_p f(\phi_p) + \frac{f}{\rho^{(0)}}\frac{\partial}{\partial z}\frac{\nabla_p(\rho^{(0)}\theta^{(2)})}{\partial\theta^{(2)}/\partial z} \tag{L.3c}$$

where the double underline represents interaction terms. Here note that in this finite amplitude limit the background PV gradient, $\nabla_p Q$, is not truly a gradient, but is still in a vectoral form.

By reformulating (40) and (A5) of DK13 to (L.2a), we have achieved that the planetary scale PV equation takes the form of the background PV (with $\nabla_p Q$) in the synoptic scale equation (L.2b). Equation (L.2a) can now be used to derive the wave activity equation.

Wave activity equation

To derive wave activity equation we multiply synoptic scale PV equation (L.2b) by $q_s^{(3)}$ (L.3a) and divide by $|\nabla_p Q|$ (e.g. Plumb 1986), which yields the wave activity equation

$$\frac{\partial \mathcal{A}_s}{\partial t_s} + \nabla_s^{3D} \cdot \mathbf{M}_s - \frac{\rho^{(0)} f \theta^{(3)}}{\partial \theta^{(2)}/\partial z} \mathbf{u}_s^{(0)} \cdot \frac{\partial}{\partial z} \left(\frac{\nabla_p Q}{|\nabla_p Q|} \right) = S_s^{wa} \tag{L.4}$$

with

$$\mathcal{A}_s = \frac{\rho^{(0)} {q_s^{(3)}}^2}{2|\nabla_p Q|}; \qquad\qquad S_s^{wa} = \frac{S_q \rho^{(0)} q_s^{(3)}}{|\nabla_p Q|} \tag{L.5}$$

$$\mathbf{M}_s = \begin{pmatrix} (u_p^{(0)} + u_s^{(0)})\mathcal{A}_s + \rho^{(0)} \left(v_s^{(0)} u_s^{(0)} \frac{\partial Q/\partial x_p}{|\nabla_p Q|} + \frac{1}{2} \left({v_s^{(0)}}^2 - {u_s^{(0)}}^2 - \frac{{\theta^{(3)}}^2}{\partial \theta^{(2)}/\partial z} \right) \frac{\partial Q/\partial y_p}{|\nabla_p Q|} \right) \\ (v_p^{(0)} + v_s^{(0)})\mathcal{A}_s + \rho^{(0)} \left(-v_s^{(0)} u_s^{(0)} \frac{\partial Q/\partial y_p}{|\nabla_p Q|} + \frac{1}{2} \left({v_s^{(0)}}^2 - {u_s^{(0)}}^2 + \frac{{\theta^{(3)}}^2}{\partial \theta^{(2)}/\partial z} \right) \frac{\partial Q/\partial x_p}{|\nabla_p Q|} \right) \\ \frac{\rho^{(0)} f \theta^{(3)}}{\partial \theta^{(2)}/\partial z} \left(u_s^{(0)} \frac{\partial Q/\partial x_p}{|\nabla_p Q|} + v_s^{(0)} \frac{\partial Q/\partial y_p}{|\nabla_p Q|} \right) \end{pmatrix} \tag{L.6}$$

where $|\nabla_p Q| = \sqrt{\nabla_p Q \cdot \nabla_p Q}$. Note that there is an additional term with $\frac{\partial}{\partial z} \left(\frac{\nabla_p Q}{|\nabla_p Q|} \right)$ in the wave activity equation (L.4), which does not disappear as there is no separation of scales in the vertical direction (and Q depends on z). Except for this additional term, (L.4) - (L.6) strongly resemble Plumb (1986) [his $\mathbf{B}$ is similar to $\mathbf{M}_s$ here], who assumed that the background is slowly varying in all dimensions (including z) and thus there the term with $\frac{\partial}{\partial z} \left(\frac{\nabla_p Q}{|\nabla_p Q|} \right)$ is negligible.

The wave activity presented in this section shows a direct interaction between the planetary and synoptic waves as the planetary scale PV (background PV gradient) and planetary scale velocities ($u_p^{(0)}$,$v_p^{(0)}$) directly enter the synoptic scale wave activity equation. One could regard the term with $\frac{\partial}{\partial z} \left(\frac{\nabla_p Q}{|\nabla_p Q|} \right)$ as a conversion term between the planetary and synoptic scale waves.

The planetary scale PV equation generally includes the vertical velocity [(40) in DK13] and the PV resembles the Ertel PV, and if the vertical derivative and velocity are replaced by the horizontal gradients as in (L.3b) and (L.3c), the PV does not take an explicit form. Therefore, for a more accurate wave activity derivation one should consider using the Hamiltonian formulation (e.g. Shepherd 1990) which is generally used for deriving finite amplitude wave activity theories.

L.2 Finite Amplitude Anisotropic Regime

The finite amplitude anisotropic regime refers to the system of equations derived in the fourth Chapter of Dolaptchiev (2008), where the planetary and synoptic wave interaction was studied (without the presence of the zonal mean flow), similarly to the above finite amplitude isotropic regime. Dolaptchiev (2008) derived the PV equations, but has not derived the wave activity equation, which is presented here. The anisotropic regime refers to the case where the separation of planetary and synoptic scales in latitude is relaxed (i.e. planetary and synoptic waves evolve on the same meridional scale ϕ_s).

The assumptions include an example of the asymptotic series for the potential temperature [see (4.1) in Dolaptchiev 2008]

$$\theta = 1 + \varepsilon^2 \theta^{(2)}(\lambda_p, z, t_p) + \varepsilon^3 \theta^{(3)}(\lambda_p, \lambda_s, \phi_s, z, t_p, t_s) + ... \tag{L.7}$$

where the notation is as in section L.1, i.e. the same scale separation. Another assumption involves the Taylor expansion for $\sin\phi = \sin(\phi_p + \varepsilon\phi_s)$ and for $\cos^{-1}\phi = \cos^{-1}(\phi_p + \varepsilon\phi_s)$ [(4.2) and (4.3) in Dolaptchiev 2008, respectively]. Note that here ϕ_p is constant and only ϕ_s varies (representing deviations from ϕ_p), which means that both the Coriolis paramter ($f_o = \sin\phi_p$) and beta parameter ($\beta = \cos\phi_p/a$) are constants. For the details of this expansion refer to Dolaptchiev (2008). Note that because the second order in the above asymptotic series (L.7) only depends on λ_p and not on ϕ_p, the leading order planetary scale velocity only includes the meridional component ($v_p^{(0)}$), whereas the synoptic scales retain a similar form to the isotropic regime. Note though that because there is no ϕ_p we must keep in mind that the zonal velocity on the ϕ_s scale is not necessarily synoptic velocity only (even though it will be called $u_s^{(0)}$ below), as it may have planetary contributions. Similarly, because ϕ_p is constant, ∇_p here generally includes the zonal derivative only (unless otherwise stated), whereas ∇_s includes both zonal and meridional derivatives.

Dolaptchiev (2008) then derived the PV equation for several asymptotic orders. Here we focus on the leading order of the PV budget and derive the wave activity for it.

PV equations

As in section L.1, the synoptic scale PV is used to derive the wave activity equation, whereas the planetary scale PV is essentially representing the background PV equation. Dolaptchiev

(2008)'s leading order PV equation is given in (4.28) and can be rewritten using geostrophic balance as

$$\frac{\partial q_s^{(3)}}{\partial t_s} + \nabla_s \cdot \left((\underline{\underline{\mathbf{u}_p^{(0)}}} + \mathbf{u}_s^{(0)}) q_s^{(3)} \right) + \beta v_s^{(0)} + u_s^{(0)} \underline{\underline{\frac{\partial q_p^{(2)}}{\partial x_p}}} = -\beta v_p^{(0)} - \frac{\partial q_p^{(2)}}{\partial t_p} \tag{L.8}$$

with

$$q_s^{(3)} = \frac{1}{f_o} \nabla_s^2 \pi^{(3)} + \frac{f_o}{\rho^{(0)}} \frac{\partial}{\partial z} \left(\frac{\rho^{(0)} \theta^{(3)}}{\partial \theta^{(2)} / \partial z} \right) \tag{L.9a}$$

$$\frac{\partial q_p^{(2)}}{\partial t_p} = \frac{f_o}{\rho^{(0)}} \frac{\partial}{\partial z} \left(\frac{\rho^{(0)} \partial \theta^{(2)} / \partial t_p}{\partial \theta^{(2)} / \partial z} \right) \tag{L.9b}$$

$$\frac{\partial q_p^{(2)}}{\partial x_p} = \frac{f_o}{\rho^{(0)}} \frac{\partial}{\partial z} \left(\frac{\rho^{(0)} \partial \theta^{(2)} / \partial x_p}{\partial \theta^{(2)} / \partial z} \right) \tag{L.9c}$$

where double underline represents interaction terms, the last term in (4.28) of Dolaptchiev (2008) vanishes as the dot-product of $\nabla_p = \frac{\partial}{\partial x} \mathbf{e}_\lambda$ and $\mathbf{u}_p^{(0)} = v_p^{(0)} \mathbf{e}_\phi$ is zero, and $\partial \pi^{(3)} / \partial z$ in (4.30) of Dolaptchiev (2008) was replaced by $\theta^{(3)}$ through hydrostatic balance [(4.18) in Dolaptchiev 2008]. Note that the source-sink terms are omitted here for simplicity (set to zero).

To obtain the planetary and synoptic PV equations we average (L.8) over t_s and λ_s, but not over ϕ_s as both synoptic and planetary scale waves evolve on this meridional scale. The equation that remains after the 'synoptic' scale average is the planetary scale PV, then we subtract the planetary scale PV from (L.8) to obtain the synoptic scale PV. Note that Dolaptchiev (2008) averaged also over ϕ_s, which is why his results are different. The above procedure yields the planetary and synoptic scale PV equations

Planetary scale

$$\frac{\partial q_p^{(2)}}{\partial t_p} + \beta v_p^{(0)} + \underline{\underline{C}} = 0 \tag{L.10a}$$

Synoptic scale

$$\frac{\partial q_s^{(3)}}{\partial t_s} + \nabla_s \cdot \left((\underline{\underline{\mathbf{u}_p^{(0)}}} + \mathbf{u}_s^{(0)}) q_s^{(3)} \right) + \mathbf{u}_s^{(0)} \cdot \underline{\underline{\nabla_p Q}} - \underline{\underline{C}} = 0 \tag{L.10b}$$

with

$$\nabla_p Q = \left(\frac{\partial q_p^{(2)}}{\partial x_p}, \beta \right) \tag{L.11a}$$

$$C = \frac{\partial}{\partial \tilde{y}_s} \left(\overline{(v_s^{(0)} + v_p^{(0)}) q_s^{(3)}}^{\lambda_s, t_s} \right) + \overline{u_s^{(0)}}^{\lambda_s, t_s} \frac{\partial q_p^{(2)}}{\partial x_p} \tag{L.11b}$$

where C is the conversion (and interaction) term between the synoptic and planetary PVs, and the background PV gradient, $\nabla_p Q$, is again not an explicit gradient, but is still in a vectoral form. Equation (L.10b) can now be used to derive the synoptic scale enstrophy and wave activity equations. Note that there is again no explicit planetary scale PV as in section L.1, but there is now a conversion (and interaction) term C that was not present in the isotropic regime.

Enstrophy and wave activity equations

To derive the enstrophy equation, we multiply (L.10b) by $q_s^{(3)}$, which gives

$$\underbrace{\frac{1}{2} \frac{\partial q_s^{(3)2}}{\partial t_s}}_{\text{enstrophy tendency}} + \underbrace{q_s^{(3)} \mathbf{u}_s^{(0)} \cdot \underline{\underline{\nabla_p Q}}}_{\text{eddy PV flux}} + \underbrace{\frac{1}{2} \nabla_s \cdot \left((\underline{\underline{\mathbf{u}_p^{(0)}}} + \mathbf{u}_s^{(0)}) q_s^{(3)2} \right) - q_s^{(3)} \underline{\underline{C}}}_{\text{eddy enstrophy flux}} = 0. \tag{L.12}$$

Equation (L.12) suggests leading order contributions of eddy entrophy fluxes to the enstrophy budget along with the eddy PV fluxes that are conventionally present in this budget. Note that this effect does not vanish under zonal averaging, and that the eddy entrophy flux also appears in the finite amplitude isotropic regime, but lacks the term $q_s^{(3)} C$ (as stated above). Birner et al. (2013) have argued that the upgradient PV fluxes that are found on the poleward flank of the jet stream are associated with the eddy enstrophy fluxes, which act as a conversion between the planetary and synoptic waves (consistent with the above equations). These upgradient PV fluxes were also associated with the planetary scale waves (planetary enstrophy) in the observations (Birner et al., 2013). A more recent study (Dwyer and O'Gorman, 2017), on the other hand, argued that in an idealised moist atmosphere general circulation model these upgradient PV fluxes are mainly associated with diabatic processes (convection). To further elucidate which processes are dominating the upgradient PV fluxes, a hierarchy of models should be used.

To derive a wave activity equation divide the enstrophy equation (L.12) by $|\nabla_p Q|$ (e.g.

Plumb 1986), which yields a wave activity equation similar to the one in section L.1

$$\frac{\partial \mathcal{A}_s}{\partial t_s} + \nabla_s^{3D} \cdot \mathbf{M}_s - \frac{\rho^{(0)} f \theta^{(3)}}{\partial \theta^{(2)}/\partial z} \mathbf{u}_s^{(0)} \cdot \frac{\partial}{\partial z} \left(\frac{\nabla_p Q}{|\nabla_p Q|} \right) - \frac{\rho^{(0)} q_s^{(3)} C}{|\nabla_p Q|} = 0 \tag{L.13}$$

with

$$\mathcal{A}_s = \frac{\rho^{(0)} {q_s^{(3)}}^2}{2|\nabla_p Q|} \tag{L.14}$$

$$\mathbf{M}_s = \begin{pmatrix} u_s^{(0)} \mathcal{A}_s + \rho^{(0)} \left(v_s^{(0)} u_s^{(0)} \frac{\partial q_p^{(2)}/\partial x_p}{|\nabla_p Q|} + \frac{1}{2} \left({v_s^{(0)}}^2 - {u_s^{(0)}}^2 - \frac{{\theta^{(3)}}^2}{\partial \theta^{(2)}/\partial z} \right) \frac{\beta}{|\nabla_p Q|} \right) \\ (v_p^{(0)} + v_s^{(0)}) \mathcal{A}_s + \rho^{(0)} \left(-v_s^{(0)} u_s^{(0)} \frac{\beta}{|\nabla_p Q|} + \frac{1}{2} \left({v_s^{(0)}}^2 - {u_s^{(0)}}^2 + \frac{{\theta^{(3)}}^2}{\partial \theta^{(2)}/\partial z} \right) \frac{\partial q_p^{(2)}/\partial x_p}{|\nabla_p Q|} \right) \\ \frac{\rho^{(0)} f \theta^{(3)}}{\partial \theta^{(2)}/\partial z} \left(u_s^{(0)} \frac{\partial q_p^{(2)}/\partial x_p}{|\nabla_p Q|} + v_s^{(0)} \frac{\beta}{|\nabla_p Q|} \right) \end{pmatrix} \tag{L.15}$$

where $|\nabla_p Q| = \sqrt{\nabla_p Q \cdot \nabla_p Q}$. Note that there is again an additional term with $\frac{\partial}{\partial z} \left(\frac{\nabla_p Q}{|\nabla_p Q|} \right)$ in the wave activity equation (L.13), which does not disappear as there is no separation of scales in the vertical direction (and Q depends on z). Another additional term (compared with the isotropic regime) arises here due to the conversion C between the planetary and synoptic waves.

The wave activity presented in this section shows a direct interaction and conversion between the planetary and synoptic waves as the planetary scale PV (background PV gradient) and planetary scale velocities ($u_p^{(0)}$,$v_p^{(0)}$) directly enter the synoptic scale wave activity equation and both are present in C. One could regard the term with $\frac{\partial}{\partial z} \left(\frac{\nabla_p Q}{|\nabla_p Q|} \right)$ as an additional conversion term between the planetary and synoptic scale waves.

Again, for a more accurate wave activity derivation one should consider using the Hamiltonian formulation (e.g. Shepherd 1990) which is generally used for deriving the finite amplitude wave activity theories.

L.3 Small Amplitude Anisotropic Regime

The small amplitude anisotropic regime refers to a small amplitude version of the anisotropic regime presented above that was based on the fourth Chapter of Dolaptchiev (2008), with the separation of planetary and synoptic scales in latitude relaxed (i.e. zonal mean flow, planetary and synoptic waves evolve on the same meridional scale ϕ_s). As in Chapter 2 we add the zonal

mean flow to the system of equations and linearise the system.

The assumption for the asymptotic series for the potential temperature of the small amplitude anisotropic regime is

$$\theta = 1 + \varepsilon^2\theta^{(2)}(z) + \varepsilon^3\theta^{(3)}(\lambda_p, \phi_s, z, t_p) + \varepsilon^4\theta^{(4)}(\lambda_p, \lambda_s, \phi_s, z, t_p, t_s)... \tag{L.16}$$

where the notation is as in section L.2, i.e. the same scale separation. As in Dolaptchiev (2008) [section L.2], there is the Taylor expansion for $\sin\phi = \sin(\phi_p + \varepsilon\phi_s)$ and for $\cos^{-1}\phi = \cos^{-1}(\phi_p + \varepsilon\phi_s)$ [(4.2) and (4.3) in Dolaptchiev 2008, respectively], with ϕ_p a constant and only ϕ_s varying, which means that both the Coriolis paramter ($f_o = \sin\phi_p$) and beta parameter ($\beta = \cos\phi_p/a$) are constants. As in the previous section (section L.2), ∇_p only includes the derivatives with respect to longitude, whereas ∇_s includes both meridional and zonal derivatives. As this regime has not been studied before, we provide a more complete derivation of the wave activity equations than for the finite amplitude limits mentioned above, starting from the basic momentum, continuity and thermodynamic equations. The derivation follows Chapter 2 and Dolaptchiev (2008), and is hence not given in detail. Note that the source-sink terms are omitted for simplicity.

Multiscale asymptotic version of the primitive equations

Hydrostatic balance

Following Dolaptchiev (2008), the hydrostatic balance of the anisotropic regime takes a similar form to the isotropic regime of Chapter 2

$$\frac{\partial p^{(i)}}{\partial z} = -\rho^{(i)}; \qquad i = 0, ..., 4. \tag{L.17}$$

This can be rewritten using potential temperature θ through the ideal gas law (2.1f) at different asymptotic orders as

$$\mathcal{O}(\varepsilon^2): \qquad \theta^{(2)} = \frac{\partial \pi^{(2)}}{\partial z} \tag{L.18}$$

$$\mathcal{O}(\varepsilon^3): \qquad \theta^{(3)} = \frac{\partial \pi^{(3)}}{\partial z} \tag{L.19}$$

$$\mathcal{O}(\varepsilon^4): \qquad \theta^{(4)} = \frac{\partial \pi^{(4)}}{\partial z} + \frac{\theta^{(2)}}{\rho^{(0)}} \frac{\partial p^{(2)}}{\partial z} + \frac{p^{(2)} \gamma^{-1} (\gamma^{-1} - 1)}{2 p^{(0)2}} \tag{L.20}$$

where $\gamma = c_p / c_v \approx 7/5$ is isentropic exponent, $\theta^{(2)}$ and $p^{(2)}$ only depend on z from (L.16), hence any horizontal derivatives of $\theta^{(4)}$ only involve $\partial \pi^{(4)} / \partial z$.

Momentum equation

Following Dolaptchiev (2008) and Chapter 2 we can derive the horizontal momentum equations from the primitive equations' u- and v-momentum equations. The different asymptotic orders become

$$\mathcal{O}(\varepsilon): \qquad f_o \mathbf{e}_r \times \mathbf{u}^{(0)} = -\nabla_s \pi^{(3)} = -\frac{\partial \pi^{(3)}}{\partial y_s} \mathbf{e}_\phi \tag{L.21}$$

$$\mathcal{O}(\varepsilon^2): \qquad f_o \mathbf{e}_r \times \mathbf{u}^{(1)} + \phi_s \cos\phi_p \mathbf{e}_r \times \mathbf{u}^{(0)} = -(\nabla_p \pi^{(3)} + \nabla_s \pi^{(4)}) \tag{L.22}$$

$$f_o \mathbf{e}_r \times \mathbf{u}^{(1)} - \frac{\phi_s \cos\phi_p}{f_o} \frac{\partial \pi^{(3)}}{\partial y_s} \mathbf{e}_\phi = -(\frac{\partial \pi^{(3)}}{\partial x_p} \mathbf{e}_\lambda + \nabla_s \pi^{(4)})$$

$$\mathcal{O}(\varepsilon^3): \qquad \frac{\partial \mathbf{u}^{(1)}}{\partial t_s} + \frac{\partial \mathbf{u}^{(0)}}{\partial t_p} + \mathbf{u}^{(0)} \cdot \nabla_s \mathbf{u}^{(1)} + \mathbf{u}^{(1)} \cdot \nabla_s \mathbf{u}^{(0)} + \mathbf{u}^{(0)} \cdot \nabla_p \mathbf{u}^{(0)}$$

$$+ f_o \mathbf{e}_r \times \mathbf{u}^{(2)} + \phi_s \cos\phi_p \mathbf{e}_r \times \mathbf{u}^{(1)} + \frac{\phi_s^2 \sin\phi_p}{2} \mathbf{e}_r \times \mathbf{u}^{(0)} + \frac{u^{(0)2} \tan\phi_p}{a} \mathbf{e}_\phi$$

$$= -(\nabla_p \pi^{(4)} + \nabla_s \pi^{(5)}) + \frac{\rho^{(2)}}{\rho^{(0)}} \nabla_s \pi^{(3)} - \phi_s \tan\phi_p (\nabla_s \pi^{(4)} + \nabla_p \pi^{(3)}) \tag{L.23}$$

where vertical velocities are not present as the continuity and thermodynamic equations show that $w^{(0,1,2,3)} = 0$. The terms with ϕ_s and ϕ_s^2 come from the Taylor expansions of $\cos\phi$ and $\sin\phi$ [see (4.2)-(4.4) in Dolaptchiev 2008]. Equation (L.23) is then used to derive the vorticity equation. Note that (L.22) does not imply a geostrophic balance for $\mathbf{u}^{(1)}$ as was the case in Chapter 2. Instead, $\mathbf{u}^{(1)}$ depends on $\mathbf{u}^{(0)}$ as well as the pressure gradients, which has implications for direct interactions between the synoptic, planetary and zonal mean flow components (see

below). The left-hand-side of (L.22) resembles the ageostrophic correction to geostrophic winds, i.e. $f_o \mathbf{e}_r \times \mathbf{u}_a + \beta y_s \mathbf{e}_r \times \mathbf{u}_g$, where subscripts a and g refer to ageostrophic and geostrophic components of wind, respectively [see also (6.10) in Holton (2004)].

Thermal wind balance

Using the hydrostatic balance (L.18)-(L.20) and momentum equations (L.21)-(L.22), we can derive the thermal wind balance as in Chapter 2. This yields

$$\frac{\partial u^{(0)}}{\partial z} = -f_o^{-1} \frac{\partial \theta^{(3)}}{\partial y_s} \tag{L.24}$$

$$\frac{\partial v^{(1)}}{\partial z} = -f_o^{-1} \frac{\partial \theta^{(4)}}{\partial x_s} - f_o^{-1} \frac{\partial \theta^{(3)}}{\partial x_p} \tag{L.25}$$

$$\frac{\partial u^{(1)}}{\partial z} = -f_o^{-1} \frac{\partial \theta^{(4)}}{\partial y_s} + \underbrace{\frac{\phi_s \cos\phi_p}{f_o^2} \frac{\partial \theta^{(3)}}{\partial y_s}}_{= -f_o^{-1} \phi_s \cos\phi_p \partial u^{(0)}/\partial z} . \tag{L.26}$$

Thermodynamic equation

The thermodynamic equation at fifth order only implies that $w^{(3)} = 0$, hence the sixth order thermodynamic equation is given only:

$$\mathcal{O}(\varepsilon^6): \qquad \left(\frac{\partial}{\partial t_s} + \frac{\partial}{\partial x_s}\right)\theta^{(4)} + \left(\frac{\partial}{\partial t_p} + \frac{\partial}{\partial x_p}\right)\theta^{(3)} + v^{(1)} \frac{\partial \theta^{(3)}}{\partial y_s} + w^{(4)} \frac{\partial \theta^{(2)}}{\partial z} = 0. \tag{L.27}$$

This equation is used to eliminate $w^{(4)}$ from the vorticity equation to obtain the PV equations.

Continuity equation

The continuity equations at different orders are:

$$\mathcal{O}(\varepsilon^0 - \varepsilon^2): \qquad \frac{\partial}{\partial z}\left(\rho^{(0)} w^{(i)}\right) = 0; \qquad i = 0, 1, 2 \tag{L.28}$$

$$\mathcal{O}(\varepsilon^3): \qquad \nabla_p \cdot (\rho^{(0)} \mathbf{u}^{(0)}) + \nabla_s \cdot (\rho^{(0)} \mathbf{u}^{(1)}) + \frac{\partial}{\partial z}\left(\rho^{(0)} w^{(3)}\right) = 0 \rightarrow \qquad w^{(3)} = 0 \tag{L.29}$$

where the latter follows from

$$\mathcal{O}(\varepsilon^3): \qquad \nabla_p \cdot (\rho^{(0)} \mathbf{u}^{(0)}) + \nabla_s \cdot (\rho^{(0)} \mathbf{u}^{(1)}) = 0 \tag{L.30}$$

and also from the thermodynamic equation at fifth order as mentioned above. The next order continuity equation that helps us eliminate $\mathbf{u}^{(2)}$ from the vorticity equation (see below) is

$$\mathcal{O}(\varepsilon^4): \quad \nabla_p \cdot (\rho^{(0)}\mathbf{u}^{(1)}) + \nabla_s \cdot (\rho^{(0)}\mathbf{u}^{(2)}) - \tan\phi_p \frac{\partial}{\partial y_s}\left(\rho^{(0)} v^{(1)} \phi_s\right) + \frac{\partial}{\partial z}\left(\rho^{(0)} w^{(4)}\right) = 0. \quad \text{(L.31)}$$

Here the extra term with ϕ_s again comes from the Taylor expansions [(4.2)-(4.4) in Dolaptchiev 2008].

Vorticity equation

To find the vorticity equation follow Chapter 2 and Dolaptchiev 2008. First take $\mathbf{e}_r \cdot \nabla_s \times$(L.23), which yields

$$\frac{\partial \zeta^{(1)}}{\partial t_s} + \frac{\partial \zeta^{(0)}}{\partial t_p} + \frac{\partial}{\partial x_s}\left(u^{(0)}\frac{\partial v^{(1)}}{\partial y_s}\right) - \frac{\partial}{\partial y_s}\left(u^{(0)}\frac{\partial u^{(1)}}{\partial x_s}\right) + \frac{\partial}{\partial x_s}\left(v^{(1)}\frac{\partial u^{(0)}}{\partial y_s}\right) - \frac{\partial}{\partial y_s}\left(\frac{1}{2}\frac{\partial u^{(0)2}}{\partial x_p}\right)$$
$$+ f_o \nabla_s \cdot \mathbf{u}^{(2)} + \phi_s \cos\phi_p \nabla_s \cdot \mathbf{u}^{(1)} + v^{(1)}\beta = \tan\phi_p f_o \frac{\partial}{\partial y_s}\left(\phi_s v^{(1)}\right) + \frac{\partial^2 \pi^{(4)}}{\partial x_p \partial y_s} \quad \text{(L.32)}$$

where $\zeta^{(1)} = \frac{\partial v^{(1)}}{\partial x_s} - \frac{\partial u^{(1)}}{\partial \tilde{y}_s}$, $\zeta^{(0)} = -\frac{\partial u^{(0)}}{\partial \tilde{y}_s}$, and recall that $u^{(1)}$ is related to $u^{(0)}$ via (L.22). As $\mathbf{u}^{(2)}$ is unknown, we use the continuity equation (L.31) to eliminate it (which also eliminates some other terms). This gives

$$\frac{\partial \zeta^{(1)}}{\partial t_s} + \frac{\partial \zeta^{(0)}}{\partial t_p} + \frac{\partial}{\partial x_s}\left(u^{(0)}\frac{\partial v^{(1)}}{\partial y_s}\right) - \frac{\partial}{\partial y_s}\left(u^{(0)}\frac{\partial u^{(1)}}{\partial x_s}\right) + \frac{\partial}{\partial x_s}\left(v^{(1)}\frac{\partial u^{(0)}}{\partial y_s}\right)$$
$$- \frac{\partial}{\partial y_s}\left(\frac{1}{2}\frac{\partial u^{(0)2}}{\partial x_p}\right) + \frac{\partial}{\partial x_p}\left(\phi_s \cos\phi_p u^{(0)}\right) - \frac{f_o}{\rho^{(0)}}\frac{\partial}{\partial z}\left(\rho^{(0)} w^{(4)}\right) + \nabla_s \cdot \left(\phi_s \cos\phi_p \mathbf{u}^{(1)}\right) = 0. \quad \text{(L.33)}$$

Here note that

$$\frac{\partial}{\partial x_p}\left(\phi_s \cos\phi_p u^{(0)}\right) + \nabla_s \cdot \left(\phi_s \cos\phi_p \mathbf{u}^{(1)}\right) = \beta v^{(1)} \quad \text{(L.34)}$$

with $\beta = \cos\phi_p / a$, and the other terms vanish via (L.30).

L. OTHER MULTISCALE ASYMPTOTIC REGIMES AND WAVE ACTIVITY THEORY

PV equations

To further eliminate the unknown $w^{(4)}$ in (L.33) we can use the thermodynamic equation (L.27), which together with the thermal wind balance (L.24)-(L.25) gives the PV equation

$$\left(\frac{\partial}{\partial t_s}+\frac{\partial}{\partial x_s}\right)q_s^{(4)}+v_s^{(1)}\left(\beta+\frac{\partial\zeta^{(0)}}{\partial y_s}\right)=\left(\frac{\partial}{\partial t_p}+\frac{\partial}{\partial x_p}\right)q_p^{(3)}+v_p^{(1)}\left(\beta+\frac{\partial\zeta^{(0)}}{\partial y_s}\right) \tag{L.35}$$

with

$$q_s^{(4)}=\zeta^{(1)}+\frac{f_o}{\rho^{(0)}}\frac{\partial}{\partial z}\left(\frac{\rho^{(0)}\theta^{(4)}}{\partial\theta^{(2)}/\partial z}\right) \tag{L.36}$$

$$q_p^{(3)}=\zeta^{(0)}+\frac{f_o}{\rho^{(0)}}\frac{\partial}{\partial z}\left(\frac{\rho^{(0)}\theta^{(3)}}{\partial\theta^{(2)}/\partial z}\right). \tag{L.37}$$

Equation (L.35) can then be further split into planetary and synoptic components by averaging over λ_s, t_s as in section L.2, yielding

Planetary scale PV

$$\left(\frac{\partial}{\partial t_p}+\frac{\partial}{\partial x_p}\right)q_p^{(3)}+v_p^{(1)}\hat{\beta}=0 \tag{L.38}$$

Synoptic scale PV

$$\left(\frac{\partial}{\partial t_s}+\frac{\partial}{\partial x_s}\right)q_s^{(4)}+v_s^{(1)}\hat{\beta}=0 \tag{L.39}$$

where $\hat{\beta}=\beta+\frac{\partial\zeta^{(0)}}{\partial y_s}$ is the background PV gradient. Notice that the background PV gradient and planetary scale PV share $\zeta^{(0)}$, i.e. zonal mean flow and planetary scale waves share vorticity; also note again that $\zeta^{(1)}$ is related to $\zeta^{(0)}$ via (L.22). This means that the PV of the background flow, planetary PV and synoptic PV are all related.

The background PV gradient in this case only involves the beta-parameter (β) and the vorticity gradient ($\partial\zeta^{(0)}/\partial y_s=-\partial^2u^{(0)}/\partial y_s^2$), i.e. it only represents barotropic instability. However, given that $\zeta^{(0)}$ is present also in the planetary PV equation (as well as synoptic), baroclinic instability must be present through those processes [via the stretching terms in (L.36)-(L.37)]. Note that this is a consequence of the initial assumption (L.16), where $\theta^{(2)}$ depends only on the vertical coordinate and not on the horizontal ones, leading to $\partial\theta^{(2)}/\partial y_s=0$. The dependence of the static stability (related to $\partial\theta^{(2)}/\partial z$) on vertical coordinate only is also assumed in the

QG system though there the background PV gradient involves the stretching term, but there is no planetary PV. Hence, one could view the planetary PV and background PV as the QG background flow.

Enstrophy and wave activity equations

The enstrophy equation can be obtained by multiplying (L.38) and (L.39) by $q_p^{(3)}$ and $q_s^{(4)}$, respectively, yielding

Planetary scale enstrophy

$$\left(\frac{\partial}{\partial t_p}+\frac{\partial}{\partial x_p}\right)\frac{q_p^{(3)2}}{2}+q_p^{(3)}v_p^{(1)}\hat{\beta}=0 \tag{L.40}$$

Synoptic scale enstrophy

$$\left(\frac{\partial}{\partial t_s}+\frac{\partial}{\partial x_s}\right)\frac{q_s^{(4)2}}{2}+q_s^{(4)}v_s^{(1)}\hat{\beta}=0. \tag{L.41}$$

Notice that the meridional eddy enstrophy flux is not present in this small amplitude limit compared with the finite amplitude case, and is also absent in the isotropic small amplitude regime [Chapter 2]. This suggests that the finite amplitude limit must be used to explain the eddy enstrophy flux signal found in Birner et al. (2013), who also mentioned it. Also, unlike in the isotropic small amplitude limit of Chapter 2, the PV and entrophy equations are here linked through the $u^{(0)}$, which appears in the background PV gradient as well as in the synoptic and planetary PVs/entrophies as already mentioned above.

To derive the wave activity equations for the planetary and synoptic waves, we must divide (L.40)-(L.41) by the background PV gradient ($\hat{\beta}$) and multiply equations by $\rho^{(0)}$, which gives

Planetary scale wave activity

$$\frac{\partial \mathcal{A}_p}{\partial t_p}+\nabla_p^{3D}\cdot\mathbf{F}_p=-\frac{\mathcal{A}_p}{\hat{\beta}}\left(\frac{\partial \hat{\beta}}{\partial t_p}+\frac{\partial u^{(0)}\hat{\beta}}{\partial x_p}\right) \tag{L.42}$$

Synoptic scale wave activity

$$\frac{\partial \mathcal{A}_s}{\partial t_s}+\nabla_s^{3D}\cdot\mathbf{F}_s=0 \tag{L.43}$$

with

$$\mathcal{A}_p = \frac{\rho^{(0)} q_p^{(3)2}}{2\hat{\beta}}; \qquad \mathcal{A}_s = \frac{\rho^{(0)} q_s^{(4)2}}{2\hat{\beta}} \tag{L.44}$$

$$\nabla_p^{3D} = \left(\frac{\partial}{\partial x_p}, \frac{\partial}{\partial y_s}, \frac{\partial}{\partial z}\right); \qquad \nabla_s^{3D} = \left(\frac{\partial}{\partial x_s}, \frac{\partial}{\partial y_s}, \frac{\partial}{\partial z}\right) \tag{L.45}$$

$$\mathbf{F}_s = \left[u^{(0)}\mathcal{A}_p + \frac{\rho^{(0)}}{2}\left(v_s^{(1)2} - u^{(1)2} - \frac{\theta^{(4)2}}{\partial\theta^{(2)}/\partial z}\right), -\rho^{(0)} u^{(1)} v_s^{(1)}, \frac{f_o \rho^{(0)} \theta^{(4)} v_s^{(1)}}{\partial\theta^{(2)}/\partial z}\right] \tag{L.46}$$

$$\mathbf{F}_p = \left[u^{(0)}\mathcal{A}_s - \frac{\rho^{(0)}}{2}\left(u^{(0)2} + \frac{\theta^{(3)2}}{\partial\theta^{(2)}/\partial z}\right), -\rho^{(0)} u^{(0)} v_p^{(1)}, \frac{f_o \rho^{(0)} \theta^{(3)} v_p^{(1)}}{\partial\theta^{(2)}/\partial z}\right]. \tag{L.47}$$

While the synoptic scale wave activity equation (L.43) resembles the isotropic wave activity equation (2.13), the planetary wave activity has additional mean flow forcing (through $\hat{\beta}$) on the right hand side of (L.42), and the EP flux ($\mathbf{F}_p$) includes the momentum flux term that was absent in the isotropic limit. There is also a difference in $u^{(1)}$ that is present in the EP flux ($\mathbf{F}_s$) as it includes $u^{(0)}$ as mentioned above.

In order to complete the equation sets presented in this Appendix, we should link the wave activity equations to the mean flow equations (e.g. transformed Eulerian mean and non-acceleration theorem), and for the finite amplitude limit also consider using the Hamiltonian structure. This is left for future work.

Bibliography

Ambaum, M. H. P., 2004: Calculating EOFs and principal component time-series. Technical report, University of Reading.

— 2010: *Thermal physics of the atmosphere*. John Wiley & Sons, Ltd, 239 pp.

Ambaum, M. H. P., B. J. Hoskins, and D. B. Stephenson, 2001: Arctic Oscillation or North Atlantic Oscillation? *J. Atmos. Sci.*, **14**, 3495–3507.

Ambaum, M. H. P. and L. Novak, 2014: A nonlinear oscillator describing storm track variability. *Quart. J. Roy. Meteor. Soc.*, **140**, 2680–2684.

Ambrizzi, T., B. J. Hoskins, and H.-H. Hsu, 1995: Rossby wave propagation and teleconnection patterns in the austral winter. *J. Atmos. Sci.*, **52**, 3661–3672.

Andrews, D. G., J. R. Holton, and C. B. Leovy, 1987: *Middle atmosphere dynamics*. Academic Press, 489 pp.

Andrews, D. G. and M. E. McIntyre, 1976: Planetary waves in horizontal and vertical shear: the generalized eliassen-palm relation and the mean zonal acceleration. *J. Atmos. Sci.*, **33**, 2031–2048.

Barnston, A. G. and R. E. Livezey, 1987: Classification, seasonality and persistence of low-frequency atmospheric circulation patterns. *Mon. Wea. Rev.*, **115**, 1083–1126.

Birner, T., D. W. J. Thompson, and T. G. Shepherd, 2013: Upgradient eddy fluxes of potential vorticity near the subtropical jet. *Geophys. Res. Lett.*, **40**, 5988–5993, doi:10.1002/2013GL057728.

Blanco-Fuentes, J. and P. Zurita-Gotor, 2011: The driving of baroclinic anomalies at different timescales. *Geophys. Res. Lett.*, **38**, 1–7, doi:10.1029/2011GL049785, l23805.

Bloomfield, P., 2000: *Fourier analysis of time series: an introduction*. Wiley, 286 pp.

Boljka, L. and T. G. Shepherd, 2018: A multiscale asymptotic theory of extratropical wave-mean flow interaction. *J. Atmos. Sci.*, **75**, 1833–1852, doi:10.1175/JAS-D-17-0307.1.

BIBLIOGRAPHY

Boljka, L., T. G. Shepherd, and M. Blackburn, 2018: On the coupling between barotropic and baroclinic modes of extratropical atmospheric variability. *J. Atmos. Sci.*, **75**, 1853–1871, doi:10.1175/JAS-D-17-0370.1.

Boutle, I. A., S. E. Belcher, and R. S. Plant, 2011: Moisture transport in midlatitude cyclones. *Quart. J. Roy. Meteor. Soc.*, **137**, 360–373, doi:10.1002/qj.783.

Branstator, G., 1995: Organization of storm track anomalies by recurring low-frequency circulation anomalies. *J. Atmos. Sci.*, **52**, 207–226.

Brayshaw, D. J., B. Hoskins, and M. Blackburn, 2009: The basic ingredients of the North Atlantic storm track. Part I: Land-sea contrast and orography. *J. Atmos. Sci.*, **66**, 2539–2558, doi:10.1175/2009JAS3078.1.

Byrne, N. J., T. G. Shepherd, T. Woollings, and R. A. Plumb, 2016: Annular modes and apparent eddy feedbacks in the southern hemisphere. *Geophys. Res. Lett.*, **43**, 3897–3902, doi:10.1002/2016GL068851.

Cai, M. and M. Mak, 1990: Symbiotic relation between planetary and synoptic-scale waves. *J. Atmos. Sci.*, **47**, 2953–2968.

Cai, M., S. Yang, H. M. van den Dool, and V. E. Kousky, 2007: Dynamical implications of the orientation of atmospheric eddies: a local energetics perspective. *Tellus A*, **59**, 127–140, doi:10.1111/j.1600-0870.2006.00213.x.

Chang, E. K. M., 2005: The impact of wave packets propagating across asia on pacific cyclone development. *Mon. Wea. Rev.*, **133**, 1998–2015, doi:10.1175/MWR2953.1.

Chang, E. K. M. and D. B. Yu, 1999: Characteristics of wave packets in the upper troposphere. part i: Northern hemisphere winter. *J. Atmos. Sci.*, **56**, 1708–1728.

Charney, J. G. and M. E. Stern, 1962: On the stability of internal baroclinic jets in a rotating atmosphere. *J. Atmos. Sci.*, **19**, 159–172.

Dee, D. P., S. M. Uppala, A. J. Simmons, P. Berrisford, P. Poli, S. Kobayashi, U. Andrae, M. A. Balmaseda, G. Balsamo, P. Bauer, P. Bechtold, A. C. M. Beljaars, L. van de Berg, J. Bidlot, N. Bormann, C. Delsol, R. Dragani, M. Fuentes, A. J. Geer, L. Haimberger, S. B. Healy, H. Hersbach, E. V. Hlm, L. Isaksen, P. Kllberg, M. Khler, M. Matricardi, A. P. McNally, B. M. Monge-Sanz, J.-J. Morcrette, B.-K. Park, C. Peubey, P. de Rosnay, C. Tavolato, J.-N. Thpaut, and F. Vitart, 2011: The ERA-Interim reanalysis: configuration and performance of the data assimilation system. *Quart. J. Roy. Meteor. Soc.*, **137**, 553 – 597, doi:10.1002/qj.828.

Dolaptchiev, S. I., 2008: *Asymptotic Models for Planetary Scale Atmosheric Motions*. Ph.D. thesis, Free University Berlin.

Dolaptchiev, S. I. and R. Klein, 2009: Planetary geostrophic equations for the atmosphere with evolution of the barotropic flow. *Dyn. Atmos. Oceans*, **46**, 46–61.

— 2013: A multiscale model for the planetary and synoptic motions in the atmosphere. *J. Atmos. Sci.*, **70**, 2963–2981.

Donohoe, A. and D. S. Battisti, 2009: The amplitude asymmetry between synoptic cyclones and anticyclones: Implications for filtering methods in feature tracking. *Mon. Wea. Rev.*, **137**, 3874–3887, doi:10.1175/2009MWR2837.1.

Drouard, M., G. Rivire, and P. Arbogast, 2015: The link between the north pacific climate variability and the north atlantic oscillation via downstream propagation of synoptic waves. *J. Climate*, **28**, 3957–3976, doi:10.1175/JCLI-D-14-00552.1.

Duchon, C. E., 1979: Lanczos filtering in one and two dimensions. *J. Appl. Meteor.*, **19**, 1016–1022.

Dwyer, J. G. and P. A. O'Gorman, 2017: Moist formulations of the Eliassen-Palm flux and their connection to the surface westerlies. *J. Atmos. Sci.*, **74**, 513–530, doi:10.1175/JAS-D-16-0111.1.

Edmon, H. J., B. J. Hoskins, and M. E. McIntyre, 1980: Eliassen-Palm cross sections for the troposphere. *J. Atmos. Sci.*, **37**, 2600–2616.

Eliassen, A. and E. Palm, 1961: On the transfer of energy in stationary mountain waves. *Geofys. Pub.*, **22**, 1–3.

Gerber, E. P., S. Voronin, and L. M. Polvani, 2008: Testing the annular mode autocorrelation time scale in simple atmospheric general circulation models. *Mon. Wea. Rev.*, **136**, 1523–1536, doi:10.1175/2007MWR2211.1.

Haidvogel, D. B. and I. M. Held, 1980: Homogeneous quasi-geostrophic turbulence driven by a uniform temperature gradient. *J. Atmos. Sci.*, **37**, 2644–2660.

Haigh, J. D., M. Blackburn, and R. Day, 2005: The response of tropospheric circulation to perturbations in lower-stratospheric temperature. *J. Climate*, **18**, 3672–3685, doi:10.1175/JCLI3472.1.

Hartmann, D. L. and F. Lo, 1998: Wave-driven zonal flow vacillation in the Southern Hemisphere. *J. Atmos. Sci.*, **55**, 1303–1315.

Haynes, P. H. and T. G. Shepherd, 1989: The importance of surface pressure changes in the response of the atmosphere to zonally-symmetric thermal and mechanical forcing. *Quart. J. Roy. Meteor. Soc.*, **115**, 1181–1208.

Held, I. M., 2005: The gap between simulation and understanding in climate modeling. *Bull. Am. Meteorol. Soc.*, **86**, 1609 1614.

Held, I. M. and B. J. Hoskins, 1985: Large-scale eddies and the general circulation of the troposphere. *Issues in Atmospheric and Oceanic Modeling*, B. Saltzman, ed., Elsevier, volume 28 of *Advances in Geophysics*, 3 – 31.

Held, I. M., R. L. Panetta, and R. T. Pierrehumbert, 1985: Stationary external rossby waves in vertical shear. *J. Atmos. Sci.*, **42**, 865–883.

Held, I. M. and M. J. Suarez, 1994: A proposal for the intercomparison of the dynamical cores of atmospheric general circulation models. *Bull. Amer. Meteor. Soc.*, **75**, 1825–1830.

Holton, J. R., 2004: *An introduction to dynamic meteorology*. Elsevier Inc., fourth edition, 535 pp.

Honda, M. and H. Nakamura, 2001: Interannual seesaw between the aleutian and icelandic lows. part ii: Its significance in the interannual variability over the wintertime northern hemisphere. *J. Climate*, **14**, 4512–4529.

Honda, M., H. Nakamura, J. Ukita, I. Kousaka, and K. Takeuchi, 2001: Interannual seesaw between the aleutian and icelandic lows. part i: Seasonal dependence and life cycle. *J. Climate*, **14**, 1029–1042.

Honda, M., S. Yamane, and H. Nakamura, 2007: Inter-basin link between the north pacific and north atlantic in the upper tropospheric circulation: Its dominance and seasonal dependence. *J. Meteor. Soc. Japan. Ser. II*, **85**, 899–908, doi:10.2151/jmsj.85.899.

Hoskins, B. J. and T. Ambrizzi, 1993: Rossby wave propagation on a realistic longitudinally varying flow. *J. Atmos. Sci.*, **50**, 1661–1671.

Hoskins, B. J. and K. I. Hodges, 2002: New perspectives on the northern hemisphere winter storm tracks. *J. Atmos. Sci.*, **59**, 1041–1061.

Hoskins, B. J. and I. N. James, 2014: *Fluid dynamics of the midlatitude atmosphere*. John Wiley & Sons, Ltd, 408 pp.

Hoskins, B. J., I. N. James, and G. White, 1983: The shape, propagation and mean-flow interaction of large-scale weather systems. *J. Atmos. Sci.*, **40**, 1595–1612.

Hoskins, B. J. and P. J. Valdes, 1990: On the existence of storm-tracks. *J. Atmos. Sci.*, **47**, 1854–1864.

Huang, C. S. Y. and N. Nakamura, 2017: Local wave activity budgets of the wintertime Northern Hemisphere: Implication for the Pacific and Atlantic storm tracks. *Geophys. Res. Lett.*, **44**, 5673–5682, doi:10.1002/2017GL073760.

James, I. N., 1994: *Introduction to circulating atmospheres*. Cambridge University Press, 422 pp.

Kalnay, E., M. Kanamitsu, R. Kistler, W. Collins, D. Deaven, L. Gandin, M. Iredell, S. Saha, G. White, J. Woollen, Y. Zhu, M. Chelliah, W. Ebisuzaki, W. Higgins, J. Janowiak, K. C. Mo, C. Ropelewski, J. Wang, A. Leetmaa, R. Reynolds, R. Jenne, and D. Joseph, 1996: The NCEP/NCAR 40-year reanalysis project. *Bull. Amer. Meteor. Soc.*, **77**, 437–472.

Kaspi, Y. and T. Schneider, 2011: Downstream self-destruction of storm tracks. *J. Atmos. Sci.*, **68**, 2459–2464, doi:10.1175/JAS-D-10-05002.1.

— 2013: The role of stationary eddies in shaping midlatitude storm tracks. *J. Atmos. Sci.*, **70**, 2596–2613, doi:10.1175/JAS-D-12-082.1.

Kidson, J. W., 1988: Indices of the Southern Hemisphere zonal wind. *J. Climate*, **1**, 183–194.

Klein, R., 2000: Asymptotic analyses for atmospheric flows and the construction of asymptotically adaptive numerical methods. *Zeitschr. Angew. Math. Mech.*, **80**, 765–770.

— 2004: An applied mathematical view of theoretical meteorology. in Applied Mathematics Entering the 21st Century, invited talks at the ICIAM 2003 Conference (J.M. Hill and R. Moore, eds.). *SIAM proceedings in Applied Mathematic*, **116**, 177–219.

Lorenz, D. J. and D. L. Hartmann, 2001: Eddy-zonal flow feedback in the southern hemisphere. *J. Atmos. Sci.*, **58**, 3312–3327.

— 2003: Eddyzonal flow feedback in the northern hemisphere winter. *J. Climate*, **16**, 1212–1227.

Lorenz, E. N., 1955: Available potential energy and the maintenance of the general circulation. *Tellus*, **7**, 157–167.

Luo, D., 2005: A barotropic Rossby soliton model for block-eddy interaction. part I: Effect of topography. *J. Atmos. Sci.*, **62**, 5–21.

Luo, D., A. R. Lupo, and H. Wan, 2007: Dynamics of eddy-driven low-frequency dipole modes. part I: A simple model of North Atlantic Oscillations. *J. Atmos. Sci.*, **64**, 3–28, doi:10.1175/JAS3818.1.

Marques, C. A. F., A. Rocha, J. a. CorteReal, J. M. Castanheira, J. Ferreira, and P. MeloGon¸calves, 2009: Global atmospheric energetics from NCEP-reanalysis 2 and ECMWF-ERA40 reanalysis. *Int. J. Climatol.*, **29**, 159–174, doi:10.1002/joc.1704.

NASA, 1976: *U.S. Standard atmosphere*. U.S. Government Printing Office, 227 pp.

Neale, R. B. and B. J. Hoskins, 2000: A standard test for AGCMs including their physical parametrizations: I: the proposal. *Atmosph. Sci. Lett.*, **1**, 101–107.

Pedlosky, J., 1970: Finite-amplitude baroclinic waves. *J. Atmos. Sci.*, **27**, 15–30.

— 1987: *Geophysical Fluid Dynamics*. Springer: New York, NY, 710 pp.

Pfeffer, R. L., 1987: Comparison of conventional and transformed Eulerian diagnostics in the troposphere. *Quart. J. Roy. Meteor. Soc.*, **113**, 237–254.

— 1992: A study of eddy-induced fluctuations of the zonal-mean wind using conventional and transformed Eulerian diagnostics. *J. Atmos. Sci.*, **49**, 1036–1050.

Phillips, N. A., 1963: Geostrophic motion. *Rev. Geophys.*, **1**, 123–175.

Plumb, R. A., 1983: A new look at the energy cycle. *J. Atmos. Sci.*, **40**, 1669–1688.

— 1985: On the three-dimensional propagation of stationary waves. *J. Atmos. Sci.*, **42**, 217–229.

— 1986: Three-dimensional propagation of transient quasi-geostrophic eddies and its relationship with the eddy forcing of the time-mean flow. *J. Atmos. Sci.*, **43**, 1657–1678.

Polvani, L. M. and P. J. Kushner, 2002: Tropospheric response to stratospheric perturbations in a relatively simple general circulation model. *Geophys. Res. Lett.*, **29**, 18–1–18–4.

Robinson, W. A., 2000: A baroclinic mechanism for the eddy feedback on the zonal index. *J. Atmos. Sci.*, **57**, 415–422.

Rodionov, S. N., J. E. Overland, and N. A. Bond, 2005: The aleutian low and winter climatic conditions in the bering sea. part i: Classification. *J. Climate*, **18**, 160–177, doi:10.1175/JCLI3253.1.

Shaw, T. A., M. Baldwin, E. A. Barnes, R. Caballero, C. I. Garfinkel, Y.-T. Hwang, C. Li, P. A. O'Gorman, G. Rivire, I. R. Simpson, and A. Voigt, 2016: Storm track processes and the opposing influences of climate change. *Nature Geoscience*, **9**, 656–664, doi:10.1038/ngeo2783.

Shepherd, T. G., 1990: Symmetries, conservation laws, and hamiltonian structure in geophysical fluid dynamics. *Adv. Geophys*, **32**, 287–338.

— 2014: Atmospheric circulation as a source of uncertainty in climate change projections. *Nature Geoscience*, **7**, 703–708.

Sheshadri, A. and R. A. Plumb, 2017: Propagating annular modes: Empirical orthogonal functions, principal oscillation patterns, and time scales. *J. Atmos. Sci.*, **74**, 1345–1361, doi:10.1175/JAS-D-16-0291.1.

Sheshadri, A., R. A. Plumb, and E. P. Gerber, 2015: Seasonal variability of the polar stratospheric vortex in an idealised AGCM with varying tropospheric wave forcing. *J. Atmos. Sci.*, **72**, 2248–2266.

Simmons, A. J. and B. J. Hoskins, 1978: The life cycles of some nonlinear baroclinic waves. *J. Atmos. Sci.*, **35**, 414–432.

Simpson, I. R., P. Hitchcock, T. G. Shepherd, and J. F. Scinocca, 2011: Stratospheric variability and tropospheric annular-mode timescales. *Geophys. Res. Lett.*, **38**, 1–6, doi:10.1029/2011GL049304, l20806.

Simpson, I. R., T. A. Shaw, and R. Seager, 2014: A diagnosis of the seasonally and longitudinally varying midlatitude circulation response to global warming. *J. Atmos. Sci.*, **71**, 2489–2515.

Sparrow, S., M. Blackburn, and J. D. Haigh, 2009: Annular variability and eddy-zonal flow interactions in a simplified atmospheric GCM. part I: characterization of high- and low-frequency behaviour. *J. Atmos. Sci.*, **66**, 3075–3094.

Thompson, D. W. J. and E. A. Barnes, 2014: Periodic variability in the large-scale Southern Hemisphere atmospheric circulation. *Science*, **343**, 641–645.

Thompson, D. W. J., B. R. Crow, and E. A. Barnes, 2017: Intraseasonal periodicity in the Southern Hemisphere circulation on regional spatial scales. *J. Atmos. Sci.*, **74**, 865–877, doi:10.1175/JAS-D-16-0094.1.

Thompson, D. W. J. and Y. Li, 2015: Baroclinic and barotropic annular variability in the Northern Hemisphere. *J. Atmos. Sci.*, **72**, 1117–1136.

Thompson, D. W. J. and J. M. Wallace, 2000: Annular modes in the extratropical circulation. part i: Month-to-month variability. *J. Clim.*, **13**, 1000–1016.

Thompson, D. W. J. and J. D. Woodworth, 2014: Barotropic and baroclinic annular variability in the Southern Hemisphere. *J. Atmos. Sci.*, **71**, 1480–1493.

Thorncroft, C. D., B. J. Hoskins, and M. E. McIntyre, 1993: Two paradigms of baroclinic-wave life-cycle behaviour. *Quart. J. Roy. Meteor. Soc.*, **119**, 17–55, doi:10.1002/qj.49711950903.

Valdes, P. J. and B. J. Hoskins, 1989: Linear stationary wave simulations of the time-mean climatological flow. *J. Atmos, Sci.*, **46**, 2509–2527.

— 1991: Nonlinear orographically forced planetary waves. *J. Atmos. Sci.*, **48**, 2089–2106.

Vallis, G. K., 2006: *Atmospheric and Oceanic Fluid Dynamics*. Cambridge University Press, 745 pp.

Vallis, G. K., E. P. Gerber, P. J. Kushner, and B. A. Cash, 2004: A mechanism and simple dynamical model of the North Atlantic Oscillation and annular modes. *J. Atmos. Sci.*, **61**, 264–280.

van Niekerk, A., J. F. Scinocca, and T. G. Shepherd, 2017: The modulation of stationary waves, and their response to climate change, by parameterized orographic drag. *J. Atmos. Sci.*, **74**, 2557–2574, doi:10.1175/JAS-D-17-0085.1.

Wallace, J. M. and D. S. Gutzler, 1981: Teleconnections in the geopotential height field during the northern hemisphere winter. *Mon. Wea. Rev.*, **109**, 784–812.

Wallace, J. M., G.-H. Lim, and M. L. Blackmon, 1988: Relationship between cyclone tracks, anticyclone tracks and baroclinic waveguides. *J. Atmos. Sci.*, **45**, 439–462.

Walters, D., N. Wood, S. Vosper, and S. Milton, 2014: ENDGame: A new dynamical core for seamless atmospheric prediction. Technical report, Met Office.

Wang, L., J. Lu, and Z. Kuang, 2018: A robust increase of the intraseasonal periodic behavior of the precipitation and eddy kinetic energy in a warming climate. *Geophys. Res. Lett.*, in press, doi:10.1029/2018GL078495.

Wang, L. and N. Nakamura, 2015: Covariation of finite-amplitude wave activity and the zonal mean flow in the midlatitude troposphere: 1. Theory and application to the Southern Hemisphere summer. *Geophys. Res. Lett.*, **42**, 8192–8200.

— 2016: Covariation of finite-amplitude wave activity and the zonal-mean flow in the midlatitude troposphere. Part II: Eddy forcing spectra and the periodic behavior in the Southern Hemisphere summer. *J. Atmos. Sci.*, **73**, 4731–4752, doi:10.1175/JAS-D-16-0091.1.

Williamson, D. L., M. Blackburn, K. Nakajima, W. Ohfuchi, Y. O. Takahashi, Y.-Y. Hayashi, H. Nakamura, M. Ishiwatari, J. L. McGregor, H. Borth, V. Wirth, H. Frank, P. Bechtold, N. P. Wedi, H. Tomita, M. Satoh, M. Zhao, I. M. Held, M. J. Suarez, M.-I. Lee, M. Watanabe, M. Kimoto, Y. Liu, Z. Wang, A. Molod, K. Rajendran, A. Kitoh, and R. Stratton, 2013: The aqua-planet experiment (APE): Response to changed meridional SST profile. *J. Meteor. Soc. Japan*, **91A**, 57–89.

Woollings, T., A. Hannachi, and B. J. Hoskins, 2010: Variability of the North Atlantic eddy-driven jet stream. *Quart. J. Roy. Meteor. Soc.*, **136**, 856–868, doi:10.1002/qj.625.

Zurita-Gotor, P., 2017: Low-frequency suppression of Southern Hemisphere tropospheric eddy heat flux. *Geophys. Res. Lett.*, **44**, 2007–2015, doi:10.1002/2016GL072247.